

Disorder-free non-ergodic quantum dynamics in Noisy Intermediate Scale Quantum devices

Dissertation

zur Erlangung des akademischen Grades
doctor rerum naturalium
(Dr. rer. nat.)



vorgelegt

dem Fachbereich für Physik, Mathematik und Informatik
der Johannes Gutenberg-Universität Mainz

Riccardo Javier Valencia Tortora
geboren am July 14 1995 in Rom, Italien

Mainz, den December 4, 2024

Riccardo Javier Valencia Tortora
Institut für Physik
Komet 7
Johannes Gutenberg-Universität Mainz
Staudingerweg 7
55128 Mainz

D77 / Dissertation der Johannes Gutenberg-Universität Mainz

Datum der mündlichen Prüfung: 22. November 2024

ABSTRACT. We are currently living in an exciting era, where long sought quantum phenomena are starting to be simulated in synthetic quantum systems, fulfilling the original idea by Feynman behind quantum computers:

“Nature isn’t classical, dammit, and if you want to make a simulation of Nature, you’d better make it quantum mechanical, and by golly it’s a wonderful problem because it doesn’t look so easy.”

R. P. Feynmann

However, despite the huge success of current platforms, all of them suffer from a common problem: scalability and noise. Indeed, current platforms are limited to 100 quantum constituents (e.g. qubits) in the best case scenarios, and the inevitable coupling to the environment leads to uncontrolled errors. The problem of noisy and relatively small available platforms permeates the community so much that our time has been termed as the *Noisy-Intermediate-Scale-Quantum* (NISQ) era by J. Preskill. Overcoming such problems constitutes the current biggest challenge in the field. Additionally, the difficulty in robustly storing quantum information represents an important limiting factor that mitigates the large-scale adoption of modern quantum technologies. Indeed, even without external sources of decoherence, interacting quantum systems generally tend to *thermalize* making most of the memory effectively lost, except the one contained in the (typically few) conserved quantities, in agreement with statistical mechanics. However, there exist mechanisms that can prevent the onset of thermalization, and thus make the above picture not true. This opens up the possibility that local quantum information could be passively protected, since dynamics would be not able to wash the memory of the initial state. This thesis goes in this direction, focusing on non-ergodicity in quantum systems and their possible application in aiding quantum information tasks. Specifically, we discuss different ergodicity-breaking mechanisms displayed in simple translationally invariant models, known as Kinetically Constrained Models. We then explore potential ways for leveraging these ergodicity-breaking properties, particularly in the protection of quantum information and in the preparation of states useful for quantum information tasks, such as the multi-mode version of bosonic Gaussian states. Then, we demonstrate the practical relevance of these models by providing routes for implementing them in current NISQ devices based on Rydberg atoms and superconducting circuits.

List of Publications

Part I and Part II are based on the following publications:

- [1] “*Kinetically Constrained Quantum Dynamics in Superconducting Circuits*” (PRX Quantum 3, 020346 (2022)).
Riccardo J. Valencia-Tortora, Nicola Pancotti, Jamir Marino.
- [2] “*State-dependent mobility edge in kinetically constrained models*” (arXiv: 2407.12909; to appear in Phys. Rev. X Quantum)
Manthan Badbaria, Nicola Pancotti, Rajeev Singh, Jamir Marino, and **Riccardo J. Valencia-Tortora**.
- [3] “*Rydberg platform for non-ergodic chiral quantum dynamics*” (Phys. Rev. Lett. 132, 223201 (2024))
Riccardo J. Valencia-Tortora, Nicola Pancotti, Michael Fleischhauer, Hannes Bernien, Jamir Marino.

Part III is based on the following publication:

- [4] “*Crafting the dynamical structure of synchronization by harnessing bosonic multilevel cavity QED*” (Phys. Rev. Research 5, 023112 (2023), Editors’ Suggestion)
Riccardo J. Valencia-Tortora, Shane P. Kelly, Tobias Donner, Giovanna Morigi, Rosario Fazio, Jamir Marino.

Other articles published during the Ph.D. course:

- [5] “*Relaxation of the order-parameter statistics and dynamical confinement*” (Europhysics Letters (2020))
Riccardo J. Valencia-Tortora, Pasquale Calabrese, Mario Collura.
- [6] “*Zeno crossovers in the entanglement speed of spin chains with noisy impurities*” (J. Stat. Mech. (2022) 103101)
Abhijit P. Chaudhari, Shane P. Kelly, **Riccardo J. Valencia-Tortora**, Jamir Marino.
- [7] “*Zeno physics of the Ising chain with symmetry-breaking boundary dephasing*” (arXiv:2404.04255; to be submitted to Phys. Rev. B)
Umar Javed, **Riccardo J. Valencia-Tortora**, Jamir Marino, Vadim Oganesyan, Michael Kolodrubetz.

Contents

List of Publications	v
Chapter 1. Introduction	1
Chapter 2. Quantum Thermalization	5
2.1. An operatorial definition	5
2.2. Entanglement and thermalization	7
2.3. The Eigenstate Thermalization Hypothesis	8
2.4. A different route: from states to operators	11
2.5. Consequences of thermalization	12
Part I. Escaping the doom of thermalization	13
Chapter 3. Utilizing localization in bosonic systems	19
3.1. The bosonic Quantum East Model	21
3.2. Localization transition	23
3.3. Localized states engineering	32
3.4. Impact of coupling to the environment	40
3.5. Perspectives	47
Chapter 4. Mobility edge in a translational invariant system	49
4.1. Quantum East model	50
4.2. Does the system display a mobility edge?	52
4.3. Dynamical proxy of non-thermal eigenstates	55
4.4. State-dependent mobility edge	57
4.5. Connection with random unitary circuits	69
4.6. Discussion and Perspectives	70
Chapter 5. Beyond localization: quantum many-body scars, confinement, and Hilbert space shattering	73
5.1. A universal model for different ergodicity-breaking mechanisms	74
5.2. Hilbert space fragmentation and Krylov restricted thermalization	77
5.3. From quantum many-body scars to confinement and localization	80
Part II. Realizing ergodicity-breaking mechanisms in NISQ devices	85

Chapter 6. A Rydberg platform for non-ergodic chiral quantum dynamics	89
6.1. Why Rydberg atoms?	90
6.2. Chiral interactions in Rydberg arrays	91
6.3. Details on the experimental setup	95
6.4. Comparison between the full model and the effective one	97
6.5. Tuning the degree of chirality and the classical regime	100
Chapter 7. Non-ergodic quantum dynamics in superconducting circuits	103
7.1. Why superconducting circuits?	104
7.2. Realization of the bosonic quantum East model in superconducting circuits	
	104
Part III. A different route for non-ergodicity: from short range to all-to-all interactions	111
Chapter 8. Crafting the dynamical structure of synchronization by harnessing bosonic multilevel cavity QED	115
8.1. Introduction	116
8.2. The model	119
8.3. Mean field limit	122
8.4. Classification of dynamical responses	125
8.5. Homogeneous systems	133
8.6. Effects of inhomogeneous fields	138
8.7. Experimental implementation	143
8.8. Discussion	145
Appendix A. Supplemental information for Chapter 3	149
A.1. Role of on-site density-density interaction	149
A.2. Scaling analysis in Λ	151
A.3. Gaussianity and non-Gaussianity in the ground state	153
A.4. Numerical methods	154
Appendix B. Supplemental information for Chapter 4	155
B.1. Dynamics of entanglement entropy in the quantum East model	155
B.2. Finite size scaling	156
B.3. Role of equilibrium localization length ξ	157
Appendix C. Supplemental information for Chapter 7	159
C.1. Perturbative construction of the generator S of the Schrieffer-Wolff transformation	159
C.2. Commutator of the Hamiltonian with the generator S of the Schrieffer-Wolff transformation	160

C.3. Low-anharmonicity limit	162
C.4. Rotating frame of reference	163
Appendix D. Supplemental information for Chapter 8	165
D.1. Computation of the Lyapunov exponent	165
D.2. Chaos induced upon trading $SU(2)$ with $SU(3)$ interactions in three-level system	166
D.3. Chaos induced by a finite fraction of Schrödinger cat states in $SU(3)$ spin-exchange Hamiltonian	166
D.4. Optimization procedure	168
D.5. Dynamics with cavity losses	169
Bibliography	171

x

:

CHAPTER 1

Introduction

Despite being far from a fully fault-tolerant universal quantum computer [8], many platforms have reached enough control to allow the investigation of quantum phenomena in regimes hardly accessible by any other means [9–11]. For instance, long sought quantum phenomena, such as topological order [12, 13], non-abelian anyons [14], as well as quantum dynamics [15–19], can be realized and observed in synthetic systems, opening up the venue for unprecedented investigations. Such investigations have been performed adopting either a *digital* or *analogical* approach. The digital approach is typically based on mimicking the Hamiltonian by applying gates [8, 20, 21]. Instead, the analogical approach is based on finding ways to make the system at hand be described by the Hamiltonian of interest [22, 23]. In such cases, the Hamiltonian is typically implemented by properly tuning external parameters, such as frequency and strength of external lasers, which depends on the specific platform (e.g. neutral atoms, trapped ions, superconducting circuits) at hand. Between the digital and analog approach, the former is far more general than the latter, as given a universal set of gates we could simulate *any* Hamiltonian. However, the digital approach still suffers from limited fidelity of the available gates, leading to propagating errors in the simulation. Consequently, the analog approach is still more developed than the digital one concerning quantum simulations and is fulfilling the original idea by Feynmann of using quantum systems for simulating quantum systems [24]. However, despite the huge success of current platforms, all of them suffer from a common problem: scalability and noise. Indeed, most of the platforms are limited to ~ 100 quantum constituents, e.g. qubits, and the inevitable coupling to the environment leads to uncontrolled errors. Such errors could be potentially tamed via quantum error-correction protocols [25–27]. However, their adoption is still far from being practically useful due to the enormous resources needed. Essentially, we are currently living in the so-called *Noisy-Intermediate-Scale-Quantum* (NISQ) era, as termed by J. Preskill in his seminal paper [9]. Overcoming such problems currently constitutes the biggest challenge in the field, and different routes are taken both from an engineering point of view, by mitigating undesired effects, and fundamental ones. For instance, possible routes involve the design of architectures where entangling gates are not limited to the nearest-neighbor, potentially allowing a speeding up in the entangling of the system and therefore effectively mitigating the decoherence problems [28, 29]. Instead, from a fundamental point of view a great effort is put into devising new

kinds of qubits. Specifically, a possible route involves the realization of exotic phases of matter in order to practically exploit them for aiding quantum information processing. The most prominent example in such direction is non-abelian anyons, which could serve as robust logical qubits on which implement logical operations via *braiding*, namely by encoding the operations in the way space-time trajectories are knotted [30].

Another important limiting factor against a large-scale adoption of modern quantum technologies is the difficulty in robustly storing quantum information [9]. Indeed, even without external sources of decoherence, interacting quantum systems generally tend to make the memory of the initial state virtually inaccessible under their own dynamics. Such inaccessibility is a manifestation of thermalization and could be framed as the scattering of *local* operators (e.g. a single Pauli operator) into an exponentially large number of complex (*non-local*) operators (e.g. strings of Pauli operators) under Heisenberg evolution [31–36]. Such scattering has an immediate consequence in the capability to practically retrieve the information initially stored in the local operator, e.g. the polarization in a spin model, since it would be necessary to measure highly non-local operators as dynamics continue. Therefore, as experimental measures are generally restricted to simple operators, most of the information of the initial state is washed out except for the few conserved quantities of the system, in agreement with the onset of thermalization and statistical mechanics.

However, there exist mechanisms that can prevent the onset of thermalization, and thus make the above picture not true. In recent years many mechanisms have been investigated, including strongly disordered many-body localized systems [37, 38], in which thermalization is impeded by the presence of disordered potentials, to “fracton” systems, in which dynamical constraints induce fragmentation on the space of reachable configurations [39–46], and quantum scarred systems, in which certain classes of initial states show coherent oscillations for times longer than typical relaxation times [47–60]. Mitigating thermalization opens up the possibility that dynamics is not able to wash the memory of the initial state, keep local observables simple under Heisenberg evolution and so experimentally measurable, and make local quantum information passively protected. This thesis goes in such direction, with a particular focus on ergodicity-breaking mechanisms and their potential in aiding quantum information tasks.

In Part I we discuss different ergodicity-breaking mechanisms displayed in simple translationally invariant models, known as Kinetically Constrained Models. We then explore potential ways for leveraging these ergodicity-breaking properties, particularly in the protection of quantum information and in the preparation of states useful for quantum information tasks, such as the multi-mode version of bosonic Gaussian states. Despite

the models we consider are intrinsically interesting from a fundamental standpoint, they hold also practical relevance since they can be realized in current NISQ devices based on Rydberg atoms and superconducting circuits. The details regarding their experimental implementation will be the object of Part II. While most of the work here presented concerns low-dimensional systems with short-range interaction, in Part III we will do a detour in the realm of all-to-all interacting systems. Such kind of interactions is relevant as they naturally appear in cavity-QED setups, in which a cold gas couples to few or several electromagnetic modes in an optical cavity [61–66]. In such systems, due to the all-to-all interacting nature, the dynamics occur at the level of macroscopic classical objects, making quantum effects suppressed with their ‘size’, typically controlled by the number of particles [67–71]. As a consequence, the system will tend to behave classically up to times parametrically large in the number of its constituents, after which quantum effects can no longer be neglected. Intriguingly, in this pre-thermal regime, it is possible to observe dynamical responses which would be prohibited at equilibrium. However, it looks like in this pre-thermal regime we are restricted to observing phenomena ‘classical’ in nature. In such direction, we will challenge this common belief that quantum effects are mostly irrelevant in this pre-thermal regime, by showing how microscopic quantum effects could have a dramatic impact in dictating the macroscopic dynamical response of the system.

Before delving into the description of the various ergodicity-breaking mechanisms, it is first necessary to address a key question: what does it mean that an isolated quantum system thermalizes? Indeed, unitarity would lead us to think that it is virtually impossible for an initially pure state to be described by a statistical mixture, i.e. a mixed state, under its own dynamics. In the next chapter, we address such a question.

CHAPTER 2

Quantum Thermalization

Executive Summary. In this Chapter, we provide a brief summary of the concept of thermalization in isolated quantum systems. We first provide an operatorial definition of thermalization and then discuss the mechanisms that can lead to its establishment even when initializing a pure state.

What is new? All the results in this chapter are taken from pre-existing literature prior to the work carried out in this thesis.

Organization of the Chapter.

- In Sec. 2.1 we provide an operatorial definition of thermalization in isolated quantum systems.
- In Sec. 2.2 we discuss the connection between entanglement and thermalization;
- In Sec. 2.3 we briefly present the Eigenstate Thermalization Hypothesis, which constitutes the most successful known theory in explaining the onset of thermalization;
- In Sec. 2.4, we briefly discuss an alternative point of view about the onset of thermalization based on shifting from states to operators.
- In Sec. 2.5 we discuss the implications of thermalization.

2.1. AN OPERATORIAL DEFINITION

Statistical mechanics provide a powerful framework connecting the microscopic world to the macroscopic one. However, since its foundation, the conceptual puzzle of how irreversibility rises from reversible processes still lacks a rigorous solution. In classical systems, the ergodic hypothesis provides an operational approach, namely a system is assumed to explore with equal probability each accessible configuration under its own dynamics. Such assumption implies the equivalence between time-averages and ensemble averages [72],

$$\frac{1}{T} \int_0^T d\tau O(\tau) = \langle O \rangle_{\text{ensemble}}. \quad (2.1)$$

But how and when a system is ergodic? Such a question still lacks a completely satisfactory answer. However, it is generally believed that interacting Hamiltonian systems are likely chaotic due to non-linearities in their equations of motion, and are thus expected to densely explore the whole accessible phase-space, and be potentially ergodic. On more intuitive grounds, in an interacting classical system, the scattering processes between particles are typically expected to redistribute energy and make equipartition theorem and fluctuation-dissipation theorem dynamically settle in, even when the system is initially prepared in a highly non-thermal distribution [72].

Right after the formulation of quantum mechanics, the tools of statistical mechanics were immediately applied to the quantum domain with huge success. However, the onset of thermalization in an isolated quantum system upon initializing a pure state has been, and still is, a subject of debate. Indeed, in quantum mechanics there is no notion of trajectories in phase-space, due to the Heisenberg uncertainty principle, and the linearity of Schrödinger equation prevents a straightforward definition of chaos. Additionally, how can we reconcile the unitarity of the Hamiltonian dynamics with the mixedness of a thermal ensemble to which you would expect the system to evolve to?

To exemplify this, let us consider a quantum system described by a Hamiltonian \hat{H} and an initial pure state $|\psi(0)\rangle$. If $|\psi(0)\rangle$ is not an eigenstate of the Hamiltonian, it will undergo nontrivial evolution under \hat{H} and remain pure, implying that it cannot be described by a statistical mixture (as expected by statistical mechanics), namely

$$|\psi(t)\rangle = e^{-i\hat{H}t}|\psi(0)\rangle \nrightarrow \hat{\rho}(\beta) = \frac{e^{-\beta\hat{H}}}{Z}, \quad (2.2)$$

where $Z = \text{Tr}e^{-\beta\hat{H}}$ is the partition function and β is an inverse of a temperature (setting the Boltzmann constant $k_B = 1$) set by imposing the conservation of energy

$$\langle\psi(0)|\hat{H}|\psi(0)\rangle = \text{Tr}(\hat{H}e^{-\beta\hat{H}})/Z. \quad (2.3)$$

From Eq. (2.2), the emergence of statistical mechanics in a purely quantum system looks like a hopeless task.

A possible route to solving such a dilemma is by observing that although a state is *globally* pure, it can appear mixed when looked at *locally*, which is relevant as we are mostly limited in measuring local observables in experiments [73, 74]. Indeed, in most cases, when measuring local observables on the evolved state $|\psi(t)\rangle$, the expectation values measured on it are compatible with the one computed on a mixed state, generally given by the thermal ensemble constraint to the conserved quantities of the system. In other words, statistical mechanics dynamically settles locally. More formally, let us look at a certain subset A of the physical space. As previously said, the shift from global to local can be justified from an experimentally oriented point of view: in the real world, measures are mostly limited to *local* observables. As there are different definitions of

locality, we stress that we adopt the following definition: an operator \mathcal{O} is said to be local if it can be written as a sum of terms where each of them acts nontrivially (differently from the identity) on a finite region in the thermodynamic limit. As an example, given a one-dimensional system of length N , the operator $\sum_j \mathcal{O}_j \mathcal{O}_{j+k}$, where \mathcal{O}_j is an operator which acts on a finite number of sites around the j -th one, is local if k does not scale with N . Having established the notion of locality we are interested in, the rest of the system, in which we are not interested as we are not measuring it, could be seen as an effective ‘bath’. In other words, as we are interested solely in the information contained in A the ones contained in its complementary A_c can be thrown away, or more formally traced out as

$$\hat{\rho}_A(t) = \text{Tr}_{A_c} \hat{\rho}_S(t), \quad (2.4)$$

where $\hat{\rho}_S(t)$ is the density matrix describing the whole system S , while $\hat{\rho}_A(t)$ describes solely the region A . In the case discussed above, we would have $\hat{\rho}_S(t) = |\psi(t)\rangle\langle\psi(t)|$. Given $\hat{\rho}_A(t)$, we can compute the observable of interest as

$$\text{Tr}[\hat{\rho}_S(t)\mathcal{O}_A] = \text{Tr}[\hat{\rho}_A(t)\mathcal{O}_A], \quad (2.5)$$

from which we say that a system thermalizes if the long time expectation value tends toward the one expected from statistical mechanics, namely

$$\lim_{T \rightarrow \infty} \frac{1}{T} \int_0^T dt \text{Tr}[\hat{\rho}_A(t)\mathcal{O}_A] = \text{Tr}[\hat{\rho}_{\text{Gibbs}} \mathcal{O}_A] / Z. \quad (2.6)$$

since the argument holds for any local operator \mathcal{O}_A , and since the state remains most of the time near its time-averaged value, we have also a punctual convergence (without the need of time averages). Specifically, we have the following chain of equality

$$\lim_{t \rightarrow \infty} \hat{\rho}(t) = |\psi(t)\rangle\langle\psi(t)| \rightarrow \hat{\rho}_A(t) = \text{Tr}_{A_c} \hat{\rho}(t) = \hat{\rho}_{\text{thermal}}, \quad (2.7)$$

which, in other words, states that a system thermalizes if it evolves towards a state which is locally indistinguishable from a thermal one [74, 75].

2.2. ENTANGLEMENT AND THERMALIZATION

In the previous section, we have given an operatorial definition of quantum thermalization, which allows us to reconcile the unitarity of quantum mechanics and the mixedness of statistical mixtures expected by statistical mechanics. However, we did not answer the questions about when and how thermalization occurs. Let us first address the question linked to ‘how’ this is widely regarded to occur. In the classical world, thermalization is generally expected to settle in thanks to scattering processes between the particles. However, in the quantum one, there is no well-defined notion of trajectories,

making such mechanism not well defined¹. Thus, it is necessary a different mechanism in the quantum world. In such direction, it is widely regarded that thermalization in a quantum system occurs as a result of the presence of entanglement [80]. Indeed, the quantumness (entanglement) in a system leads also to the formation of thermal entropy when we look at the system locally [23, 73, 81–83]. A canonical example of this point is the Bell state of two spatially separated spins: although the full quantum state is pure, local measurements of just one of the spins reveal a statistical mixture with reduced purity. Let us explicitly see this:

$$\begin{aligned} |\psi\rangle &= \frac{1}{\sqrt{2}} (|\uparrow\rangle_A |\downarrow\rangle_B + |\downarrow\rangle_A |\uparrow\rangle_B), \\ \Rightarrow \hat{\rho}_A &= \text{Tr}_B(|\psi\rangle\langle\psi|) = \frac{1}{2} (|\uparrow\rangle_A \langle\uparrow| + |\downarrow\rangle_A \langle\downarrow|). \end{aligned} \quad (2.8)$$

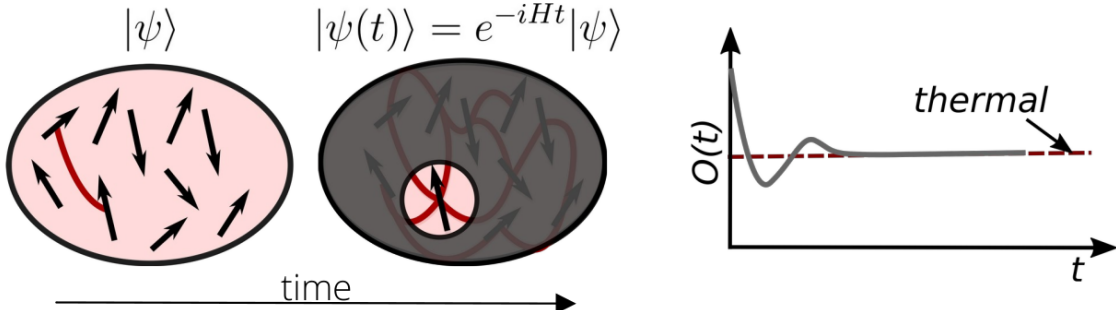
This local statistical mixture is distinct from a superposition because no operation on the single spin can remove these fluctuations or restore its quantum purity. In such a way, the spin's entanglement with another spin creates local entropy, which is called entanglement entropy. As this picture can be extended to generic states, it also applies to the evolved state $|\psi(t)\rangle$ for typical interacting Hamiltonians, meaning that as entanglement entropy grows (as generally observed), it dynamically becomes locally indistinguishable from a statistical thermal mixture (see Fig. 2.1 for a sketch). The need for entanglement to make thermalization occur can be also shown by looking at the definition of thermalization formalized in Eq. (2.6). There, we have assumed that the partial trace over A_c on the density matrix describing the whole system $\hat{\rho}_S$ gives rise to a mixed state, which holds solely if there is entanglement between A and its complementary A_c .

Having given a possible mechanism behind the onset of thermalization in the quantum world, it is still missing the answer about ‘when’ thermalization settles in. Indeed, the fact that a pure state can appear locally mixed, does not imply that the mixed state describing it is the one expected from statistical mechanics, e.g. a thermal ensemble. In the next section, we cover such a point by discussing the most successful theory, the Eigenstate Thermalization Hypothesis, which provides an answer to this.

2.3. THE EIGENSTATE THERMALIZATION HYPOTHESIS

In the previous section, we have given an operatorial definition of quantum thermalization and a phenomenological explanation of its onset based on entanglement. However,

¹Attempts in such direction involves systems with a well defined semiclassical limit (see e.g. Refs. [76–79]).



Local information gets scattered **non** locally

FIGURE 2.1. Sketch representing the onset of statistical mechanics in an isolated quantum system under its own unitary dynamics. Given a system described by the Hamiltonian H and initial quantum state $|\psi\rangle$, different from an eigenstate of H , this will nontrivially evolve in time. Throughout this process, entanglement grows in the system, symbolically represented by connecting red bonds. Consequently, upon local observation of the system, e.g. by measuring local observables like magnetization, most of the information regarding the state is effectively lost except for the (typically few) conserved quantities. As a result, after the initial transient where other details of the initial state still matter, the expectation values of local observables tend to be the ones predicted by statistical mechanics.

the answer to ‘when’ this occurs is still lacking. A possible route is based on looking at the spectral properties of the Hamiltonian \hat{H} governing the dynamics of the system of interest. In such regard, the most successful theory is the Eigenstate Thermalization Hypothesis (ETH) [84–89]. The ETH roughly states that in order to make thermalization occur, all the eigenstates of \hat{H} has to be thermal in nature, namely the expectation value of any local observable measures on the eigenstates depend solely on the conserved quantities of the system itself. In order to be more concrete and formal, let us consider the same scenario discussed in the previous section. Specifically, let us consider a non-integrable Hamiltonian \hat{H} of N interacting constituents (e.g. spins). For simplicity, let us assume there are no degeneracies in the spectrum so that the eigenvalues $\{E_n\}$ and eigenstates $\{|E_n\rangle\}$ of \hat{H} are in one-to-one correspondence. Upon initializing a $|\psi(0)\rangle$, which is not an eigenstate of the Hamiltonian \hat{H} , it will undergo a non-trivial evolution given by the solution to the time-dependent Schrödinger equation

$$|\psi(t)\rangle = \sum_n c_n e^{-iE_n t} |E_n\rangle, \quad (2.9)$$

where $c_n = \langle E_n | \psi(0) \rangle$ is the overlap of the initial state $|\psi(0)\rangle$ with the n -th eigenstate of the Hamiltonian. As previously said, thermalization can be defined locally, and thus

let us look at the time evolution of a local observable \mathcal{O}_A acting on a region A ,

$$\langle \psi(t) | \hat{\mathcal{O}}_A | \psi(t) \rangle = \sum_{n,m} e^{-i(E_m - E_n)t} c_n^* c_m \langle n | \hat{\mathcal{O}}_A | m \rangle. \quad (2.10)$$

As the notion of thermalization is formulated at the level of time-averages, let us compute the latter

$$\overline{\mathcal{O}_A} = \lim_{T \rightarrow \infty} \frac{1}{T} \int_0^T dt \langle \psi(t) | \hat{\mathcal{O}}_A | \psi(t) \rangle = \sum_n |c_n|^2 \langle n | \hat{\mathcal{O}}_A | n \rangle \quad (2.11)$$

where we have neglected oscillating terms using the Riemann-Lebesgue lemma. If a system thermalizes, we expect that Eq. (2.6) holds. Now, restricting to short-range interacting systems, the equivalence of ensembles holds, making it possible to trade the canonical average (considered in Eq. (2.6)) with the microcanonical one, namely

$$\langle \mathcal{O}_A \rangle_{\text{MC}} = \text{Tr}[\hat{\rho}_{\text{MC}} \hat{\mathcal{O}}_A] \equiv \frac{1}{\mathcal{N}(E)\Delta} \sum_{E-\Delta/2 \leq E_n \leq E+\Delta/2} \langle E_n | \hat{\mathcal{O}}_A | E_n \rangle, \quad (2.12)$$

where $\mathcal{N}(E)$ is the density of states at energy E . By direct comparison between Eq. (2.11) and Eq. (2.12), we observe that such equality does not seem to hold for all initial states $|\psi(0)\rangle$, since the former is a weighted sum over all the eigenstates, while instead the latter is a uniform sum over all the eigenstates within a small energy window. However, the two could be put in connection by two additional assumptions: (i) the $|c_n|$ are non-zero in a small energy window; (ii) the diagonal elements of the operator $\hat{\mathcal{O}}_A$ depends smoothly on the energy E , namely $\langle E_n | \hat{\mathcal{O}}_A | E_n \rangle = \mathcal{O}_A(E)$. The condition (i) is reasonable if the initial state $|\psi(0)\rangle$ has small fluctuations around the mean energy, i.e.

$$\frac{\sqrt{\langle \psi(0) | \hat{H}^2 | \psi(0) \rangle - \langle \psi(0) | \hat{H} | \psi(0) \rangle^2}}{\langle \psi(0) | \hat{H} | \psi(0) \rangle} \ll 1. \quad (2.13)$$

The condition (ii) is instead the hallmark of the Eigenstate Thermalization Hypothesis [84–89]. Assuming (i) and (ii) to hold, we straightforwardly obtain

$$\overline{\mathcal{O}_A} = \mathcal{O}_A(E) \sum_n |c_n|^2 = \mathcal{O}_A(E) = \langle \mathcal{O}_A \rangle_{\text{MC}}, \quad (2.14)$$

since $\sum_n |c_n|^2 = 1$. In such a manner, we proved a weak form of thermalization, namely on average. However, it is possible to prove a stronger version, by making an assumption on the off-diagonal terms of the operators, which is still the object of the ETH. Indeed, the ETH states that the matrix elements of a typical local observable \mathcal{O}_A computed on the eigenstates of an interacting non-integrable Hamiltonian are of the form [87]

$$\langle E_n | \hat{\mathcal{O}}_A | E_m \rangle = \mathcal{O}(\bar{E}) \delta_{n,m} + e^{-S(\bar{E})/2} f_{\mathcal{O}}(\bar{E}, \omega) R_{n,m}, \quad (2.15)$$

where $\bar{E} = (E_n + E_m)/2$, $\omega = (E_n - E_m)/2$ and $S(\bar{E}) = \log \mathcal{N}(\bar{E})$ is the thermodynamic entropy. The coefficients $R_{n,m}$ are random numbers, with a vanishing average and unit

variance. Due to the extensivity of the thermodynamic entropy, the off-diagonal terms are exponentially suppressed in the system size. As a consequence, we immediately see that the fluctuations around the time-average are exponentially suppressed as

$$\overline{\mathcal{O}_A^2} - \overline{\mathcal{O}_A}^2 = \sum_n \sum_{m \neq n} |c_n|^2 |c_m|^2 |\langle E_m | \hat{\mathcal{O}}_A | E_n \rangle|^2 \leq e^{-S(E)} \quad (2.16)$$

with E the energy of the initial state. In summary, ETH states a strong version of thermalization: not only on average, but also at a given time, up to small fluctuations. Additionally, since the argument holds for any local operator $\hat{\mathcal{O}}_A$, and since the state remains most of the time near its time-averaged value, we have also a punctual convergence (without the need of time averages). Specifically, we have

$$\hat{\rho}(t) = |\psi(t)\rangle\langle\psi(t)| \Rightarrow \hat{\rho}_A(t) = \text{Tr}_{\bar{A}}\hat{\rho}(t) \rightarrow \hat{\rho}_{\text{thermal}} \quad (2.17)$$

which is the same as in Eq. (2.6).

2.4. A DIFFERENT ROUTE: FROM STATES TO OPERATORS

So far, we have discussed thermalization in quantum systems focusing on states, while instead operators have been solely used to define a notion of locality. However, in the past years, a complementary approach has been proposed based on shifting from states to operators. The key observation is that, in Heisenberg-picture evolution, simple local operators generally evolve into highly nonlocal ones in interacting theories. To exemplify this, let us consider the Heisenberg evolution of the Pauli operator $\hat{\sigma}_k^z$ in a one-dimensional quantum Ising model, with Hamiltonian $\hat{H} = \sum_j \hat{\sigma}_j^x \hat{\sigma}_{j+1}^x + \sum_j \hat{\sigma}_j^z$. We have,

$$\begin{aligned} \hat{\sigma}_k^z(t) &= e^{i\hat{H}t} \hat{\sigma}_k^z e^{-i\hat{H}t} \\ &= \hat{\sigma}_k^z + it[\hat{H}, \hat{\sigma}_k^z] + \frac{(it)^2}{2!} [\hat{H}, [\hat{H}, \hat{\sigma}_k^z]] + \dots \\ &= \hat{\sigma}_k^z + it (\hat{\sigma}_{k-1}^x [\hat{\sigma}_k^x, \hat{\sigma}_k^z] + [\hat{\sigma}_k^x, \hat{\sigma}_k^z] \hat{\sigma}_{k+1}^x) + \mathcal{O}(t^2) \\ &= \hat{\sigma}_k^z + 2t (\hat{\sigma}_{k-1}^x \hat{\sigma}_k^y + \hat{\sigma}_k^y \hat{\sigma}_{k+1}^x) + \mathcal{O}(t^2), \end{aligned} \quad (2.18)$$

where it is evident that the support of the operator will grow in time. As a consequence, operators flow from simple to highly complex ones, eventually becoming so complex that they cannot be computed. However, the increase in complexity can eventually lead to a simpler description in the spirit of statistical mechanics: the operators decay in highly non-local objects that serve as a thermodynamic bath when we look at it locally so that a statistical description should emerge and become exact. This picture has been confirmed in random unitary models [31–33], where dynamics is governed by

the application of random gates without being bound to a specific realistic model, as well as more realistic systems [34–36].

2.5. CONSEQUENCES OF THERMALIZATION

The onset of thermalization has many consequences. The most remarkable one is that computing local quantities becomes an easy task. Indeed, neglecting the initial transient, it is enough to compute expectation values over the thermal ensemble compatible with the conserved quantities of the system, without the need to compute the evolution of the whole state (which is typically a hard task). Additionally, as the system thermalizes, it is possible to perform a sort of coarse grain operation. Namely, it is possible to pass from a microscopic unitary description of a system (exact and reversible dynamics), governed by quantum mechanics, to a macroscopic hydrodynamic description (approximate and irreversible dynamics) of quantum systems governed by partial differential equations, i.e. continuity equations [31–36]. From a computational point of view, the onset of thermalization is a huge advantage, as it implies no need to have a microscopic quantum description of the system for most practical purposes. However, despite its predictive power, the fact that statistical mechanics works so well implies also that many specific features of the system are not relevant in dictating its properties. Indeed, thermalization implies that most of the features of the initial state are effectively ‘lost’ in highly nonlocal operators, making the system evolve towards a thermal distribution containing information solely of the (typically few) conserved quantities of the system, such as energy. In other words, the memory of the initial configuration is rapidly washed out. On one hand, the irrelevance of the initial condition is a blessing, as it is not needed to have knowledge on the microscopic details of the system, but on the other hand, it is a damnation, as it prevents to encode and store information in such states different from their conserved quantities. Nonetheless, as we will discuss now, there exist mechanisms that could impede the onset of thermalization by making the system non-ergodic, opening the door for exploring phenomena beyond the paradigm imposed by statistical mechanics [90].

Part I

Escaping the doom of thermalization

In the previous Chapter, we discussed how interacting quantum systems are generally expected to thermalize and be locally described by a thermal ensemble insensitive to most of the features of the initial state, making the storage of quantum information in local observables apparently a hopeless task. However, as robust storage of quantum information is an important limiting factor that mitigates against a large-scale adoption of modern quantum technologies [9], a large effort has been put into unveiling mechanisms that could aid in protecting quantum memory.

A possible approach to impede thermalization to a featureless thermal ensemble is by considering systems with conserved quantities. Indeed, if a system conserves local quantities, we can store quantum information within them, potentially rendering the system a perfect quantum memory. The extreme case scenario is integrable systems [91] which, having an extensive number in the number of degrees of freedom of conserved quantities, fail to thermalize to a thermal ensemble. Instead, they reach a generalized Gibbs ensemble which contains the information of all the conserved quantities [92]. However, such models are generally finely tuned, and any weak perturbation eventually drives the system towards a thermal ensemble.

Another possible route to hinder the onset of thermalization is by looking at the (widely accepted) mechanisms at its origin. Specifically, while thermalization emerges as a result of scattering processes in the macroscopic classical world, we expect that the building up of entanglement in the system will lead to thermalization in the quantum one [23, 73, 81–83]. Therefore, one way to impede the onset of thermalization is by mitigating the proliferation of quantum correlations (entanglement) in the system. However, we emphasize that completely impeding the spread of quantum correlations would imply no additional advantages and features in using quantum systems over classical ones, including their utility in quantum information, metrology, and computation, as the source of quantum speedup lies in the entangled nature of the system. Thus, we anticipate that we do not desire a system with trivial, i.e., classical, properties.

In such a direction, a paradigmatic example of an ergodicity-breaking mechanism is disorder-induced localization, seen both in the well-established Anderson localization phenomenon at the single-particle level [93], and in its extension into the many-body realm, giving rise to Many-Body Localization (MBL) [38, 94, 95]. Specifically, it has been argued that a strong enough disorder could lead to localization of the eigenstates of the Hamiltonian, a zero DC current in the system, and an extreme slow growth of quantum correlations [96, 97], impeding the onset of thermalization since the system fails to act as its own thermal bath. The remarkable failure of statistical mechanics has been linked to the emergence of an extensive number of conserved quantities at strong disorder, known as local integrals of motion (LIOMs), making the system effectively

integrable [98–101]. However, strong debate still surrounds the existence of MBL as a true phase of matter in the thermodynamic limit due to the existence of avalanches of thermal bubbles whose propagation could disrupt localization [102–112]. Additionally, MBL is not robust against any weak coupling to an external bath (which is inevitable in any real-world scenario) [113–118].

Independently of whether MBL exists or not as a stable phase of matter in the thermodynamic limit, it has the merit of having spurred interest in questions concerning the onset of thermalization, as it challenges the generally held belief that statistical mechanics holds in generic interacting systems. As a result, many proposals have attempted to mitigate the onset of thermalization by confining quantum information into conserved or quasi-conserved quantities [119–135]. These proposals range from the mentioned strongly disordered many-body localized [37, 38] or glassy systems [136–143], in which thermalization is impeded by the presence of disordered potentials, to “fracton” systems, in which dynamical constraints induce fragmentation on the space of reachable configurations [39–46], and quantum scarred systems, in which certain classes of initial states show coherent oscillations for times longer than typical relaxation times [47–60]. In the same direction, researchers have started to investigate the quantum generalizations of so-called kinetically constrained models (KCMs) [144–150].

Kinetically constrained models are inspired by classical structural glasses, which were introduced to describe the extreme slowdown of thermalization resulting from excluded volume interactions between particles. Specifically, to mimic excluded volume interactions, the kinetic term of such models (e.g., a spin flip, particle hopping, and so on) is conditioned, i.e., constrained, by the configuration of the surrounding particles. For the sake of concreteness and clarity, let us consider a one-dimensional spin system, where a spin could flip, i.e. $|\uparrow\rangle_z \leftrightarrow |\downarrow\rangle_z$, solely when the previous one is in the $|\downarrow\rangle_z$ state. Going immediately to the quantum realm, such a scenario is described by the Hamiltonian

$$\hat{H} = \underbrace{\sum_j \hat{n}_j}_{\text{potential}} - e^{-s} \underbrace{\sum_j \hat{n}_j \hat{\sigma}_{j+1}^x}_{\text{kin. constrained}}, \quad (2.19)$$

where $\hat{n}_j = (1 - \hat{\sigma}_j^z)/2$, with σ_j^α the α -Pauli matrix obeying the commutation relation $[\sigma_j^x, \hat{\sigma}_k^y] = 2i\hat{\sigma}_k^z$, is the projector on the $|\downarrow\rangle_z$ state. The kinetic constraint is $\sum_j \hat{n}_j \hat{\sigma}_{j+1}^x$, and it is controlled by e^{-s} , where such parametrization is chosen just for historical reasons due to its original connection with classical structural glasses [138]. To improve clarity, in Fig. 2.2 we show a sketch of the action of the Hamiltonian in Eq. (2.19) to a product state with a single excited spin. The Hamiltonian in Eq. (2.19) is called the quantum East model, where ‘East’ comes from the fact that its action is nontrivial

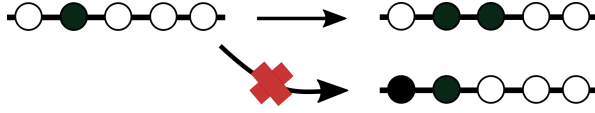


FIGURE 2.2. Sketch representing the action (arrow) of the Hamiltonian of the quantum East model (cf. Eq. (2.19)) on a spin chain with a single excitation (black dot) surrounded by de-excited spins (white dots). The kinetic constraint acts nontrivially only to the right (East) of the excited spins, while instead other processes (e.g. spin flips to the left) are prohibited as represented by the red cross.

solely towards the East/right of an excitation. The quantum East model has been subject of intense research owing to its remarkable properties [140, 151–155]. Indeed, despite its apparent simplicity, it hosts remarkable phenomena, including disorder-free localization and a dynamical phase transition between a fast thermalizing phase to a slow one. Such dynamical phase transition will be the object of investigation in this thesis.

So far we have considered spin systems. However, we are not strictly limited to work with them. Indeed, we could immediately design a system where instead of having finite dimensional constituents (spins), we have infinite dimensional ones (bosons). In such a context, inspired by the quantum East model above, a possible KCM could be characterized by a kinetic term that acts nontrivially on a certain site solely if the previous is occupied. For instance, we could think of a conditioned drive field whose strength is controlled by the number of particles on the previous site. The Hamiltonian describing such a scenario would be

$$H = \underbrace{\sum_j \hat{n}_j + \epsilon \sum_j \hat{n}_j^2 + U \sum_j \hat{n}_j \hat{n}_{j+1}}_{\text{potential}} - \underbrace{e^{-s} \sum_j \hat{n}_j (\hat{a}_{j+1} + \hat{a}_{j+1}^\dagger)}_{\text{kin. constrained}}, \quad (2.20)$$

where \hat{a}_j and \hat{a}_j^\dagger are bosonic annihilation and creation operators acting on site j respectively; $\hat{n}_j = \hat{a}_j^\dagger \hat{a}_j$; e^{-s} controls the constrained creation and annihilation of bosons; ϵ is the on-site density-density interaction; and U is the nearest-neighbor density-density interaction. As a remark, the kinetic constraint is reminiscent of the coupling typically encountered in optomechanical systems [156], where an harmonic oscillator (the mechanical part) is driven via radiative pressure exerted by an incoming radiative field (optical part). We will see that this analogy will aid in discussing the properties of such model, including disorder-free localization.

As it could be guessed, the KCMs we could define are virtually infinite. However, defining an arbitrarily large class of models without any criteria sounds like a not so enlightening task. Instead, here we opt for a more physics-motivated picture. Specifically,

after investigating the properties of the models above, we study the impact of deformations of the kinetic term. We will show that minimal modifications on the kinetic term have a dramatic impact on the dynamical features of the system. Specifically, we will show that, upon tuning such constraint, we could select a different ergodicity-breaking mechanism at will, not limiting to localization, but realizing other forms such as quantum many-body scars [157], Hilbert space shattering [158], and confinement [131].

So far, we have listed possible routes via which thermalization could be avoided. However, despite unveiling mechanisms that could hinder thermalization is fundamentally interesting on its own, an interesting question concerns how to exploit such mechanisms. A possible direction is, as mentioned above, to use non-ergodicity to impede the spreading of quantum information into highly non-local, and thus virtually inaccessible, degrees of freedom. Another possibility is to utilize these properties for engineering and preparing quantum states with interesting characteristics. Specifically, in the bosonic quantum East model, we will show how we can prepare the localized many-mode version of single-mode bosonic Gaussian states relevant in quantum information processing and metrology [159] via simple adiabatic protocols.

Looking for practical ways to harness these properties is not only stimulating from an intellectual point of view but holds also practical relevance as these mechanisms could be realized in current platforms. In such direction, our contribution concerns the proposal of two experimental setups where *all* the model here discussed can be analogically simulated. Specifically, the bosonic quantum East model can be realized in superconducting circuits, while instead the spin version (and deformations) can be realized in Rydberg arrays. This will be the object of Part II of this thesis. However, as we enter real-world scenarios, an immediate question immediately arises: how are the features of these models affected by the inevitable coupling of the system with the environment? In this part, we will address such a question showing that the phenomena discussed persist against some source of dissipation.

Structure of Part I

As above stated, the systems described by the Hamiltonians in Eqs. (2.19) and (2.20), and deformation of the former, will be the subject of Part I. Specifically, this Part is organized as follows

- In Chapter 3 we show that localization could be realized in translational invariant systems. We do so by focusing on the low-energy domain of the bosonic version of the East model (cf. Eq. (2.20)). In doing so, we unveil an emergent representation of the Hamiltonian in terms of localized operators, in a fashion

reminiscent of LIOMs in MBL, which is able to capture low energy properties, both at equilibrium and out-of-equilibrium. We then exploit the localization of the system for the adiabatic preparation of the many-mode localized version of metrologically relevant states, such as Gaussian states and cat states, which are Gaussian with respect to the localized operators just introduced. Finally, we show how localization is not disrupted by some forms of dissipation.

- In Chapter 4 we quantitatively explore ergodicity-breaking features at finite energy density in the spin version of the quantum East model (cf. Eq. (2.19)). We do so by proposing and testing a novel complexity-oriented proxy for detecting non-thermal eigenstates. We discover the existence of a (possibly sharp) transition between a non-thermal and thermal region along the spectrum, reminiscent of a mobility edge. Our finding challenges the common belief that the latter is exclusive of disordered systems, i.e. MBL.
- In Chapter 5 we show how upon performing minimal modifications of the kinetic constraint in the quantum East model, the dynamical features are completely altered. Specifically, we will show how to control and select at will different ergodicity-breaking mechanisms not limiting to localization, but realizing other forms such as quantum many-body scars, Hilbert space shattering, and confinement.

CHAPTER 3

Utilizing localization in bosonic systems

Most of the content in this Chapter is in:

- “*Kinetically Constrained Quantum Dynamics in Superconducting Circuits*” (PRX Quantum 3, 020346 (2022))
Riccardo J. Valencia-Tortora, Nicola Pancotti, Jamir Marino.

Executive Summary. We discuss the properties of the kinetically constrained bosonic quantum East model. We show by a combination of analytics, exact diagonalization, and tensor networks, that the system displays localization of the ground state, namely the corresponding wavefunctions contain nontrivial excitations only on a small compact region of the lattice and they are in the vacuum state everywhere else. The bosonic generalization of the spin-1/2 East model opens up several directions including the construction of many-body versions of archetypal states that are relevant for quantum information applications such as coherent states, squeezed states, and cat states [160]. Specifically, we will show how upon initializing bosonic Gaussian states on a single site, we can prepare their localized version which possess the same properties as their single-mode counterparts, although they are supported on a few neighboring sites. Indeed, we show how these states, despite being no longer Gaussian with respect to the bare bosonic operators, are still Gaussian with respect to dressed bosonic operators. We provide a formal description of these dressed operators by proposing a simple adiabatic protocol that connects the bare ones, i.e. the usual single-mode bosonic operators (e.g. \hat{a}_i), to their dressed version, which we name *superbosonic* creation-annihilation operators. These operators fulfill the canonical bosonic commutation relations and they are exponentially localized in the neighborhood of a given site on the lattice. Moreover, we show how the low-energy physics of the Hamiltonian, both at equilibrium and out-of-equilibrium, admits an effective, non-interacting, theory at low temperature in terms of the *superbosonic* operators, in a fashion reminiscent of the 1-bit construction in MBL [98–101]. Finally, we discuss the impact of dissipative channels in the system, showing how the localization properties are robust against some kind of dissipation and could also aid in passively protecting the stored quantum information.

What is new? All results of this chapter represent novel research results.

Organization of the Chapter

- In Sec. 3.1, we introduce the Hamiltonian of the model, enumerate its symmetries, and compare it to previous works on similar models.
- In Sec. 3.2 we show that the ground state displays a localized phase, namely the corresponding wavefunctions contain nontrivial excitations only on a small compact region of the lattice and they are in the vacuum state everywhere else. We support our findings by combining numerical and analytical approaches.
- In Sec. 3.3 we exploit the localized properties of the system devising an adiabatic protocol for building the many-body versions of states that are relevant for quantum information applications such as coherent states, squeezed states, and cat states [160]. In doing so, we define a set of *superbosonic* creation-annihilation operators (Sec. 3.3). These operators fulfill the canonical bosonic commutation relations, are adiabatically connected to their bare version, and they are exponentially localized in the neighborhood of a given site on the lattice. Additionally, we show that the Hamiltonian can be written as a non-interacting theory in terms of these localized operators, similar to the 1-bit construction in MBL [98–101].
- In Sec. 3.4, we couple the system to different noise sources and, via a detailed numerical analysis, we show that localized states retain some memory of their initial condition even in the presence of strong dissipation. First, we consider the effects of dephasing noise coupled to bosonic occupations, which preserves the “East symmetry” (see the definition in Sec. 3.1). In this scenario, the localized states are barely altered by the environment. We show that the fidelity between the time-evolved state and the initial state decays exponentially with a long decoherence time, controlled by the parameters of the Hamiltonian, the initial state, and the strength of the noise. Second, we consider the effects of particle losses that break the “East symmetry.” As expected in this situation, the magnitude of the fidelity decays exponentially fast in time, with a decoherence time that is parametrically small in the loss rate. It is important to stress that as the localized states have non-trivial structure only on a small support, any external noise that does not act in their immediate vicinity leaves them essentially invariant. This set of noise-resilient properties renders the many-body states studied in this work qualitatively different from localization induced by disorder, which is inherently fragile to decoherence (for studies on MBL systems coupled to a bath or external noise see Refs. [113–118]).

This Chapter is composed by a rearrangement of the author’s publication [1].

3.1. THE BOSONIC QUANTUM EAST MODEL

We investigate the following Hamiltonian with open boundary conditions

$$H = -\frac{1}{2} \sum_{j=0}^L \hat{n}_j \left[e^{-s} \left(\hat{a}_{j+1} + \hat{a}_{j+1}^\dagger \right) - \epsilon \hat{n}_j - U \hat{n}_{j+1} - 1 \right], \quad (3.1)$$

where \hat{a}_j and \hat{a}_j^\dagger are bosonic annihilation and creation operators acting on site j respectively; e^{-s} controls the constrained creation and annihilation of bosons; ϵ is the on-site density-density interaction; and U is the nearest-neighbor density-density interaction.

As discussed in the introduction of Part I, Eq. (3.1) is a kinetically constrained “East” model. The unidirectional constrained feature has consequences for the accessible portion of the Hilbert space by the dynamics. Namely, any initial state with a product of vacua from the left edge up to a given site in the bulk will exhibit nontrivial dynamics only on the right side of the lattice after the first occupied site. For sake of concreteness, let us consider the state $|00100\dots 0\rangle$. Via subsequent application of the Hamiltonian given in Eq. (3.1) we have,

$$\begin{array}{c} |00120\dots 0\rangle \dots \\ \nearrow \\ |00100\dots 0\rangle \rightarrow |00110\dots 0\rangle \rightarrow |001110\dots 0\rangle \dots \\ \searrow \\ |00100\dots 0\rangle \dots \end{array} \quad (3.2)$$

where \rightarrow represents the action of the constrained creation and annihilation of bosons at each step of perturbation theory. The occupation of the first nonvacant site and of those at its left cannot change as a consequence of the “East” constraint. More formally, the Hamiltonian commutes with the projectors

$$P(n_0, k) = \mathcal{P}_{0,j}^{\otimes_{j=0}^{k-1}} \otimes \mathcal{P}_{n_0,k} \otimes \mathbf{1}_j^{\otimes_{j>k}}, \quad (3.3)$$

where $\mathcal{P}_{s,j} = |s\rangle_{jj}\langle s|$ is the projector on the Fock state with s particles on site j , $\mathbf{1}_j$ is the identity acting on site j , and k and n_0 are, respectively, the position and occupation of the first nonvacant site. We can split the Hilbert space into dynamically disconnected sectors $\mathcal{H}_{n_0,k}$, such that the action of $P(n_0, k)$ is equivalent to the identity, while the action of the other projectors gives zero. For example, the state $|00100\dots 0\rangle \in \mathcal{H}_{1,2}$ (note that the first site index is 0). Furthermore, since $\sum_{k=0}^L \sum_{n_0=1}^{\infty} P(n_0, k) = \mathbf{1}$ these sectors $\{\mathcal{H}_{k,n_0}\}$ constitute a complete and orthogonal basis of the whole Hilbert space \mathcal{H} , namely $\mathcal{H} = \bigoplus_{k=0}^L \bigoplus_{n_0=1}^{\infty} \mathcal{H}_{n_0,k}$.

In the following, we focus on a certain block specified by k , n_0 , and the number of “active” sites L right next to the k -th one. Since the action of H on sites to the left of the k -th one is trivial, the index k is physically irrelevant for our purpose and we therefore choose $k = 0$ without any loss generality. Exploiting this property, we write the Hamiltonian given in Eq. (3.1) as $H_{L+1} = \sum_{n_0} H_{L+1}(n_0)$, where $H_{L+1}(n_0)$ is

$$H_{L+1}(n_0) = \hat{h}_1 + \begin{aligned} & - \frac{1}{2} \sum_{j=1}^L \hat{n}_j \left[e^{-s} \left(\hat{a}_{j+1} + \hat{a}_{j+1}^\dagger \right) - \epsilon \hat{n}_j - U \hat{n}_{j+1} - 1 \right], \end{aligned} \quad (3.4)$$

with $\hat{h}_1 \equiv -\frac{1}{2} n_0 \left[e^{-s} \left(\hat{a}_1 + \hat{a}_1^\dagger \right) - \epsilon n_0 - U \hat{n}_1 - 1 \right]$ and $n_0 \in \mathbb{N}^+$. Furthermore, since $H_{L+1}(n_0)$ commutes with the operators acting on the $(L+1)$ -th site, we can represent it as the sum of an infinite number of commuting terms $H_{L+1}(n_0) = \sum_{\beta_r} H_L^{\beta_r}(n_0) \otimes \Pi_{L+1}^{\beta_r}$, where Π_L^β is the projector over the eigenstate $|\beta_r\rangle$ with eigenvalue $\beta_r = rU - e^{-2s}/U$ of the operator $\left(U \hat{n}_{L+1} - e^{-s} \left(\hat{a}_{L+1} + \hat{a}_{L+1}^\dagger \right) \right)$, where $r \in \mathbb{N}$, and,

$$H_L^{\beta_r}(n_0) = \hat{h}_1 + \begin{aligned} & - \frac{1}{2} \sum_{j=1}^{L-1} \hat{n}_j \left[e^{-s} \left(\hat{a}_{j+1} + \hat{a}_{j+1}^\dagger \right) - \epsilon \hat{n}_j - U \hat{n}_{j+1} - 1 \right] + \\ & + \frac{1}{2} \hat{n}_L [\beta_r + \epsilon \hat{n}_L + 1]. \end{aligned} \quad (3.5)$$

In Sec. 3.2, we focus on the properties of the ground state of the Hamiltonian given in Eq. (3.5) within a certain symmetry sector.

3.1.1. Connection with previous works

The Hamiltonian given in Eq. (3.1) can be linked to its spin-1/2 version [151] by setting $U = \epsilon = 0$ and replacing the bosons with hard-core ones. Since the Hilbert space of each spin is finite, the “East” symmetry is largely reduced with respect to the bosonic case. Each symmetry sector $\mathcal{H}_{k,n_0=1}$ is specified only by the position of the first excitation, since n_0 is bound to be zero or one. The ground state properties within a symmetry sector $\mathcal{H}_{k,n_0=1}$, where the position k of the first nonempty is again irrelevant, have been investigated in Ref. [151]. It has been observed that the probability of finding an occupied site in the ground state decays exponentially fast around the first occupied site when $s > 0$, namely

$$\langle \hat{n}_j \rangle \sim \exp(-j/\xi(s)), \quad (3.6)$$

where the expectation value is taken on the ground state and we introduce the localization length $\xi > 0$. The localization length ξ is the typical distance from the first

occupied site such that the state becomes a trivial product state that is well approximated by the vacuum. The localization of the ground state does not have an impact solely at low energy densities, but it has been argued to be linked to a dynamical transition from a fast thermalizing regime to a slow, non-ergodic one [140, 151], also at finite energy densities. In particular, in Ref. [151], it has been argued that the slow dynamics is a byproduct of the localized nature of the low-energy eigenstates of the model. Such connection stems from the possibility to use the localized ground state, together with strings of empty sites, as building blocks to construct exponentially many “slow” states in the size of the system by their concatenation (we provide further details in Chapter 4 where the finite-energy properties of the quantum East model are the central focus).

The dynamical transition observed in Ref. [151] is not guaranteed to survive in the bosonic case. In fact, the amplitude for “eastern” particle creation can now be enhanced by the prefactor n_0 in the bosonic case, suggesting that the transition may be qualitatively established when $(n_0 e^{-s}) \sim 1$. This would imply a critical value $s_c \propto \log n_0$, which is parametrically large in n_0 , pushing the extension of the localized phase up to $s \rightarrow \infty$. Nonetheless, we show in Sec. 3.2 that a localized phase still occurs for $s > 0$ whenever repulsive interactions are included in Eq. (3.1).

3.2. LOCALIZATION TRANSITION

In this section we show that the Hamiltonian in Eq. (3.5) displays a localization-delocalization transition at finite s and $U > 0$. We give numerical evidence corroborated by analytical observations that repulsive interactions are necessary to observe such a transition at finite s . We use the inverse localization length ξ^{-1} controlling the decay of the average occupation number in space (cf. Eq. (3.6)), as proxy for the transition.

In the following, we fix $\epsilon = 0$ and the symmetry sector $\beta_{r=0}$ in Eq. (3.5), unless mentioned otherwise. The additional nonlinear term proportional to ϵ would complicate the analysis from a technical standpoint without altering the main contents of the paper. For the sake of clarity, Appendix A.1 shows that, for $U = 0$ and $\epsilon > 0$, the localization properties of the ground state remain qualitatively similar to those discussed in the main text.

In order to investigate the properties of the ground state, we resort to a combination of mean-field arguments, exact diagonalization (ED), and density matrix renormalization group (DMRG) methods [161]. Since we aim to explore large system sizes, we mainly resort to the DMRG and we use ED as a benchmark when both methods can be used.

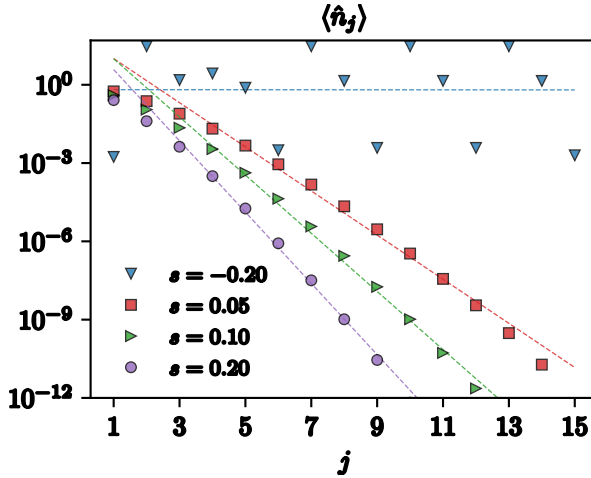


FIGURE 3.1. The average occupation number of the ground state for different values of s at fixed nearest-neighbor density-density interaction $U = 1$. We fix $L = 15$, a cutoff $\Lambda = 30$ to the maximal occupation number, and $n_0 = 1$. In the plot, we do not display the occupation n_0 of the zeroth site that fixes the “East symmetry” sector. The dashed lines are the exponential fit, the slope of which is $-1/\xi$, where ξ is the localization length (cf. Eq. (3.6)). Image taken from Ref. [1].

Interestingly, we find that mean field is able to analytically predict the location of the transition point obtained via the DMRG.

We compute the ground state $|\psi_0(n_0)\rangle$ at fixed n_0 , s , and U . We fix the system size at $L = 15$. This value is sufficiently large to capture the localized tail of the ground state, without relevant finite-size effects. Although the local Fock space is infinite, in order to treat the model numerically, we need to fix a finite cutoff Λ . We work with Fock states $|0\rangle$ through $|\Lambda\rangle$, such that the spin-1/2 case of Ref. [151] is recovered at $\Lambda = 1$. In Sec. 3.2.2, we show how localization is only mildly dependent on the sector selected by the occupation n_0 of the zeroth site. Accordingly, in the following, we set $n_0 = 1$.

The Hamiltonian is one dimensional, local, and gapped at finite Λ ; therefore, its ground state can be efficiently accessed via a matrix product state (MPS) formulation of the DMRG [161]. The main source of error is given by the finite cutoff Λ . Indeed, the properties of $|\psi_0(n_0)\rangle$ can change nontrivially as a function of Λ . More precisely, for any finite cutoff Λ , the model falls into the class of localized systems studied in Ref. [151]. As a result, $|\psi_0(n_0)\rangle$ is always localized for a large enough s at finite Λ but this does not imply localization for $\Lambda \rightarrow \infty$. Indeed, although $U > 0$ makes the spectrum of the Hamiltonian in Eq. (3.1) bounded from below, it does not ensure that its ground state is still localized in space when s is finite. In the following, we extract the $\Lambda \rightarrow \infty$ limit via a scaling analysis.

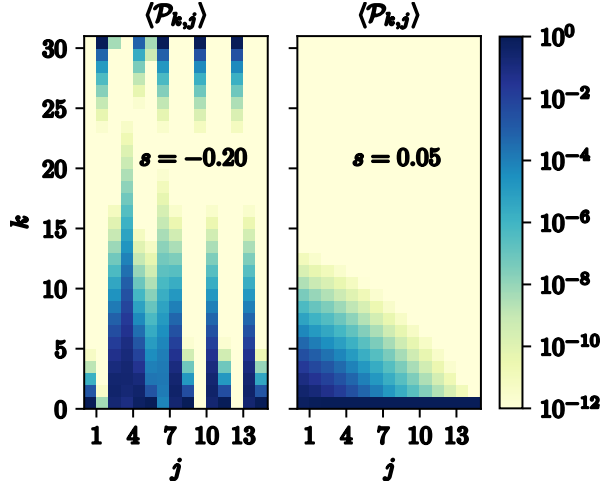


FIGURE 3.2. The probability of having $k \in [0, \Lambda]$ bosons on site $j \in [1, L]$ in the ground state. In the plot, we do not display the occupation n_0 of the zeroth site that fixes the “East symmetry” sector. We fix $L = 15$, $\Lambda = 30$, $n_0 = 1$ and $U = 1$. In the left panel, we consider a typical configuration in the delocalized phase ($s = -0.20$). The cutoff is saturated over many sites. The staggered feature is due to the repulsive nearest-neighbor interaction. In the right panel, we consider a typical localized ground state ($s = 0.05$). Along each site j , the probability of having k bosons, $\langle \mathcal{P}_{k,j} \rangle$, drops exponentially fast with k . The light color means that the value is smaller than 10^{-12} . Image taken from Ref. [1].

In Fig. 3.1, we show the average occupation number $\langle \hat{n}_j \rangle$ as a function of site j for some values of s at fixed $U = 1$. For s not large enough, the average occupation does not change smoothly with the site j and it saturates the cutoff Λ , meaning that there are strong finite-cutoff effects. In contrast, for s large enough, the occupation decays exponentially in j , matches Eq. (3.6) well, and does not change upon increasing the cutoff Λ . The value of s at which this change of behavior occurs depends on U , as we discuss in more detail in this section.

In order to check the effects of a finite Λ cutoff, we compute the probability of having k bosons on site j , namely the expectation value of the projector $\mathcal{P}_{k,j} = |k\rangle_{jj}\langle k|$, where $|k\rangle_j$ is the Fock state with k particles on site j . In Fig. 3.2, we show $\langle \mathcal{P}_{k,j} \rangle$ as a function of k and j for typical localized and delocalized ground states, respectively. The results in the delocalized phase are not reliable, since the observable suffers finite-cutoff effects. Instead, in the localized phase,

$$\langle \mathcal{P}_{k,j} \rangle \sim e^{-k/\xi_{F,j}}, \quad (3.7)$$

with $\xi_{F,j} > 0$ for any site j . The exponential decay in the localized phase sheds additional light on the fact that the system is well described by a finite effective cutoff (for additional details, see Appendix A.2).

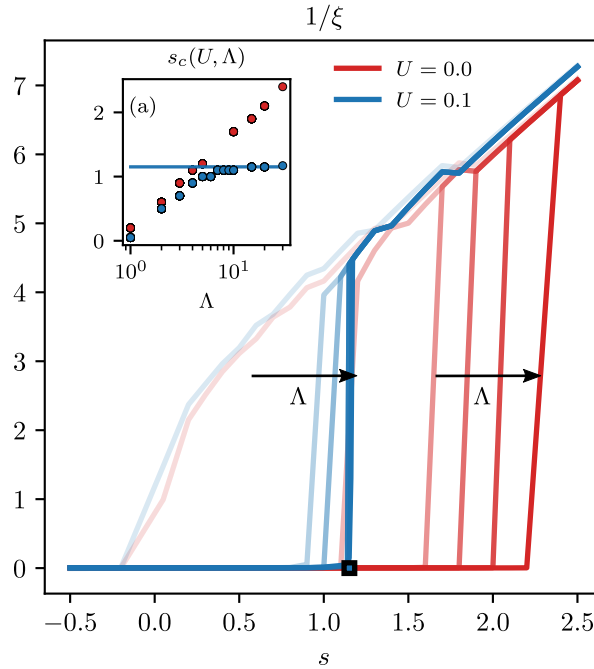


FIGURE 3.3. The inverse of the localization length ξ in a system of $L = 15$ “active” sites in the symmetry sector $n_0 = 1$ and $\beta_{r=0}$. The main plot shows the inverse of the localization length ξ^{-1} as a function of s for different values of $\Lambda \in [1, 30]$ and U . The darker lines correspond to larger values of Λ . The square is the mean-field estimate of s_c in the bosonic case ($\Lambda = \infty$). The inset (a) shows the behavior of $s_c(U, \Lambda)$ as a function of Λ for $U = 0$ (red) and $U = 0.1$ (blue). The circles correspond to numerically extracted values from the DMRG results, while the continuous lines are the mean-field estimate $s_c \approx \log(1/\sqrt{U})$, which matches the numerics at large Λ . Image taken from Ref. [1].

For each value of U and Λ , the inverse of the localization length goes from values smaller than or equal to zero to positive values as s increases. We identify the region where $1/\xi \leq 0$ as the delocalized phase, while the region where $1/\xi > 0$ is identified as the localized phase. In the delocalized phase, strong finite cutoff effects can lead to a positive localization length ξ . In order not to mistakenly identify these points as belonging to the localized phase, we fix a threshold $\lambda > 0$ and for each Λ and U we identify the transition point $s_c(U, \Lambda)$ as the value of s such that $1/\xi \leq \lambda$ and $1/\xi > \lambda$ for s smaller and greater than $s_c(U, \Lambda)$, respectively. We choose $\lambda \approx 10^{-1}$. The results are weakly affected by this choice of λ . Furthermore, the precise location of the transition point $s_c(U, \Lambda)$ is beyond the scope of this thesis, since we are interested in engineering states deep in the localized phase, as we discuss extensively in Sec. 3.3.

As discussed above, in the delocalized phase, results are strongly dependent on the cutoff, since the average occupations always saturate their artificial upper bound. This

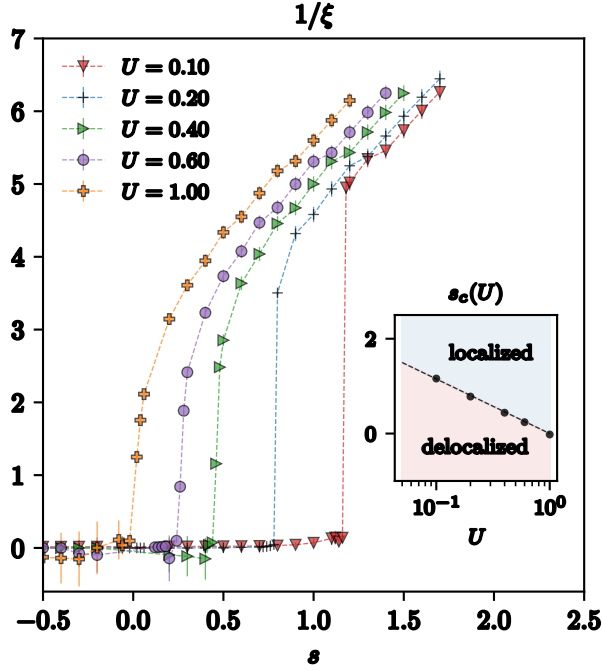


FIGURE 3.4. The inverse of the localization length ξ in a system of $L = 15$ “active” sites in the symmetry sector $n_0 = 1$ and $\beta_{r=0}$. We fix the cutoff $\Lambda = 30$. The main plot shows the inverse of the localization length ξ^{-1} as a function of s for different values of U . We plot the error bars on top of each point. In the inset we plot the transition point $s_c(U)$ as a function of U . The dots represent the extracted $s_c(U) \equiv \lim_{\Lambda \rightarrow \infty} s_c(U, \Lambda)$. The dashed line is the mean-field estimate for the transition point $s_c^{\text{MF}}(U) = \log(1/\sqrt{U})$. Image taken from Ref. [1].

circumstance allows us to draw only qualitative conclusions on the physics at $s < s_c$ in the case of the bosonic East model ($\Lambda \rightarrow \infty$).

In Fig. 3.3, we show the inverse of the localization length ξ swiping s for different values of Λ at fixed U . For $U = 0$, the transition point $s_c(U = 0, \Lambda)$ always increases with Λ . Instead, when $U > 0$, the transition point converges to a finite value independent of Λ for $\Lambda \rightarrow \infty$. In Fig. 3.3.(a), we show the numerically extracted transition point $s_c(U, \Lambda)$ as a function of Λ and U . For $U > 0$, it is possible to extract a finite value of $s_c(U) \equiv \lim_{\Lambda \rightarrow \infty} s_c(U, \Lambda)$. Instead, for $U = 0$, the transition point scales as $s_c(U = 0, \Lambda) \propto \log(\Lambda)$, suggesting that in the actual bosonic system we have $s_c(U = 0) = \infty$, meaning that there is no transition. Therefore, whenever $U > 0$, the system undergoes a delocalized-localized transition at finite $s_c(U)$. In Fig. 3.4, we show the inverse of the localization length ξ as a function of s for different values of U at fixed Λ . The transition point s_c depends on the competition between the dynamical term, controlled by e^{-s} , and the nearest-neighbor density term, proportional to U . The former favors the delocalization of the state, while the latter favors its localization.

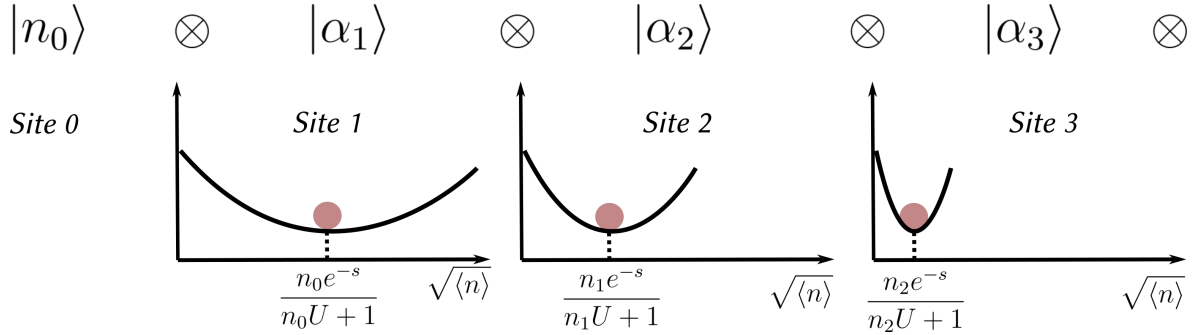


FIGURE 3.5. Sketch of the ground state assuming a mean-field ansatz, i.e. no entanglement. The bosonic quantum East model could be interpreted as a chain of interacting harmonic oscillators which are parametrically driven by the occupation of the previous site. Upon fixing the first site in a Fock state $|n_0\rangle$ with n_0 bosons, the Hamiltonian describing the first site is given by a driven harmonic oscillator, which has as ground state a bosonic coherent state with amplitude $\alpha_1 = \sqrt{n_0 e^{-s}} / (n_0 U + 1)$. In turn such state pumps the second site, and so on. If the driving term $\propto e^{-s}$ is weaker than the dressed frequency of the harmonic oscillator $n_0 U + 1$, we expect the ground state to be localized.

Indeed, in the $U \rightarrow 0$ limit, we provide evidence that the bosonic system is always delocalized if $s < \infty$. Instead, in the large U limit, the Hamiltonian is approximated by $U \sum_i \hat{n}_i \hat{n}_{i+1} + \hat{n}_i$, the ground state of which in a specific symmetry sector at given total particle number is simply $|n_0\rangle |00\dots 0\rangle$.

3.2.1. An intuitive picture: chain of parametrically driven anharmonic oscillators

The role of the interaction term U in the localization of the bosonic system can be appreciated in a mean-field treatment. We project the Hamiltonian into the manifold of coherent product states $|\phi\rangle = \bigotimes_{j=1}^L |\alpha_j\rangle_j$, with $\hat{a}_j |\alpha_j\rangle_j = \alpha_j |\alpha_j\rangle_j$. We evaluate the Hamiltonian given in Eq. (3.4) in this basis:

$$\langle \phi | H(n_0) | \phi \rangle = -\frac{1}{2} \sum_{j=0}^L |\alpha_j|^2 (2e^{-s} \alpha_{j+1} - U |\alpha_{j+1}|^2 - 1), \quad (3.8)$$

where $|\alpha_j|^2$ is the average number of particles in the coherent state at site j . From unidirectionality of the interaction, we can write $\langle \phi | H(n_0) | \phi \rangle = -\frac{1}{2} \sum_j |\alpha_j|^2 h_j(\alpha_{j+1}, s, U)$, where $h_j(\alpha_{j+1}, s, U) = (2e^{-s} \alpha_{j+1} - U |\alpha_{j+1}|^2 - 1)$. For energetic stability the effective field $h_j(\alpha_{j+1}, s, U)$ on site j should be negative:

$$\begin{aligned} (2e^{-s} \alpha_{j+1} - U |\alpha_{j+1}|^2 - 1) &< 0 \Rightarrow \\ \Rightarrow s > \log \left(\frac{2\alpha_{j+1}}{1 + U |\alpha_{j+1}|^2} \right) &\equiv s_c(\alpha_{j+1}). \end{aligned} \quad (3.9)$$

Since the system does not conserve the number of particles there can be an unbounded number of excitations in the ground state within a fixed symmetry sector. Therefore, in order to have localization at a mean-field level it is necessary that Eq. (3.9) holds for any value of $\alpha_{j+1} \in [0, \infty)$, namely $s > \max_{\alpha_{j+1}} s_c(\alpha_{j+1})$, and for all sites. For $U > 0$, such condition is satisfied if $s > \log(1/\sqrt{U})$, which turns to be in very good agreement with the DMRG numerical findings (see Fig. 3.4). Instead, for $U \leq 0$, there is no finite value of s that fulfills Eq. (3.9) for all α_{j+1} .

The mean field treatment just discussed could be further appreciated interpreting the bosonic quantum East model as a chain of coupled optomechanical systems [156] (cf. Fig. 3.5). Adopting such picture, the calculation just carried out translate in a stability condition of such system. When the system is stable, localization of excitations occurs. Instead, when the system is unstable the system favours an unbouded number of excitations, leading to delocalization. Intuitively, the system localizes if the j -th oscillator is non-resonant (due to U), and not strong enough (small e^{-s}) to excite the following one. Otherwise, the system is able to be more and more excited, favouring delocalization.

More quantitatively, the excellent agreement between the DMRG and the mean-field analysis can be explained by observing that the ground state $|\psi_0\rangle$ (excluding the zeroth site, which fixes the symmetry sector) obtained via the DMRG is well approximated via a product state, namely $|\psi_0\rangle \approx \bigotimes_{j=1}^L |\phi_j\rangle$. To further investigate the nature of the state $|\psi_0\rangle$, we consider the correlator $\Delta_j \equiv (\langle \hat{n}_j \hat{n}_{j+1} \rangle - \langle \hat{n}_j \rangle \langle \hat{n}_{j+1} \rangle)$. We use this operator as a proxy for non-Gaussian correlations. We compare Δ_j computed on the ground state obtained via the DMRG and the one computed assuming that the same state is Gaussian in the operators $\{\hat{a}_j^{(\dagger)}\}_{j=1}^L$, using Wick's theorem. As shown in Appendix A.3, the closer we are to the transition point s_c , the more the state develops non-Gaussian features at distances $j \lesssim \xi$. On the contrary, deep in the localized phase, the Gaussian *ansatz* captures the actual correlations at all sites well. Indeed, in the large s limit, the Hamiltonian turns out to be diagonal in the number basis, namely $H(s \gg 1) \sim \sum_j (\hat{n}_j \hat{n}_{j+1} + \hat{n}_j)$, the ground state of which is $|n_0\rangle |00 \dots 0\rangle$, which is a product state of Gaussian states (excluding the zeroth site, which fixes the symmetry sector).

The localized tail can be explained also via the adiabatic theorem. Indeed, the Hamiltonian is gapped in the localized phase when $U > 0$; therefore, we can adiabatically connect two ground states within it. In particular, we can link any localized ground state to the one at $s = \infty$. This choice is particularly convenient since the Hamiltonian is diagonal in the number basis at $s = \infty$, $H(s \rightarrow \infty) = \sum_{j=1}^L (U \hat{n}_j \hat{n}_{j+1} + \hat{n}_j)/2$ and its ground state at fixed symmetry sector is simply $|n_0\rangle \bigotimes_{j=1}^L |0\rangle_j$. Then, the evolution

with the adiabatically changing Hamiltonian will dress the initial site with an exponentially localized tail. In Sec. 3.3, we further exploit the adiabatic theorem to design the many-body version of a variety of states that are relevant in quantum-information setups, such as coherent states, cat states, and squeezed states.

3.2.2. Properties of the localized ground state in different symmetry sectors

So far, we have focused on the case where the first non-empty site is occupied by $n_0 = 1$ bosons. However, a natural question is whether upon changing n_0 the system is still localized. Indeed, following the qualitative argument carried out in Sec. 3.2.1, we could naively envision the scenario where the larger is the occupation n_0 of the 0-th site, the more the following one is parametrically pumped, and so on. Instead, we observe that thanks to the interacting terms, such picture does not hold. Indeed, it is true that the drive increase its strength, but also the potential term does, which balance its effect. This can be straightforwardly seen from the mean-field argument summarized in Fig. 3.5, where the occupation in the first site, for large n_0 , scales as e^{-s}/U , which is independent on n_0 . Nonetheless, this mean-field argument could be disrupted by quantum fluctuations. Consequently, we carry out a detailed analysis using tensor-network

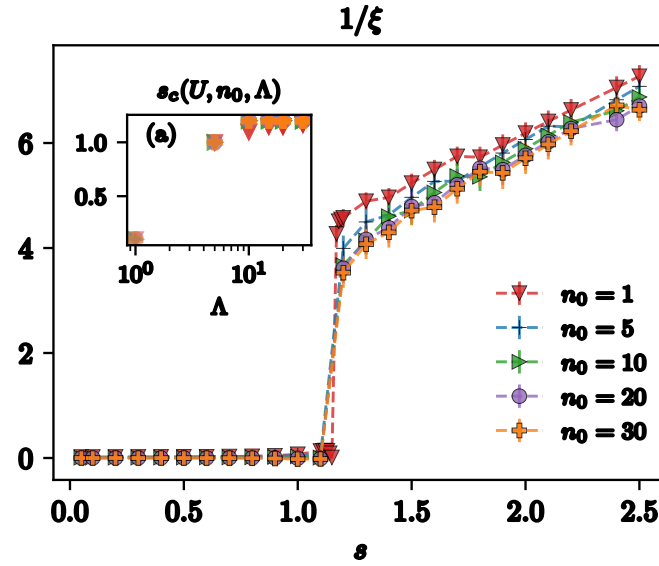


FIGURE 3.6. The inverse of localization length ξ in a system of $L = 15$ “active” sites upon changing s for different values of $n_0 = 1$. We fix $U = 0.1$. The main plot shows the inverse of the localization length ξ^{-1} as a function of s for $\Lambda = 30$. The inset (a) shows the behavior of s_c as a function of Λ for different values of n_0 . The circles correspond to numerically extracted values from DMRG results. The points are indistinguishable upon changing n_0 for $\Lambda \gtrsim 10$. Image taken from Ref. [1].

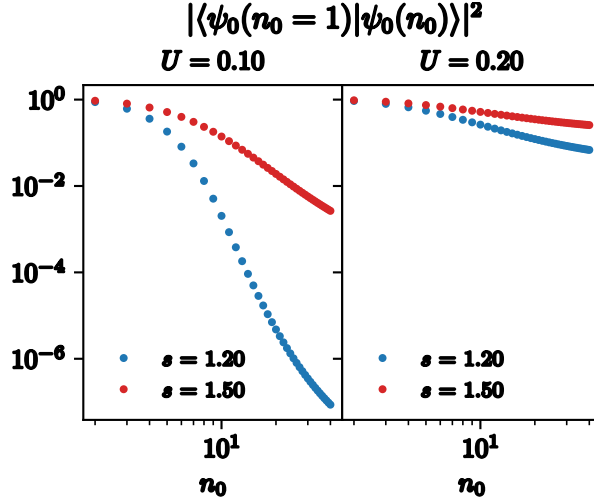


FIGURE 3.7. The overlap of the exponential tail as a function of $n_0 \in [2, 40]$ for two different values of $U = \{0.1, 0.2\}$ and $s = \{1.20, 1.50\}$. We choose these values of U and s since we are not so deep in the localized phase. The more the system is within the localized phase, the more the localized tails are weakly dependent on n_0 . Image taken from Ref. [1].

methods, as performed in Sec. 3.2. Doing so, we discuss the properties of the ground state upon changing the symmetry sector specified by the occupation n_0 of the first nonempty site. We confirm that the transition point and the exponential decaying tail of the ground state occupation is weakly dependent on n_0 . We discuss the dependence of the ground state energy on n_0 , which will be relevant in performing adiabatic protocols for preparing localized states of practical interest in Sec. 3.3.

We perform the same scaling analysis as a function of the cutoff Λ discussed in Sec. 3.2 (see Fig. 3.6). We extract the transition point s_c for different values of n_0 from the inverse of the localization length ξ . The existence of a finite critical point s_c in the $\Lambda \rightarrow \infty$ limit turns out to be weakly dependent on the specific symmetry sector n_0 at fixed U . We investigate the dependence of the localized tail of the ground state $|\psi_0(n_0)\rangle$ as a function of n_0 (we exclude the first site, which fixes the symmetry). To this end, we compute $|\langle\psi_0(n_0=1)|\psi_0(n_0)\rangle|^2$, with $n_0 \geq 1$ (see Fig. 3.7). We fix $n_0 = 1$ as a reference as we want to see whether or not the tail is weakly dependent on n_0 . All the ground states are computed by fixing $\Lambda = 30$. The overlap $|\langle\psi_0(n_0)|\psi_0(n_0=1)\rangle|$ strongly depends on s and U . Indeed, the more the system is in the localized phase, the more the exponentially localized tail is weakly dependent on n_0 . Therefore, deep in the localized phase, $|\psi_0(n_0)\rangle$ is approximately independent on the specific sector n_0 and we can write

$$|\tilde{n}_0\rangle \equiv |n_0\rangle \otimes |\psi_0(n_0)\rangle \approx |n_0\rangle \otimes |\psi_0\rangle, \quad (3.10)$$

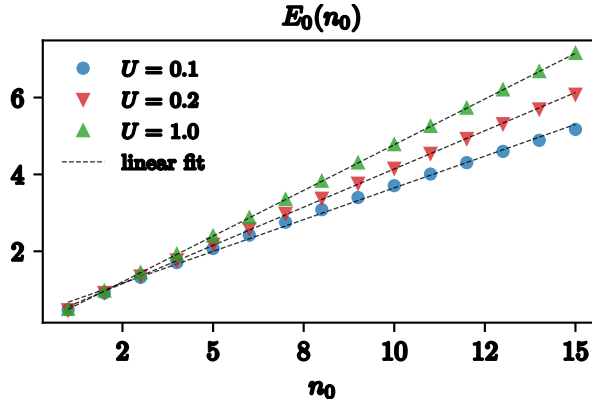


FIGURE 3.8. The energies of the ground state as a function of n_0 for different values of U at fixed $s = 1.5 > s_c(U)$ and cutoff $\Lambda = 15$. The dashed lines are the linear fit. The more we are deep in the localized phase, the more $E(n_0) \propto n_0$. Image taken from Ref. [1].

where $|\psi_0\rangle$ is explicitly independent of n_0 .

The weak dependence of $|\psi_0(n_0)\rangle$ with respect to n_0 has consequences on the ground state energy. Indeed, the expectation value of the Hamiltonian on Eq. (3.10) is

$$E_0(n_0) \equiv \langle \tilde{n}_0 | \hat{H} | \tilde{n}_0 \rangle \approx \frac{1}{2} n_0 + \mathcal{O}(n_0 e^{-1/\xi(n_0)}), \quad (3.11)$$

where $\langle \hat{n}_j \rangle \sim e^{-j/\xi(n_0)}$ since we are in the localized phase. In Fig. 3.8, we give a numerical evidence of Eq. (3.11).

3.3. LOCALIZED STATES ENGINEERING

In Sec. 3.2, we have discussed the localization properties of the ground state of the bosonic quantum East model within each symmetry sector specified by the occupation n_0 of the first nonvacant site. In this section, we show that the ground states of different symmetry sectors are connected via bosonic creation and annihilation operators. We use this infinite set of localized states to construct the localized versions of cat, coherent, and squeezed states that are relevant for quantum-information purposes. These states share the same properties as their single-mode counterparts, although they are supported on a few neighboring sites toward the East as the ground states.

Starting with a given symmetry sector fixed by n_0 , our aim is to find operators \mathcal{A} and \mathcal{A}^\dagger that obey the bosonic canonical commutation relations $[\mathcal{A}, \mathcal{A}^\dagger] = 1$, with the defining property

$$(\mathcal{A}^\dagger)^{n_0} |0\rangle = \mathcal{N} |n_0\rangle \otimes |\psi_0(n_0)\rangle := \mathcal{N} |\tilde{n}_0\rangle, \quad (3.12)$$

where $|\psi_0(n_0)\rangle$ is the localized tail of the ground state at fixed symmetry sector n_0 and \mathcal{N} is a constant. In other words, by acting n_0 times on the bosonic vacuum state with the operator \mathcal{A}^\dagger , we aim to retrieve the localized ground state of the Hamiltonian in Eq. (3.1) in the symmetry sector with n_0 particles on the first nonvacant site. From now on, we refer to these operators as *superbosonic* creation and annihilation operators since, in contrast to single site annihilation and creation operators, they act on a localized region of the system, by creating or destroying a bosonic localized tail along the chain. Likewise, we refer to the localized ground states $|\tilde{n}_0\rangle$ as *superbosons*.

In order to find an explicit form for such operators, we employ the adiabatic theorem. From numerical evidence our Hamiltonian, is gapped within the whole localized phase (see Fig. 3.9). Therefore, there exists a slow tuning of s that enables us to connect two localized ground states at fixed values of U and n_0 . We consider such a unitary transformation $\mathcal{U}(s, U)$ linking the ground state for $s = \infty$ with the target one at $s > s_c(U)$ in a fixed symmetry sector specified by the occupation n_0 of the first nonvacant site. We fix $s = \infty$ as our starting point since the Hamiltonian is diagonal in the number operator when $s \rightarrow \infty$ and its ground state is simply the tensor product $|n_0\rangle \otimes_{j \geq 1} |0\rangle_j$. By the adiabatic theorem, the unitary operator takes the following form [162, 163]:

$$\mathcal{U}(s, U) = \mathcal{T} \exp \left[-i \int_0^T dt H(s(t)) \right], \quad (3.13)$$

where \mathcal{T} indicates the time-ordering operator and $s(t)$ is a function that interpolates from $s(t = 0) = \infty$ and $s(t = T) = s$. The function $s(t)$ has to be chosen such that it satisfies [162, 163],

$$\frac{1}{\Delta(t)^2} \max_{n \neq 0} \left| \langle \Psi_n(t) | \dot{H}(t) | \Psi_0(t) \rangle \right| \ll 1, \quad (3.14)$$

at all times t . In Eq. (3.14), the state $|\Psi_n(t)\rangle$ is the n -th excited eigenstate of the Hamiltonian computed at time t ; $\dot{H}(t)$ is the time derivative of the Hamiltonian, which encodes the information about the specific protocol; finally, $\Delta(t) \equiv E_1(t) - E_0(t)$ is the gap at time t . For a reasonably fast protocol, we require $\Delta(s) \sim \mathcal{O}(1)$ in the parameter regime of interest. We write $H(s(t)) = H(s = \infty) + J(t)V$, where $H(s = \infty) = \sum_j (\hat{n}_j + U\hat{n}_j\hat{n}_{j+1})/2$, and $V = \sum_j \hat{n}_j(\hat{a}_{j+1} + \hat{a}_{j+1}^\dagger)$ is the coupling that we adiabatically switch on through the time-dependent protocol $J(t) = -e^{-s(t)}/2$. The time derivative of the Hamiltonian then reads $\dot{H}(t) = \dot{J}(t)V$. Let us focus on the perturbation V and the gap Δ at first and then on the specific protocol $J(t)$. In Fig. 3.9, we show the gap of the Hamiltonian and the maximum matrix element $\max_n V_n(s) \equiv \langle \psi_n(s) | V | \psi_0(s) \rangle$ connecting the ground to the n -th excited state as a function of s at fixed U . Within the localized phase, the gap is $\mathcal{O}(1)$ and the maximum matrix element $\max_n V_n(s) \sim n_0$, where n_0 is the occupation of the first nonempty site fixing the symmetry sector. Due to the kinetic constraint, the largest matrix element $\max_n V_n(s)$

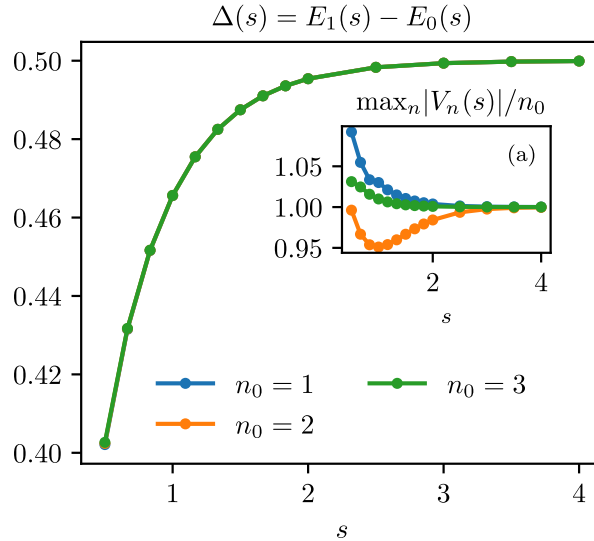


FIGURE 3.9. The gap of the Hamiltonian in Eq. (3.5) as a function of $s \in [0.5, 4]$ for different values of the occupation n_0 of the first nonempty site. The inset (a) shows the maximum matrix element $\max_n V_n(s)/n_0 \equiv \max_n \langle \psi_n(s) | V | \psi_0(s) \rangle / n_0$ of the perturbation $V = \sum_j \hat{n}_j (\hat{a}_{j+1} + \hat{a}_{j+1}^\dagger)$ between the n -th excited state and the ground state at fixed s . We fix a system size $L = 6$, cutoff $\Lambda = 3$ and nearest-neighbor density-density interaction $U = 1$. The transition point is at $s_c(U = 1) \approx 0$. The results are weakly affected (of the order of few percent) by the finite cutoff Λ for $s \lesssim 2$. Image taken from Ref. [1].

is between the localized ground state and the second localized state perturbatively close to the product states $|n_0 100 \dots \rangle$ (note that this is not necessarily the first excited state). Therefore, the leading contribution comes from the first few sites, since the other terms are exponentially suppressed in the localization length of $|\Psi_0\rangle$. Let us consider, as a possible adiabatic protocol, the linear ramping $J(t) = -e^{-s}t/(2T)$, where $t \in [0, T]$, with T as the total duration time. From Eq. (3.14), the total time T has to satisfy $T \gg n_0 e^{-s}$. Recall that we set the on-site bare frequency of the bosons as our energy scale and therefore the time T is expressed in that unit as well. In Chapter 7, we propose a possible experimental implementation of the bosonic quantum East model based on superconducting qubits. The typical on-site bare frequency of superconducting qubits is $\mathcal{O}(\text{GHz})$, leading to $T \gg (n_0 e^{-s})\text{ns} \sim 1\text{ns}$, which is within the typical coherence time of $\mathcal{O}(1\mu\text{s})$ of state-of-the-art superconducting qubits [164].

For $s(t)$ that satisfies Eq. (3.14), we obtain

$$\mathcal{U}(s, U) |n_0\rangle_0 \bigotimes_{j=1}^L |0\rangle = e^{i\theta} |\tilde{n}_0\rangle, \quad (3.15)$$

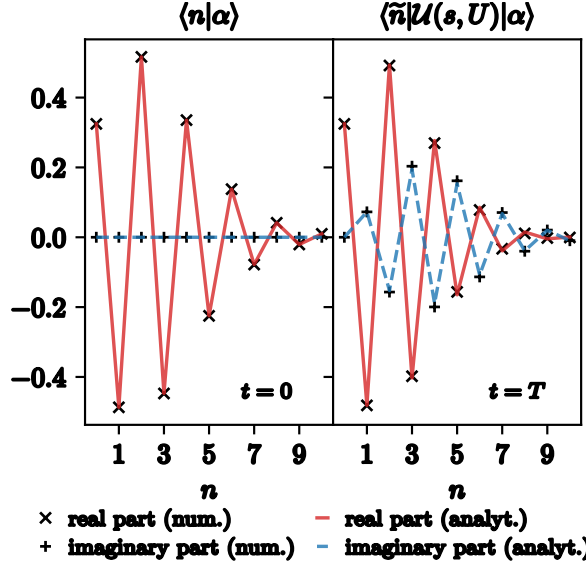


FIGURE 3.10. At $t = 0$, the system is prepared in a single-body coherent state $|\alpha\rangle = |\alpha\rangle_0 \bigotimes_{j=1}^L |0\rangle_j$, where $|\alpha\rangle_0$ is a coherent state on the first site with $\alpha = 1.5$. At time $t \geq 0$, we apply the adiabatic protocol defined in Eq. (3.13) to the state $|\alpha\rangle$ up to time $t = T$, obtaining $|\tilde{\alpha}'\rangle$. In the left panel, we compute the probability amplitudes $\langle n|\alpha\rangle$, where $|n\rangle = |n\rangle_0 \bigotimes_{j=1}^L |0\rangle_j$ is an eigenstate of the number operator \hat{n}_0 . The data (symbols) match the amplitudes of a single-site coherent state with $\alpha = 1.5$ (continuous and dashed line). In the right panel, we compute the probability amplitudes $\langle \tilde{n}|\mathcal{U}(s, U)|\alpha\rangle$, where $|\tilde{n}\rangle$ is a *superboson* (cf. Eq. (3.12)) with n excitations on the first site. The data (symbols) match the amplitudes of the localized version of a coherent state defined in Eq. (3.19) well, with $\alpha' = 1.5e^{1.42i}$ (continuous and dashed line). Image taken from Ref. [1].

where θ is a phase acquired during the adiabatic time evolution [162, 163]. Using $|n_0\rangle_0 = (\hat{a}_0^\dagger)^{n_0} |0\rangle / \sqrt{n_0!}$ and $\mathcal{U}(s, U)|00\dots 0\rangle = |00\dots 0\rangle$, we obtain

$$(\mathcal{A}(s, U)^\dagger)^{n_0} |\tilde{0}\rangle = e^{i\theta} \sqrt{n_0!} |\tilde{n}_0\rangle, \quad (3.16)$$

where $|\tilde{0}\rangle \equiv |00\dots 0\rangle$ and $\mathcal{A}(s, U)^\dagger = \mathcal{U}(s, U) \hat{a}_0^\dagger \mathcal{U}(s, U)^\dagger$. We can straightforwardly generalize Eq. (3.16) taking into account the position j starting from which we want to embed the state $|\tilde{n}_0\rangle$. We define $\mathcal{A}_j(s, U)^\dagger = \mathcal{U}(s, U) \hat{a}_j^\dagger \mathcal{U}(s, U)^\dagger$, the action n_0 times of which on the bosonic vacuum generates the state $|0\rangle_\ell^{\otimes \ell < j} \otimes |\tilde{n}_0\rangle$. Differently from the generic interacting case, the dressed operator $\mathcal{A}_j^{(\dagger)}(s, U)$ acts nontrivially in a region exponentially localized around j . The operator $\mathcal{A}_j(s, U)^{(\dagger)}$ satisfies the bosonic commutation relations, since they are connected via a unitary transform to the bare bosonic operators $\hat{a}_j^{(\dagger)}$. Therefore, they are bosonic operators. As anticipated, we call the operators $\mathcal{A}_j(s, U)^{(\dagger)}$ *superbosonic annihilation(creation)* operators.

Since the transition point s_c is essentially independent of the value of n_0 (see Appendix 3.2.2), we can design a protocol that obeys the adiabatic theorem for any initial state $|n_0\rangle \otimes |0\dots 0\rangle$. Furthermore, since these states belong to dynamically disconnected symmetry sectors, $\mathcal{H}_{k=0, n_0}$, for any values of s and U , it is possible to adiabatically evolve them independently of each other. Therefore, any linear combination of initial states turns under the adiabatic protocol into

$$\begin{aligned} \mathcal{U}(s, U) \sum_{n_0} c_{n_0} |n_0\rangle \otimes |0\dots 0\rangle &= \sum_{n_0} c_{n_0} (\mathcal{A}(s, u)^\dagger)^{n_0} |\tilde{0}\rangle \\ &= \sum_{n_0} c_{n_0} e^{i\theta(n_0, s, U, T)} |\tilde{n}_0\rangle, \end{aligned} \quad (3.17)$$

where $\theta(n_0, s, U, T)$ is the phase acquired during the adiabatic time evolution. As discussed in Sec. 3.2.2, deep in the localized phase the spectrum depends linearly on n_0 , with small corrections. Since the phase acquired during the adiabatic evolution depends on the energy of the given state during the protocol, we have $\theta(n_0, s, U, T) \sim n_0 f(s, U, T)$, where $f(s, U, T)$ is a function that is dependent on the specific protocol. This has important consequences for the state engineering we discuss in the following. As an example, let us consider as initial state of the adiabatic preparation the coherent state $|\alpha\rangle \equiv |\alpha\rangle_0 \otimes_{j \geq 1} |0\rangle_j$, where

$$|\alpha\rangle_0 = \sum_{n=0}^{\infty} \frac{e^{-|\alpha|^2/2} \alpha^n}{\sqrt{n!}} |n\rangle_0. \quad (3.18)$$

Using Eq. (3.17), the state $|\alpha\rangle$ turns into

$$\begin{aligned} \mathcal{U}(s, U)|\alpha\rangle &= \sum_{n=0}^{\infty} \frac{e^{-|\alpha|^2/2} \alpha^n}{\sqrt{n!}} e^{i\theta(n, s, U, T)} |\tilde{n}\rangle \\ &= \sum_{n=0}^{\infty} \frac{e^{-|\alpha'|^2/2} \alpha'^n}{\sqrt{n!}} |\tilde{n}\rangle, \end{aligned} \quad (3.19)$$

where $\alpha' = \alpha e^{if(s, U, T)}$. In Fig. 3.10, we compute the overlap between $\mathcal{U}(s(t), U)|\alpha\rangle$ and the *superbosons* $|\tilde{n}(s(t), U)\rangle$ for different values of α at the initial time $t = 0$ and at the final time $t = T$ of the adiabatic transformation. At the initial time, we have $\mathcal{U}(s(0), U)|\alpha\rangle = |\alpha\rangle$ and $|\tilde{n}(s(0), U)\rangle = |n\rangle \otimes |00\dots 0\rangle$. At the final time we have $|\tilde{n}(s(T), U)\rangle = |\tilde{n}\rangle$. In Fig. 3.10, the overlaps are in very good agreement with Eq. (3.19) and we obtain the desired state in Eq. (3.19) with a fidelity ≈ 0.9994 for $\alpha = 1.5$. We expect that when α is large, the fidelity achieved by the protocol becomes small, since corrections to the linear dependence of $\theta(n, s, U, T)$ from n become important. We call the localized version of a coherent state $|\tilde{\alpha}\rangle \equiv \mathcal{U}(s, U)|\alpha\rangle$ a *supercoherent* state.

Analogously, we perform the same analysis considering as initial state a cat state $|C\rangle$ on site $j = 0$. Indeed, since the phase factor $e^{if(s, U, T)}$ does not depend on α , given a

cat state

$$|C\rangle \bigotimes_{j>1} |0\rangle_j = \frac{1}{\mathcal{N}} (|\alpha\rangle_0 + e^{i\phi} |-\alpha\rangle_0) \bigotimes_{j>1} |0\rangle_j, \quad (3.20)$$

where \mathcal{N} is a normalization constant, its localized version is

$$|\tilde{C}\rangle = \frac{1}{\mathcal{N}} (|\tilde{\alpha}'\rangle + e^{i\phi} |-\tilde{\alpha}'\rangle) \quad (3.21)$$

where $|\tilde{C}\rangle \equiv \mathcal{U}(s, U)|C\rangle$, and $\alpha' = \alpha e^{if(s, U, T)}$. We call $|\tilde{C}\rangle$ a *supercat* state.

We can extend Eq. (3.19) to states of the form

$$|\psi\rangle = |00\dots 0\rangle \otimes \left(\sum_{n=0}^{\infty} \rho_n \beta^{\theta n} |n\rangle_j \right) \otimes |00\dots 0\rangle, \quad (3.22)$$

where $\rho_n \in \mathbb{R}$ and $\beta, \theta \in \mathbb{C}$. Indeed, if we apply the adiabatic protocol to the state defined in Eq. (3.22), the phase acquired can be absorbed into β . Coherent states, cat states, and squeezed states all fall into the class described in Eq. (3.22). In other words, using the adiabatic protocol, not only can we engineer the localized versions of states such as coherent and squeezed states but we can do so preserving their single-mode properties.

For instance, the localized versions of coherent and squeezed states can be implemented either via the adiabatic time evolution or the application of an operator \mathcal{M} that is linear or quadratic in the superbosonic operators \mathcal{A} . The operator \mathcal{M} can be obtained applying the adiabatic protocol to its single-site counterpart M , namely $\mathcal{M} = \mathcal{U}(s, U)M\mathcal{U}(s, U)^\dagger$. For instance, we define the dressed displacement operator,

$$\mathcal{D}(\alpha) = \exp(\alpha \mathcal{A}^\dagger - \alpha^* \mathcal{A}), \quad (3.23)$$

where $\alpha \in \mathbb{C}$ is the displacement parameter, and the dressed squeezed operator,

$$\mathcal{S}(\zeta) = \exp\left[\frac{1}{2} (\zeta^* \mathcal{A}^2 - h.c.)\right], \quad (3.24)$$

where $\zeta \in \mathbb{C}$ is the squeezing parameter, the action of which on the vacuum creates a *supercoherent* and *supersqueezed* state, respectively. However, the most natural way to prepare such states is by starting from their single-mode version and then adiabatically turning on the off-diagonal term $\propto e^{-s}$ in the Hamiltonian. Note that these states are Gaussian with respect to the *superbosonic* operators $\mathcal{A}^{(\dagger)}$ and not with respect to the bare operators $\hat{a}^{(\dagger)}$. We call these states *super-Gaussian*.

We find that *superbosons* $|\tilde{n}_0\rangle$, with different n_0 and the same position j of the first nonvacant site, are connected via the operators $\mathcal{A}_j^{(\dagger)}$. We see that their localized feature makes their energies approximately evenly spaced as a function of n_0 (cf. Appendix 3.2.2). The evenly spaced energies of different ground states and the fact that

the different ground states are connected via a bosonic operator $\mathcal{A}_j(s, U)^{(\dagger)}$ resemble the features of a quadratic Hamiltonian, such as the one-dimensional harmonic oscillator. Adding up these properties, the action of the interacting Hamiltonian $H(s, U)$ in Eq. (3.1) in the manifold of the ground states is approximatively equivalent to a free theory in the *superbosonic* operators $\mathcal{A}_j(s, U)^{(\dagger)}$, namely

$$H(s, U) \approx \sum_{j=-\infty}^{+\infty} \epsilon_0 \mathcal{A}_j(s, U)^{\dagger} \mathcal{A}_j(s, U). \quad (3.25)$$

the eigenstates of which are $\bigotimes_{j=-\infty}^{+\infty} (\mathcal{A}_j(s, U)^{\dagger})^{k_j} |0\rangle$, where $k_j \in [0, \infty)$. The effective Hamiltonian in Eq. (3.25) well captures the action of the full Hamiltonian Eq. (3.1) on a *superboson* $|\tilde{n}\rangle$ well up to a certain n that is parametrically large in s and U , since corrections to the evenly spaced feature of the ground states energies become important as n increases. Moreover, the effective Hamiltonian in Eq. (3.25) neglects the interaction between neighboring *superbosons*. Therefore, in the infinite set of eigenstates of Eq. (3.25), only those given by *superbosons* separated by a large number of empty sites with respect to the typical localization length ξ approximate eigenstates of the original model well (up to corrections that are exponentially small with the distance of two *superbosons*). For instance, the state $\mathcal{A}_1(s, U)^{\dagger} \mathcal{A}_{j \gg \xi}(s, U)^{\dagger} |0\rangle$, which describes two far localized excitations, is an eigenstate of the effective theory in Eq. (3.25) and, approximately, of the original Hamiltonian in Eq. (3.1). Instead, the state $\mathcal{A}_1(s, U)^{\dagger} \mathcal{A}_2(s, U)^{\dagger} |0\rangle$, which describes two nearly localized excitations, is an eigenstate of Eq. (3.25) with energy $2\epsilon_0$, while it is not an eigenstate of the original model Eq. (3.1), since we are neglecting the contribution coming from the interacting part of the Hamiltonian. Despite these limitations, the effective Hamiltonian in Eq. (3.25) captures the equilibrium properties in the localized phase and the dynamical features of states such as the *supercat* state and *supersqueezed* state well when the interacting part bewteen *superbosons* can be neglected. In this regard, the properties of the localized phase of quantum East models are reminiscent of the l -bits construction in MBL [98–101].

Let us consider a *supercat* state $|\psi(t=0)\rangle = |\tilde{\mathcal{C}}\rangle$ defined in Eq. (3.21) as initial state in order to test the effective quadratic theory in Eq. (3.25). We evolve it and compute the fidelity

$$\mathcal{F}(t) = |\langle \psi(t) | \psi(t=0) \rangle|^2. \quad (3.26)$$

As shown in Fig. 3.11, the fidelity displays almost perfect oscillations at short times, followed by a drop and almost perfect revivals. The short-time behavior is compatible with a rotation of the *supercat* state in the *dressed* phase-space $\tilde{X}_0 = (\mathcal{A}_0 + \mathcal{A}_0^{\dagger})$ and $\tilde{P}_0 = -i(\mathcal{A}_0 - \mathcal{A}_0^{\dagger})$, as expected from the effective Hamiltonian in Eq. (3.25). We can approximately compute the dynamics of the *supercat* state $|\tilde{\mathcal{C}}\rangle$ generated by Eq. (3.25) as

$$e^{-iHt} |\tilde{\mathcal{C}}\rangle \approx \frac{1}{N} \left(|\tilde{\alpha}(t)\rangle + e^{i\phi} |-\tilde{\alpha}(t)\rangle \right), \quad (3.27)$$

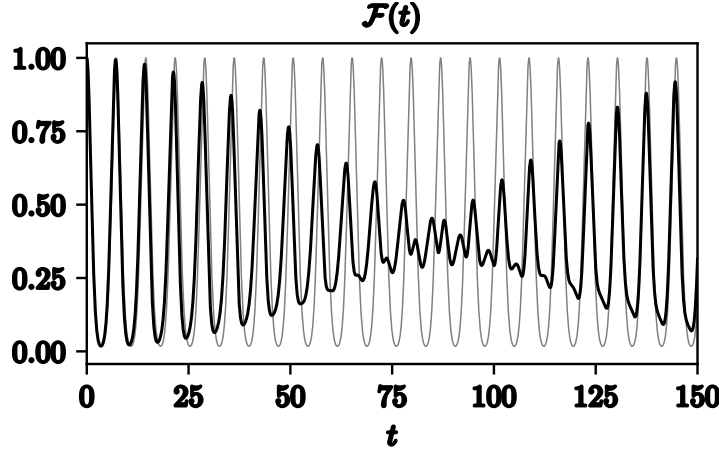


FIGURE 3.11. The coherent dynamics of a *supercat* state with $\alpha = 1.5$. We simulate a system of size $L = 15$. We fix $s = 1$ and $U = 1$. We show the dynamics of the fidelity \mathcal{F} (dark black line). The light black line is the expected value from the effective quadratic theory in Eq. (3.25) with a numerically extracted $\epsilon_0 \approx 0.43$. Image taken from Ref. [1].

where $\alpha(t) = \alpha(t = 0)e^{-i\epsilon_0 t}$. The state in Eq. (3.27) is a rotating *supercat* state in the *dressed* space. From Eq. (3.27) we can estimate the expected fidelity. In Fig. 3.11, we compare the expected value and the numerical results. The former matches the numerical results up to times parametrically large in s and $1/\alpha$. On the one hand, nonlinear corrections are suppressed the more the system is localized. On the other, corrections to the linear dependence of the energies $\langle \tilde{n} | \hat{H} | \tilde{n} \rangle$ become important the larger n is or, equivalently, α , leading to dephasing processes [165]. The revivals can be explained considering nonlinear effects; indeed, perfect revivals are observed for single-mode cat states with self-Kerr interaction [166] (for a circuit-QED implementation, see Ref. [167]). Differently from the latter case, we have an extended state and nearest-neighbor density-density interactions. As a consequence, pushing the simulations to longer times we observe no perfect revivals as in the case of single bosonic modes with Kerr nonlinearities. Such behavior might be captured by improving the effective theory introduced in Eq. (3.25), adding nonlinearities in the basis of *superbosonic* degrees of freedom. This is beyond our current scope and therefore left as a potential interesting follow-up.

We can extend these dynamical properties to any state prepared via the adiabatic protocol starting from a state of the form given in Eq. (3.22). Indeed, these states evolve analogously to the *supercat* state under the effective quadratic theory defined in Eq. (3.25). The *super-Gaussian* states fall into this class. Once again, we highlight that these states are Gaussian with respect to the *superbosonic* operators $\mathcal{A}^{(\dagger)}$ but not with respect to the bare operators $\hat{a}^{(\dagger)}$.

We have discussed the application of the adiabatic protocol to a single-site state embedded in the vacuum; however, this extends directly to more general initial states. For instance, we could have started from a product state made of single-body states separated by a large number of empty sites, with respect to the localization length ξ , or from a superposition of those. At the end of the protocol, each one will be dressed independently from the others. Therefore, the final state will be made of localized states concatenated one after the other.

3.4. IMPACT OF COUPLING TO THE ENVIRONMENT

So far, we have assumed the system to be completely isolated from the environment. However, any realistic device is inevitably coupled to the environment, and it is thus necessary to assess how the phenomena discussed so far are affected by such coupling. To this aim, in this section, we investigate the dynamical properties of the localized states introduced in Sec. 3.3 when coupled to the environment. Here, we study the effects of two different couplings with an external bath, namely a global dephasing due to a noise coupled to the local densities, which commutes with the “East” symmetry, and global losses, which break the “East” symmetry. Both of these couplings are experimentally relevant in superconducting circuits setups [164], which are at the core of the experimental implementation we will discuss in Chapter 7. We provide numerical evidence that local information is erased very slowly when the environment is coupled via densities to the system. We show how the characteristic time scales depend on the parameters of the Hamiltonian, the initial state, and the strength of the coupling to the environment. On the contrary, we show that losses are highly disruptive and that the time scales are dependent on the strength of the coupling to the environment and the initial state, while the underlying coherent dynamics does not play a substantial role. At the end of the section, we show that the typical couplings to the environment currently achieved in superconducting circuits are small enough to make the effects of the coherent dynamics appreciable and observable in the presence of losses.

We consider the following Lindblad master equation:

$$\dot{\hat{\rho}} = -i[\hat{H}, \hat{\rho}] + \gamma \sum_j \left(\hat{L}_j \hat{\rho} \hat{L}_j^\dagger - \frac{1}{2} \left\{ \hat{L}_j^\dagger \hat{L}_j, \hat{\rho} \right\} \right), \quad (3.28)$$

where $\hat{\rho}$ is the state of the system, \hat{H} is the Hamiltonian in Eq. (3.1) with $\epsilon = 0$, \hat{L}_j is the quantum jump operator acting on site j and γ is the corresponding rate. In order to efficiently simulate the Lindblad master equation in Eq. (3.28), we resort to the quantum trajectories algorithm, which is based on defining the effective non-Hermitian

Hamiltonian

$$\hat{H}_{\text{eff}} = \hat{H} - i \frac{\gamma}{2} \sum_j \hat{L}_j^\dagger \hat{L}_j, \quad (3.29)$$

and alternating the action of the Hamiltonian given in Eq. (3.29) with the jump operators $\{\hat{L}_j\}$ based on a stochastic process (for the details, we refer to Refs. [168, 169]). The dynamics of any observable \hat{O} result from averaging over N different uncorrelated stochastic trajectories labeled by $\eta \in [1, N]$,

$$\langle \hat{O}(t) \rangle = \langle \mathcal{O}_\eta(t) \rangle_\eta, \quad \mathcal{O}_\eta(t) = {}_\eta \langle \psi(t) | \hat{O} | \psi(t) \rangle_\eta, \quad (3.30)$$

where $|\psi(t)\rangle_\eta$ is the state for a given stochastic trajectory $\eta \in [1, N]$ at time t and $\langle \cdot \rangle_\eta$ denotes the average over the different trajectories. We resort to tensor-network methods for performing the simulations (see Appendix A.4). We consider two different jump operators, namely $\hat{L}_j = \hat{n}_j$ and $\hat{L}_j = \hat{a}_j$. The former corresponds to dephasing, while the latter corresponds to losses. We choose such jump operators in order to investigate the effects of the environment when it preserves the “East” symmetry, as for the dephasing process, or when it does not, as for the global losses. Both situations are relevant in superconducting-circuit setups [164]. We compute the observables averaging over 1000 to 3000 stochastic realizations depending on the value of γ and the jump operator.

We study the dynamical properties of *superbosons* $|\tilde{n}\rangle$ defined in Eq. (3.12), since they constitute the building blocks of any localized state that we can engineer. Then, we turn our attention to a paradigmatic superposition of *superbosons*, namely the *supercat* state, providing arguments to extend our findings to a class of states to which *supersqueezed* and *supercoherent* states belong. We consider as initial state $|\psi_k(t=0)\rangle = \bigotimes_{j=-\infty}^{k-1} |0\rangle_j \otimes |\tilde{n}\rangle$, where the subscript k in $|\psi_k(t=0)\rangle$ refers to the position of the first site of the embedded *superboson*. Since $|\tilde{n}\rangle$ is localized with localization length ξ (cf. Eq. (3.6)), we can truncate its support to $L' \gg \xi$ sites. Thus, our initial state is

$$|\psi_k(t=0)\rangle = |0\rangle_j^{\otimes_{j=-\infty}^{k-1}} \otimes |\tilde{n}\rangle_{L'} \otimes |0\rangle_j^{\otimes_{j=k+L'}^{+\infty}}, \quad (3.31)$$

where L' is the size of the *superboson* support.

In a generic non-integrable system, we expect information about initial states encoded in local observables to be washed out fast. Here, we want to study how localization and slow dynamics instead protect the information encoded in local quantities. We compute the fidelity and the imbalance. The fidelity (cf. Eq. (3.26)) provides global information about the state and sets an upper bound on the time dependence of the expectation value of any local observable. Nonetheless, the fidelity is highly sensitive to any local perturbation of the state. Indeed, it is enough to have even a single occupied site far from the superbosons $|\tilde{n}\rangle$ to make Eq. (3.26) negligibly small. Among all the possible local observables, we want to investigate if the initial localized peak remains

well resolved. We therefore compute the imbalance between the occupation of the initial peak and the second highest peak in the system, namely

$$\mathcal{I} = \frac{n_k - \max_{j \neq k} n_j}{n_k + \max_{j \neq k} n_j}, \quad (3.32)$$

where k is the position of the first site of the embedded state (cf. Eq. (3.31)). The imbalance $\mathcal{I} \in [-1, 1]$ and for $\mathcal{I} > 0$ the initial peak is the largest one in the system. When dissipation enters in the form of a dephasing noise coupled to the bosonic densities, the Lindblad equation respects the “East” symmetry. The jump operators commute with the operator in Eq. (3.3). Thus, the n excitations on the first site of the *superbosons* $|\tilde{n}\rangle$ and the empty sites to its left are conserved. Furthermore, since the the jump operators are not able to generate excitations out of the vacuum and the state is exponentially localized, we can keep only a few empty sites to the left of $|\tilde{n}\rangle_{L'}$ without introducing relevant size effects. For the set of parameters that we choose, restricting the *superboson* support to $L' \approx 10$ sites and keeping only one empty site to its right turns out to be sufficient. Thus, our initial state is

$$|\psi(t=0)\rangle = |\tilde{n}_0\rangle_{L'} \otimes |0\rangle. \quad (3.33)$$

In Fig. 3.12 we show the dynamics of the fidelity and imbalance for different values of s and noise strength γ keeping $U = 1$, starting from the state in Eq. (3.33) with $n_0 = 1$. The imbalance displays an exponential decay $\mathcal{I}(t) \sim \mathcal{I}(0)e^{-t/\tau}$, with τ dependent on the initial state, the parameters of the Hamiltonian, and the coupling strength γ with the external bath. The decay time τ increases the more the system is in the localized phase and the larger is the initial occupation n_0 , while it decreases with the noise strength γ as $\tau \propto 1/\gamma$. Therefore, the time decay τ can be enhanced by either tuning the parameters of the Hamiltonian or embedding a *superboson* with n_0 large (cf. Eq. (3.33)). On the one hand, increasing s or U helps to protect the local memory at longer times, at the cost of making the initial state less entangled. Indeed, in the $s, U \rightarrow \infty$ limit, the Hamiltonian tends to $\propto \sum_i (U n_i n_{i+1} + n_i)$, the ground state of which is a product state of eigenstates of number operators. On the other hand, we can exploit the bosonic nature of the system and embed a *superboson* with a larger initial n_0 , keeping s small and enhancing the initial state entanglement. It is important to stress that despite the exponential feature of the decay, the time scale τ is generally very large with respect to the time scales of the coherent dynamics of the system. From Eq. (3.32), and inspecting the late times average occupation number, the initial peak remains still well resolved and so does the information encoded within it.

The fidelity decays exponentially fast in time $\mathcal{F}(t) \sim e^{-t/\tau'}$, with a decoherence time τ' dependent on the parameters of the Hamiltonian, the initial state, and the strength of the noise. Analogously to the decay time τ of the imbalance, the decoherence time τ' increases the more the system is in the localized phase and decreases with the noise

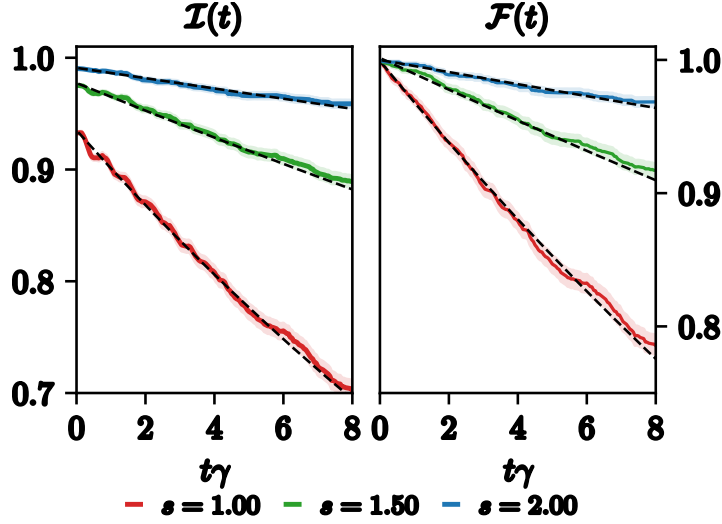


FIGURE 3.12. The time evolution of the imbalance (cf. Eq. (3.32)) and fidelity (cf. Eq. (3.26)) starting from the state in Eq. (3.33) and subjected to the dissipative dynamics given by Eq. (3.28) with quantum jump operator $\hat{L}_j = \hat{n}_j$. We fix $n_0 = 1$, $U = 1$, $\gamma = 0.1$ and we swipe across different values of $s \in [1, 2]$. The initial value $I(0)$ ranges from ≈ 0.93 to ≈ 0.99 as s increases. We show results for $s = \{1, 1.5, 2\}$, on top of which we plot the exponential fit (dashed black line). Both plots are in linear-linear scale. The light area surrounding the curves represents the statistical error due to the finite number of sampled trajectories. Image taken from Ref. [1].

strength γ as $\tau' \propto 1/\gamma$. Contrary to the imbalance, the fidelity drops faster the larger is n_0 . Indeed, the conserved initial occupation n_0 pumps excitations on the next site, reducing the typical coherent time scales by approximatively $1/(n_0 e^{-s})$ and effectively enhancing the effects of the environment.

Under the action of single-body losses, the dynamics no longer preserve the “East” symmetry. Indeed, losses can deplete the occupation of the first site, which fixes the “East” symmetry sector.

Since the vacuum is invariant under the action of losses and coherent dynamics cannot create excitations to the West of the initial embedded *superboson*, we can still consider Eq. (3.33) as our initial state. In Fig. 3.13, we show the dynamics of the fidelity and imbalance for different values of n_0 , keeping $U = 1$, $s = 1.5$ and $\gamma = 0.1$ fixed. Losses turn out to be detrimental to the initial state independent of the parameters of the Hamiltonian. Instead, the height of the initial peak plays a substantial role in enhancing the conservation of the imbalance. Intuitively, if the first site n_0 is highly occupied at time $t = 0$, it will require longer times to drain all the particles. This leads to an initial *plateaux* in the imbalance, followed by an exponential decay toward the minimum value $I(t \rightarrow \infty) = -1$. The decay is well fitted by $I(t) = (A e^{-t/\tau} - 1)$ at long times,

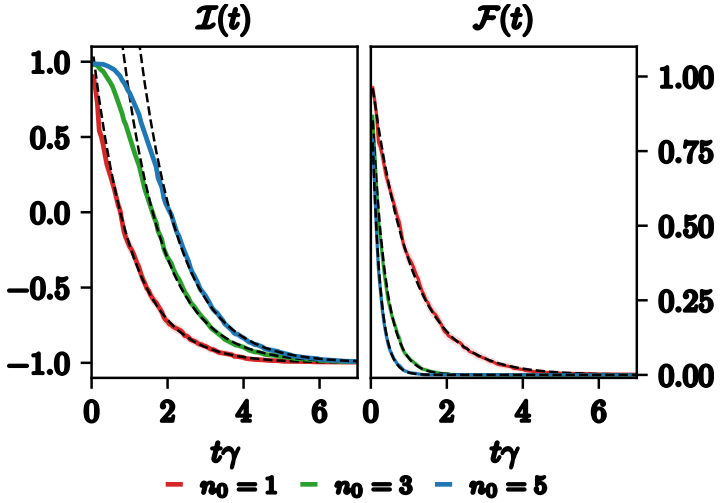


FIGURE 3.13. The time evolution of the imbalance (cf. Eq. (3.32)) and fidelity (cf. Eq. (3.26)) starting from the state in Eq. (3.33), with $n_0 \in \{1, 3, 5\}$, and subjected to the dissipative dynamics given by Eq. (3.28) with quantum jump operator $\hat{L}_j = \hat{a}_j$. We fix $U = 1$, $s = 1.50$ ($e^{-s} \approx 0.22$), and $\gamma = 0.1$. The imbalance initial value is $\mathcal{I}(0) \approx 0.99$. In the main figures we show results for three different values of $n_0 = \{1, 3, 5\}$, on top of which we plot the exponential fit (dashed black line). The imbalance and fidelity decay as an exponential (the dashed lines are the associated fits). Both plots are in linear-linear scale. The light area surrounding the curves represents the statistical error due to the finite number of sampled trajectories. Image taken from Ref. [1].

where $\tau \propto 1/\gamma$ is the relaxation time and A is a constant. The insensitivity of the time decay with respect to the parameters of the Hamiltonian indicates that the slow dynamics do not provide additional protection against this type of coupling to the environment. Indeed, the decay of the imbalance is due to the emission of particles from the first occupied site, which fixes the symmetry sector, and since the coherent dynamics cannot create excitations on top of it the initial peak is depleted in time $\propto 1/\gamma$. The fidelity drops to zero exponentially fast, as expected, with a decay time that is parametrically small in the occupation of the initial peak. Indeed, the higher the peak is, the larger is the probability that the emission occurs, which immediately produces a state orthogonal to the initial one.

Despite losses being more detrimental with respect to dephasing, we show at the end of the section that the coherent dynamics takes place on time scales that are small with respect to the relaxation time in typical superconducting circuits (cf. Chapter 7 for the experimental implementation of the bosonic quantum East model).

Note that we can immediately extend our analysis to a large variety of states. For instance, we can consider states given by the superposition of *superbosons* embedded

in different regions of the systems, namely

$$|\Psi\rangle \propto |\psi_k(t=0)\rangle + e^{i\theta}|\psi_s(t=0)\rangle, \quad (3.34)$$

where $|\psi_k(t=0)\rangle$ is defined in Eq. (3.31), θ is a phase, and $|s - k| \gg \xi$. These two states are weakly coupled by the coherent and dissipative dynamics. In a first approximation, we can apply our analysis to each of them separately, and therefore predict their dynamics easily.

The extension of these results to superposition of *superbosons* embedded in the same support (cf. Eq. (3.17)) is less trivial and depends on the specific coupling to the environment. For instance, a coupling that does not preserve the “East” symmetry makes the different states dynamically connected, likely leading to different results from the ones observed for the single *superbosons*. On the other hand, a coupling which preserves the “East” symmetry can also lead to additional phenomena such as dephasing processes between the superimposed states. Indeed, we observe that coupling to the densities is also detrimental. We give further details in Sec. 3.4.1, exploring the effects of local dephasing in the system.

3.4.1. Local dephasing

We now investigate the effects of local dephasing in the dynamical properties of a state given by the superposition of *superbosons* embedded in the same support. Among the possible choices, we consider a paradigmatic *super-Gaussian* state, namely the *supercat* state, and then we generalize.

We consider local dephasing due to noise coupled to the densities (see e.g. [170]). In the case of local dephasing acting on a compact support \mathcal{S} , the effective theory in Eq. (3.29) turns into

$$\hat{H}_{\text{eff}} = \hat{H} - i\frac{\gamma}{2} \sum_{j \in \mathcal{S}} \hat{L}_j^\dagger \hat{L}_j, \quad (3.35)$$

where the summation is along the support \mathcal{S} . We consider $\hat{L}_j = \hat{n}_j$ as jump operator.

We study the impact of the dephasing as a function of the strength γ and the extension of its support \mathcal{S} . Since the dephasing preserves the “East” symmetry, we can once again focus on system comprising a few sites without introducing relevant finite-size effects. We initialize our system in the state

$$|\psi(t=0)\rangle = |\tilde{\mathcal{C}}\rangle_L, \quad (3.36)$$

where $|\tilde{C}\rangle_L$ is a *supercat* state (cf. Eq. (3.21)) with support L and average number of particles $|\alpha|^2$. A support of $L = 10$ turns out to be large enough for the parameters explored ($\alpha = 1.50$, $s = 1.5$ and $U = 1$). In Fig. 3.14 we show the dynamics of the fidelity as a function of the coupling strength γ and support \mathcal{S} . The *supercat* state is still localized in space for any γ and \mathcal{S} . Nonetheless, the coherence of the state is highly dependent on γ and \mathcal{S} . Indeed, local dephasing is highly disruptive in an exponentially localized region around the peak, where the state is mostly located. If, instead, the local dephasing acts on a region far from the localized peak it does not produce any appreciable effect. More precisely, we estimate that the typical time τ at which the embedded state is appreciably affected by the noise scales as $\tau \sim \min_{|k-j| \in \mathcal{S}} 1/(\gamma \langle n_j \rangle) \sim \min_{|k-j| \in \mathcal{S}} e^{|k-j|/\xi}/\gamma$, where k is the site where the peak is located. We numerically verify the polynomial dependence of τ on γ . On the contrary, it is not possible to extract the dependence on the support \mathcal{S} with high enough accuracy from the times explored, because of the

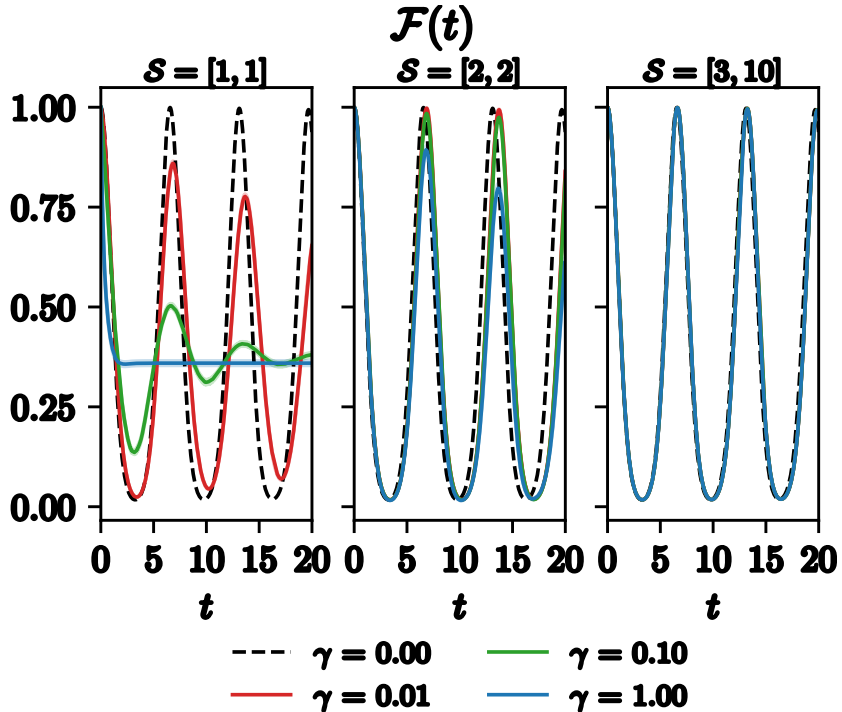


FIGURE 3.14. The dynamics of the fidelity (cf. Eq. (3.26)) of a *supercat* state with $\alpha = 1.5$ upon changing the noise strength γ and its support $\mathcal{S} = [a, b]$, starting from site a and ending at site b . We fix $U = 1$ and $s = 1.5$. The initial state is exponentially localized around the site $j = 1$. The dephasing is highly disruptive only in an exponentially localized region around the peak (see the first two columns). Instead, if it acts on a region far from the localized peak, it does not produce any appreciable effect at the scale shown in the plots. The light area surrounding the curves represents the statistical error due to the finite number of sampled trajectories. Image taken from Ref. [1].

slowness of the decay.

Our findings can be extended to other channels that do not necessarily preserve the ‘‘East’’ symmetry. For instance, losses acting far from the localized peak will not affect local information encoded in the localized state. Furthermore, we expect that the observed dynamical properties can be easily extended to any state prepared via the adiabatic protocol from a state of the form given in Eq. (3.22), to which *super-Gaussian* states belong.

In this section we have discussed the effects of dephasing and losses, without much emphasis on the actual value of the coupling strength γ to the environment in typical superconducting circuits (cf. Chapter. 7 for the implementation). As previously mentioned, we set the on-site bare frequency of bosons as our energy scale, which is $\mathcal{O}(\text{GHz})$ in typical superconducting circuits [164]. The typical strength of the coupling to the environment γ is $\mathcal{O}(\text{MHz})$ [164]. Therefore, $\gamma \approx 10^{-3}$ in our nondimensional units. As a consequence, coherent dynamics take place on smaller scales with respect to the operational times of typical superconducting platforms of $\mathcal{O}(1\mu\text{s})$, hinting that the physics of localized states is potentially observable in state-of-the-art experiments. Corroboration of this statement with more quantitative calculations would require an *ab initio* study of the dynamics of the architecture introduced in Chapter. 7, which constitutes an interesting follow-up project *per se*.

3.5. PERSPECTIVES

The implementation of a kinetically constrained East model using superconducting circuits represents a bridge between the two communities of circuit-QED and nonergodic quantum dynamics. It has the potential to attract the former toward fundamental questions regarding dynamical phase transitions and to stimulate the latter toward the search for quantum-information and metrological applications of constrained dynamics. Our explicit construction of localized analogs of squeezed and cat states relying on the East constraint represents a first stepping stone in this direction.

A fruitful prosecution of this work is the study of an analog of the mobility edge separating localized from delocalized states in the spectrum of East models (for the mobility edge in MBL see Refs. [37, 38]). An understanding of how such a mobility edge scales with Λ , is essential for predicting the onset of dynamical transitions in platforms with unidirectional constraints, as well as of practical interest. For instance, a mobility edge at finite energy density is a feature of direct relevance for experimental realizations,

since it would yield the conditions for performing efficient quantum manipulations deep in the localized phase when finite-temperature or heating effects are present. This will be object of Chapter 4.

A related interesting question is the survival of the effective integrable description of the localized phase discussed in Sec. 3.3 upon increasing the density of energy above the ground state. This would have implications for heat and particle transport features of the East model in the nonergodic phase, which would be governed by the effective integrable description in (3.25), as it happens for MBL systems [171].

The insensitivity to noise acting away from localized peaks could open up a path toward the study of the protection of spatially separated macroscopic superpositions of superbosonic states. Given the slow decay of localized wave packets in the presence of noise, one could conceive the storage and noise resilience of long-lived many-body entangled states in faraway regions, with applications to quantum communication.

CHAPTER 4

Mobility edge in a translational invariant system

Most of the content in this Chapter is in:

- “*State-dependent mobility edge in kinetically constrained models*” (arXiv: 2407.12909; to appear in Phys. Rev. X Quantum)
Manthan Badbaria, Nicola Pancotti, Rajeev Singh, Jamir Marino, and **Riccardo J. Valencia-Tortora**.

Executive Summary. In the previous Chapter, we have shown not only that translational invariant systems could display localization, but it could be also harnessed for preparing the localized version of metrologically relevant quantum states. However, most of the discussion has been carried out focusing on the low energy limits. Here instead, we aim to investigate the properties at finite energy density. However, an operative definition of a finite-energy in a bosonic system with an unbounded spectrum is hard. Indeed, the system considered does not conserve the number of excitations, and so the most excited state has virtually infinite energy even after fixing all the conserved quantities. As a consequence, in the bosonic case, we cannot define a location along the spectrum, and everything looks formally equivalent to ‘low energy’ physics. In order to circumvent such issues, we trade bosons with finite-dimensional constituents, i.e. spin-1/2. In such a manner, we obtain the quantum East model whose low-energy properties have been already extensively investigated [3, 140, 151–153] (see also Refs. [154, 155] for the Floquet version). Here, building on the signatures of a dynamical phase transition separating a fast and slow thermalizing phase [151] at finite energy density, we aim to further investigate the finite energy density physics. However, computing excited eigenstates is typically limited to small system sizes accessible by Exact Diagonalization. In order to circumvent such limitations, we propose a novel complexity-oriented proxy based on tensor-networks for detecting non-thermal features along the spectrum. Using such a proxy, we unveil that the quantum East model hosts a sort of mobility edge along the spectrum, namely it displays non-thermal features up to a finite energy density, while instead, it appears thermal above it. We further provide evidence of the predictive power of our proxy by finding a large family of non-thermal localized eigenstates at finite energy density. We then discuss the implication of our results in the context of random unitary circuits, providing arguments that the class of *tilted*-CNOTs based circuits, i.e. circuits made of CNOTs and single site gates diagonal

in the computational basis (not necessarily belonging to the Clifford gates), display regimes where they can be efficiently simulated on a classical computer. This finding expands the known classes of circuits efficiently simulable, alongside Clifford circuits, MBL inspired circuits [172], as well as fractonic random circuits [42, 173].

What is new? All results of this chapter represent novel research results.

Organization of the Chapter

- In Sec. 4.1 we introduce the quantum East model and discuss its known properties, in order to frame our contribution discussed in Sec. 4.2.
- In Sec. 4.3 we introduce the complexity-oriented dynamical proxy of dynamical phase transitions based on tensor-networks.
- In Sec. 4.4 we test our proxy providing evidence of the existence of a thermal to non-thermal dynamical phase transitions in the quantum East model. Then, we carry out a careful analysis (cf Secs. 4.4.4, 4.4.5) and identify the class of non-thermal eigenstates mostly responsible of the observed behavior. We then find them using DMRG-inspired algorithm (i.e., DMRG-X) in Sec. 4.4.6, further fueling the effectiveness of our complexity-oriented proxy in detecting the presence of non-thermal eigenstates.
- In Sec. 4.5 we discuss the implications of our results in the context of random unitary circuits, providing arguments that the class of *tilted*-CNOTs based circuits, i.e. circuits made of CNOTs and single site gates diagonal in the computational basis (not necessarily belonging to the Clifford gates), display regimes where they can be efficiently simulated on a classical computer. This finding expands the known classes of circuits efficiently simulable, alongside Clifford circuits, MBL inspired circuits [172], as well as fractonic random circuits [42, 173].
- In Sec. 4.6 we conclude the Chapter and we discuss some possible follow-up ideas inspired by our results that could be of interest to pursue.

This Chapter is composed by a rearrangement of the author's publication [2].

4.1. QUANTUM EAST MODEL

We study the quantum East model [1, 140, 151] in open boundary conditions with Hamiltonian

$$\hat{H} = -\frac{1}{2} \sum_{j=0}^N \hat{n}_j (e^{-s} \hat{\sigma}_{j+1}^x - 1), \quad (4.1)$$

where $\hat{\sigma}_j^\alpha$ is the Pauli- α matrix on site j ; $\hat{n}_j = (1 - \hat{\sigma}_j^z)/2$ is the projector onto the state $|1\rangle$ in the local z basis. The term \hat{n}_j in Eq. (4.1) is the kinetic constraint, which translates to a nontrivial action of the Hamiltonian solely to the right ('East') of a previously excited ($|1\rangle$) site. Consequently, the Hamiltonian acts trivially on empty strings without any excited sites to its left, making a so-called 'East symmetry' manifest: starting from the left, the location and occupation of the first excited spin cannot change. Thus, the Hilbert space splits into N dynamically disconnected sectors indexed with the position of the first occupied site $|1\rangle$; i.e. the k -th sector has $(k - 1)$ zeros preceding $|1\rangle$ on the k -th site. This feature is in stark contrast with systems undergoing Hilbert space fragmentation, where the number of disconnected subspaces is $\mathcal{O}(\exp(N))$ [42, 158, 174] (see Sec. 5.2 for a comparison with Hilbert space fragmentation). Because of the trivial action of Hamiltonian on empty sites, the results do not depend on the sector considered in the thermodynamic limit. Thus, we fix $k = 1$, without loss of generality. Once the 'East symmetry' sector is fixed, any product state can be dynamically accessed by any other. In other words, the sector is irreducible, as the Hamiltonian does not possess any other nontrivial (excluding the energy) conserved quantity.

4.1.1. *Localization and slow thermalization*

Despite being non-integrable and translational invariant, it has been shown that the quantum East model displays a dynamical transition separating a fast and slow thermalizing phase as a result of the competition of the kinetic term, controlled by e^{-s} , and the potential one $\propto \sum_j \hat{n}_j$ [140, 151]. Intuitively, when the kinetic term dominates ($s \lesssim 0$), excitations propagate ballistically, making the details of the initial state rapidly lost, while instead when it is small $s \gtrsim 0$, excitations propagate slowly, making the details of the initial state *potentially* matter up to long times. In Ref. [151] it was shown that such dynamical transition can be linked to the existence of a first-order delocalization-localization quantum phase transition upon changing the parameter s . Specifically, when $s < 0$ the ground state is delocalized; namely, the wave function is spread along the lattice with homogeneous probability and amplitude of finding an occupied site. Instead, the ground state is localized for $s > 0$, namely the corresponding wave functions contain nontrivial excitations only on a small region of the lattice around the first excitation fixing the East symmetry, while it is approximately in the vacuum state everywhere else. Specifically, for $s > 0$ the probability of finding an occupied site in the ground state decays exponentially as [151]

$$\langle \hat{n}_j \rangle \sim e^{-j/\xi}, \quad (4.2)$$

where ξ is the localization length, parametrically small in s , beyond which the ground state can be approximated as a product state of empty sites. As mentioned above, the

localization of the ground state is linked to the possible slow thermalization at finite energy densities [151]. Specifically, in Ref. [151], it has been shown that empty strings together with the localized ground state form a basis for building an exponentially large number of area-law states arbitrarily close to true eigenstates of the Hamiltonian, which in turn can affect the dynamics of a large family of initial states. However, such construction is not able to capture all the non-thermal states the system hosts, as it is mostly limited to low-energy ones. Therefore, there is still a lack of a complete understanding of the dynamical phase transition at finite-energy density and in particular in the middle of the spectrum, corresponding to infinite temperature states.

4.2. DOES THE SYSTEM DISPLAY A MOBILITY EDGE?

Here, we aim to investigate the dynamical phase transition of the quantum East model more closely. Specifically, we focus on whether the system hosts a mobility edge, i.e. a separation of a thermal region and a localized one in the spectrum of the Hamiltonian, despite being disorder-free. Indeed, the quantum East model stands as an excellent candidate capable of exhibiting a mobility edge in addition to being a paradigmatic example of a disorder-free localized system. This challenges the common belief that a mobility edge is exclusive to disordered systems [175–177]. However, in Ref. [151], Exact Diagonalization calculations suggest that the spectrum of the quantum East model does not exhibit a distinct separation between non-thermal eigenstates and thermal ones (which we replicate in Fig. 4.1), as instead observed in MBL systems with a mobility edge [95, 175, 176, 178]. Instead, its spectrum displays features more reminiscent to quantum many-body scarred (QMBS) systems, where few non-thermal eigenstates are distributed along the spectrum [157, 158]. Nevertheless, it is crucial to highlight that, in the quantum East model, the non-thermal eigenstates are not evenly spaced in the spectrum and their number grows exponentially with the system size, contrary to in QMBS systems where they are evenly spaced in energy and constitute a zero fraction of the spectrum in the thermodynamic limit. Nonetheless, it might seem as if our task of having a disorder-free mobility-edge is destined to fail. However, within the same context, it has been shown that the non-thermal eigenstates exhibit significant overlap with product states (see Fig. 4.1). This observation presents an intriguing possibility: the existence of a ‘state-dependent mobility edge.’ Specifically, the system behaves akin to having a many-body mobility edge for a large class of initial states, such as product states. To draw an analogy, we can envision a scenario resembling quantum many-body scarred systems, where the impact of the non-thermal eigenstates significantly influences the dynamics of some initial states. In this scenario, however, the exponential abundance of non-thermal eigenstates suggests the potential for non-thermal behavior

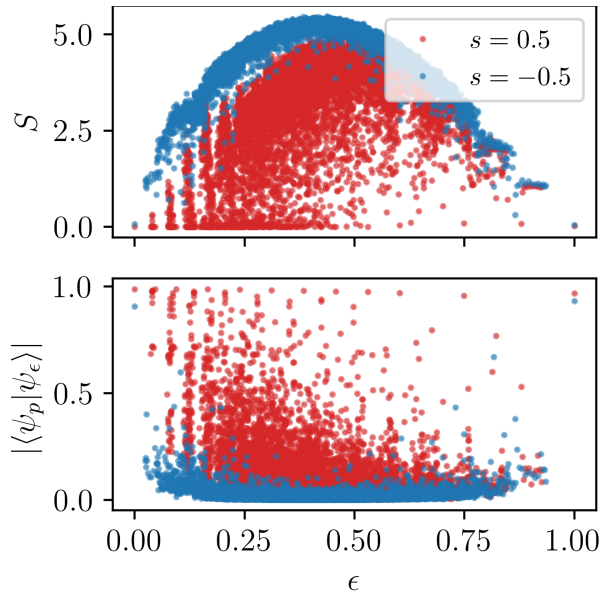


FIGURE 4.1. Half-cut entanglement entropy (upper panel) of the eigenstates $|\psi_\epsilon\rangle$ of the quantum East model (cf. Eq. (4.1)) and overlap between $|\psi_\epsilon\rangle$ and its best approximating product state $|\psi_p\rangle$ (lower panel) as a function of the normalized energy $\epsilon = (E - E_{\min})/(E_{\max} - E_{\min})$. In the delocalized phase ($s < 0$) the spectrum appears to be thermal, as typical for non-integrable systems. Instead, in the localized phase ($s > 0$) there are (exponentially) many non-thermal eigenstates with large overlap with product states. We show data for $N = 13$ sites. Image taken from Ref. [2].

to become prevalent across a wide range of initial states, particularly among product states. This question not only captivates theoretical interest but also holds practical relevance. Indeed, as product states are the easily preparable initial states in current NISQ devices, understanding this behavior becomes crucial for experimental investigations [3, 179–185]. In order to mitigate the limitations due to exponentially large Hilbert space, which limits exact diagonalization to small system sizes, in the following we propose a novel proxy of non-thermal eigenstates in the spectrum based on tensor-networks.

For generic one-dimensional non-integrable systems, tensor networks stand out as a widely accepted standard for their efficiency. However, while these methods are less susceptible to the curse of dimensionality, they still have limitations, particularly in handling dynamics. Specifically, the resources required—i.e., the bond dimension—typically scale exponentially with time. This occurs as the entanglement typically increases linearly in highly non-equilibrium dynamics (e.g., quench protocols) since finite-energy volume-law eigenstates of the Hamiltonian participate predominantly in the dynamics [186]. However, the presence of non-thermal eigenstates, e.g. eigenstates with little entanglement, could significantly reduce complexity and enable efficient simulations for

‘long’ times, as for instance in MBL systems [96, 97, 187]. We note that the constraints faced by tensor networks in handling dynamics align with our starting goal of investigating the properties of the eigenstates of a Hamiltonian by assessing the efficiency of performing classical simulations. To be more specific, we categorize a computational task as ‘hard’ (or ‘easy’) if the required computational resources scale (sub-)exponentially. We distinguish complexity along the space and time domain. For the time domain, we adopt the bond dimension χ of the matrix product state representation of the evolved states as a measure of complexity. We choose χ due to its connection with entanglement, which is widely regarded as an indicator of ‘hardness’ in representing quantum states in a classical computer. If χ grows (sub-)exponentially in time the task is said to be (‘easy’) ‘hard.’ We then correlate the complexity of simulating the dynamics of product states via tensor networks with the absence, if the task is ‘hard,’ or presence, if the task is ‘easy,’ of non-thermal eigenstates. Instead, for the complexity along the space domain, we look at the degree of separability of the evolved state, which directly reflects on the dimension of the accessible Hilbert space. If the state is inseparable, the complexity of representing it scales exponentially with the system size making the task of representing it ‘hard,’ as typical in interacting quantum systems. Instead, if the state is separable (at least approximately), the resources (e.g. memory storage in a computer) needed scale polynomially in the system size making its representation ‘easy.’ In the following, we refer, for simplicity, to the complexity along the time domain and space domain as time-complexity and space-complexity, respectively. Summarizing, space-complexity provides us information about the way the accessible Hilbert space is explored, while instead, time-complexity about the properties of the states dynamically visited during such exploration.

As we have defined more formally our goal, we now list our main findings (which are summarized in Fig. 4.2):

- (1) Time-complexity is typically ‘hard’ in the delocalized phase, as expected for generic non-integrable models, while instead it is typically ‘easy’ deep in the localized phase, analogously to MBL systems (cf. Sec. 4.4.3);
- (2) Near the critical point, on the localized side, we observe both ‘easy’ and ‘hard’ time-complexity region as we tune the energy density of the initial state at fixed Hamiltonian parameters, indicating the existence of a disorder-free mobility-edge (cf. Sec. 4.4.3);
- (3) The typically ‘hard’ and ‘easy’ time-complexity regions are separated by a crossover where details of the initial state, beyond the conserved quantities (i.e. the energy), matter in dictating the time-complexity (cf. Sec. 4.4.4). This is in agreement with the observations of Refs. [140, 151], where heterogeneity of the initial state plays a key role in glassy-like kinetically constrained models;

- (4) Combining the Lieb-Robinson bound [188] on the propagation velocity of quantum correlations with the heterogeneity characterizing glassy-like systems, we observe, upon initializing product states in the computational basis, a crossover from ‘easy’ to ‘hard’ in the space-complexity as a function of time. Specifically, in the ‘easy’ regime, the state is approximately separable and its dynamics can be faithfully computed by the dynamics of suitably chosen subsystems, neglecting the boundary terms connecting them. Instead, in the ‘hard’ regime the state is non-separable and such boundary terms have to be taken into account;
- (5) We link the points above by observing the existence of *localized kink states* at finite energy density (cf. Sec. 4.4.6), fueling the effectiveness of our complexity-oriented proxy in detecting thermal to non-thermal dynamical phase transitions;
- (6) We discuss the implications of our results in the context of random unitary circuits, providing evidence that the class of *tilted*-CNOTs based circuits, i.e. circuits made of CNOTs and single site gates diagonal in the computational basis (not necessarily belonging to the Clifford gates), display regimes where they can be efficiently simulated on a classical computer.

4.3. DYNAMICAL PROXY OF NON-THERMAL EIGENSTATES

To overcome the limitations faced by exact diagonalization, here we propose a complexity-oriented proxy based on tensor-networks for detecting non-thermal eigenstates. Our approach is based on the observation that typical thermalizing systems display an exponential growth of the bond dimension during dynamics, as opposed to systems displaying non-thermal behavior (e.g. MBL systems) where instead the bond dimension grows polynomially in time [96, 97]. An intermediate scenario is constituted by systems with a mobility edge, i.e. systems displaying non-thermal eigenstates in a certain energy window, and thermal ones in the others. Specifically, in such system we envision that the complexity of simulating the dynamics depends on the energy of the specific state at hand, potentially allowing a distinction between the two regions.

We take inspiration from Refs. [177, 189]. Specifically, in Ref. [189], the authors have considered a fully MBL system, i.e. with all eigenstates localized, showing that tensor-networks allow to efficiently simulate the dynamics of *observables* in the localized phase, while instead it is computationally hard in the thermal one. Computing the dynamics of observables generally involves democratically the full spectrum of the Hamiltonian, not allowing to selectively excite more a part of the spectrum with respect to

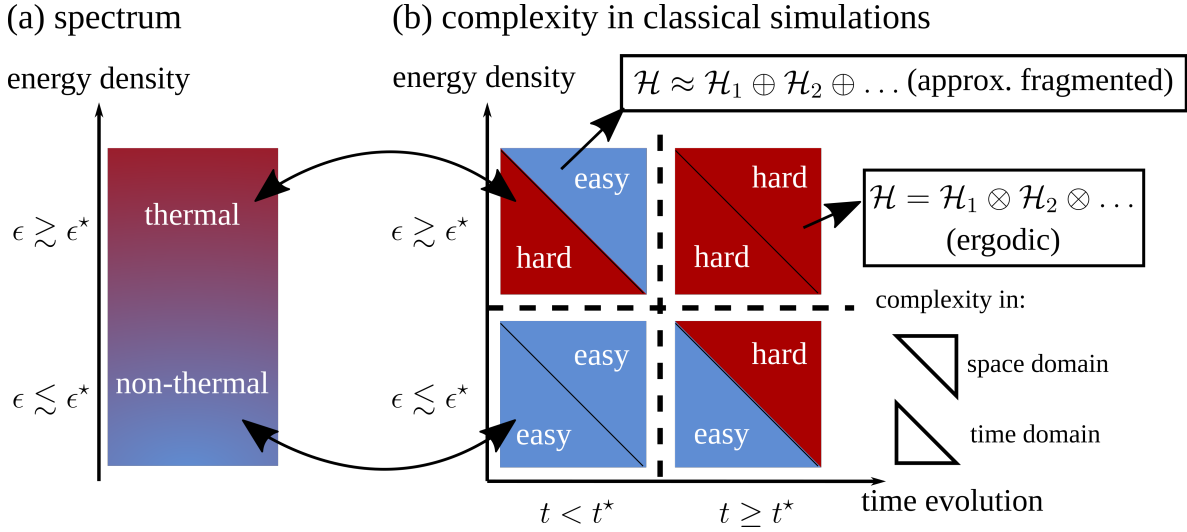


FIGURE 4.2. Cartoon summarizing the complexity phase diagram of simulating the dynamics of initial product states (cf. Eq. (4.3)) in the quantum East model both in time and space domain, as a function of the energy density $\epsilon \in [0, 1]$ of the initial state and the time t reached. Each box is split into two triangles which encode the complexity either along the space domain (upper triangle) or along the time domain (lower triangle). A simulation is (easy) hard in the time domain if the computational resources needed, i.e. the bond-dimension of the tensor network, grows (sub-)exponentially in time. Instead, a simulation is easy (hard) in the space domain if the accessible Hilbert space \mathcal{H} is, at least approximately, (in)separable. Simulations are easy in the time domain if the energy density (although other features play a role, see Sec. 4.4.4) is below a certain energy density ϵ^* , dependent on the parameters of the Hamiltonian, indicating the existence of a mobility edge in the spectrum (cf. Sec. 4.4.3). Additionally, during the time evolution of initial product states, upon allowing a small error in the dynamics, the evolved state is separable up to a time $\sim t^*$, controlled by the Hamiltonian and features of the initial state (cf. Sec. 4.4.5). As a consequence, the accessible Hilbert space \mathcal{H} can be expressed as a direct sum of smaller disconnected Hilbert spaces \mathcal{H}_i , in a fashion reminiscent of *fragmented* systems [42, 158, 174]. Image taken from Ref. [2].

the others. A possible way to overcome such limitation is by taking inspiration from Ref. [177], where it was shown how quench dynamics of initial states with small energy variance could allow the detection of a mobility edge in the spectrum.

Here, we combine the two approaches, adding to the approach carried in Ref. [189] an ‘energy resolution,’ by considering the dynamics of initial product *states*, not of observables. Specifically, we first select initial states with a small energy variance so that the eigenstates of the Hamiltonian participating in the dynamics are mostly within a

small energy window. Then, we use the way the bond dimension χ grows in time as a measure of time-complexity. In typical non-integrable systems, we expect an exponential growth of χ after a quench, as the bipartite entanglement entropy $S \propto \log \chi$ grows linearly in time [186]. Instead, a sub-exponential growth of χ could indicate the existence of non-thermal eigenstates in the spectrum. In the following, we label it as an ('easy') 'hard' task if the bond dimension needed scales (sub-)exponentially in time. In such a manner, we can potentially locate a mobility edge within the spectrum at fixed parameters of the Hamiltonian.

4.4. STATE-DEPENDENT MOBILITY EDGE

In this section, we locate the state-dependent mobility edge using as a proxy the time-complexity of evolving initial product states as a function of their properties, i.e. energy density and spatial structure, and the Hamiltonian parameters.

We perform the time-evolution using tensor networks, and we employ the maximum bond dimension $\chi_{\max}(t)$ of the matrix product state (MPS) as a metric for time-complexity, due to its connection with the amount of entanglement in the system. Adopting this measure, we can distinguish time-complexity regions characterized by qualitative different growths in time of the bond dimension. Specifically, we say that simulating dynamics is ('easy') 'hard' if the necessary resources grow (sub-)exponentially in time. While the exponential behavior is typical in the delocalized phase ($s < 0$), as expected for generic non-integrable models, we remarkably observe all the different regimes in the localized phase ($s > 0$) also at finite energy density, indicating the existence of a mobility edge (cf. Sec. 4.4.3). We show the huge impact of the heterogeneity in the initial state (cf. Sec. 4.4.4), characteristic of glassy-like kinetically constrained models, in dictating the time-complexity. Combining the Lieb-Robinson bound and the dynamical heterogeneity, we discover a crossover in space-complexity from an 'easy' regime, where the evolved state is separable (up to negligible contributions), to a 'hard' one, where the evolved state is non-separable (cf. Sec. 4.4.5). Building on these results, we discover a large family of localized states with finite energy density responsible for the observed behavior for many initial states considered (cf. Sec. 4.4.6). This last finding corroborates the sensitivity of our complexity-oriented proxy to non-thermal eigenstates of the Hamiltonian.

4.4.1. Initial states

As we are interested in investigating the existence of a ‘state-dependent mobility edge’, we need to specify the class of states of our interest. To our ends, we investigate the dynamics of initial product states in the computational basis

$$|\psi\rangle = |1\rangle \bigotimes_{k=1}^N |0/1\rangle_k, \quad (4.3)$$

where we keep the first site fixed to $|1\rangle$, making the dynamics occur in the largest irreducible ‘East’ symmetry sector of our model, while $|0/1\rangle$ could be either $|0\rangle$ or $|1\rangle$. As discussed in Sec. 4.3, a quench protocol could be used to probe information about the eigenstates when the energy variance of the initial state is small. Product states as the one in Eq. (4.3), with M excitations ($|1\rangle$), have

$$\begin{aligned} \langle\psi|\hat{H}|\psi\rangle &= \frac{M}{2}, & \langle\psi|\hat{H}^2|\psi\rangle &= \frac{e^{-2s}}{4}M + \frac{M^2}{4}, \\ \frac{\sqrt{\Delta H}}{\langle\psi|\hat{H}|\psi\rangle} &= \frac{e^{-s}\sqrt{M}}{M} \sim \frac{1}{\sqrt{M}}, \end{aligned} \quad (4.4)$$

where $\Delta H \equiv \langle\psi|\hat{H}^2|\psi\rangle - \langle\psi|\hat{H}|\psi\rangle^2$. Since we are interested in making statements at finite energy density (i.e. we want $\langle\hat{H}\rangle/N$ finite for $N \rightarrow \infty$), we set $M = mN$, with $m \in [0, 1]$ the density of excitations. In such a manner, the energy density is finite while the relative fluctuation around the mean goes to zero in the thermodynamic limit. Thus, such states are good candidates for analyzing the spectrum of the quantum East model. Notice that the average energy depends solely on m and not on their location, allowing us to isolate the impact of the spatial structure in the dynamics keeping it fixed.

4.4.2. Details on the numerical methods

For a fixed value of s and m , we sample up to 100 random product states to mitigate sample biases, and we simulate their dynamics using the Time Evolving Block Decimation algorithm [190]. We keep the Schmidt singular values larger than 10^{-14} and we set the timestep $\Delta t = 10^{-3}$. We stop the simulation when either the maximum allowed bond dimension equal to 512 or the time $T = 64$ is reached. For each simulation, we investigate how the max bond dimension $\chi_{\max}(t) = \max_{j \in [1, N-1]} \chi_j(t)$ grows in time by fitting either a polynomial ($\propto x^{\alpha t}$) or exponential ($\propto \exp\{rt\}$) function, where α and r are positive constants, depending on which one better approximates the data. Then, we link such behavior to the spectral properties of the Hamiltonian, as detailed in Sec. 4.3. We highlight that trotterizing the continuous-time dynamics induces undesired errors

tied to the finite time step. However, we do not expect the quantity of interest (i.e., the way the bond dimension grows) to be qualitatively affected by such errors, provided that we use a small enough time step. We present results on system size $N = 30$, as our statements are not appreciably affected upon increasing N (cf. Appendix B.2 for a detailed scaling analysis in N). In the following, we investigate dynamics as a function of the average energy, and their spatial structure (e.g. distance of initial excitations). All the results were obtained using the python package quimb [191].

4.4.3. *Role of energy density*

Here we focus on the impact of the energy density of the initial states in Eq. (4.3) in dictating the time-complexity of simulating the dynamics. While time-complexity is typically ‘hard’ in the delocalized phase ($s < 0$), as expected for generic non-integrable models, we remarkably observe both ‘easy’ and ‘hard’ regimes in the localized phase ($s > 0$) also at finite energy density, indicating the existence of a state-dependent mobility edge.

To extract the behavior in the thermodynamic limit, we measure the energy with respect to the ground state and most excited state energies, namely the normalized energy density $\epsilon = (\langle \hat{H} \rangle - E_{\min}) / (E_{\max} - E_{\min})$, where E_{\min} and E_{\max} are the energy of the ground state and the most excited state (which can be computed via DMRG minimizing the energy of $-\hat{H}$), respectively. Despite the advantage of initializing product states (cf. Eq. (4.3)) in isolating the interplay of their properties, e.g. the initial distribution of excitations, they have a drawback: they do not always allow an efficient sampling over ϵ . Specifically, as s decreases, it is not possible to sample from the extremes of the spectrum, as the ground state and the most excited states are ‘far’ from the singly occupied state and the completely filled state, respectively. Nonetheless, as we are mostly interested in the central region of the spectrum, associated with high-temperature states, such limitation does not play a major role in our results.

In Fig. 4.3(a), we show the fraction $f_{\text{easy}} \in [0, 1]$ of states for which time-complexity is ‘easy’, i.e. $\chi_{\max}(t)$ grows sub-exponentially in time, as a function of ϵ and s . As expected, in the delocalized phase ($s < 0$) the system mostly displays exponential growth of the bond dimension ($f_{\text{easy}} \approx 0$) as we move towards the middle of the spectrum ϵ (cf. Fig. 4.3a), reflecting the thermal nature of the whole spectrum. On the other hand, for $s > 0$ we observe regions where f_{easy} is large not only near the extreme of the spectrum, but also at finite energy density ϵ (cf. Fig. 4.3(b)). We infer that such behavior is linked to the fact that, for s large enough a non-negligible fraction

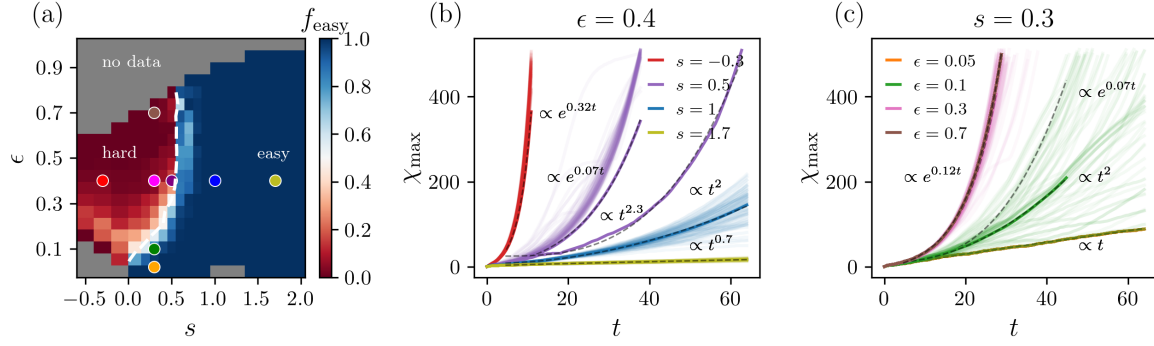


FIGURE 4.3. (a) Fraction of sampled initial product states (cf. Eq. (4.3)) for which time-complexity is ‘easy’ $f_{\text{easy}} \in [0, 1]$ as a function of the normalized energy density $\epsilon = (\langle H \rangle - E_{\min}) / (E_{\max} - E_{\min})$ and s . The grey region indicates the lack of data, as the chosen initial states (cf Eq. (4.3)) do not span the whole energy spectrum. The white dashed line serves solely as guidance to indicate where $f_{\text{easy}} = 0.5$. Deep in the localized and delocalized phase, the behavior displays typicality, namely either $f_{\text{easy}} \approx 0$ (typically ‘hard’) or $f_{\text{easy}} \approx 1$ (typically ‘easy’) weakly depending on ϵ . Near the transition point on the localized side ($0 \lesssim s \lesssim 0.5$) f_{easy} highly depends on ϵ , giving evidence of the existence of a mobility edge along the spectrum. (b-c) Dynamics of $\chi_{\text{max}}(t)$ for all the sampled states for different values of s and ϵ , marked in (a). The dashed lines represent fits for some representative states. Deep in the ‘easy’ and ‘hard’ regime the growth of $\chi_{\text{max}}(t)$ weakly depends on the parameters of the initial states. Instead, in the regions separating typically ‘hard’ or ‘easy’ we observe a wide range of growth behavior even for states with the same s and ϵ , signaling a key role played by other features of the initial state, such as its spatial structure. Image taken from Ref. [2].

of highly excited eigenstates becomes non-thermal, with the fraction increasing with s . Remarkably, for $0 \lesssim s \lesssim 0.5$ (cf. Fig. 4.3(c)), we observe as ϵ increases an ‘inversion’ of f_{easy} , namely for small ϵ the dynamics is typically ‘simple’ to be simulated ($f_{\text{easy}} \approx 1$), while moving towards the center of the spectrum dynamics is typically ‘hard’ to be simulated ($f_{\text{easy}} \approx 0$). Such inversion provides further evidence of the existence of a state-dependent mobility edge in the spectrum. We highlight that the many-body spectrum is not symmetric with respect to $\epsilon = 0.5$, e.g. the maximally excited state is always delocalized, thus there are no reasons to expect a symmetric mobility edge. In between the two extreme regions, we observe a crossover region where typicality is lost since the time-complexity highly depends on the specific states at hand at fixed ϵ (e.g. see Fig. 4.3(c) for $\epsilon = 0.1$), indicating that other features are playing a role in the dynamics. We further investigate such dependence in the following section.

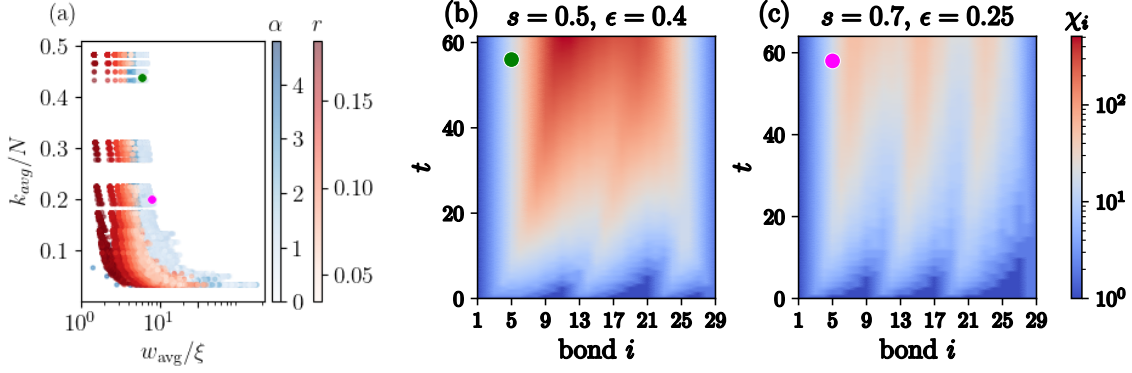


FIGURE 4.4. (a) The same data presented in Fig. 4.3 labeled by the average size of clusters of consecutive excitations ($|1\rangle$) normalized by N (k_{avg}/N) vs average distance between clusters in units of ξ (w_{avg}/ξ), with ξ the localization length of the ground state at the respective value of s . The red dots correspond to states whose time-complexity is ‘hard’ (exponential growth of the max bond-dimension), with r the exponent. Instead, the blue dots correspond to states whose time-complexity is ‘easy’ (sub-exponential growth of the max bond-dimension), with α the power-law exponent. We observe that time-complexity is typically ‘hard’ if either k_{avg}/N increases and w_{avg}/ξ decreases. In (b) and (c), we show the dynamics of the bond dimension χ_i along each cut as a function of time for two representative states. In (b), clusters of excitations have started to entangle beyond a transient time. Whereas in (c), clusters of excitations haven’t entangled yet due to the presence of large islands of consecutive $|0\rangle$ s. Image taken from Ref. [2].

4.4.4. Role of spatial structure

Here, we investigate the role of the initial state structure in the time-complexity of classically simulating the system dynamics. In doing so, we show how the size of excited regions and their distance plays a crucial role in dictating the time-complexity of simulating their dynamics. Additionally, we unify the observation of Refs. [140, 151] adopting as typical length scale the localization length of the ground state, highlighting its predicting power also in understanding finite-energy density phenomena.

In typical thermalizing systems, dynamics is strongly dependent solely on the few conserved quantities of the system (e.g. energy density ϵ), while instead in slow thermalizing systems, such as the quantum East model, memory of the initial state can be retrieved at long times [151] and its structure can influence the dynamics [140]. The role of the structure in dictating dynamics is reminiscent of the dynamical heterogeneity of glassy-like systems, which can be described via classical kinetically constrained models [192, 193]. Hence the role of initial state structure needs to be taken into account, and here

we use dynamical heterogeneity as an indicator of slow thermalization. To be able to differentiate the states sampled (cf. Eq. (4.3)) that have the same energy density ϵ , we need parameters that capture their spatial heterogeneity. In Ref. [140], it has been observed a close connection between slow-thermalization and the size w of inactive regions given by strings of consecutive $|0\rangle$. Such observation has been qualitatively rationalized in Ref. [151], linking it to the existence of a finite localization length ξ of the ground state. We derive intuition from these results and combine the dependence of dynamics on the localization length ξ and w defining the parameter w_{avg}/ξ , where w_{avg} is the average distance between clusters of excitations in the initial state at hand. In Appendix B.3 we show that without rescaling with ξ the quantity is less informative in capturing the salient features. Additionally, since dynamics primarily occur in the densely excited regions, we also label the states as a function of the average size k_{avg} of the cluster of excitations, which is also in a one-to-one correspondence with the average energy (cf. Eq. (4.4)).

Using k_{avg} and w_{avg} for characterizing the sampled initial states, in Fig. 4.4(a) we observe their predictive power in capturing, for most initial states, whether the time-complexity is ‘easy’ (blue markers) or ‘hard’ (red markers) for $s > 0$. Specifically, as k_{avg} increases the simulations are typically harder, while instead, the opposite occurs as excitations are farther apart. Such behavior could be understood as the interplay of dynamics within each cluster of excitations and between different ones. Intuitively, if clusters are far from each other on average, the time-complexity is mostly dictated by the single cluster dynamics since the propagating front generating from each cluster generates little entanglement. In turn, the larger the cluster is, and so is its energy, the more it is hard to simulate. A possible analogy is given by looking at the system as a collection of subsystems with a certain temperature, directly linked to the number of excitations, separated by completely inactive regions at zero temperature: if the inert regions are too extended, the hottest source dominates the hardness in simulating the dynamics. Such a picture is supported by inspecting more closely how the bond dimension, or equivalently entanglement, at each possible bipartition, evolves in time (cf. Fig 4.4(b,c)). Specifically, Fig. 4.4(c) shows an ‘easy’ simulation for $s > 0$. We notice that the clusters of excitations are not strongly entangled due to the presence of large inactive regions between them. This heterogeneity in entanglement is referred to as dynamical heterogeneity and is an indicator of slow thermalization similar to what’s observed in classical glasses [192, 193]. Fig. 4.4(b) shows a state in the transition region for $s > 0$, where we can see that islands of excitations have started to appreciably entangle beyond a transient time.

The distinction between inactive and active regions opens up the possibility of understanding the dynamics of generic product states in terms of concatenated and weakly entangled clusters in the localized phase. We further investigate this observation in the next sections.

4.4.5. Crossover in space-complexity

We have observed that the structure of the initial state plays a leading role in dictating the time-complexity in the localized phase. Such a dependence stems from the sharp differentiation between active and inactive regions in kinetically constrained models. Here, we go a step further showing that such distinction also leads to a crossover in the space-complexity from an approximately fragmented regime, where the state is almost separable, to a fully ergodic one, where the state is non-separable.

Heterogeneity is a hallmark of classical glassy systems, which manifests also in their quantum counterpart as observed in other studies [141, 193]. The quantum East model makes no exception, as it is evident from the dynamics of various observables, such as occupation number and entanglement entropy. This is particularly evident upon initializing product states (cf. Eq. (4.3)) characterized by excited and de-excited regions, and looking at the dynamics of the bond dimension on each cut (see Fig. 4.4(b-c)). This heterogeneity opens up the possibility of distinguishing two timescales: one where dynamics occurs *mostly* within each cluster of excitations (intra-cluster), and another when it also *appreciably* involves different clusters of excitations (inter-cluster). Specifically, we could define a time t^* up to which the system is approximately separable, since the entanglement between the different clusters is negligible, and the whole dynamics is encoded in the dynamics of each cluster separately. The approximate separability could be formalized using the Lieb-Robinson bound [188]: quantum correlations propagate at most ballistically with exponentially small corrections in systems with a finite Hilbert space (e.g. spins) and short-range interactions. In KCMs, empty regions are completely inactive, and the finite velocity of propagation of entanglement in the system (upon neglecting the exponentially small correction in the distance) implies the separability just mentioned up to time t^* , where the active regions appreciably merge. As a consequence, an initial product state (cf. Eq. (4.3)) with \mathcal{N} cluster evolves as

$$|\psi(t)\rangle \approx \begin{cases} \bigotimes_{n=1}^{\mathcal{N}} |\psi_n(t)\rangle \in \bigoplus_{n=1}^{\mathcal{N}} \mathcal{H}_n & t \lesssim t^*, \\ |\psi(t)\rangle \in \bigotimes_{n=1}^{\mathcal{N}} \mathcal{H}_k & t \gtrsim t^*, \end{cases} \quad (4.5)$$

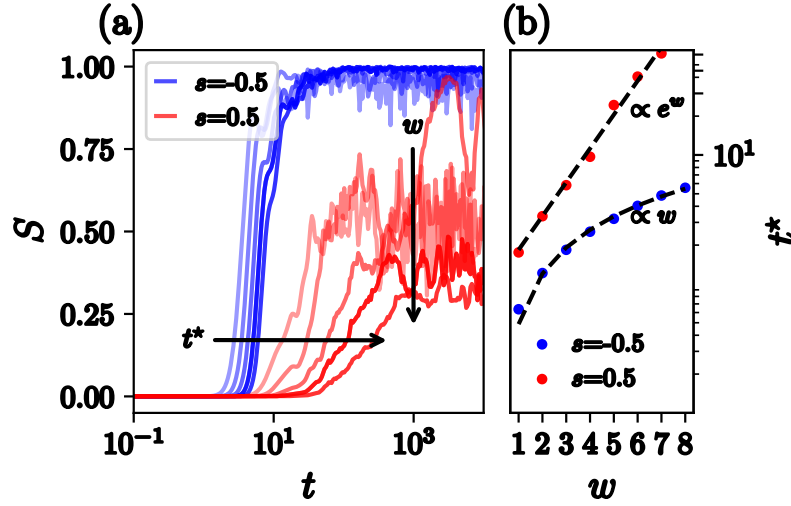


FIGURE 4.5. Dynamics of the entanglement entropy S , computed on the last bond, upon initializing the state $|111\rangle \otimes |0\rangle^w \otimes |1\rangle$ with $w \in [1, 8]$ in the delocalized ($s < 0$) and localized phase ($s > 0$). The long-time values of S are independent of w as expected in the thermalizing regime ($s = -0.5$), whereas it decreases as w increases for $s = 0.5$ indicating localization. (b) Time t^* at which the two clusters appreciably entangled, i.e. when $S > \Delta$, as a function of w . We set $\Delta = 10^{-2}$ for the sake of concreteness (see text for a more compelling discussion in terms of Lieb-Robinson bound). In the delocalized phase ($s < 0$), t^* grows linearly in w as excitations propagate ballistically. Instead, t^* grows exponentially in w in the localized phase ($s > 0$), due to the extreme slowdown in dynamics. The results were obtained via exact diagonalization [191]. Image taken from Ref. [2].

where $|\psi_n(t)\rangle$ is the time-evolved state describing the n -th cluster. In other words, the evolved state is given by a product state of each cluster, i.e. it is separable (up to exponentially small corrections from the propagating fronts). The transition from approximate separability to fully ergodic is accompanied by a change in the dimension of the Hilbert space \mathcal{D} potentially accessible. Specifically,

$$\mathcal{D}(t) = \begin{cases} \sim \mathcal{N} \times 2^{N/\mathcal{N}} & t \lesssim t^*, \\ 2^N & t \gtrsim t^*, \end{cases} \quad (4.6)$$

which in words translates, keeping N/\mathcal{N} fixed, to a transition in the dimension of the accessible Hilbert space from polynomial to exponential in the system size N . Such transition could be interpreted as a transition between a Hilbert space fragmented regime [42, 158, 174] to a fully ergodic one. However, we once more highlight that such a transition is present in the quantum East model upon neglecting the exponential small corrections coming from the Lieb-Robinson bound.

As the Lieb-Robinson bound constitutes an upper bound, it is in principle possible to observe slower than ballistic propagation. This is the case for the quantum East model, where the propagation could be exponentially slow in the localized phase. As a consequence, the dependence of the time t^* with the distance w , defined as the number of empty sites $|0\rangle$ between two clusters, strongly depends on whether the system is delocalized or localized. To show such dependence, let us look at the evolution of the entanglement entropy between two clusters at a distance w and define a (arbitrary) threshold Δ , so that we consider the two clusters not entangled the entanglement entropy along a cut separating the two clusters is less than Δ . The specific value of Δ is arbitrary and chosen just to show the dependence of t^* on w (cf. Fig. 4.5). In the delocalized phase, t^* grows linearly in w as excitations propagate ballistically. Instead, t^* grows exponentially in w in the localized phase, due to the extreme slowdown in dynamics (cf. Fig. 4.5(b)).

Since t^* could be very large in the system size, our observation could prove valuable in different directions:

- (1) For time $t < t^*$ the dynamics of the whole system can be efficiently simulated as a collection of its subsystems neglecting the gates connecting the different ones making a negligible error. We highlight that a similar idea has been already proposed to perform digital quantum evolution more efficiently [194], although for generic systems it is necessary to keep track of the terms connecting the different regions.
- (2) Separability up to time t^* justifies the investigation of smaller system sizes in order to grasp the behavior of larger ones. Specifically, from Eq. (4.5), the dynamics of a product state given by \mathcal{N} cluster is completely encoded looking at the dynamics of \mathcal{N} single-cluster states up to time t^* .

Based on (2), we now investigate the time-complexity in simulating the time evolution of single-cluster states. We will show that such investigation not only will confirm the observed time-complexity in the previous sections, but also allow us to identify a class of area-law states responsible for such behavior. This will provide evidence of the sensitivity of our complexity-oriented proxy to non-thermal eigenstates.

4.4.6. *Localization at finite energy-density*

Following the conclusions of the previous section, we investigate the time-complexity of simulating the dynamics of the kink states

$$|\mathbf{k}\rangle = |1\rangle^k \otimes |00\ldots 0\rangle. \quad (4.7)$$

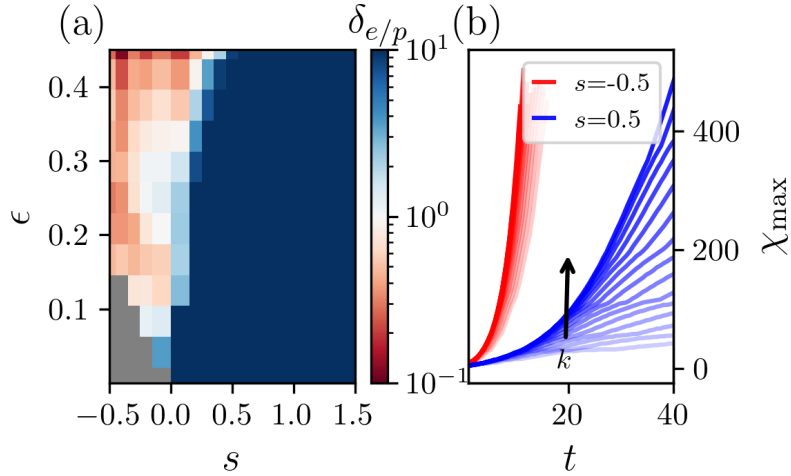


FIGURE 4.6. Time-complexity of evolving kink states $|\mathbf{k}\rangle = \otimes_{j=1}^k |1\rangle \otimes_{j=k+1}^N |0\rangle$ with $k \in [1, N/2]$. Polynomial and exponential fits are performed to determine the complexity of simulating these states. (a) Relative error $\delta_{e/p}$ between the exponential and polynomial fits as a function of energy density ϵ and s . For $\delta_{e/p} < 1$, the state is ‘hard’ to simulate. Conversely, for $\delta_{e/p} > 1$, the state is ‘easy’ to simulate. We see a complexity trend similar to the one observed in Fig. 4.3(a), signaling that most of the complexity of simulating product states could be understood in terms of the evolution of kink states. (b) Dynamics of χ_{\max} for kink states with varying k , in the delocalized ($s = -0.5$) regime and in the localized ($s = 0.5$) regime. In the delocalized regime, states are ‘hard’ to simulate irrespective of k . Instead, in the localized regime, k has a huge impact on the time-complexity. The results were obtained setting $N = 30$ and are not appreciably affected upon increasing N . Image taken from Ref. [2].

As always for product states in the computational basis, we have a one-to-one correspondence between k and the energy density ϵ . Since we now have a single state for each point in the parameter space ϵ vs s , we show in Fig. 4.6 the relative error $\delta_{p/e}$ between the polynomial and the exponential fit performed on the time evolution of the max bond dimension $\chi_{\max}(t)$. If $\delta_{p/e} > 1$, the exponential fit is better, while instead viceversa if $\delta_{p/e} < 1$. We observe that the time-complexity of simulating kink states follows a similar trend as the one observed in Fig. 4.3(a). This signals that, as expected, the hardest part to simulate is given by regions densely excited, or in other terms the ‘hottest’ regions.

To better understand our observations, we more closely investigate the eigenstates of the Hamiltonian. In particular, from Exact Diagonalization calculations, we observe that the kink states in Eq. (4.7) have a large overlap with a limited number of eigenstates of the Hamiltonian deep in the localized phase. Inspecting more closely the eigenstates

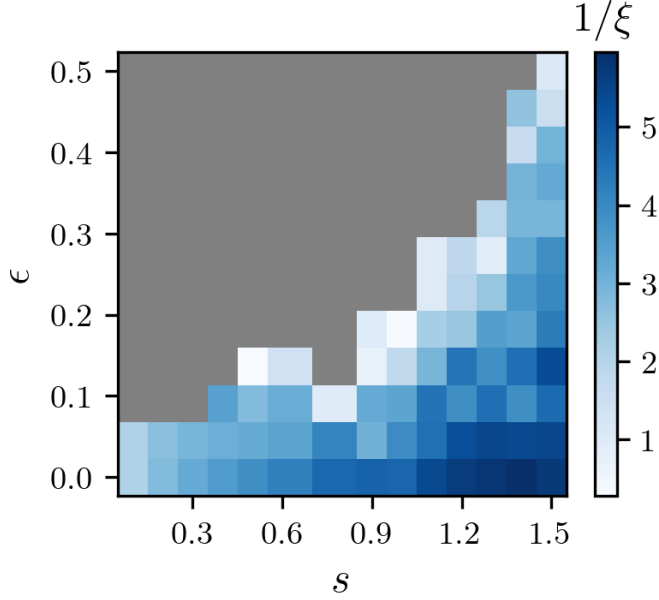


FIGURE 4.7. Inverse of the localization length ξ of localized kink eigenstates (variance of energy $< 10^{-5}$) obtained via DMRG-X [195], as a function of their energy density $\epsilon = (\langle H \rangle - E_{\min})/(E_{\max} - E_{\min})$ in a system of size $N = 30$. The algorithm converges not only at zero energy density ($\epsilon = 0$), corresponding to the ground state, but also at finite energy $\epsilon > 0$, indicating the existence of localized kink-states along the spectrum for $s > 0$. Image taken from Ref. [2].

with whom the overlap is the largest, we observe that such states have a density profile similar to a kink state with an additional localized tail on the right edge. We term these eigenstates as *localized kink states*. Due to the limited system sizes accessible via Exact Diagonalization, we further characterize such states resorting to DMRG-X, a variation of the standard DMRG, which allows finding area-law eigenstates which are ‘near’ (large inner product) to the initial state provided [195]. In our case, we seed the kink states (cf. Eq. (4.7)) and let the algorithm find the best approximating eigenstate, setting a maximal bond dimension of 100. For each of these states, the algorithm could either fail to converge, which we interpret as the absence of a localized kink state, or converge. In Fig. 4.7 we show the localization length ξ of the states for which the algorithm was able to converge (we set as convergence criteria a variance of the Hamiltonian $< 10^{-5}$). We observe that the algorithm can find a state with $\epsilon = 0$, faithfully reproducing the results from DMRG, as it corresponds to the ground state of the Hamiltonian. Additionally, the algorithm can find other localized states at finite energy density as s increases, corresponding to the localized kink states above introduced. We observe that ξ is parametrically small in s , while instead it is parametrically large in ϵ .

Similarly to what has been done in Ref. [151], we could use the localized kink together with empty strings as building blocks for defining a large class of states close to eigenstates of the Hamiltonian for larger system sizes. To show this, let us name $|\tilde{k}^N\rangle$ the localized kink-states, with k the number of excitations in the kink and N the system size. First of all, we observe that the state

$$|\Psi_k^L\rangle \equiv |\tilde{k}^N\rangle \otimes |0\rangle^{\otimes(L-N)}, \quad (4.8)$$

with support on $L > N$ sites, has energy variance

$$\langle \Psi_k^L | \Delta \hat{H} | \Psi_k^L \rangle \sim e^{-s} \langle \tilde{k}^N | \hat{n}_N | \tilde{k}^N \rangle \sim e^{-s} e^{-(N-k)/\xi} \quad (4.9)$$

which depend solely on the occupation on the last site of the state $|\Psi_k^L\rangle$, since the only contribution to the variance comes from the boundary term between $|\tilde{k}^N\rangle$ and the subsequent string of empty sites. As an exact eigenstate has energy variance equal to zero, here we aim to make the variance in Eq. (4.9) as small as possible. Since the variance in Eq. (4.9) is independent on L , it is small if $\xi > 0$, i.e. $|\tilde{k}^N\rangle$ is localized, and $(N - k) \gg \xi$. Since ξ does not scale with N , for large N the second condition is satisfied if $k/N \ll 1$, which can be fulfilled for $k < cN$ with $c \ll 1$ a small constant and $k < N^p$ with $p < 1$. Recalling the correspondence between the number of excitations and the average energy, the former case corresponds to states with an extensive energy, while the latter to states with a sub-extensive one. The bound in k imposed is quite strict in practice and could be relaxed by observing the exponential dependence of the variance on $(N - k)/\xi$. Specifically, by setting a target variance ε in Eq. (4.9), it would be enough to have $(N - k) \sim \xi \log(1/\varepsilon)$.

Having proven that the localized kink states found at finite N are quasi-eigenstates of larger systems, we can do a step further. Specifically, we could use the states $|\tilde{k}\rangle$ as a basis for slowly evolving states in a system of size $L > N$. Allowing $k \in [0, k_{\max}]$, where $|\tilde{0}\rangle \equiv |0\rangle^{\otimes N}$ and k_{\max} corresponds to the maximum number of excitations for which the system display localization, the number of states we can define is $(k_{\max} + 1)^{L/N}$. Let us call $|\Psi^L\rangle \in \{|\tilde{0}^N\rangle, |\tilde{1}^N\rangle, \dots, |\tilde{k}_{\max}^N\rangle\}^{\otimes L/N}$ a state given by the tensor product of localized kink states. Since $|\tilde{0}^N\rangle$ blocks do not contribute to the variance, the only contribution comes from the states $|\tilde{k}^N\rangle$ with $k \geq 1$, giving

$$\langle \Psi^L | \Delta \hat{H} | \Psi^L \rangle \sim e^{-s} \sum_{j=1}^{\mathcal{M}} e^{-(N-k_j)/\xi} < \mathcal{M} e^{-(N-k_{\max})/\xi}, \quad (4.10)$$

where \mathcal{M} is the number of states $|\tilde{k}\rangle$ with $k \geq 1$, and k_j is the size of the j -th concatenated localized kink state. We highlight that \mathcal{M} is potentially unbounded in the thermodynamic limit, making the variance inevitably large. The energy is given by

$$\langle \Psi^L | \hat{H} | \Psi^L \rangle \sim \sum_{j=1}^{\mathcal{M}} \langle \tilde{k}_j | \hat{H} | \tilde{k}_j \rangle \sim \sum_{j=1}^{\mathcal{M}} k_j. \quad (4.11)$$

We aim to find a trade-off between small variance and finite energy density. To this aim, let us assume we embed the maximum number of localized states possible, namely $\mathcal{M} = L/N$, and consider that the kink states embedded have $k \sim cN$, with $c \ll 1$. Let us consider the case where $N = L^\alpha$, with $\alpha < 1$, to which corresponds $\mathcal{M} = L^{1-\alpha}$ and $k \sim cL^\alpha$. For this parametrization, we have $\langle \Psi^L | \hat{H} | \Psi^L \rangle \sim cL$ and $\langle \Psi^L | \Delta \hat{H} | \Psi^L \rangle < L^{1-\alpha} e^{-L^\alpha/\xi}$, implying that we can have many states with small variance (and therefore slow dynamics [151]) and finite energy density.

The existence of localized kink states allows us to rationalize the ease of simulating the dynamics of a large class of initial states also at finite energy density, namely the ones with ‘large’ empty regions, deep in the localized phase. Indeed, such states have a large overlap with states given by product states of localized kink states, which we have shown have small energy variances and are thus slowly evolving. Additionally, this further provides evidence of the effectiveness of our complexity-oriented quantity for detecting the presence of thermal and non-thermal eigenstates. However, we observe that the localized states here identified do not allow us to explain the dynamics of *all* the product states simulated. Indeed, based on our numerical results, we do not find localized kink states at large energy density for $s \lesssim 1$, while instead looking at time-complexity as well as small system size exact diagonalization (cf. Fig. 4.1) we would argue that non-thermal eigenstates should exist. This opens up the possibility that non-thermal eigenstates qualitatively different from localized kink states exist. We leave this as a possible direction for future investigation.

4.5. CONNECTION WITH RANDOM UNITARY CIRCUITS

The results obtained in the quantum East model open up the intriguing possibility that the corresponding quantum circuit could be efficiently simulable as well. More concretely, the generator of the dynamics could be Trotterized as

$$e^{-i\hat{H}T} = \prod_{n=1}^{T/\Delta t} e^{-i\hat{H}\Delta t} \approx \prod_{n=1}^{T/\Delta t} \left(\prod_{j=1}^{N-1} e^{-i\hat{h}_{j,j+1}\Delta t} \right) \quad (4.12)$$

where the two-sites operator $e^{-i\hat{h}_{j,j+1}\Delta t}$ for the quantum East model results equal to

$$e^{-i\hat{h}_{j,j+1}\Delta t} = e^{iJ\hat{n}_j\hat{\sigma}_{j+1}^x\Delta t/2} e^{-i\hat{n}_j\Delta t/2} \quad (4.13)$$

where $J \equiv e^{-s}$. By using the definition of the exponential of an operator, together with $\hat{n}_j^k = \hat{n}_j$ for $k > 0$, and $(\hat{\sigma}_j^x)^k = 1$ for k even, we can write the evolution operator

exactly as a *tilted*-CNOT.

$$\begin{aligned}
 e^{-i\hat{h}_{j,j+1}\Delta t} &= U_j + U_{j,j+1} \\
 U_j &= 1 - \hat{n}_j + \hat{n}_j \cos(J\Delta t/2)e^{-i\Delta t/2} \\
 U_{j,j+1} &= i\hat{n}_j \hat{\sigma}_{j+1}^x \sin(J\Delta t/2)e^{-i\Delta t/2}
 \end{aligned} \tag{4.14}$$

This opens up the possibility that a subgroup of such a family of circuits, which does not belong to Clifford circuits, could be efficiently simulated via classical algorithms. However, a bit of care is needed, since the circuit does not conserve the energy in the system, and could thus invalidate the application of our findings. However, we argue that this is not necessarily the case, since also the Floquet version of the quantum East model [155] has been shown to display localization. As a consequence, the family of *tilted*-CNOTs could be a novel family of circuits that can be simulated efficiently, alongside Clifford, MBL inspired [172], as well as fractonic random circuits [42, 173]. We reserve a detailed investigation of this for future work.

4.6. DISCUSSION AND PERSPECTIVES

Here, we have proposed a method to probe thermal to non-thermal dynamical phase transitions by assessing whether simulating the quantum dynamics could be efficiently computed using classical algorithms. We used tensor networks as classical algorithms, widely regarded as the most efficient approach for addressing generic one-dimensional systems, and tested our idea to characterize the dynamical phase transition in the paradigmatic quantum East model. In doing so, we have identified two different time-complexity classes, ‘hard’ and ‘easy’. In the (‘easy’) ‘hard’ regime, the bond dimension scales (sub-)exponentially in time. We have then linked the time-complexity of simulating the dynamics of product states with the absence of non-thermal eigenstates when the task is ‘hard,’ or their presence when the task is ‘easy.’ We have fueled our hypothesis by inspecting portions of the spectrum of the Hamiltonian. Specifically, we have identified the class of eigenstates that mostly dictate the dynamics observed, i.e. localized states at finite energy density, and we have shown their existence in large-scale numerics using DMRG-X, reaching system sizes well beyond the ones accessible using exact diagonalization. We have also defined another type of complexity, space-complexity. We have defined space-complexity as (‘hard’) ‘easy’ if the evolved state is (in)separable in space. In the model at hand the sharp differentiation of active and inactive regions, typical in any kinetically constrained model, leads to a crossover in the space-complexity. Specifically, Eq. (4.5) could be read as a dynamical transition in the accessible Hilbert space upon performing a small error on the state. Intriguingly, the transition encoded in Eq. (4.5) is reminiscent of the dynamical transition in the

complexity of performing the so-called Sampling task [196, 197]. The sampling problem involves the extraction of events according to the probability distribution provided by the many-body quantum state, and it is widely regarded as a leading contender in demonstrating provable quantum advantage. Additionally, and more relevant for us, the sampling problem has gathered attention also for defining novel kinds of dynamical phase transitions linked to an easy to hard transition during dynamics, which could already happen in free bosons systems in a lattice [198]. Specifically, in Ref. [198], it was considered free bosons sparsely located along a lattice: for times smaller than the time at which particle interfere, controlled by the Lieb-Robinson bound, the task is easy as quantum particles behave as distinguishable classical ones; for larger times than the interference time the task becomes hard, as interference between particles can no longer be disregarded. This strongly resembles the transition encoded in Eq. (4.5).

4.6.1. *Future directions*

Our results open up several possible directions: (i) use time-complexity for detecting the properties of the eigenstates in other systems, such as MBL. This would allow to reach larger scale systems than the one accessible to exact diagonalization, and thus aid the extraction of properties (i.e. non-thermal nature of the spectrum) in the thermodynamic limit; (ii) use space-complexity for investigating the connectivity and properties of the Hilbert space, such as the presence of extreme slowdown in the exploration of the Hilbert space which reflects in slow thermalization [199]; (iii) application of more formal complexity theoretical arguments in discussing the sampling task in kinetically constrained models, in a fashion reminiscent of what has been done in MBL systems [187]; (iv) investigate the circuit version of other kinetically constrained models (e.g. the Fredrickson-Andersen model) displaying slow thermalization, so that it could identify other classes of efficiently simulable circuits. The latter would aid the identification of tasks that could show a genuine quantum advantage.

CHAPTER 5

Beyond localization: quantum many-body scars, confinement, and Hilbert space shattering

Most of the content in this Chapter is in:

- “*A Rydberg platform for non-ergodic chiral quantum dynamics*” (arXiv: 2309.12392; to appear in Phys. Rev. Letter)

Riccardo J. Valencia-Tortora, Nicola Pancotti, Michael Fleischhauer, Hannes Bernien, Jamir Marino.

Executive Summary. In the previous Chapters we have discussed non-ergodicity tied to localization, both at low and finite energy density. However, localization is not the only way via which thermalization could be impeded. Indeed, in recent years a number of other mechanisms have been discovered and experimentally observed, such as quantum many-body scars [15, 47, 48, 52, 56, 58, 200], where a few non-thermal excited states can lead to non-relaxing dynamics; Hilbert space shattering [42], where a set of nontrivial conserved quantities make the Hilbert space get shattered in an exponentially large number, in the system size, of disconnected subspaces; confinement induced by many-body interactions [59, 131, 201, 202], where an emergent attractive potential between quasi-particles impede the propagation of entanglement in the system. Here, we will show that upon performing a minimal modification to the nature of the kinetic constraint in the quantum East model, all these mechanisms can be observed. Specifically, by making the constraint either tighter or looser, namely, the condition that has to be fulfilled involves more or fewer surrounding particles, a different ergodicity-breaking mechanism occurs. Although the choice of the different kinetic constraints may seem arbitrary at first sight, we will show that the kinetically constrained model proposed here could be readily realized in current Rydberg atoms platforms. In these platforms, the different ergodicity-breaking mechanisms could be selected by simply adjusting the strength of external classical drive fields. We anticipate that this will be the main focus of Part II.

What is new? All results of this chapter represent novel research results.

Organization of the Chapter

- In Sec. 5.1 we present the model of our interest and enumerate its symmetries as a function of its parameters.
- In Sec. 5.2 we make a small detour and discuss the concept of Hilbert space shattering and Krylov-restricted thermalization due to its relevance for the system here investigated.
- In Sec. 5.3 we discuss the different ergodicity-breaking mechanisms the system displays in the various parameter regimes.

This Chapter is composed by a rearrangement of the author's publication [3].

5.1. A UNIVERSAL MODEL FOR DIFFERENT ERGODICITY-BREAKING MECHANISMS

The main focus of the Chapter will be the following Hamiltonian

$$\begin{aligned} \hat{H} = & \frac{\Omega_1}{2} \sum_j \hat{n}_j \hat{\sigma}_{j+1}^x (1 - \hat{n}_{j+2}) + \frac{\Omega_2}{2} \sum_j \hat{n}_j \hat{\sigma}_{j+1}^x \hat{n}_{j+2} + \\ & + \epsilon \sum_j \hat{n}_j + V_{\text{NNN}} \sum_j \hat{n}_j \hat{n}_{j+2}, \end{aligned} \quad (5.1)$$

where $\hat{n}_j = (1 - \hat{\sigma}_j^z)/2$, with σ_j^α the α -Pauli matrix obeying the commutation relation $[\hat{\sigma}_j^x, \hat{\sigma}_k^y] = 2i\delta_{j,k}\hat{\sigma}_j^z$. The kinetically constrained model in Eq. (5.1) could be seen as a deformation of the quantum East model investigated in Chapter 4. Indeed, if we set $\Omega_{1,2} = -e^{-s}$ and $V_{\text{NNN}} = 0$ we recover the quantum East model. The deformations considered here are not purely theoretically driven but also experimentally motivated, as the model in Eq. (5.1) can be realized in current Rydberg experiments, as we will discuss in Part II. Due to its experimentally driven nature, we highlight the presence of an additional next-nearest neighbor interaction controlled by V_{NNN} , which naturally appears in Rydberg arrays as a result of the van der Waals interactions between atoms in the Rydberg state. Additionally, the kinetic constraints are controlled by $\Omega_{1,2}$ since, in the experimental setup we will discuss, they correspond to the Rabi frequencies, i.e., strength, of a set of classical drive fields acting on the system.

For clarity, let us explain the action of each kinetic constraint. The term controlled by Ω_1 controls spin-flips conditioned on having the previous atom in the $|1\rangle$ state, which corresponds to the Rydberg state (an electronic state with a large principal quantum number $\gtrsim 70$) in the experiment, and the following one in the $|0\rangle$ state, which corresponds to the ground state of the atom, taken as a non-Rydberg state (e.g. an electronic state with a principal quantum number ~ 5). Instead, the term controlled by Ω_2 leads to spin flips when both neighboring atoms are in the $|1\rangle$ state. More compactly, we

have

$$\begin{aligned} \Omega_1 \hat{n}_j \hat{\sigma}_{j+1}^x (1 - \hat{n}_{j+2}) : & \quad 100 \leftrightarrow 110, \\ \Omega_2 \hat{n}_j \hat{\sigma}_{j+1}^x \hat{n}_{j+2} : & \quad 101 \leftrightarrow 111. \end{aligned} \quad (5.2)$$

As is evident, controlling Ω_1 and Ω_2 allows us to control the nature of the kinetic constraint and in turn how excitations ($|1\rangle$) propagate in the system. Specifically, the first term in Eq. (5.2) controls how strings of excitation (consecutive strings of $|1\rangle$) shrink and grow. We highlight that such shrink/growth occurs solely on the right edge of each cluster, since the kinetic constrained term has a notion of *directionality* (this is a key feature of the model at hand, as we will further discuss in this Chapter). Instead, the second term in Eq. (5.2) controls how strings of excitations can merge and split. The interplay of these two qualitatively different processes will be the focus of this Chapter. Indeed, we will show that upon tuning the ratio Ω_1/Ω_2 the dynamics not only change quantitatively, but it displays different forms of ergodicity-breaking mechanisms tied to the specific constraint at play. Specifically, the system could display non-ergodicity due to either localization, confinement, or quantum many-body scars depending on the values of $\Omega_{1,2}$:

- for $\Omega_{1,2} \neq 0$ the system inherits the features of the quantum East model (which is realized for $\Omega_1 = \Omega_2$) and could display localization;
- for $\Omega_1 \neq 0$ and $\Omega_2 = 0$, the system displays confinement, namely the excitations cannot freely spread but they remain spatially confined, impeding in turn the propagation of entanglement in the system;
- for $\Omega_1 = 0$ and $\Omega_2 \neq 0$, we obtain a Hamiltonian which can be connected to the paradigmatic PXP model, which has been shown to host quantum many-body scars, namely few non-thermal eigenstates in the spectrum. In the latter case, the system typically behaves as a generic non-integrable system displaying fast thermalization for most of initial states. However, this is not the case for a certain class of initial states, which are of relevance as they could be easily prepared in experiments, which instead display long-lived oscillations of various observables (including the fidelity) contrary to what is expected in a fastly thermalizing system. This behavior has been shown to arise due to the small fraction of non-thermal eigenstates along the spectrum. Despite their limited number, these eigenstates exhibit significant overlap with the initial states, which in turn inherit their non-thermal properties.

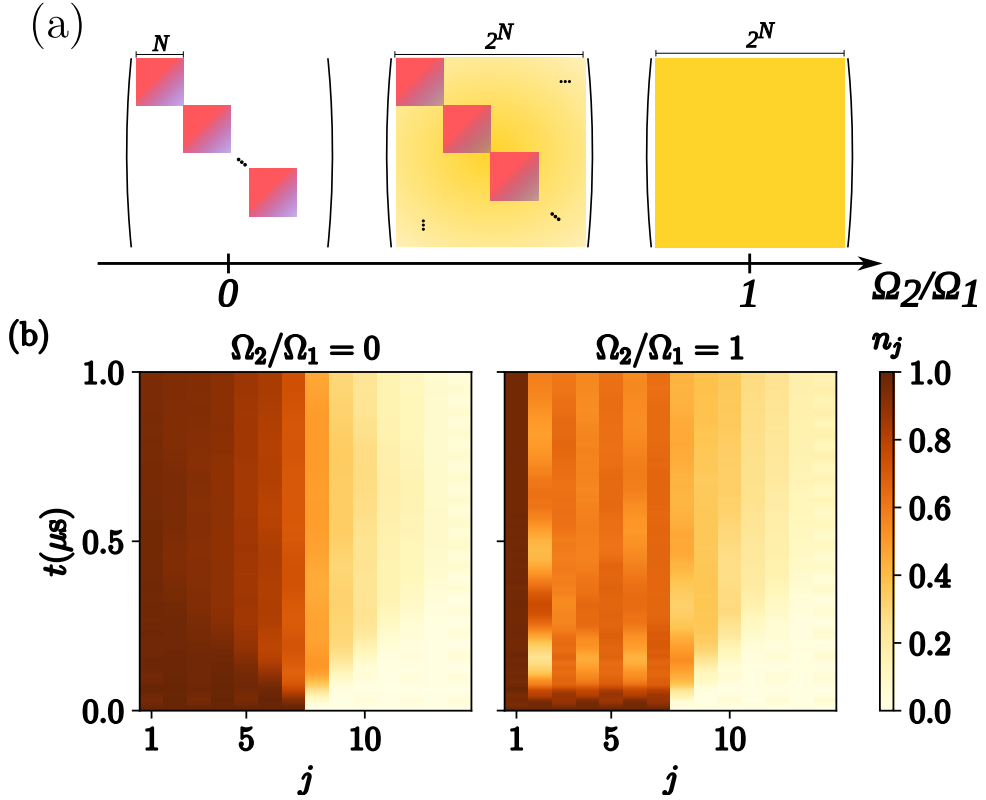


FIGURE 5.1. (a) Sketch of the accessible Hilbert space, at fixed East symmetry sector, in a system of size N as a function of the Rabi frequencies $\Omega_{1,2}$ (dynamics are initialized in product states). Colors indicate allowed transitions and they are in one-to-one correspondence with those used for the drive fields in Fig. 6.1(a). Blank spaces indicate forbidden transitions. For $\Omega_1 \neq 0$ and $\Omega_2 = 0$ strings of excitations can only shrink/expand without merging/splitting, leading to Hilbert space *shattering*; for $\Omega_2/\Omega_1 \neq 0$, strings achieve complete mobility, rendering the system ergodic, as any product state becomes accessible from any other. For $\Omega_2/\Omega_1 = 1$ we recover the quantum East model [140, 151]. (b) Dynamics of the density profile starting from the product state with first half sites excited ($|1\rangle$) and the rest in $|0\rangle$ in the shattered ($\Omega_2 = 0$) and ergodic regime ($\Omega_{1,2} \neq 0$). Image taken from Ref. [3].

5.1.1. Symmetries of the Hamiltonian

Despite the deformation with respect to the canonical quantum East model investigated in the previous Chapters, the Hamiltonian in Eq. (5.1) still belongs to the family of kinetically constrained quantum East models, where dynamics are activated solely to the right of excited sites. We remind that East models are characterized by a so-called ‘East symmetry’ [151], which implies that empty regions without any excitation to their left remain frozen. As a consequence, the location of the first excitation encountered starting from the left edge of the system does not change (see Fig. 6.1 (c)), and the

Hilbert space splits into N disconnected sectors, with N the system size. We have an additional tool at our disposal with respect to the quantum East model, namely the parameters $\Omega_{1,2}$ (which correspond to the Rabi frequencies of the incident drive fields in the experimental implementation we propose in Chapter 6). Indeed, once the East symmetry sector is specified by the location of the first excitation, we can further shape the accessible Hilbert space by simply changing the relative power of the drive fields Ω_1 and Ω_2 (cf. Fig. 5.1(a)), which directly reflects in the mobility of excitations. Specifically, we anticipate that with a single drive field the East symmetry sector *shatters* in $\mathcal{O}(e^N)$ disconnected sectors [174], while when both are active it is irreducible [151], meaning the dynamics connect all states (see Fig. 5.1). Then, we will illustrate the mechanisms by which in each regime the onset of thermalization considerably slows down within each irreducible sector, exhibiting scars, confinement, and localization.

However, before delving into discussing the different regimes, we have mentioned Hilbert space shattering providing a definition, i.e. a system with an exponentially large number of disconnected subspaces, yet without further clarifications on its characteristics. Thus, before delving into discussing the different regimes, we briefly review the notion of Hilbert space shattering and also Krylov restricted thermalization we will adopt afterward.

5.2. HILBERT SPACE FRAGMENTATION AND KRYLOV RESTRICTED THERMALIZATION

In this section we review the notion of Hilbert space fragmentation by briefly summarizing the main properties of fragmented systems, while we refer to, e.g., Ref. [158] for a more comprehensive and complete discussion.

Given a Hamiltonian \hat{H} , the Hilbert space \mathcal{H} on which it acts can be generally decomposed into dynamically disconnected subspaces $\{\mathcal{H}_n\}$, referred to as Krylov subspaces, as

$$\mathcal{H} = \bigoplus_{n=1}^Q \mathcal{H}_n, \quad \mathcal{H}_n = \text{span}_t \{e^{-i\hat{H}t} |\psi_n\rangle\}, \quad (5.3)$$

where Q is the number of Krylov subspaces and

$$\text{span}_t \{e^{-i\hat{H}t} |\psi_n\rangle\} \equiv \text{span} \{|\psi_n\rangle, \hat{H}|\psi_n\rangle, \hat{H}^2|\psi_n\rangle, \dots\} \quad (5.4)$$

denotes the subspace spanned by the time evolution of the state $|\psi_n\rangle$. The states $|\psi_n\rangle$ are chosen so that they are not eigenstates of the Hamiltonian and their Krylov subspaces are distinct. More concretely, $|\psi_n\rangle$ are typically chosen to be product states, as they are

the ones more easily accessible experimentally, although recent works are investigating the case where they are entangled states [152, 174, 203]. In doing such decomposition, a key question concerns how many Krylov subspaces the system displays, as well as the properties of each of them. Concerning the number Q of Krylov subspaces, we can distinguish two main scenarios depending on how Q scales with the system size N . Specifically, we could have

$$Q = \begin{cases} \mathcal{O}(N^p), & \text{with } p \geq 0 \\ \mathcal{O}(\exp(N)) \end{cases} \quad (5.5)$$

The first scenario occurs for systems exhibiting no or ‘conventional’ symmetries, where with ‘conventional’ we mean symmetries that can be written as the sum of local terms (e.g. $U(1)$ symmetry), or products of one-site unitary (e.g. \mathbb{Z}_2 symmetry). In this case, the different Krylov subspaces are labeled by the quantum numbers associated with such symmetries. Instead, in the scenario where $Q = \mathcal{O}(\exp(N))$ the system is said to be fragmented, and it occurs when the system displays non-local conserved quantities [174] (e.g. the presence of bit strings which are invariant under the action of the Hamiltonian) associated with non-conventional symmetries. See Fig. 5.2 for a pictorial representation of the structure of the Krylov sectors.

Once the different subspaces are labeled, a relevant question concerns investigating their properties, such as whether the system thermalizes or not within each Krylov subspace [204–206]. This is known as Krylov-restricted thermalization, and it will be the operative definition we will adopt. More specifically, we will investigate whether the system displays non-ergodicity in the largest irreducible Krylov sector. Indeed, if we do not resolve the nontrivial symmetries the model displays, we could choose initial states which has weight in different disconnected sectors. Consequently, we immediately see that the system cannot thermalize simply because we did not take into account all the nontrivial symmetries.

5.2.1. *Structure of the Hilbert space in our model*

As we have given an operative definition of Hilbert space shattering, we now discuss when the models here considered (cf. Eq. (5.1)) display Hilbert space shattering.

Given the definition of Hilbert space shattering, we immediately observe that the quantum East model (which we obtain for $\Omega_1 = \Omega_2$ in Eq. (5.1)) discussed in the previous Chapters does not display Hilbert space fragmentation. Indeed, it conserves (trivially) the energy and the location of the first excited site. Given that in a system of size N there are N different ways in which we can locate the first excited site, we can label

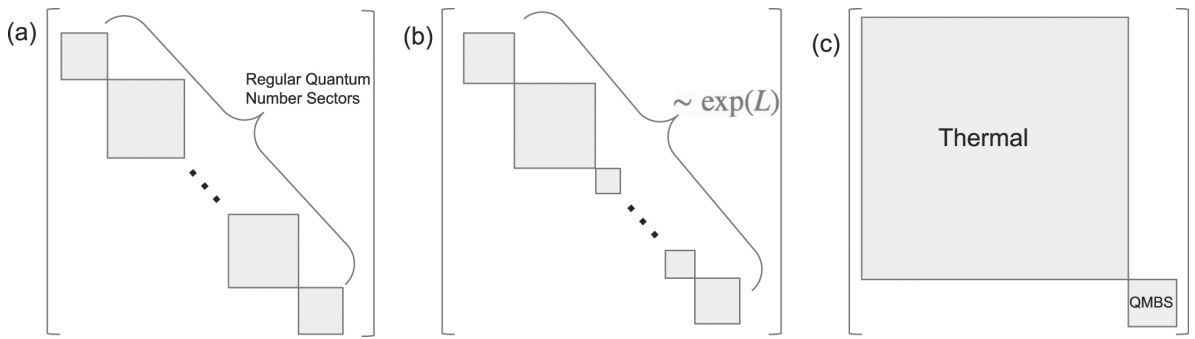


FIGURE 5.2. Schematic depiction of the block diagonal structure of the Hamiltonian showing the dynamically disconnected ‘Krylov subspaces’ in systems with (a) conventional symmetries; (b) Hilbert space shattering, where the Hilbert space gets shattered in an exponentially large number of sectors; (c) quantum many-body scars, where most of the spectrum is thermal except for a negligible fraction of states. Image taken from Ref. [158].

N different Krylov subspaces. Furthermore, each of the Krylov subspaces cannot be further reduced, namely, it is ergodic, as seeding any product state belonging to such subspace in Eq. (5.4) allows us to explore the whole subspace. However, the remarkable aspect is that despite having the possibility to explore an exponentially large Hilbert space, the way such exploration occurs undergoes a dynamical phase transition between a regime where this happens fast, to a regime where it occurs extremely slowly impeding thermalization, as we have shown in Chapter 4.

Instead, if either Ω_1 or Ω_2 are set to zero, the system displays Hilbert space fragmentation. Indeed, in such cases, the system admits frozen bit strings, namely strings which are completely invariant under the action of the Hamiltonian.

Specifically, when $\Omega_1 = 0$ and $\Omega_2 \neq 0$ the string $|00\rangle$ is frozen as it can be explicitly checked:

$$\Omega_2 \hat{n}_j \hat{\sigma}_{j+1}^x \hat{n}_{j+2} | \dots \rangle |0\rangle_j |0\rangle_{j+1} | \dots \rangle = | \dots |0\rangle_j |0\rangle_{j+1} | \dots \rangle \quad (5.6)$$

since $\hat{n}_{j+2} |0\rangle = 0$ indendently of the arbitrary quantum state $| \dots \rangle$.

Instead, when $\Omega_1 \neq 0$ and $\Omega_2 = 0$, following the same argument, the string $|01\rangle$ is frozen as can be, again, explicitly checked:

$$\Omega_1 \hat{n}_j \hat{\sigma}_{j+1}^x (1 - \hat{n}_{j+2}) | \dots \rangle |0\rangle_j |1\rangle_{j+1} | \dots \rangle = | \dots |0\rangle_j |1\rangle_{j+1} | \dots \rangle \quad (5.7)$$

Additionally, the system conserves also the number of kinks when $\Omega_2 = 0$, namely the Hamiltonian commutes with $\hat{Q} = \sum_j \hat{n}_j (1 - \hat{n}_{j+1})$ (it counts the number of $|10\rangle$ strings). In both cases, the presence of frozen bit strings leads to Hilbert space fragmentation. This can be easily checked in the $\Omega_2 = 0$ case. Indeed, we can first label $\sim N$ disconnected subspaces \mathcal{H}_k based on the number k of frozen bit strings in the system.

However, as these strings not only are conserved in number but also their location (they are frozen), we can further divide the subspaces \mathcal{H}_k just defined based on their location. Since in a system of size N with k frozen bit strings there is a combinatorial number of ways to put them, we see that the number of subspaces we can define for $k \sim N$ is exponential in N . We thus have Hilbert space fragmentation as anticipated.

Another defining property of Hilbert space shattering is whether it is *weak* or *strong*: it is *strong* if the size of the largest irreducible Krylov subspace is a vanishing fraction of the whole Hilbert space, e.g. it grows polynomially in the system size; instead, it is *weak* if the size of the largest irreducible Krylov subspace is a non-vanishing fraction of the whole Hilbert space, i.e. grows exponentially in the system size. We will see that the largest irreducible Krylov subspace could be either exponentially large in the system size (when $\Omega_1 = 0$ and $\Omega_2 \neq 0$), or increase polynomially in the system size (when $\Omega_1 \neq 0$ and $\Omega_2 = 0$) in the model investigated.

As we have discussed the structure of the Hilbert space in each regime, we now proceed to show that not only the structure of the Hilbert space changes, but also that distinct form of ergodicity-breaking mechanisms occur in the largest irreducible Krylov subspace occur.

5.3. FROM QUANTUM MANY-BODY SCARS TO CONFINEMENT AND LOCALIZATION

In this section, we show how by tuning Ω_1/Ω_2 we can induce a different ergodicity-breaking mechanism.

5.3.1. *Quantum Many-Body Scars*

For $\Omega_1 = 0$ and $\Omega_2 \neq 0$ directionality is lost and a spin flip occurs solely when both neighboring atoms are excited. Specifically, the Hamiltonian becomes

$$\hat{H} = \frac{\Omega_2}{2} \sum_j \hat{n}_j \hat{\sigma}_{j+1}^x \hat{n}_{j+2} + \epsilon \sum_j \hat{n}_j + V_{\text{NNN}} \sum_j \hat{n}_j \hat{n}_{j+2}. \quad (5.8)$$

This model, which we term QXQ-model (see also Ref. [207] for its experimental realization), is reminiscent of the well-known PXP model, in which a spin flip occurs when both neighboring atoms are in the ground state. Indeed, the PXP model and ours share the same physics as they are connected via the transformation $\hat{U} = \prod_{j=1}^N \hat{\sigma}_j^x$, which translates to interchanging $|0\rangle \leftrightarrow |1\rangle$. This includes Hilbert space *shattering* [158]

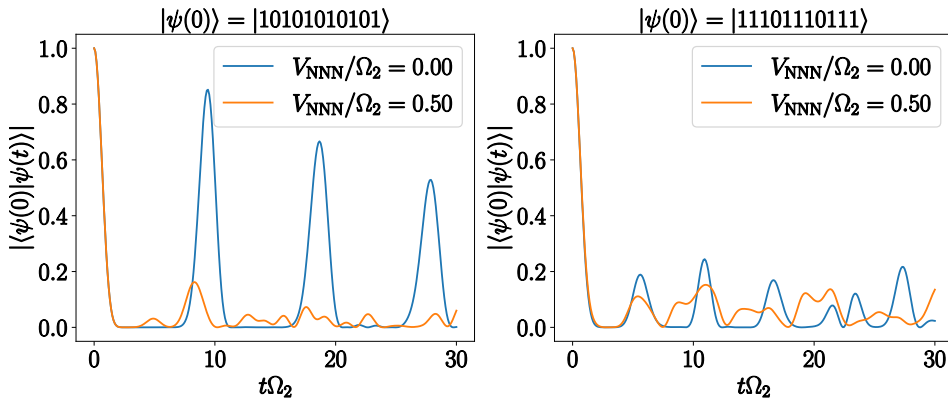


FIGURE 5.3. Dynamics of the fidelity for $\Omega_1 = 0$ and $\Omega_2 \neq 0$. The system presents scarred eigenstates along its spectrum. As a consequence, for some special initial states, the system displays long-lived oscillations (left panel), whose lifetime is affected due to long-range interactions ($V_{\text{NNN}} \neq 0$), while instead for generic initial states the system fastly thermalizes as expected (right panel).

and the presence of quantum many-body scars, which slow down the onset of thermalization when initializing specific states [15, 200]. Specifically, the PXP model (and so ours) have a spectrum that is mostly thermal except for few non-thermal, i.e. area-law, eigenstates which are (almost) evenly spaced along the spectrum. As these non-thermal states are very few, i.e. $N+1$ with N the system size, in comparison with the abundant non-thermal one, i.e. $\sim 2^N$, we might expect that they do not play a role in dictating the properties of the system. This is indeed the case in most cases, as for almost all initial states the system quickly thermalizes. However, as anticipated, it has been remarkably observed that upon initializing a certain class of initial states (e.g. Néel state) revivals, i.e. oscillations of observables where observed [15], incompatible with fast thermalization (see Fig. 5.3). As the PXP model hosts quantum many-body scars, this is the case also for our model. Also, as it occurs in the actual Rydberg experiment where the PXP has been realized, long-range interactions ($V_{\text{NNN}} \neq 0$) contribute to disrupting the perfect revivals [15].

5.3.2. Hilbert Space Shattering and confinement of excitation

When $\Omega_1 \neq 0$ and $\Omega_2 = 0$, the Hamiltonian turns into

$$\hat{H} = \frac{\Omega_1}{2} \sum_j \hat{n}_j \hat{\sigma}_{j+1}^x (1 - \hat{n}_{j+2}) + \epsilon \sum_j \hat{n}_j + V_{\text{NNN}} \sum_j \hat{n}_j \hat{n}_{j+2}, \quad (5.9)$$

where strings of consecutive excitations can shrink or grow but not merge or split ($|101\rangle \leftrightarrow |111\rangle$), making the system conserve their number, associated with the conserved

quantity $\hat{Q} = \sum_j \hat{n}_j(1 - \hat{n}_{j+1})$. Additionally, the directional character of the dynamics implies that solely the rightmost edge of each string can mode, while instead the leftmost is fixed. Indeed, the system admits $|01\rangle$ as frozen bit string, as discussed in Sec. 5.2.1, which corresponds to the leftmost edge of each cluster of excitations. Due to these constraints, each string of excitations is confined between its left edge and the left edge of the next one, and no entanglement can be generated between them during dynamics. As a result, the Hilbert space gets shattered in $\mathcal{O}(e^N)$ disconnected sectors [174], as discussed in Sec. 5.2.1. Thus, upon initializing a product state (which are the ones most easily preparable in experiments) made of \mathcal{N} -strings of excitations, the whole physics can be captured by studying the dynamics of \mathcal{N} 1-string states. Therefore, we can focus on the symmetry sector with a single string ($Q = 1$). A complete basis of single-kink states is given by $|\mathbf{k}\rangle = \bigotimes_{j=1}^k |1\rangle \bigotimes_{j=k+1}^N |0\rangle$. Adopting this basis, and using the following results:

$$\begin{aligned} \langle \mathbf{q} | \hat{n}_j \hat{n}_{j+2} | \mathbf{k} \rangle &= \delta_{q,k} \theta(k - (j + 2)), \\ \langle \mathbf{q} | \hat{n}_j \hat{\sigma}_{j+1}^x | \mathbf{k} \rangle &= \delta_{q-1,k} \delta_{j-1,k} + \delta_{q+1,k} \delta_{j,k}, \\ \langle \mathbf{q} | \hat{n}_j \hat{\sigma}_{j+1}^x \hat{n}_{j+2} | \mathbf{k} \rangle &= 0, \end{aligned} \quad (5.10)$$

by plugging them in the Hamiltonian in Eq. (5.9) represented in the same basis

$$\hat{H} = \sum_{\mathbf{k}, \mathbf{q}} \langle \mathbf{q} | \hat{H} | \mathbf{k} \rangle | \mathbf{q} \rangle \langle \mathbf{k} |, \quad (5.11)$$

we obtain

$$\hat{H} = \frac{\Omega_1}{2} \sum_{k=1}^{N-1} (| \mathbf{k} \rangle \langle \mathbf{k} + 1 | + \text{H.c.}) + \epsilon \sum_{k=1}^N k | \mathbf{k} \rangle \langle \mathbf{k} | + V_{\text{NNN}} \sum_{k=2}^N (k - 2) | \mathbf{k} \rangle \langle \mathbf{k} |, \quad (5.12)$$

where the first term controls the change of the string length, while the second the potential energy proportional to such length. Notice that the size of the Hilbert space scales polynomially with the system size N , indicating that the system displays strong Hilbert space shattering. This Hamiltonian is integrable and has been derived in several similar scenarios [59, 208–211]. Direct inspection shows that Eq. (5.12) is the well-known Hamiltonian of an electron in a lattice subjected to a constant electric field [209, 210]. In such condition, it is known that the system displays Stark localization [209], which leads to real-time Bloch oscillations of period $T_{\text{Bloch}} \sim 2\pi\Omega_1/(\epsilon + V_{\text{NNN}})$ and size $\ell_{\text{Bloch}} \sim \Omega_1/(\epsilon + V_{\text{NNN}})$ originating from the rightmost edge of the string. Hence, excitations and quantum correlations are confined, preventing thermalization, closely resembling confinement in non-integrable systems [131, 201, 202, 212].

To better observe such dynamical features, in Fig. 5.4 we show the dynamics of a kink state $\bigotimes_{j=1}^M |1\rangle \bigotimes_{j=M+1}^N |0\rangle$ with $M = N/2$ excitations, where N is the system size. Since the accessible Hilbert space by such states grows linearly in N , we can push our simulations to very large N also using exact diagonalization. For our purposes, $N = 30$

$$V_{\text{NNN}} = 0.5 \Omega_2 = 0$$

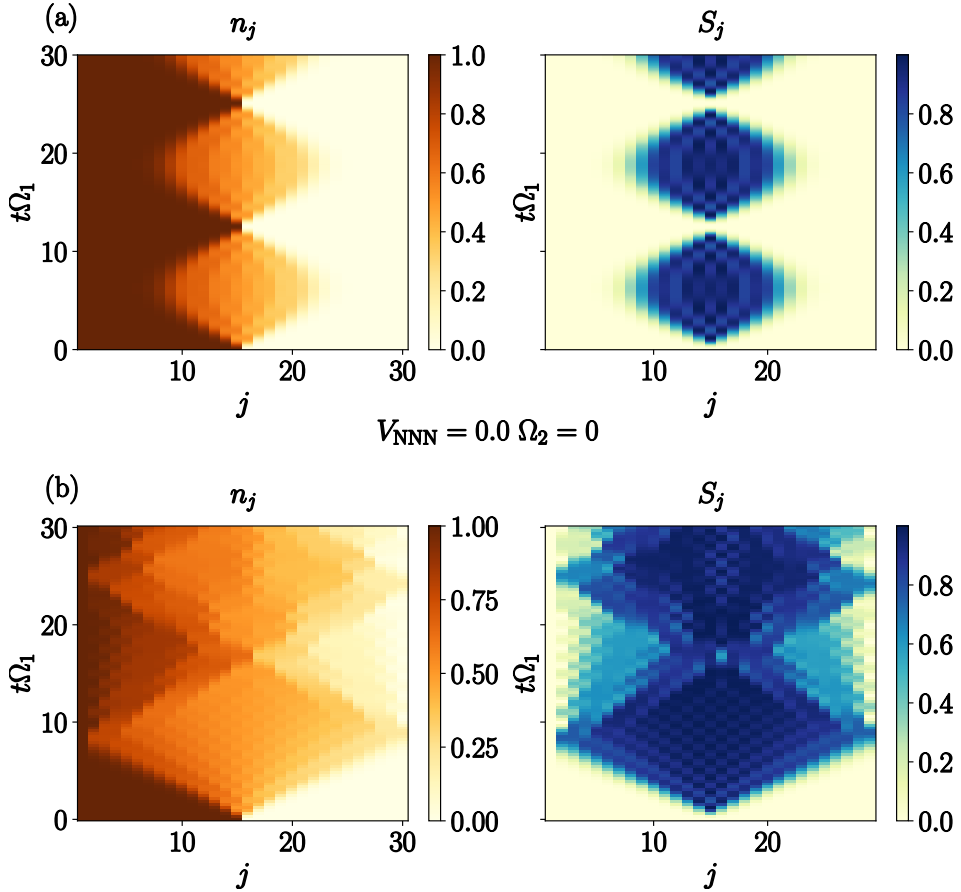


FIGURE 5.4. Dynamics in the shattered regime ($\Omega_2 = 0$, see Eq. (5.9)) of an initial kink state $\bigotimes_{j=1}^M |1\rangle \bigotimes_{j=M+1}^N |0\rangle$ with $M = N/2$ excitations, with N the system size in the confined ($V_{\text{NNN}} > 0$, upper panels) and deconfined one ($V_{\text{NNN}} = 0$, lower panels). When $V_{\text{NNN}} > 0$, the system displays real-time Bloch oscillations along the surface both at the level of occupation number, as well as in the entanglement entropy along each cut, impeding the spread of quantum correlations and thus thermalization.

is enough. As anticipated, when $\max\{|\epsilon|, |V_{\text{NNN}}|\} \neq 0$, the system displays confinement due to emerging real-time Bloch oscillations. We observe that also the entanglement entropy along each cut displays Bloch oscillation, which demonstrates how quantum correlations build up solely along the surface and remain confined, impeding thermalization. Instead, when $\max\{|\epsilon|, |V_{\text{NNN}}|\} = 0$, excitations can freely spread, as well as the entanglement, and the system quickly thermalizes towards a generalized Gibbs ensemble, since the system is integrable.

5.3.3. *Quantum East model regime*

When both drive fields are active ($\Omega_{1,2} \neq 0$), strings of excitations gain full mobility since they can shrink, grow, merge, and split (cf. Fig. 5.1(b)). Thus, the accessible Hilbert space does not shatter and any product state can be dynamically reached by any other at fixed East symmetry sector [151]. Nonetheless, it is still possible to observe an extreme slowdown of thermalization. This can be immediately seen by setting $\Omega_2/\Omega_1 = 1$, for which Eq. (5.1) reduces to the quantum East model investigated in Refs. [140, 151] apart from additional density-density interactions which do not alter the qualitative picture. Such model has been shown to display a dynamical transition separating a fast and slow thermalizing phase [140, 151] due to the competing kinetic term $\propto \Omega$ and on-site energy $\propto \epsilon$. Intuitively, if the kinetic term dominates ($\Omega_{1,2}/(2\epsilon) \gtrsim 1$) strings of excitations expand and merge ballistically, fastly washing local information of the initial configuration, while if it is subleading ($\Omega_{1,2}/(2\epsilon) \lesssim 1$), excitations can expand slowly, making possible to retrieve information about the initial conditions. Such behavior is strongly linked to the localization of the ground state and it can be observed for an exponentially large number, in the system size, of initial states [151]. As the quantum East model has been the subject of intense investigation in the course of the thesis, we will further discuss it in Part II in close connection with the experiment where it could be realized.

Part II

Realizing ergodicity-breaking mechanisms in NISQ devices

So far, we have focused on discussing different mechanisms which could hinder the onset of thermalization, without caring about their actual experimental relevance. In this part, we aim to show that the mechanisms discussed before could be *analogically* simulated in current Noisy-Intermediate-Scale-Quantum (NISQ) devices [9]. At the core of quantum analog simulations, there is the goal of making the system evolve under the desired Hamiltonian. To achieve this, the typical approach is based on a combination of:

- Use the native interactions characterizing the constituents, e.g. dipole-dipole interactions in Rydberg atoms or capacitive coupling superconducting circuits;
- If a lattice model is desired, embed the desired configuration on the way the constituents are arranged in space via, for instance, optical lattice and tweezers for Rydberg atoms, or actually welded on chip for superconducting circuits;
- Manipulate these constituents externally (e.g. via lasers) so that in the regimes of interest, e.g. small coupling, weak external drive field, far detuned laser from the atomic transition, and so on, the Hamiltonian effectively behaves as the target one.

Before continuing, we highlight that analog quantum simulations are not the only pathway for simulating quantum systems. Indeed, we observe that a major limitation of the analog approach is the possibility of typically simulating a restricted class of effective Hamiltonians in a given experimental setup. To overcome such limitations, another possible route is abandoning the analog approach in favor of the digital one. Such approach is based on devising a set of quantum gates via which the target Hamiltonian could be realized by their application. The remarkable aspect is that, if in a given platform it is possible to engineer a universal set of gates, i.e. a set of gates via which any other can be approximated with arbitrary accuracy, it is in turn possible to engineer any target Hamiltonian. It is evident that the digital approach offers way more flexibility with respect to the analog one. However, as it could be guessed, it suffers of limitations as well. Indeed, it is necessary that the gates have high enough fidelity, namely they are the desired gates with high accuracy; and are fast with respect to the typical decoherence time of the system so that you can apply many of them before your quantum system potentially behaves as a classical one. For this reason, despite being less flexible, analog quantum simulations are currently and typically more reliable for simulating a target Hamiltonian with respect to the digital approach.

For such reasons, in this Part, we will focus solely on analog approaches via which the family of models so far discussed, i.e. the spin/bosonic quantum East models and variants, can be realized. We highlight that the models we are interested in are kind of ‘unnatural’ at first glance, since they display interactions that are not symmetric

under the exchange of constituents. In particular, the kinetic term $\hat{n}_j \hat{\sigma}_{j+1}^x$ is not symmetric under exchanging neighboring sites, contrary to what it is natively available in nature. In previous works, in order to overcome such issue, some proposals have been developed based on inducing non-Hermitian (and directional) processes via dissipation (see e.g. Refs. [213–215]). Instead, here, we will show that such limitation could be overcome upon relying on purely coherent processes, without the usage of dissipation, in either Rydberg or superconducting circuits-based platforms. Specifically, this Part is organized as follows:

- In Chapter 6 we discuss an experimental protocol, realizable in current Rydberg atoms based platforms, via which the kinetically constrained spin-1/2 models can be realized. We achieve this goal by presenting a blueprint for Rydberg atomic arrays featuring chiral interactions that aren't symmetric when neighboring atoms are exchanged. Specifically, we consider a one-dimensional array with a staggered configuration of atomic positions and drive fields. In such a scenario, each atom can distinguish the neighboring atom on the left from the one on the right, since they interact with a different strength. Due to this, we will show that by driving the atoms with drive fields with a suitable frequency, we can selectively make processes resonant towards one direction and off-resonance towards the other. In summary, due to strong Van-der-Waals interactions, we can access a regime we term *directional* antiblockade, wherein an atom can change its internal state solely when an atom to its right (or left) becomes excited. As this scheme is scalable in the number of atoms, we can immediately get access and explore the many-atoms regime.
- In Chapter 7, we trade Rydberg atoms with a one-dimensional array of coupled superconducting circuits with the goal of simulating the bosonic quantum East model. We abandon the Rydberg platform as embedding a bosonic degree of freedom from spins is hard, while instead superconducting circuits are well approximated with anharmonic quantum oscillators, whose excitations are bosonic in nature. Also, in this case, we achieve our goal by driving the system with external drive fields. However, differently from the Rydberg implementation, we do not aim to make the desired processes resonant, but the target Hamiltonian will emerge in the low-energy limit as a result of second-order virtually-mediated processes. We opt for this approach as the parameters needed are the ones where superconducting circuits based platforms typically operate.

CHAPTER 6

A Rydberg platform for non-ergodic chiral quantum dynamics

Most of the content in this Chapter is in:

- “*A Rydberg platform for non-ergodic chiral quantum dynamics*” (arXiv: 2309.12392; to appear in Phys. Rev. Letter)

Executive Summary. In this Chapter, we discuss a Rydberg atoms array based platform to realize the kinetically constrained spin-1/2 models which have been the focus of Chapters 4 and 5. Specifically, we will show how to realize the Hamiltonian in Eq. (5.1), which we rewrite for the sake of understanding

$$\begin{aligned} \hat{H} = & \frac{\Omega_1}{2} \sum_j \hat{n}_j \hat{\sigma}_{j+1}^x (1 - \hat{n}_{j+2}) + \frac{\Omega_2}{2} \sum_j \hat{n}_j \hat{\sigma}_{j+1}^x \hat{n}_{j+2} + \\ & + \epsilon \sum_j \hat{n}_j + V_{\text{NNN}} \sum_j \hat{n}_j \hat{n}_{j+2}, \end{aligned} \quad (6.1)$$

where $\hat{\sigma}_j^\alpha$ is the α -Pauli operator; $\hat{n}_j = (1 - \hat{\sigma}_j^z)/2$; where $\Omega_{1,2}$ are the Rabi frequencies of external drive fields; ϵ is the detuning of the frequency of the acting drive fields from the desired resonant condition; V_{NNN} controls the next-neighbor Van-der-Waals interactions, naturally present in Rydberg arrays.

As already discussed in Chapter, by tuning $\Omega_{1,2}$ (which can be easily done in experiments), is possible to shape the kinetic constraint and in turn activate a different ergodicity-breaking mechanisms: quantum many-body scars (for $\Omega_1 = 0$ and $\Omega_2 \neq 0$); confinement (for $\Omega_1 \neq 0$ and $\Omega_2 = 0$); disorder-free localization (for $\Omega_{1,2} \neq 0$).

These mechanisms have been already discovered prior to our study. However, so far the experimental realization of each of them requested a tailored implementation. Specifically, quantum many-body scars [15, 47, 48, 52, 56, 58, 200] were realized in Rydberg arrays [15] or with superconducting qubits [216]; Hilbert space shattering [42], has been realized in ultracold atoms [46, 217] confinement of quasi-particles induced by many-body interactions [59, 131, 201, 202] was observed in trapped-ions [218]. Instead, in our proposal, these mechanisms are intricately linked to the specific constraints at play and can thus be controlled and selected by simply adjusting the strength of the external drive fields. This versatility transforms our platform into a universal quantum simulator for non-ergodic quantum dynamics. As an additional benefit, our platform allows for the implementation of the quantum East model [140, 151], which has been absent in prior

studies, albeit several Rydberg implementations have focused on related constrained models [179–185]. We highlight once again the significance of the quantum East model lies in its distinction as one of the rare cases where an interacting system undergoes a disorder-free transition between delocalization and localization in the ground state and dynamics [151], in a fashion markedly distinct from many-body localization [38, 40].

What is new? All results of this chapter represent novel research results.

Organization of the Chapter

- In Sec. 6.1 we briefly motivate why we choose a Rydberg based platform for our implementation.
- In Sec. 6.2 we propose an experimental setup of Rydberg atomic arrays featuring chiral interactions that aren't symmetric when neighboring atoms are exchanged. Specifically, we consider a one-dimensional array with a staggered configuration of atomic positions and drive fields (cf. Fig. 6.1(a)). In such a scenario, due to strong Van-der-Waals interactions, we can access a regime we term *directional* antiblockade, wherein an atom can change its internal state solely when an atom to its right (or left) becomes excited.
- In Sec. 6.3.1 we show the robustness of these mechanisms to experimental imperfections, like thermal disorder in atomic positions, and provide further details about the experimental setup needed, which we highlight is currently available. This opens up its usage in state-of-the-art platforms and for simulating exotic many-body systems displaying chiral interactions, such as directional kinetically constrained quantum models (KCMs).
- In Sec. 6.4 we test our scheme in simulating the target many-body systems (cf. Eq. (6.1)) by direct comparison between the desired result and the one achievable with realistic experimental parameters and limitations, such as limited accessible time and thermal disorder in the atomic positions.

This Chapter is composed by a rearrangement of the author's publication [3].

6.1. WHY RYDBERG ATOMS?

As mentioned throughout this thesis, despite being far from full fault-tolerant quantum computing [9], reliable analog quantum simulations are nowadays attainable across a variety of atomic, molecular optical (AMO) as well as solid-state platforms. Among them, atomic Rydberg arrays stand out prominently due to their remarkable degree of

programmability, as highlighted in various studies [15, 219–222]. This has led to ground-breaking experiments in areas such as topological order [12, 13], engineerable quantum phase transitions [15, 219, 223, 224], lattice gauge theories [201], and strongly correlated quantum dynamics [15, 17–19]. Such broad flexibility suggests opportunities in designing quantum simulators with no direct counterpart in traditional AMO or condensed matter physics. A prominent example in such direction is given by the realization of the PXP model, whose peculiar dynamical properties observed in Ref. [15] sparked considerable interest in the community. In this context, a challenge centers on creating systems hosting non-reciprocal processes that can differentiate, particularly in one dimension, between the flow of information in the right and left directions. Directionality, already when restricted to *single-particle* processes, has proven useful in various tasks, such as mitigating back-action effects [225], realizing chiral transport [226], aiding the preparation of nontrivial topological states [213, 227–229], and realizing unconventional phases of matter [138, 230]. Thus, combining directional *interactions* with the high control achieved in Rydberg platforms would pave the way for entering the realm of chiral *strongly correlated* phenomena as an uncharted frontier of quantum information processing [231]. Here, we achieve this goal by presenting a blueprint for Rydberg atomic arrays featuring chiral interactions that aren't symmetric when neighboring atoms are exchanged. While in this thesis we focus on the usage of our mechanisms in simulating strongly correlated chiral phenomena, of which the quantum East models and variations constitute a candidate, an interesting direction could be finding ways to harness such directional for applications in quantum information processing. In such regard, we highlight a recent study [232] where the mechanism we describe below has been independently discovered, which could be used in atomtronics.

6.2. CHIRAL INTERACTIONS IN RYDBERG ARRAYS

The key ingredient to engineer a directional interaction is a staggered configuration of the atomic spacings and drive fields in a Rydberg array (cf. Fig. 6.1(a)). The Hamiltonian describing such scenario, in the rotating frame with respect to the bare atomic transitions, can be written as

$$\begin{aligned} \hat{H}(t) = & \sum_{j=1}^N \left(\frac{1}{2} (\Omega_{1,j}(t) + \Omega_2(t)) \hat{\sigma}_j^+ + \text{H.c.} \right) + \\ & + V_1 \sum_{j \text{ odd}} \hat{n}_j \hat{n}_{j+1} + V_2 \sum_{j \text{ even}} \hat{n}_j \hat{n}_{j+1} + V_{\text{NNN}} \sum_{j=1}^{N-2} \hat{n}_j \hat{n}_{j+2}, \end{aligned} \quad (6.2)$$

where $\hat{\sigma}_j^+ = |1\rangle_{jj}\langle 0|$ transfers the j -th atom from the ground state $|0\rangle$ to the Rydberg state $|1\rangle$; $\hat{n}_j = |1\rangle_{jj}\langle 1|$; $\Omega_{1,j}(t)$ and $\Omega_2(t)$ are classical drive fields controllable in the experiment with Rabi frequencies Ω_1 and Ω_2 , respectively; V_1 (V_2) are Van-der-Waals interactions ($V(r) = C_6/r^6$) on odd (even) bonds; V_{NNN} is the next-nearest neighbor interaction. Throughout, we work in the regime $|V_{1,2}|, |V_1 - V_2| \gg \Omega_{1,2} \gg V_{\text{NNN}}$. In this regime, interactions play a crucial role in dictating the dynamics of the single atom. Specifically, two extreme scenarios can be realized: excited atoms either inhibit spin-flips of neighboring ones (blockade) [233], or facilitate them (antiblockade) [234]. The blockade condition occurs by setting the drive field resonant with the bare atomic transitions so that the interaction energy due to a neighboring excited atom makes it off-resonant. Instead, the antiblockade occurs when the acting drive field is detuned from the bare atomic transitions by the interaction, and thus it becomes resonant solely if a neighboring atom is excited. In translational invariant systems, each atom cannot distinguish its right neighbor from the one to its left, and so no preferable direction can appear. In our scheme instead, since $V_1 \neq V_2$, the atom can distinguish the two neighboring atoms and we can selectively make processes resonant towards one direction and off-resonance towards the other. We term this mechanism *directional* antiblockade, which implies that an atom can flip only when an atom to its right (or left) is excited. To achieve this regime, it is enough to apply a single drive field on each atom, and so we temporarily set $\Omega_2 = 0$. We now discuss two possible experimental regimes where the desired condition could be realized. Then, we provide further details on the experiment.

6.2.1. First scheme for obtaining directional antiblockade

A possible scheme is based on imprinting an additional staggered configuration in the drive field frequencies of $\Omega_{1,j}(t)$. Specifically, we can set the drive field on site j detuned by V_1 (if j is even) or V_2 (if j is odd) from the bare atomic transition, so that it is resonant solely when the atom to its left is excited and the one to its right is not, obtaining the anticipated *directional* antiblockade (see Fig. 6.1(b)). Specifically, we set

$$\Omega_j(t) = \Omega_1 \times \begin{cases} e^{-iV_1 t}, & j \text{ even} \\ e^{-iV_2 t}, & j \text{ odd.} \end{cases} \quad (6.3)$$

The net result is that an excitation seeded in the system triggers an avalanche of excitations solely towards ‘East’ (see Fig. 6.1(c)).

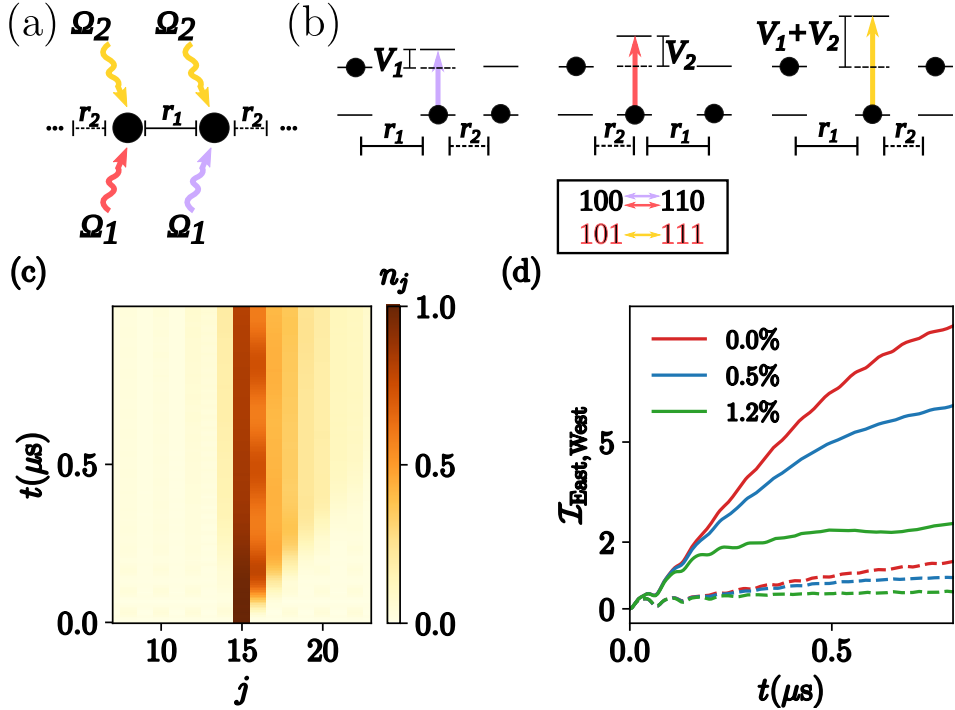


FIGURE 6.1. (a): An array of Rydberg atoms in a staggered configuration of drive fields (each color refers to a different frequency) and spacings r_1 and r_2 , with corresponding nearest-neighbor interactions V_1 and V_2 . (b): Scheme of the most resonant processes (see box) which happen exclusively at the right of excited atoms due to the *directional* antiblockade. (c): Dynamics of the density profile seeding a single excitation and including thermal disorder in the atomic positions $\tilde{\eta}_x = 0.012$ (see text). (d): Dynamics of the imbalances $\mathcal{I}_{\text{East}}$ (continuous line) and $\mathcal{I}_{\text{West}}$ (dashed line) starting from the same state as in (c) for different values of $\tilde{\eta}_x$. The imbalance $\mathcal{I}_{\text{East}}$ ($\mathcal{I}_{\text{West}}$) is defined as the sum of the average occupations to the right (left) of the initial seeded excitation. Excitations propagate preferably towards ‘East’ as desired ($\mathcal{I}_{\text{East}} > \mathcal{I}_{\text{West}}$) despite finite temperature effects. Image taken from Ref. [3].

6.2.2. Second scheme for obtaining directional antiblockade

Here we discuss a different, but equivalent, route for obtaining the *directional* antiblockade condition. Given Eq. (6.2), we set again $\Omega_2 = 0$ as it is not necessary for this purpose. In Sec. 6.2.1 we have discussed a scheme based on a staggered configuration in the atomic distances and drive field frequencies driving the atoms. Here, we retain the essential ingredient of a staggered configuration in the atomic spacings. However, instead of imprinting the staggered configuration on the drive field frequencies, which we set to be homogeneous in space, we impose the staggered configuration on the atomic transition frequencies. This condition could be achieved by site-resolved light shifts [235]. Specifically, we set the atomic transition frequencies to be detuned by $-V_1$ from the

drive field when j is even and by $-V_2$ when j is odd. In this manner, the *directional* antiblockade condition discussed in the main text emerges, as the drive field acting on the j -th atom is resonant only when the $(j - 1)$ -th atom is excited. This can be seen explicitly writing the Hamiltonian in the rotating frame with respect to the drive field, which is given by

$$\hat{H} = - \sum_{j=1}^N V_{j-1,j} \hat{n}_j + \frac{\Omega_1}{2} \sum_{j=1}^N \hat{\sigma}_j^x + V_1 \sum_{j \text{ odd}} \hat{n}_j \hat{n}_{j+1} + V_2 \sum_{j \text{ even}} \hat{n}_j \hat{n}_{j+1} + V_{\text{NNN}} \sum_{j=1}^{N-2} \hat{n}_j \hat{n}_{j+2}. \quad (6.4)$$

From Eq. (6.4), it can be seen that if the $(j - 1)$ -th is excited, the energy shift cancels the contribution from the first term on the j -th atom, making the acting drive field resonant and able to induce a spin-flip.

6.2.3. Derivation of the effective theory with both sets of drive fields

As we have discussed the experimental protocol needed to achieve the desired directionality, we here show how in such regimes the family of KCMs contained in Eq. (6.1) can be realized. Given the Hamiltonian in Eq. (6.2), we set $\Omega_{1,j}(t) = \Omega_1 e^{-i(V_{j-1,j}-\epsilon)t}$ and $\Omega_2(t) = \Omega_2 e^{-i(V_1+V_2-\epsilon)t}$, where ϵ is a (small) detuning from the desired resonant condition, obtaining

$$\begin{aligned} \hat{H}(t) = & \sum_{j=1}^N \left[\frac{1}{2} (\Omega_1 e^{-i(V_{j-1,j}-\epsilon)t} + \Omega_2 e^{-i(V_1+V_2-\epsilon)t}) \hat{\sigma}_j^+ + \text{H.c.} \right] + \\ & + V_1 \sum_{j \text{ odd}} \hat{n}_j \hat{n}_{j+1} + V_2 \sum_{j \text{ even}} \hat{n}_j \hat{n}_{j+1} + V_{\text{NNN}} \sum_{j=1}^{N-2} \hat{n}_j \hat{n}_{j+2}, \end{aligned} \quad (6.5)$$

To obtain the effective Hamiltonian, we pass in interaction picture $\hat{H}_{\text{int}} = \hat{U}^\dagger \hat{H} \hat{U} - \hat{H}_0$ with

$$\hat{U} = \exp \left[-i \hat{H}_0 t \right], \quad \hat{H}_0 = -\epsilon \sum_{j=1}^N \hat{n}_j + \sum_{j=1}^{N-1} V_{j,j+1} n_j n_{j+1}. \quad (6.6)$$

We have

$$e^{-i\epsilon \sum_j \hat{n}_j t} \sigma_j^+ e^{i\epsilon \sum_j \hat{n}_j t} = e^{-i\epsilon |1\rangle\langle 1|t} |1\rangle\langle 0| e^{i\sum_j \Delta_j |1\rangle\langle 1|t} = e^{-i\epsilon t} \sigma_j^+, \quad (6.7)$$

and, exploiting $\hat{n}_i^k = \hat{n}_i$ for $k \in \mathbb{N}^+$, we have

$$\begin{aligned}
e^{+i\sum_j V_{j-1,j}\hat{n}_{j-1}\hat{n}_j t} \hat{\sigma}_i^+ e^{-i\sum_j V_{j-1,j}\hat{n}_{j-1}\hat{n}_j t} &= e^{+iV_{i-1,i}\hat{n}_{i-1}t} \hat{\sigma}_i^+ e^{+iV_{i,i+1}\hat{n}_{i+1}t} \\
&= \left[1 + \left(\sum_{k=1}^{\infty} \frac{(iV_{i-1,i}t)^k}{k!} \right) \hat{n}_{i-1} \right] \hat{\sigma}_i^+ \left[1 + \left(\sum_{k=1}^{\infty} \frac{(iV_{i,i+1}t)^k}{k!} \right) \hat{n}_{i+1} \right] \\
&= [1 + (e^{+iV_{i-1,i}t} - 1) \hat{n}_{i-1}] \hat{\sigma}_i^+ [1 + (e^{+iV_{i,i+1}t} - 1) \hat{n}_{i+1}] \\
&= (\hat{P}_{i-1} + e^{+iV_{i-1,i}t} \hat{n}_{i-1}) \hat{\sigma}_i^+ (\hat{P}_{i+1} + e^{+iV_{i,i+1}t} \hat{n}_{i+1})
\end{aligned} \tag{6.8}$$

where we have introduced $\hat{P}_i = (1 - \hat{n}_i)$ (projector on the vacuum $|0\rangle_{jj}\langle|0\rangle$). Thus, paying attention to the boundary terms, the Hamiltonian in interaction picture is given by

$$\begin{aligned}
\hat{H}_{\text{int}} &= \frac{1}{2} \left\{ (\Omega_1 e^{-iV_2 t} + \Omega_2 e^{-i(V_1+V_2)t}) \hat{\sigma}_1^+ (\hat{P}_2 + e^{+iV_1 t} \hat{n}_2) + H.c. \right\} + \\
&+ \frac{1}{2} \sum_{j=2}^{N-1} \left\{ (\Omega_1 e^{-iV_{j-1,j} t} + \Omega_2 e^{-i(V_1+V_2)t}) (\hat{P}_{j-1} + e^{+iV_{j-1,j} t} \hat{n}_{j-1}) \hat{\sigma}_j^+ (\hat{P}_{j+1} + e^{+iV_{j,j+1} t} \hat{n}_{j+1}) + H.c. \right\} + \\
&+ \frac{1}{2} \left\{ (\Omega_1 e^{-iV_{N-1,N} t} + \Omega_2 e^{-i(V_1+V_2)t}) (\hat{P}_{N-1} + e^{+iV_{N-1,N} t} \hat{n}_{N-1}) \hat{\sigma}_N^+ + H.c. \right\} + \\
&+ \epsilon \sum_{j=1}^N \hat{n}_j + V_{\text{NNN}} \sum_{j=1}^{N-2} \hat{n}_j \hat{n}_{j+2}.
\end{aligned} \tag{6.9}$$

Given Eq. (6.9), after performing the RWA in the limit $|V_1 - V_2|, V_{1,2} \gg |\Omega_{1,2}|$, keeping the most resonant processes (the ones without any time dependence), we obtain

$$\begin{aligned}
\hat{H} &= \frac{\Omega_1}{2} \sum_j \hat{n}_j \hat{\sigma}_{j+1}^x (1 - \hat{n}_{j+2}) + \frac{\Omega_2}{2} \sum_j \hat{n}_j \hat{\sigma}_{j+1}^x \hat{n}_{j+2} + \\
&+ \epsilon \sum_j \hat{n}_j + V_{\text{NNN}} \sum_j \hat{n}_j \hat{n}_{j+2},
\end{aligned} \tag{6.10}$$

which is the desired target Hamiltonian (cf. Eq. (6.1)).

6.3. DETAILS ON THE EXPERIMENTAL SETUP

Here we provide additional details on how to generate the staggered atomic array and drive fields scheme needed to induce the *directional* antiblockade described in the main text. The atomic array could be produced by trapping the atoms in optical tweezers. Generating these beams using acousto-optic deflectors (AOD) or spatial light modulators (SLM) would allow us to achieve the desired bipartite spacing. An undesired effect due to the trapping potentials holding the atoms is a shift in the atomic energies. Specifically, we can distinguish two components: the intensity variation from trap to

trap, and the atomic motion inside the trap, which causes it to sample different intensities/AC Stark shifts in different shots of the experiment. Such effects could mildly compromise the desired *antiblockade* condition. However, unlike other experimental imperfections such as thermal disorder in the atomic positions (which we have taken into account), it is possible to completely eliminate this shift by switching the traps off entirely during the Rydberg driving [15]. This technique eliminates all potential AC Stark shifts and remains effective for approximately $10 \mu\text{s}$ of evolution time, which is the maximum time discussed in our work. With respect to the desired staggered configuration in the drive field frequencies, the latter could be applied to the atoms through the same microscope objective used for the optical tweezers [236]. This, in combination with spatial light modulators (SLM) for the driving beams, would allow the generation of the desired staggered pattern in the drive fields frequencies, i.e., $\Omega_{1,j}(t) = \Omega_1 e^{iV_{j-1,j}t}$, with Ω_1 as a constant. Additionally, the uniform drive field $\Omega_2(t) = \Omega_2 e^{i(V_1+V_2)t}$, with Ω_2 as a constant, could also be sent through the microscope objective.

6.3.1. *Experimental feasibility*

In actual experiments, the *directional* antiblockade could be spoiled by finite temperature fluctuations, inhomogeneities due to the harmonic frequency trap holding the atoms, or dephasing coming from finite laser linewidth. The first two can be taken into account including quenched disorder in the atomic positions [237]. Specifically, at low enough temperature T , the displacements $\delta\mathbf{r}_j$ from the ideal atomic positions are constant during a single experimental realization and distributed accordingly to a Gaussian distribution with zero average and width $\eta_\alpha = \sqrt{k_B T / (m\omega_\alpha^2)}$ along the α -axis, with ω_α the trapping frequency and m the atomic mass. Instead, dephasing induced by finite linewidth of the laser can be modeled by a Lindblad master equation with jump operators $\hat{L}_j = \sqrt{\gamma} \hat{n}_j^z$, with $j \in [1, N]$. Yet, in our setup, we work in regimes where $\gamma \sim 10 \text{ kHz}$ is at least two orders of magnitudes smaller than the other energy scales, and therefore it can be neglected. Specifically, we will show results up to a time of $10 \mu\text{s}$, where the dynamics can be considered purely coherent as also spontaneous decay from the Rydberg state can be neglected. We elaborate further in the conclusions and Supplemental Material on the opposite limit, where dephasing is large, illustrating how our scheme readily enables us to investigate ‘classical’ non-ergodic dynamics with directional character. For concreteness, we consider ^{87}Rb atoms located along the x -axis, at temperature $T = 3 \mu\text{K}$ and optical traps with $\omega_x = \omega_y = 5 \times \omega_z = 40 \text{ kHz}$, which give rise to an anisotropic disorder $\eta_x = \eta_y = \eta_z/5 \approx 0.1 \mu\text{m}$. We consider the atomic level $70S$ as Rydberg state which has $C_6/(2\pi) = 864 \text{ GHz}/(\mu\text{m})^6$. In the following, we measure disorder as the relative variation with respect to the mean distance, namely $\tilde{\eta}_\alpha \equiv \eta_\alpha/r_1$.

We consider Rabi frequencies $\Omega_{1,2}$ in the range between $2\pi \times 1$ MHz and $2\pi \times 5$ MHz. For this set of parameters, we found a good compromise between fast dynamics, small impact of disorder, and $\Omega_{1,2} \ll V_{j,j+1}$, the average spacings $r_1 = 6.2 \mu\text{m}$ and $r_2 = 5.4 \mu\text{m}$ (for which $\tilde{\eta}_x \approx 0.01$), to which corresponds interactions $V_1/(2\pi) = (15.0 \pm 1.0)$ MHz and $V_2/(2\pi) = (30.0 \pm 2.2)$ MHz, respectively, and $V_{\text{NNN}}/(2\pi) = (0.33 \pm 0.02)$ MHz. We note that disorder could be reduced by setting the atoms more far apart from each other, at the expense of a smaller $\Omega_{1,2}$ in order to still work in the strongly interacting regime, which in turn would lead to the observation of fewer cycles in the time window of $10\mu\text{s}$ considered. Despite we show results mostly in this parameters' regime, we keep $\tilde{\eta}_\alpha$ as a free parameter to explore different experimental scenarios. In the following, we show results averaged over 50 realizations of disorder, for which statistical errors are $\sim 1\%$ or less. As it can be seen in Fig. 6.1(c-d), the main impact of disorder is a reduction of the propagating front, while its directional character is not appreciably spoiled. Having shown the robustness of our scheme, we now proceed to discuss some models immediately accessible by simply tuning the strength of the external drive fields.

6.4. COMPARISON BETWEEN THE FULL MODEL AND THE EFFECTIVE ONE

We have discussed how chiral interactions between Rydberg atoms could be realized and provide details on the experimental setup needed for such a purpose. In doing so, we have also discussed the impact of disorder in the atomic positions due to the finite temperature in the setups. Despite the disorder contributes to impeding the spread of excitations in the system, in this section we show that the different ergodicity-breaking mechanisms are quantitatively affected, but not qualitatively. In our discussion, we focus on the QXP and quantum East model, as the features of the QXQ model are the same as the PXP model, which has been already realized in experiments.

6.4.1. *Confinement ($\Omega_2/\Omega_1 = 0$)*

In this regime, strings of excitations can only expand or shrink, making the dynamics occur solely along the surface. Thus, to better observe such dynamical features, we initialize a kink state $\bigotimes_{j=1}^M |1\rangle \bigotimes_{j=M+1}^N |0\rangle$ with $M = N/2$ excitations, where N is the system size, set to be $N \geq 50$ (see Fig. 6.2). Simulations of the effective theory (cf. Eq. (6.10)) can be efficiently carried out using Exact Diagonalization upon writing it in the kink basis (cf. Eq. (5.12)). Instead, we employ Tensor Network methods for simulating the full theory (cf. Eq. (6.2)). As stated in the main text, the system displays confinement due to emerging real-time Bloch oscillations with a period $T = 2\pi/V_{\text{NNN}}$

and width $\ell \sim \Omega_1/V_{\text{NNN}}$. In the full theory, such oscillations are still present, although suppressed due to quenched disorder in the atomic positions.

For completeness, we also show the dynamics of the entanglement entropy along each cut to demonstrate how quantum correlation builds up solely along the surface and remains confined, impeding thermalization.

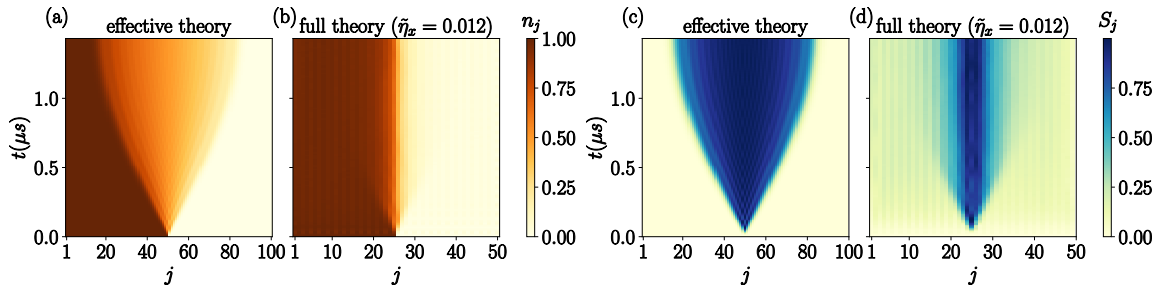


FIGURE 6.2. Dynamics in the confined regime ($\Omega_2 = 0$) of an initial kink state $\bigotimes_{j=1}^M |1\rangle \bigotimes_{j=M+1}^N |0\rangle$ with $M = N/2$ excitations, with N the system size. We compare the dynamics obtained in the ideal regime, where the effective theory (cf. Eq. (5.12)) is exact, with a realistic experimental scenario (cf. Eq. (6.2)) including positional disorder η due to thermal fluctuations. The system displays real-time Bloch oscillations along the surface both at the level of occupation number (a,b), as well as in the entanglement entropy along each cut (c,d). Parameters: $\Omega_1/V_1 = 0.2$, $V_2/V_1 = 2$, $\epsilon = 0$, $V_1 = 2\pi \times 15$ MHz. Image taken from Ref. [3].

6.4.2. ‘Quantum East Model’ ($\Omega_1/\Omega_2 \neq 0$)

When both drive fields are active ($\Omega_{1,2} \neq 0$), strings of excitations gain full mobility since they can shrink, grow, merge, and split (cf. Fig. 5.1(b)). Thus, the accessible Hilbert space does not shatter and any product state can be dynamically reached by any other at fixed East symmetry sector [151]. As a first comparison, we consider as initial state one with a single seeded excitation (cf. Fig. 6.3). We observe, similar to the confined regime, a propagating front of excitations towards the East, with additional oscillations in the bulk, attributed to the presence of ‘string-breaking terms.’ The oscillations are influenced by the strength of the external drive field, exhibiting a period $\sim \Omega_2$ (which is the Rabi frequency of the global drive controlling the ‘string-breaking’ processes) and amplitudes of near order 1.

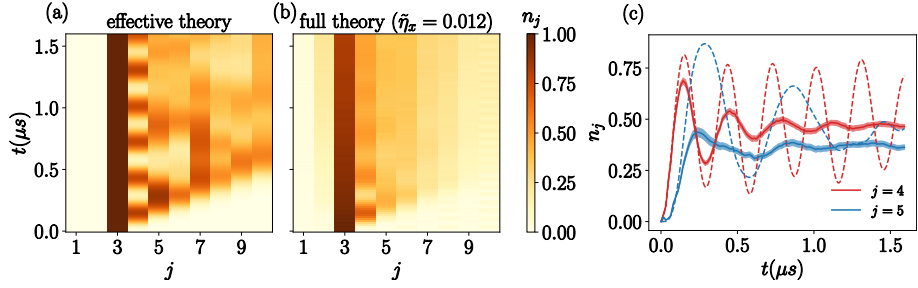


FIGURE 6.3. Dynamics in the ‘quantum East model’ regime ($\Omega_1/\Omega_2 = 1$) of an initial seeded excitations. We compare the dynamics obtained in the ideal regime, where the effective theory (cf. Eq. (6.10)) is exact, with a realistic experimental scenario (cf. Eq. (6.2)) including positional disorder η due to thermal fluctuations. The system displays both a propagating front of excitations towards the East as well as oscillations in the bulk (a,b). In (c) we show some vertical cuts of the heatmaps (a,b) for clarity, comparing the effective theory (dashed line) with the full theory (continuous line) upon averaging 100 disorder realizations. The shaded areas around the continuous lines are the statistical errors due to the finite number of sampled trajectories. Parameters: $\Omega_{1,2}/V_1 = 0.2$, $V_2/V_1 = 2$, $\epsilon = 0$, $V_1 = 2\pi \times 15$ MHz. Image taken from Ref. [3].

6.4.3. Localization in the full theory

As extensively discussed, the quantum East model has been shown to display a dynamical transition separating a fast and slow thermalizing phase [140, 151] due to the competing kinetic term $\propto \Omega$ and on-site energy $\propto \epsilon$. Intuitively, if the kinetic term dominates ($\Omega_{1,2}/(2\epsilon) \gtrsim 1$) strings of excitations expand and merge ballistically, fastly washing local information of the initial configuration, while if it is subleading ($\Omega_{1,2}/(2\epsilon) \lesssim 1$), excitations can expand slowly, making possible to retrieve information about the initial conditions. Upon introducing thermal disorder $\tilde{\eta}_\alpha$, the picture is slightly affected. Indeed, $\tilde{\eta}_\alpha$ can already induce undesired mismatches from the perfect resonant *directional* antiblockade condition. Thus, we expect the dynamics to be dictated by the competition of Ω and the joint contribution of $\tilde{\eta}_\alpha$ and ϵ . We test this by initializing a representative high-temperature product state characterized by regions with low and high densities of excitations. In the slow phase, heterogeneity in the initial state plays a crucial role in dictating the dynamics up to very long times, in contrast with typical fast thermalizing systems where all local information is quickly lost except for global conserved quantities. We chose as a proxy for distinguishing the different dynamical phases the autocorrelation function [138, 151]

$$C(t) = \frac{2}{Z} \sum_i \langle \hat{n}_i(t) \hat{n}_i(0) \rangle - 1, \quad (6.11)$$

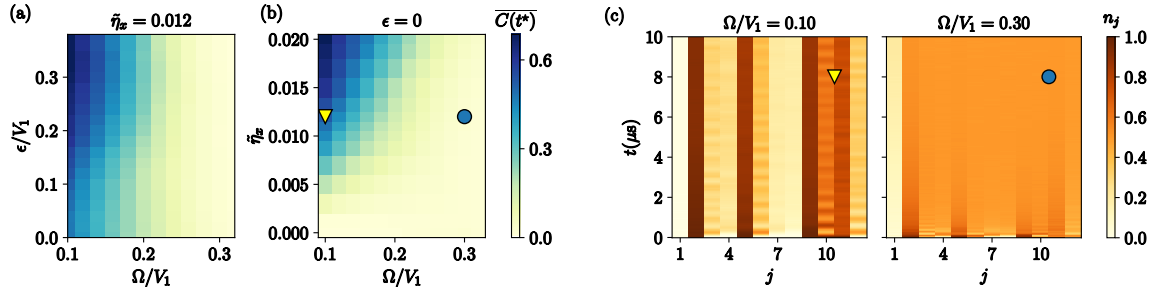


FIGURE 6.4. Dynamics in the quantum East model of Refs. [140, 151] ($\Omega_{1,2} = \Omega$) in the full theory (cf. Eq. (6.2)) initializing the state $|01010001110\rangle$. (a-b): Time-averaged autocorrelation function $\overline{C(t^*)}$ at time $t^* = 10\mu\text{s}$ keeping fixed either thermal disorder $\tilde{\eta}_x$ or detuning ϵ , respectively. For small Ω the memory of the initial state is kept up to long times ($\overline{C(t^*)} > 0$), while instead for large Ω the memory of the initial state is rapidly washed out ($\overline{C(t^*)} \approx 0$). (c): Dynamics of the density profile in the two phases (marked via symbols in (b)) at fixed thermal disorder $\tilde{\eta}_x = 0.012$ in units of the average spacing $r_1 = 6.2\mu\text{m}$ (see text). Image taken from Ref. [3].

where $Z = \sum_i \langle \hat{n}_i(0) \rangle$ is a normalization constant. For the initial product state considered, $C(t)$ is the density of the initially occupied sites at time t , to which we subtract an evenly distributed ‘background’ corresponding to an infinite temperature state, $\langle n_i \rangle = 1/2$. Thus, $C(t)$ serves as a good proxy for the memory of initial conditions, as its initial value is $C(t = 0) = 1$ and tends to zero when the system thermalizes. In Fig. 6.4(a-b) we show the time-average $\overline{C(t^*)} = \int_0^{t^*} C(\tau) d\tau / t^*$ up to experimentally accessible time windows using the full theory (cf. Eq. (6.2)) in two scenarios: either keeping fixed the thermal disorder and varying ϵ , or vice versa. As anticipated, both ϵ and $\tilde{\eta}_x$ contribute to slowing down dynamics. Indeed, in both dynamical phase diagrams, we can distinguish a phase where the system retains memory of the initial state and a phase where the system quickly thermalizes and all local memory is quickly erased.

6.5. TUNING THE DEGREE OF CHIRALITY AND THE CLASSICAL REGIME

In this Chapter, we have proposed a scheme for realizing chiral interactions in Rydberg arrays by means of a *directional* antiblockade condition, namely an atom can change its internal state only if the atom to its right (or left) is excited. Our scheme is based on ‘energetic’ arguments and gives rise to constrained interactions. While we have focused on the strictly unidirectional regime in the previous sections, we highlight that the degree of chirality in the interactions can be tuned by relaxing the condition $\Delta V \equiv$

$|V_1 - V_2| \gg \Omega$. Specifically, for $0 < \Delta V/\Omega \lesssim 1$, dynamics still has a preferable direction, but there are near-resonant processes towards the other as well (similarly to other Rydberg proposals [238, 239]). This offers a path for accessing regimes with a tunable *bias* towards one direction or the other. As an extreme example, in the zero *bias* case ($\Delta V = 0$), and by setting $\Omega_1 = \Omega_2/2$, we can effectively simulate the quantum Fredrickson-Andersen model [139, 240] with Hamiltonian

$$\hat{H} = \Omega_1 \sum_j (\hat{\sigma}_j^x \hat{n}_{j+1} + \hat{n}_j \hat{\sigma}_{j+1}^x) + \epsilon \sum_j \hat{n}_j. \quad (6.12)$$

6.5.1. Classical rate equations

Our protocol could be readily extended in the presence of dominant classical noise. In such regime, dynamics is effectively described by rate equations, with rates dependent on the detunings, interactions, and atomic configuration [179, 181], opening up to the simulation of dissipative uni-directional spin dynamics. Let us restrict for simplicity to the single drive field regime setting $\Omega_2 = 0$. We keep the detuning Δ_j of the drive field frequency from the bare atomic transition as a free parameter for generality. In the rotating frame with respect to the drive fields, the starting Hamiltonian is given by

$$\hat{H} = \sum_{j=1}^N \Delta_j \hat{n}_j + \frac{\Omega}{2} \sum_{j=1}^N \hat{\sigma}_j^x + \frac{1}{2} \sum_{i,j} V_{i,j} \hat{n}_i \hat{n}_j. \quad (6.13)$$

Due to the presence of dephasing, the full dynamics of the state $\hat{\rho}$ is given by the Lindblad master equation

$$\partial_t \hat{\rho} = -i[\hat{H}, \hat{\rho}] + \gamma \sum_j \left(\hat{n}_j \hat{\rho} \hat{n}_j - \frac{1}{2} \{ \hat{n}_j, \hat{\rho} \} \right) \quad (6.14)$$

In the previous sections, we have worked in the regime $\gamma \ll \Omega$. Now, we work in the opposite regime $\gamma \gg \Omega$. In this regime, we can distinguish fast and slow processes: the fast processes are controlled by the interacting part of the Hamiltonian and the dissipative process; the slow processes are controlled by the external drive fields. Projecting out the fast dynamics (see Ref. [179] for the derivation), the dynamics of the projected state $\hat{\mu}$ is governed by

$$\partial_t \hat{\mu} = \frac{4\Omega^2}{\gamma} \sum_j \Gamma_j (\hat{\sigma}_j^x \hat{\mu} \hat{\sigma}_j^x - \hat{\mu}), \quad (6.15)$$

with rates dependent on the parameters of the Hamiltonian, dissipation, and atomic configuration

$$\Gamma_j^{-1} = 1 + 4 \left(\frac{\Delta_j + \sum_{m \neq j} V_{j,m} \hat{n}_m}{\gamma} \right)^2. \quad (6.16)$$

Let us focus on a specific site j and fix the staggered configuration in the potentials discussed in the main text. Keeping up to nearest-neighbour terms, the rate in Eq. (6.16) turns into

$$\Gamma_j^{-1} = 1 + 4 \left(\frac{\Delta_j + V_1 \hat{n}_{j-1} + V_2 \hat{n}_{j+1}}{\gamma} \right)^2, \quad (6.17)$$

where we have assumed $V_{j-1,j} = V_1$ and $V_{j,j+1} = V_2$, without losing generality. As evident, the rate Γ_j depends on the atomic configuration and Δ_j . We aim to show that the rates are not symmetric under the exchange of the pair of excitations $(j-1) \leftrightarrow (j+1)$. To do so, in Fig. 6.5(a) we show the rate as a function of Δ_j for $V_2 = 2 \times V_1$ in the non-symmetric scenarios, namely $n_{j-1} = 1$, $n_{j+1} = 0$ and viceversa. It is evident that at fixed parameters, the rates are generally not symmetric as desired for $V_1 \neq V_2$ (except for a fine-tuned value of Δ_j at which the curves cross). As in the coherent case, the degree of directionality can be tuned via $|V_1 - V_2|$ and Δ (cf. Fig. 6.5(b)).

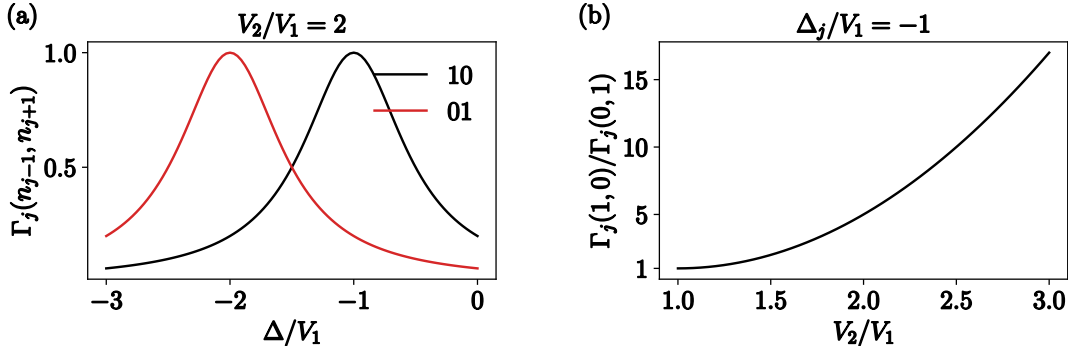


FIGURE 6.5. (a) Rate Γ_j (cf. Eq. (6.17)) at fixed $V_2/V_1 = 2$ and atomic configurations (values of n_{j-1} and n_{j+1}). As evident, the rate is not symmetric under the exchange of neighboring atoms (the two curves do not overlap). (b) Ratio of the rates Γ_j in the two scenario $n_{j-1} = 1$, $n_{j+1} = 0$ and viceversa at fixed $\Delta_j = -V_1$. In the symmetric case ($V_1 = V_2$) no notion of directionality appears ($\Gamma_j(1,0)/\Gamma_j(0,1) = 1$). Instead, for $V_1 \neq V_2$, rates display ‘chiral’ features ($\Gamma_j(1,0)/\Gamma_j(0,1) \neq 1$). The ‘chirality’ can be readily tuned by simply changing the ratio V_1/V_2 , or the detuning Δ_j . In all the calculations we have set $\gamma/V_1 = 1$. Image taken from Ref. [3].

CHAPTER 7

Non-ergodic quantum dynamics in superconducting circuits

Most of the content in this Chapter is in:

- “*Kinetically Constrained Quantum Dynamics in Superconducting Circuits*” (PRX Quantum 3, 020346 (2022))
Riccardo J. Valencia-Tortora, Nicola Pancotti, Jamir Marino.

Executive Summary. In this Chapter we discuss an analog quantum simulator of the the bosonic quantum East model discussed in Chapter 3 based on superconducting circuits. Specifically, we will show how to realize the following Hamiltonian

$$H = -\frac{1}{2} \sum_{j=0}^L \hat{n}_j \left[e^{-s} \left(\hat{a}_{j+1} + \hat{a}_{j+1}^\dagger \right) - \epsilon \hat{n}_j - U \hat{n}_{j+1} - 1 \right], \quad (7.1)$$

Our proposal is based on considering a chain of superconducting circuits coupled via simple hopping which can transfer excitations from one superconducting circuit to the neighboring one, which could be realized either via a direct capacitive coupling or via a common resonator, subjected to a suitable set of drive fields. We will show that, in the limit of weak coupling and low anharmonicity, we find an effective description of such superconducting qubits array in terms of the bosonic quantum East chain.

What is new? All results of this chapter represent novel research results.

Organization of the Chapter

- In Sec. 7.1 we briefly motivate why we choose a superconducting based platform for our implementation.
- In Sec. 7.2 we provide the details about the superconducting circuits based setup on which we can analogically implement the bosonic quantum East model (cf. Eq. (7.1)).

This Chapter is composed by a rearrangement of the author’s publication [1].

7.1. WHY SUPERCONDUCTING CIRCUITS?

In recent years, unprecedented quantum control of interacting superconducting qubits with microwave photons has been reached in circuit-QED platforms [164, 241–248]. These circuits allow quantum-information-processing tasks and the quantum simulation of paradigmatic light-matter interfaces. Superconducting Josephson junctions allows us to introduce nonlinearity in quantum electrical circuits, which is a key factor in protecting quantum resources, by making these platforms resilient to noise and errors. This is a key factor of merit for any superconducting qubit, ranging from the established transmon to, for instance, the more recently developed superconducting nonlinear asymmetric inductive element (SNAIL) [249, 250]. Here, we consider a chain of superconducting circuits (see Refs. [249, 251–258]), which can be described as anharmonic oscillators, coupled via a hopping term (cf. Fig. 7.1). In the limit of weak coupling and low anharmonicity, we find an effective description of such superconducting qubits array in terms of the bosonic quantum East chain.

7.2. REALIZATION OF THE BOSONIC QUANTUM EAST MODEL IN SUPERCONDUCTING CIRCUITS

Here, we propose an experimental implementation of the Hamiltonian in Eq. (3.1), namely

$$H = -\frac{1}{2} \sum_{j=0}^L \hat{n}_j \left[e^{-s} \left(\hat{a}_{j+1} + \hat{a}_{j+1}^\dagger \right) - \epsilon \hat{n}_j - U \hat{n}_{j+1} - 1 \right], \quad (7.2)$$

in terms of a simple superconducting-circuit setup. To this aim, we consider a chain of driven superconducting circuits.

A superconducting circuit is basically a quantized LC oscillator with capacitance C and nonlinear inductance L [164]. This nonlinear dependence can be achieved via a Josephson junction working in the superconducting regime without introducing undesired dissipative effects [164, 259, 260]. In particular, we consider here the SNAIL introduced in Ref. [250] as our building block. We consider specifically the SNAIL parameters in Ref. [261], where kinetically constrained terms (at just two sites) are obtained using the second-order nonlinearity $\propto (\hat{a}^\dagger \hat{a}^\dagger a + h.c.)$ of the SNAILs. Differently from Ref. [261], we do not use the second-order nonlinearity of SNAILs. Indeed, any superconducting circuit that can be approximated as an anharmonic oscillator with positive anharmonicity could be a suitable candidate for our setup (e.g., the C-shunt flux qubit [262]).

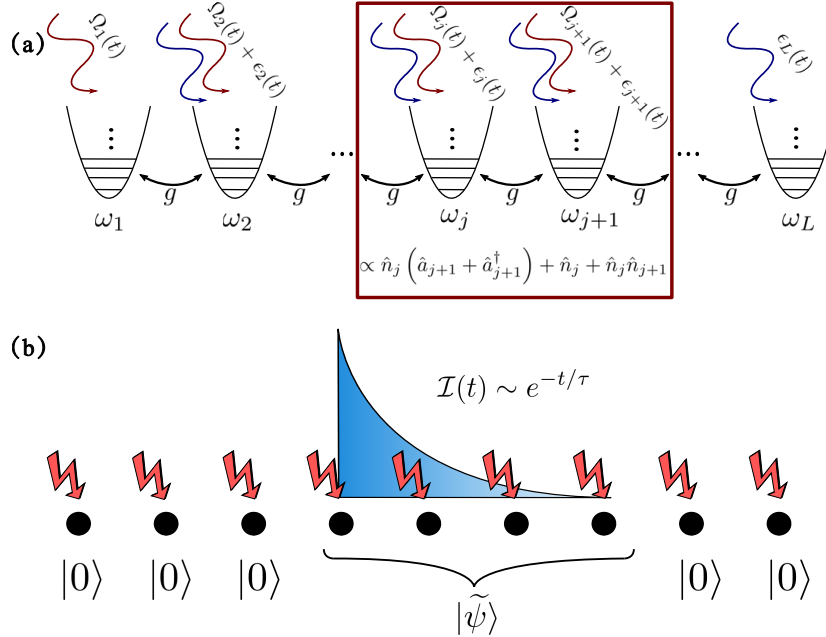


FIGURE 7.1. (a): A chain of driven superconducting qubits coupled via exchange interaction g . In the red box we write the low-energy effective interaction between the j -th and $(j+1)$ -th superconducting qubits. (b): A sketch of a localized state subject to external noise (arrows). The visibility of the initial peak with respect to the rest of the system (measured by the imbalance $\mathcal{I}(t)$) decays exponentially with a time τ much larger than the characteristic operational timescales of state-of-the-art superconducting circuits. Image taken from Ref. [1].

We consider an array of L driven superconducting circuits (SC) coupled via an exchange interaction as our starting point (see Fig. 7.1(a) for a scheme). In typical setups, the SC is used in regimes where it can be well approximated by a two-level system. This can be done as a result of the non-linearity, which makes its energy levels not evenly spaced in energy. As a result, it is possible to selectively make some levels participate more in the dynamics with respect to others, which in turn makes truncating the unbounded spectrum with a bounded one a not-so-rough approximation. However, in our proposal, we retain all the energy levels of each SC circuit. The Hamiltonian can be decomposed

as a sum of three terms, $H = H_0 + H_{\text{drive}} + V$, where

$$\begin{aligned} H_0 &= \sum_{j=1}^L \omega_j \hat{a}_j^\dagger \hat{a}_j + \frac{E_C}{2} \hat{a}_j^\dagger \hat{a}_j^\dagger \hat{a}_j \hat{a}_j, \\ H_{\text{drive}} &= \sum_{j=1}^{L-1} e^{-i\alpha_j t} \left(\Omega_j \hat{a}_j^\dagger + \epsilon_{j+1} \hat{a}_{j+1}^\dagger \right) + h.c., \\ V &= \sum_{j=1}^{L-1} g \left(\hat{a}_j \hat{a}_{j+1}^\dagger + h.c. \right), \end{aligned} \quad (7.3)$$

where \hat{a}_j^\dagger (\hat{a}_j) creates (destroys) an excitation in the j -th SC qubit; H_0 is the bare Hamiltonian of the SC qubits with qubit frequencies $\{\omega_j\}_{j=1}^L$, and anharmonicity $E_C > 0$ [164]; H_{drive} describes the action of classical drive fields on the bare SC qubits; and V describes hopping processes that can be engineered by a common bus resonator [263] or a direct capacitance [264]. An illustration of the scheme of Eq. (7.3) is given in Fig. 7.1(a). We work in the weak-coupling regime $g \ll |\omega_j - \omega_{j+1}|$ and in the low-anharmonicity limit $E_C \ll |\omega_j - \omega_{j+1}|$ for all j . The former condition is necessary in order to have far-detuned processes connected by V , and therefore to treat V in perturbation theory [265]. The low-anharmonicity limit is necessary to retrieve a bosonic model in the effective perturbative Hamiltonian achieved after treating V with a Schrieffer-Wolf transformation in the small g limit. Each SC qubit $j \in [1, L-1]$ is driven by a classical drive field of amplitude Ω_j and frequency α_j . These classical drive fields give rise to the desired interaction together with undesired single-site fields in the low-energy effective Hamiltonian [266]. In order to get rid of them, we add another drive field on each SC qubit $j \in [2, L]$ of amplitude ϵ_j and frequency α_{j-1} [267, 268].

Once again, we highlight that we are interested in exploiting the multilevel (bosonic) structure of SC qubits. Thus, we do not reduce each component of the system to a qubit. We introduce the ladder operators

$$\hat{a}_j = \sum_{\ell=0}^{\infty} \sqrt{\ell+1} |\ell, j\rangle \langle \ell+1, j| \equiv \sum_{\ell=0}^{\infty} \hat{c}_{\ell,j}, \quad (7.4)$$

where $\hat{c}_{\ell,j}$ is the ladder operator which destroys an excitation in the $(\ell+1)$ -th level and creates an excitation in the ℓ -th level on the j -th SC qubit. Analogously, we can define its Hermitian conjugate, $\hat{c}_{\ell,j}^\dagger$.

We work in the so-called dispersive regime, $g \ll \Delta_{j,j+1}$, where $\Delta_{i,j} = \omega_i - \omega_j$. In such regime, physical first-order processes resulting in the exchange of excitations between the SC are negligible, and the effect of it could be well captured by second order hopping-mediated virtual processes. Formally, such second order perturbation

theory can be carried out via a Schrieffer-Wolf transformation. In our case, we perturbatively diagonalize the Hamiltonian $H_0 + V$ to second order in g via a Schrieffer-Wolf transformation S [269]. The drive field terms in H_{drive} are modified by the same SW transformation. From now on, we neglect terms of order $\mathcal{O}(g^2\Omega_j/\Delta_{j,j+1}^2)$ and higher. We move to the frame that rotates at the frequencies of the drives and we neglect the fast oscillating terms by employing the rotating-wave approximation (RWA). Before detailing the calculations, we discuss the physics of each term in the Hamiltonian defined in Eq. (7.3). The bare Hamiltonian H_0 provides the necessary anharmonicity that we desire. The perturbation V gives rise to the nearest-neighbor interaction, a renormalization of the bare energies of the SC qubits, and some additional two-excitation processes. The drive field yields the constrained terms $\hat{n}_j(\hat{a}_{j\pm 1} + \hat{a}_{j\pm 1}^\dagger)$ toward “East” and “West”. The time dependence of the drive fields in the laboratory frame enables us to get rid of the undesired processes, such as the two-excitation processes and the “West” terms, passing in the rotating frame of the drive fields and employing the RWA.

To find the explicit form of the SW transformation, we follow the prescription in Ref. [270]. First, we compute $\eta = [H_0, V]$; we consider η with arbitrary coefficients as an *ansatz* for S . Finally, we fix these coefficients, imposing the condition $[S, H_0] = -V$. We obtain (cf. Appendix C.1)

$$S = \sum_{j=1}^{L-1} \sum_{\ell,s=0}^{\infty} \frac{g}{\tilde{\Delta}_{\ell,j+1} - \tilde{\Delta}_{s,j}} \left(\hat{c}_{s,j} \hat{c}_{\ell,j+1}^\dagger - \hat{c}_{s,j}^\dagger \hat{c}_{\ell,j+1} \right), \quad (7.5)$$

where $\tilde{\Delta}_{\ell,j} = (\omega_j + E_C \ell)$, the first summation is along the system, while the second summation is along all the levels of the SC qubits. Using the Baker-Campbell-Hausdorff expansion, the Hamiltonian in Eq. (3.1) after the SW transformation reads

$$\begin{aligned} \tilde{H} &\equiv e^S H e^{-S} \\ &\approx H_0 + H_{\text{drive}} + [S, H_{\text{drive}}] + \frac{1}{2}[S, V] + \mathcal{O}\left(\frac{g^2\Omega}{\Delta^2}\right). \end{aligned} \quad (7.6)$$

After lengthy yet standard calculations, we obtain \tilde{H} explicitly dependent on the ladder operators $\hat{c}_{\ell,j}^{(\dagger)}$ introduced in Eq. (7.4) and with coefficients dependent on the site and internal levels (see Appendix C.2). Our aim is to write \tilde{H} as a function of the bosonic operators $\hat{a}_j^{(\dagger)}$. We need to find a regime in which the coefficients in \tilde{H} are approximately independent of the specific level, so that we can use Eq. (7.4). These coefficients are similar to the one appearing in Eq. (7.5). In order to make them level independent, we need

$$\tilde{\Delta}_{\ell,j+1} - \tilde{\Delta}_{s,j} \approx \omega_{j+1} - \omega_j \equiv \Delta_{j+1,j}, \quad (7.7)$$

which holds if $|\ell - s| \ll |\Delta_{j+1,j}|/E_C$. Since the SC qubit can have an infinite number of excitations, we have $(\ell - s) \in (-\infty, +\infty)$. This means that Eq. (7.7) cannot be

satisfied for all possible ℓ and s if $E_C \neq 0$. Nonetheless, it can be achieved up to a certain value N of ℓ and s , such that $N \ll |\Delta_{j+1,j}/E_C|$. Therefore, the coefficients in \tilde{H} satisfy Eq. (7.7) up to the N -th energy level, leading to a bosonic Hamiltonian that approximates the action of the full Hamiltonian to states with an occupation that is small with respect to N (cf. Appendix C.3). The bosonic \tilde{H} still displays undesired processes, such as hopping and local fields. We move to a rotating frame of reference via the unitary transformation

$$U = \exp \left(it \sum_{j=1}^{L-1} \alpha_j \hat{n}_{j+1} \right) \quad (7.8)$$

and we neglect all the oscillating terms by employing the RWA (cf. Appendix C.4). In doing so, we get rid of almost all the undesired processes except for some local fields at the sites $j \geq 2$. These fields can be eliminated via the additional drive fields of amplitudes $\{\epsilon_j\}$, analogously to what has been done in similar scenarios (see, e.g., Refs. [267, 268]). We tune their amplitudes such that they cancel the undesired local terms. We obtain the matching condition $\epsilon_j = g\Omega_{j-1}/\Delta_{j-1,j}$, with $j \geq 2$. This leads to the effective Hamiltonian

$$\tilde{H} = \sum_{j=1}^L \tilde{\omega}_j \hat{n}_j + \frac{E_C}{2} \hat{n}_j \hat{n}_j + \frac{2g^2 E_C}{\Delta_{j,j+1}^2} \hat{n}_j \hat{n}_{j+1} + \frac{g\Omega_j E_C}{\Delta_{j,j+1}^2} \hat{n}_j (\hat{a}_{j+1}^\dagger + \hat{a}_{j+1}) \quad (7.9)$$

where $\tilde{\omega}_1 = \omega_1 - E_C/2 + \mathcal{O}(g^2/\Delta_{12})$ and $\tilde{\omega}_{j \neq 1} = \omega_j - E_C/2 - \alpha_{j-1} + \mathcal{O}(g^2/\Delta_{j,j+1})$.

We now evaluate the couplings in Eq. (7.9), considering the SAIL as our SC qubit and using the parameters of Ref. [261]. We work in the parameter regime in which the SAILS Hamiltonian is given by H_0 in Eq. (7.3). We fix $E_C \approx 150\text{MHz}$, $g = 75\text{MHz}$ and $\omega_j \approx 3\text{GHz}$. We consider the classical drive fields with amplitude $\Omega_j = -100\text{MHz}$ (the amplitude has to be negative to have the correct sign for the constrained hopping), which can be achieved by adding a π phase to the external drive fields. Any real system is inevitably coupled to the environment and SC circuits are no exception. In the context of SC circuits, two different time scales are defined, namely T_1 and T_2 [164]. The time scale T_1 is the typical time at which the coupling with the environment leads excited states to decay to lower-energy states. The time scale T_2 quantifies the coherence time of the system. For consistency with the chosen parameters (taken from Ref. [261]), we also consider, as T_1 and T_2 , the values from Ref. [261], which are $T_{1,2} \approx 1\mu\text{s}$. We fix the qubit frequencies ω_j and the drive field frequencies α_j in order to satisfy: (i) the dispersive regime, valid for $g/\Delta_{j,j+1} \ll 1$; (ii) the low-anharmonicity limit, $E_C \ll \Delta_{j,j+1}$; (iii) the validity of the RWA, namely $|\alpha_j| \gg \Omega_j$, $|\alpha_{j+1} - \alpha_j| \gg \Omega_j$ and $|\alpha_{j+2} - \alpha_j| > g\Omega_{j+2}/\Delta_{j+1,j+2}$; (iv) $\tilde{\omega}_j \approx \omega_j - \alpha_{j-1} > 0$ for $j > 1$, necessary in order to have localization; (v) $1/T_{1,2}$ small with respect to the typical energies in the effective

	$j = 1$	$j = 2$	$j = 3$	$j = 4$	$j = 5$
$\alpha_j(\text{GHz})$	0.75	1.6	0.65	1.7	0.75
$\omega_j(\text{GHz})$	3	3.75	4.5	3.75	4.5

TABLE 7.1. A possible configuration for the external classical drive field frequencies $\{\alpha_j\}$ and bare frequency $\{\omega_j\}$ of SNAILs for the experimental implementation of the bosonic quantum East model in a system of size $L = 5$. For bigger system sizes, it is enough to periodically repeat the configuration from site $j = 2$ to $j = 5$. The other parameters are as follows: anharmonicity $E_C = 150\text{MHz}$, bare capacitive coupling $g = 75\text{MHz}$, and classical drive field amplitude $\Omega = -100\text{MHz}$. Table taken from Ref. [1].

Hamiltonian in Eq. (7.9); and (vi) the system is in the localized phase.

The more stringent conditions are given by (ii) and (v). A good trade-off between (ii) and (v) is obtained at $|\Delta_{j,j+1}| \equiv \Delta \approx 5E_C \approx 750\text{MHz}$, for which the typical time scale of the kinetically constrained term is approximately $T_{1,2}/2$. We have $g/\Delta_{j,j+1} \approx 0.1$, meaning that (i) is reasonably satisfied. Condition (iii) is satisfied by a staggered configuration of the drive field frequencies with an additional inhomogeneity between next-neighbor drive field frequencies, for instance: $\alpha_j = \alpha_{j-1} + (-1)^j(\delta + (j-1)\zeta)$ for $j \in [2, 4]$ and boundary condition $\alpha_1 \gg \Omega$ (for larger systems, it is enough to periodically repeat the configuration of the frequencies), with $\delta \gg \Omega$, $\alpha_1 \gg \Omega$, and $\zeta \gg g\Omega/\Delta \approx 10\text{MHz}$. Condition (iv) is satisfied by a staggered configuration of the qubit frequencies as well: $\omega_{j+1} = \omega_j + (-1)^j\Delta$ for $j \geq 2$, $\omega_2 = \omega_1 + \Delta$, with boundary condition $\omega_1 > \alpha_1$. For instance, we can consider $\alpha_1 = 750\text{MHz}$, $\delta = 750\text{MHz}$, $\zeta = 100\text{MHz}$, and $\omega_1 = 3\text{GHz}$. These conditions lead to Eq. (7.9) being almost translationally invariant (except for inhomogeneities in the frequencies $\tilde{\omega}_j$ of the order of approximately 5%, which can be eliminated via a more fine-tuned choice of $\{\omega_j\}$). Moreover, condition (vi) is satisfied for this set of parameters. In Table 7.1, we summarize a possible set of parameters available in state-of-the-art superconducting circuits for implementing the bosonic quantum East model.

Part III

A different route for non-ergodicity: from short range to all-to-all interactions

In the previous parts we have discussed different mechanisms that could impede the onset of thermalization in translational invariant systems (cf. Part I), together with proposals where models hosting such phenomena could be realized (cf. Part. II). Here, we conclude our journey in delving into non-ergodic phenomena by taking a different route. While so far we have focused on short-range interacting systems, it is currently possible to engineer highly non-local interactions up to the regime where each constituent interacts with any other one with the same magnitude (all-to-all interactions). Such regime can be realized in cavity-QED platforms, in which a cold gas couples to few or several electromagnetic modes in an optical cavity [61–66] (see Fig. 7.2). In such setups, the cavity is not empty but hosts photonic modes (whose features depend on the cavity itself), which can interact in a democratic manner with the atoms placed inside the cavity. A typically realized photon-mediated process is the creation (or annihilation) of a photon as a result of the de-excitation (or excitation) of an atom. Specifically, assuming that only two atomic levels mostly participate in the dynamics, so that we can approximate the (potentially complex) atom with a simple two-level system described by a pseudo spin-1/2 $\hat{\sigma}$, the process just described is governed by the Hamiltonian [271]

$$H_{\text{light-matter}} = g(\hat{\sigma}^+ \hat{a} + \hat{a}^\dagger \hat{\sigma}^-), \quad (7.10)$$

which is known as Jaynes-Cummings coupling. Upon considering a collection of L atoms, if they are located far enough apart so that interference effects [272] and atom-atom interactions can be neglected, the system is governed by the Hamiltonian

$$H_{\text{light-matter}} = g \sum_{j=1}^L (\hat{\sigma}_j^+ \hat{a} + \hat{a}^\dagger \hat{\sigma}_j^-), \quad (7.11)$$

which, apparently, describes a set of independent spins. However, this is not the case as the atoms absorb/emit the same kind of photons. As a consequence, the atoms are effectively interacting. Such influence can be made explicit by assuming that the photon is the fastest degree of freedom, a regime that can be experimentally achieved, so that it is a good approximation to adiabatically eliminate it [273–277]. Specifically, in the regime where the photon dynamics (controlled, for instance, by its frequency) is faster than the photon-matter dynamics, controlled by g , the photon mediates an exchange of excitations between the atoms via a second order virtual process (emission/absorption

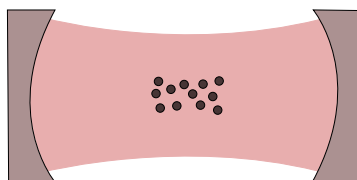


FIGURE 7.2. Cartoon of a typical cavity-QED setups in which N atoms (black dots) interact via a common cavity field (red area).

or viceversa). Since all the atoms within the cavity are involved, after performing such a procedure, we obtain an all-to-all spin-exchange Hamiltonian

$$H \sim \sum_{i,j=1}^L \hat{\sigma}_i^+ \hat{\sigma}_j^-, \quad (7.12)$$

which is completely non-local and insensitive to the dimensionality of the system. In such scenario, it is evident that the system tends to behave collectively since the Hamiltonian can be exactly written as a function of the collective operators $\hat{S}^+ = \sum_{j=1}^L \hat{\sigma}_j^+$ and $\hat{S}^- = (\hat{S}^+)^{\dagger}$ as

$$H \sim \hat{S}^+ \hat{S}^-. \quad (7.13)$$

As dynamics occur at the level of macroscopic and classical objects, quantum effects are suppressed with their size ($\sim L$). The fact that the large spins are classical objects in the large L limit can be rationalized upon observing that the commutator $[\hat{S}^+, \hat{S}^-] = 2\hat{S}^z$ is subleading when the spin is large. To see this explicitly, let us trade large objects (which scales with L) with $O(1)$ objects by defining $\hat{S}^+ = L\hat{s}^+$. Plugging this in the commutator, we observe $[\hat{s}^+, \hat{s}^-] \sim 1/L \rightarrow 0$ for $L \rightarrow \infty$, proving our statement. As dynamics preserve the collective nature of the system, the system will tend to behave classically up to times parametrically large in L , after which quantum effects can no longer be neglected [67–71]. Since quantum effects are suppressed as $1/L$ in the initial transient regime, quantum thermalization is by definition not possible, as the system is incapable of building substantial entanglement. In other words, the system naturally displays a pre-thermal regime which can be extended in time upon increasing the system size L . However, it looks like this pre-thermal regime cannot display features different from the ones accessible classically. This is in contrast with the ergodicity-breaking mechanisms discussed in Part I, where also the non-ergodic phase was characterized by quantum effects. Our contribution challenges such common belief. Specifically, in Chapter 8 we will show that quantum effects could dictate the dynamical response also at the level of collective objects upon trading two-level systems with multi-level ones, whose investigation has gathered increasing attention in the last years [278–291]. In particular, we will show how quantum correlations allow us to *craft* the collective dynamical response of the system.

CHAPTER 8

Crafting the dynamical structure of synchronization by harnessing bosonic multilevel cavity QED

Most of the content in this Chapter is in:

- “*Crafting the dynamical structure of synchronization by harnessing bosonic multilevel cavity QED*” (Phys. Rev. Research 5, 023112 (2023), Editors’ Suggestion)

Riccardo J. Valencia-Tortora, Shane P. Kelly, Tobias Donner, Giovanna Morigi, Rosario Fazio, Jamir Marino.

Executive Summary. In this Chapter we discuss the features of the collective dynamical response in a cavity-QED with multi-level bosonic atoms inside. We show how, upon going beyond the paradigmatic two-level approximation and entering into the N -level case, with the matter described by $SU(N)$ spins, it is possible to influence and control the collective dynamical response via microscopic quantum effects.

What is new? All results of this chapter represent novel research results.

Organization of the Chapter

- In Sec. 8.1 we provide a brief overview of cavity-QED, with the aim to provide the context to better frame our contribution.
- In Sec. 8.2 we illustrate the model which we will investigate.
- In Sec. 8.3, we provide a compelling discussion on the regimes we consider and the approximations we perform.
- In Sec. 8.4 we discuss the different dynamical responses the system could display, together with a hypothesis concerning all-to-all interacting models. Such hypothesis, which we term *dynamical reduction hypothesis*, briefly states that an all-to-all interacting system tends to behave collectively even in the presence of single-body term which explicitly breaks the collective nature of the system. We will show how this hypothesis will prove useful in predicting the dynamical responses the system can display.
- In Sec. 8.5 we show the predictive power of our hypothesis in the case where the Hamiltonian is permutational invariant, namely it is invariant under the

exchange of any pairs of atoms. In such context, we will also show how the dynamical response can change upon introducing quantum fluctuations when considering $SU(N)$ spins with $N > 2$. Such a finding is in contrast to the typically investigated $SU(2)$ spin case, where quantum fluctuations are not expected to play a role.

- In Sec. 8.6 we show how our hypothesis holds also in the presence of terms that explicitly break the permutational invariance. Specifically, we will show how an optimized effective single-body Hamiltonian is able to quantitatively reproduce the dynamics of a many-body system.
- In Sec. 8.7 we present a possible experimental cavity-QED platform where the model we investigate could be realized.
- In Sec. 8.8 we conclude by discussing possible extensions of our work.

This Chapter is composed by a rearrangement of the author's publication [4].

8.1. INTRODUCTION

Tailoring light-matter interactions is at the root of numerous technological or experimental applications in quantum optics, and it has generated a persistent drive for better control of atoms and photons since the advent of modern molecular and atomic physics. For instance, the pursuit to create precision clocks and sensors has lead to the development of cavity QED systems in which a cold gas couples to few or several electromagnetic modes in an optical cavity [61–66]. Such systems can be brought out of equilibrium to generate reproducible many-body dynamics which show complex behavior including self-organization [64, 292–300] and dynamical phase transitions [61, 66, 297, 301–305], quantum squeezed and non-Gaussian entangled states [306–312], time crystals [313–316], and glassy dynamics [294, 298, 317, 318]. This rich phenomenology comes from a high degree of tunability in such systems, allowing control over local external fields, detunings between cavity mode and applied drive fields, the ability to couple multiple atomic levels to the cavity field [65, 283, 286, 294, 319–322], and more recently the realization of programmable geometries for light-matter interactions [323–325].

Recently, the theoretical and experimental investigation of multilevel cavity systems has gathered increasing attention. Current progress includes dissipative state preparation of entangled dark states [278–280], multicriticality in generalized Dicke-type models [281, 282], incommensurate time crystalline phases [283–285], correlated pair creations and phase-coherence protection via spin-exchange interactions [286–288], spin

squeezing and atomic clock precision enhancement [289–291]. Yet, the quenched dynamics in multilevel cavity systems is widely unexplored and the few individual results lack an organizing principle.

Here, we propose a unifying framework for the dynamics after a quench of all-to-all connected multilevel systems. We show that the flexible control endowed by bosonic multilevel atoms is sufficient to reproduce established dynamical phases and beyond. We explain how the dynamical response can be crafted into these new and existing dynamical phases by introducing a reduction of dynamics to a few-body effective classical evolution, valid regardless of the underlying integrability of the model. Of particular note, we demonstrate how quantum correlations in the initial state can drive a transition between a regular and chaotic synchronized phases.

Our analysis extends the established phenomenology of the two-level Tavis-Cummings model with local inhomogeneous fields. This two-level model is integrable [68], and allows for the emergent collective many-body dynamics to be exactly described through an effective few-body Hamiltonian [326–336]. In particular, the few body model yields predictions for the dynamical responses of collective observables $S(t)$, such as the collective spin raising operator, given by the macroscopic sum of several individual constituents [326, 329, 330, 333–337]. The resulting dynamical phases are best presented in terms of the possible synchronization between the local atomic degree of freedoms (spins-1/2) which evolve with a frequency set by the competition of their local field and collective photon-mediated interactions. In the desynchronized phase, which we call Phase-I as shorthand, all the spins evolve independently as a result of dominant classical dephasing processes imprinted by the local inhomogeneous fields, thus $S(t)$ relaxes to zero. In the synchronized phase, collective interactions lock the phase precession and we can distinguish three different scenarios in which $S(t)$ either relaxes to a stationary value (Phase-II), up to a phase of a Goldstone mode [326] associated to a global $U(1)$ symmetry, or its magnitude enters self-generated oscillatory dynamics, corresponding to a Higgs mode [326], either periodic (Phase-III), or aperiodic (Phase-IV). While Phase-I and Phase-II describe relaxation to a steady state up to an irrelevant global phase, Phase-III and Phase-IV are instead examples of a self-generated oscillating synchronization phenomenon without an external driving force [338–341].

8.1.1. *Summary of results*

Here we investigate dynamics beyond two-level approximations by considering \mathcal{N}_a bosonic atoms, each hosting N levels which realize $SU(N)$ spins. The additional structure due

to the bosonic statistics allows us to naturally consider both classical and quantum initial states (c.f. Sec. 8.3.1). Using this flexibility in the initial state, and also the tunability of Hamiltonian parameters, we show how to craft not only the dynamical responses present in the two-level integrable setup (from Phase-I up to Phase-IV), but also how to access a novel chaotic dynamical response. This chaotic response, which we refer to as Phase-IV*, again has all atoms synchronized but with the dynamics of the average atomic coherences characterized by exponential sensitivity to initial conditions. The self-generated chaotic Phase-IV* emerges from the interplay of initial quantum correlations, and the collective interactions mediated by the cavity field. It is therefore qualitatively different from chaos induced by other mechanisms as due to additional local interactions [342] or external pump [315, 343–346].

In order to show how to craft and control these dynamical responses, we introduce a generalization of the reduction hypothesis used for two level systems. Specifically, we propose that the different dynamical phases (Phase-I up to Phase-IV*) all correspond to a different effective few body Hamiltonian that depends on the global symmetries of the many body system, degree of inhomogeneity, W , number of atomic levels N , and degree of quantum correlations in the initial state, quantified by a parameter p (cf. Sec. 8.5.2). Then, by considering an appropriate classical limit arising in the limit of large system size (cf. Sec. 8.3), we apply the Liouville-Arnold theorem to the effective Hamiltonian to identify a correspondence between the dynamical phases and the effective Hamiltonians. Using physical arguments for the nature of the effective Hamiltonian, we then predict how to tune between different dynamical responses. The result is an intuitive control over the rich dynamical response possible in multilevel cavity QED. See Fig. 8.1 for a cartoon of the different dynamical responses for $N = 3$ level atoms, using as a proxy the synchronized (or de-synchronized) evolution of the magnitude of the average intra-level coherences in the ensemble.

We conclude by discussing the potential universality of the reduction hypothesis. In particular, we conjecture it applies not only for state-of-the-art cavity QED experiments (cf. Sec. 8.7), but could find potential applications in other fields. Following Refs. [347, 348], where cavity QED platforms are proposed to model the dynamics of s -wave and $(p + ip)$ -wave BCS superconductors, our results could find potential applications to lattice systems with local $SU(N)$ interactions, such as $SU(N)$ Hubbard models [349–352]. Another possible outreach of our results could consist in noticing that the N levels of the atoms could be used as a synthetic dimension, with the geometry fixed by the photon-mediated processes, as for instance in a synthetic ladder system [353, 354]. Furthermore, since we consider bosonic systems, our results could potentially find

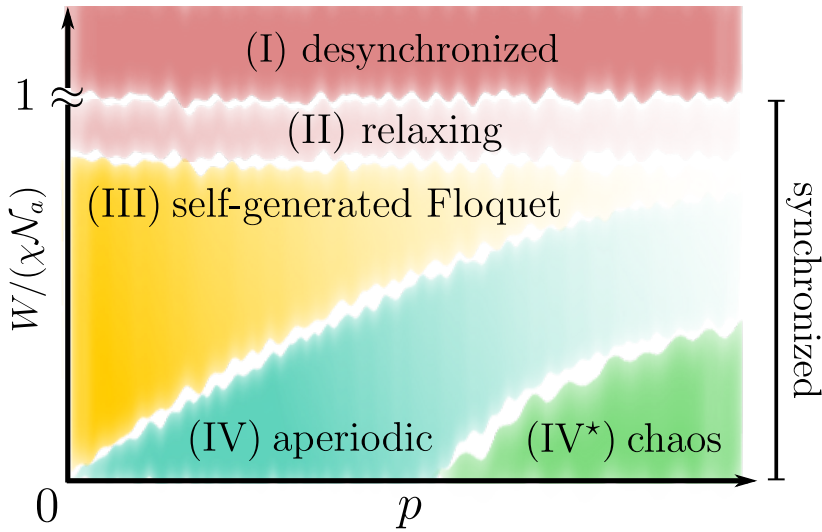


FIGURE 8.1. Cartoon of the possible dynamical responses of intra-level phase coherence in a photon-mediated spin-exchange model between $SU(3)$ spins, as a function of the degree of inhomogeneity of the local fields W , and of quantum correlations in the initial state parameterized by p . At $p = 0$ each site is initialized in the same bosonic coherent state. For $p > 0$, there are finite quantum correlations in the system. The parameter p tunes from bosonic coherent states ($p = 0$) to a multimode Schrödinger cat state ($p > 0$) initialized on each site. The susceptibility of the dynamical response to quantum correlations is strictly linked to having $SU(N)$ spins with $N > 2$, thus cannot be achieved considering two-level systems. Up to inhomogeneity $W/(\chi N_a) \approx 1$, the system is in the synchronized phase. At larger inhomogeneities, the system enters in the desynchronized phase and all phase coherence is washed (Phase-I). In the synchronized phase, phase coherence relaxes asymptotically to a nonzero value up to a phase associated to a global $U(1)$ symmetry (Phase-II), or its magnitude enters a self-generated oscillatory dynamics, either periodic (Phase-III), or aperiodic (Phase-IV), as well as potentially chaotic (Phase-IV*). In this last case dynamics are exponentially sensitive to changes in initial conditions. Image taken from Ref. [4].

applications in spinor Bose-Einstein condensates [355, 356] or in molecules embedded in a cavity, where bosons could be identified as their vibrational modes [357, 358].

8.2. THE MODEL

We consider a system of N_a bosonic atoms interacting via a single photonic mode of a cavity. The atoms are cooled to the motional ground state and evenly distributed among L different atomic ensembles labeled by a site index j . Within each site (ensemble), the atoms are indistinguishable and can occupy N different atomic levels with energies

that are site- and level-dependent. We consider the atoms sufficiently far apart for interatomic interactions to be negligible. The photon-matter interaction mediates atom number conserving processes where the absorption and/or the emission of a cavity photon results in an atom transitioning from level n to levels $n \pm 1$ within the same site, with a rate generally dependent on the specific level n . The associated many-body light-matter Hamiltonian reads

$$\begin{aligned} \hat{H} = & \omega_0 \hat{a}^\dagger \hat{a} + \sum_{j=1}^L \sum_{n=1}^N h_n^{(j)} \hat{b}_{n,j}^\dagger \hat{b}_{n,j} + \\ & + \sum_{j=1}^L \sum_{n=1}^{N-1} \left[g_n \left(\hat{b}_{n+1,j}^\dagger \hat{b}_{n,j} \hat{a} + h.c. \right) + \lambda_n \left(\hat{b}_{n+1,j}^\dagger \hat{b}_{n,j} \hat{a}^\dagger + h.c. \right) \right], \end{aligned} \quad (8.1)$$

where $\hat{a}^{(\dagger)}$ is the bosonic annihilation (creation) operator of the cavity photon; $\hat{b}_{n,j}^{(\dagger)}$ is the bosonic annihilation (creation) operator on site $j \in [1, L]$ and level $n \in [1, N]$, with energy splitting $h_n^{(j)}$; g_n and λ_n are the single-particle photon-matter couplings which controls rotating and co-rotating processes, respectively. Tuning g_n and λ_n enables us to pass from a generalized multilevel Dicke model, when $g_n, \lambda_n \neq 0$, to the multilevel Tavis-Cummings model, when $\lambda_n = 0$. Here, we consider dynamics on time scales where dissipative processes are sub-dominant compared to coherent evolution (cf. Sec. 8.8.1).

When the cavity is far detuned from the atomic transitions, the photon does not actively participate in dynamics of Eq. (8.1) but instead mediates virtual atom-atom interactions [359]. This occurs in the limit $\omega_0 \gg \max\{h_n^{(j)}, g_n \sqrt{N_a}, \lambda_n \sqrt{N_a}\}$, where the factor $\sqrt{N_a}$ comes from the cooperative enhancement given by the N_a atoms [67, 360]. The mediated interaction results in an effective atoms-only Hamiltonian of the form

$$\begin{aligned} \hat{H} = & \sum_{j=1}^L \sum_{n=1}^N h_n^{(j)} \hat{\Sigma}_{n,n}^{(j)} + \\ & - \sum_{m,n=1}^{N-1} \left[\chi_{n,m} \hat{\Sigma}_{n+1,n} \hat{\Sigma}_{m,m+1} + \zeta_{n,m} \hat{\Sigma}_{n,n+1} \hat{\Sigma}_{m+1,m} + \right. \\ & \left. + \nu_{n,m} \hat{\Sigma}_{n+1,n} \hat{\Sigma}_{m+1,m} + \nu_{m,n} \hat{\Sigma}_{n,n+1} \hat{\Sigma}_{m,m+1} \right], \end{aligned} \quad (8.2)$$

where $\chi_{n,m} \equiv g_n g_m / \omega_0$; $\zeta_{n,m} \equiv \lambda_n \lambda_m / \omega_0$; $\nu_{n,m} \equiv \lambda_n g_m / \omega_0$. For convenience, we have written the Hamiltonian in Eq. (8.2) as a function of the operators

$$\hat{\Sigma}_{n,m}^{(j)} = \hat{b}_{n,j}^\dagger \hat{b}_{m,j}, \quad (8.3)$$

$$\hat{\Sigma}_{n,m} = \sum_{j=1}^L \hat{\Sigma}_{n,m}^{(j)}. \quad (8.4)$$

The operators $\{\hat{\Sigma}_{n,m}^{(j)}\}$ are generators of the $SU(N)$ group [265, 361] and they obey the commutation relations $[\hat{\Sigma}_{n,m}^{(i)}, \hat{\Sigma}_{k,l}^{(j)}] = \delta_{i,j}(\hat{\Sigma}_{n,l}^{(i)}\delta_{m,k} - \hat{\Sigma}_{k,m}^{(j)}\delta_{n,l})$, and $(\hat{\Sigma}_{n,m}^{(j)})^\dagger = \hat{\Sigma}_{m,n}^{(j)}$.

The regime we are mostly interested in is $\nu_{n,m} = \zeta_{n,m} = 0$, which translates to $\lambda_n = 0$. In this limit, the Hamiltonian in Eq. (8.2) turns into a spin-exchange interaction Hamiltonian between $SU(N)$ spins with rates $\{\chi_{n,m}\}$ and inhomogeneous fields, $h_n^{(j)}$. In the following, we set the collective spin-exchange rate $\chi\mathcal{N}_a = \mathcal{N}_a \sum_{n=1}^{N-1} \chi_{n,n}$ as our energy scale, such that the time-scales of our results are independent of the number of atoms \mathcal{N}_a in the system. An implementation of the spin exchange model in Eq. (8.2) is offered in Sec. 8.7.

Below, we consider both situations when the energies of the atomic levels are homogeneous and when they are inhomogenous. In the latter situation, we expect our results to hold for various forms of inhomogenities, but we will in particular focus on the situations when the atomic levels on each site are in an evenly spaced ladder configuration with spacing $\Delta h_j \equiv (h_{n+1}^{(j)} - h_n^{(j)})$ sampled from a box distribution with zero average and width W . In this case, the Hamiltonian is spatially homogeneous for $W = 0$, and spatially inhomogeneous for $W > 0$. At $W = 0$ we can make precise predictions of the dynamical responses as a function of the features of the initial state and multilevel structure. Then, we show numerically their robustness against many-body dynamics due to inhomogenities ($W > 0$), in a fashion reminiscent of a synchronization phenomenon.

Given an evenly spaced ladder configuration within each site, the Hamiltonians in Eq. (8.1) and Eq. (8.2) can, for certain values of the couplings g_n and λ_n , be written in terms of the generators of a subgroup of $SU(N)$. For instance, in the $N = 3$ level case, if $g_n = g$ and $\lambda_n = \lambda$, the Hamiltonian can be written as a function of the generators of a $SU(2)$ subgroup of $SU(3)$. Specifically, only the $SU(2)$ operators $\hat{S}_j^- = \sqrt{2}(\hat{\Sigma}_{1,2}^{(j)} + \hat{\Sigma}_{2,3}^{(j)})$, $\hat{S}_j^+ = (\hat{S}_j^-)^\dagger$, and $\hat{S}_j^z = (\hat{\Sigma}_{3,3}^{(j)} - \hat{\Sigma}_{1,1}^{(j)})$ are required to represent the Hamiltonian, and as a consequence, the dynamics can be more simply described by the dynamics of these $SU(2)$ spins. For instance, we recover the spin-1 Dicke model for $\lambda = g$ and the spin-1 Tavis-Cummings model for $\lambda = 0$ in Eq. (8.1). Since we aim to explore the impact of genuine interactions between $SU(N)$ spins, we fix g_n and λ_n such that the dynamics cannot be restricted to a subgroup of $SU(N)$, if not otherwise specified. An important exception is the three-level case, where the system can enter in a chaotic phase upon passing from interactions between $SU(2)$ to $SU(3)$ spins (see Sec. 8.5.2). We highlight that while the interactions considered lead to nontrivial effects in the $SU(N)$ degrees of freedom, they are not $SU(N)$ -symmetric.

8.3. MEAN FIELD LIMIT

Given a generic interacting Hamiltonian, the dynamics of any n -point correlation function depends on higher order correlation functions – a structure known as the BBGKY hierarchy [362]. In fully connected systems, as in our case, the hierarchy can be efficiently truncated starting from separable states, or in other words, from a Gutzwiller-type ansatz [363]

$$|\Psi\rangle = \otimes_{j=1}^L |\psi_j\rangle \otimes |\alpha\rangle, \quad (8.5)$$

where $|\psi_j\rangle$ is a generic state on the j -th atom, and $|\alpha\rangle$ is a bosonic coherent state describing the cavity field. Given $|\Psi\rangle$ in Eq. (8.5), the hierarchy can be truncated as $\langle \hat{\Sigma}_{n,m}^{(j)} \hat{a} \rangle = \langle \hat{\Sigma}_{n,m}^{(j)} \rangle \langle \hat{a} \rangle$ and $\langle \hat{\Sigma}_{n,m}^{(j)} \hat{\Sigma}_{r,s} \rangle = \langle \hat{\Sigma}_{n,m}^{(j)} \rangle \langle \hat{\Sigma}_{r,s} \rangle$ up to $1/L$ corrections [67–71]. Here and from now on, we assume all expectation values are taken with respect to the state $|\Psi\rangle$, i.e. $\langle \hat{o}(t) \rangle \equiv \langle \Psi | \hat{o}(t) | \Psi \rangle$. In the limit $L \rightarrow \infty$ no additional quantum correlations build up in time, hence the equation of motions of one-point and two-points correlation functions are exactly closed at all times and the state $|\Psi\rangle$ remains an exact ansatz of the many-body state.

Combining the large L limit and the nature of the interaction in the Hamiltonian, the dynamics of $\langle \hat{\Sigma}^{(j)} \rangle$ and $\langle \hat{a} \rangle$ can be accordingly obtained in the mean field limit of the Hamiltonians in Eq. (8.1) and Eq. (8.2). This is achieved replacing the operators $\hat{\Sigma}_{n,m}^{(j)}$ and $\hat{a}^{(\dagger)}$ by classical $SU(N)$ spins and photon amplitude given by

$$\begin{aligned} \Sigma_{n,m}^{(j)} &= \langle \hat{\Sigma}_{n,m}^{(j)} \rangle / (\mathcal{N}_a / L), \\ a &= \langle \hat{a} \rangle / \sqrt{\mathcal{N}_a}, \end{aligned} \quad (8.6)$$

with \mathcal{N}_a / L the average number of bosonic excitations per site and by substituting the commutators with Poisson brackets. The same dynamics can be obtained starting from the Heisenberg equation of motions and then taking the expectation value on the state $|\Psi\rangle$ in Eq. (8.5) [361] truncating the hierarchy as discussed above.

The hierarchy can be further truncated at first order in the bosonic operators if the one-body reduced density matrix $\Sigma^{(j)}$, with matrix elements $\Sigma_{n,m}^{(j)}$, is pure ($\text{Tr}[(\Sigma^{(j)})^2] = 1$), namely there are no quantum correlations on a given site j . For instance, if the state $|\psi_j\rangle$ in Eq. (8.5) is a bosonic coherent state on each level of site j , the matrix $\Sigma^{(j)}$ is pure and straightforwardly factorized as $\Sigma_{n,m}^{(j)} = \langle \hat{b}_{n,j}^\dagger \rangle \langle \hat{b}_{m,j} \rangle$. The truncation at first order in the bosonic operators well approximates the full dynamics up to corrections which are suppressed [364] in both the number of sites L and the occupation on each site \mathcal{N}_a / L . Therefore, in the limit $\mathcal{N}_a \rightarrow \infty$, the hierarchy is exactly truncated at first order in the bosonic amplitudes $\langle \hat{b}_{n,j}^{(\dagger)} \rangle$ and $\langle \hat{a} \rangle$, at all times. In this limit, their dynamics can be equivalently obtained in the classical limit of the Hamiltonians in Eq. (8.1) and

Eq. (8.2) by replacing the bosonic operators $\hat{b}_{n,j}^{(\dagger)}$ and \hat{a} by the classical fields

$$\begin{aligned} b_{n,j} &= \langle \hat{b}_{n,j} \rangle / \sqrt{\mathcal{N}_a / L}, \\ a &= \langle \hat{a} \rangle / \sqrt{\mathcal{N}_a}, \end{aligned} \tag{8.7}$$

and replacing commutators with Poisson brackets.

In the following sections we will investigate the collective dynamical response of multi-level atoms in both mean field limits. We will show that the dynamical response could be highly susceptible to quantum correlations in the multilevel atom case, while it is insensitive in the two-level case.

8.3.1. Initial states

Here we derive general results that can be applied to any state of the form given in Eq. (8.5). As discussed in Sec. 8.3 we distinguish two different classical limits, arising in the large L limit, corresponding to the one-body reduced density matrix $\Sigma^{(j)}$ on site j being pure or mixed, respectively. For the sake of concreteness, we now present a few states corresponding to the two cases discussed above. The first two states are a bosonic coherent state and a $SU(N)$ spin-coherent state, both having no quantum correlations and a one-body reduced density matrix that is pure. While the other is a multimode Schrödinger cat state, whose one-body reduced density matrix on a given site is mixed reflecting the presence of quantum correlations.

Coherent states. The most general bosonic coherent state $|\psi_j\rangle$ on a given site j reads

$$\begin{aligned} |\psi_j\rangle &= \exp \left(\boldsymbol{\gamma}_j \cdot \hat{\mathbf{b}}_j^\dagger - h.c. \right) |0\rangle \equiv |\tilde{\gamma}_j\rangle, \\ \boldsymbol{\gamma}_j &\equiv (\gamma_{1,j}, \gamma_{2,j}, \dots, \gamma_{N,j}), \\ \hat{\mathbf{b}}_j^\dagger &\equiv (\hat{b}_{1,j}^\dagger, \hat{b}_{2,j}^\dagger, \dots, \hat{b}_{N,j}^\dagger), \end{aligned} \tag{8.8}$$

with $\gamma_{n,j} \in \mathbb{C}$ the amplitude of the bosonic coherent state on the n -th level and site j , so that the average number of particles per site is $\sum_{n=1}^N |\gamma_{n,j}|^2 = \mathcal{N}_a / L$. We highlight that the state in Eq. (8.8) does not have an exact number of particles. Nonetheless, since the fluctuations of the number of particles are subleading with respect to the mean in the limit we consider ($\mathcal{N}_a / L \rightarrow \infty$), the mean field treatment is unaffected. Such a state has a pure single particle reduced density matrix, and will have an evolution captured by a mean field limit characterized by the classical variables $b_{n,j}$ and a .

$SU(N)$ spin-coherent states. The second example of state with pure one-body reduced density matrix is given by the superposition: $|\psi_j\rangle = \sum_{n=1}^N \gamma_{n,j} \hat{b}_{n,j}^\dagger |0\rangle$, which has

one excitation per site. Once again, in this case, the mean field limit applies. Furthermore, the choice to truncate to one particle per site is insensitive of particles' statistics: either a fermion or boson could be the single particle occupying the site, as we further elaborate in the concluding section, Sec. 8.8.2. Such a state is the single particle limit of the more general \mathcal{N}_a/L particle $SU(N)$ spin-coherent state [265] defined by

$$|\psi_j\rangle = \frac{1}{\sqrt{(\mathcal{N}_a/L)!}} \left(\sum_{n=1}^N \gamma_{n,j} \hat{b}_{n,j}^\dagger \right)^{\mathcal{N}_a/L} |0\rangle, \quad (8.9)$$

which again has a pure one-body reduced density matrix reflecting a lack of quantum correlations. Thus, the dynamics of the classical variables $b_{n,j}$ and a perfectly describe the dynamics of both the bosonic and $SU(N)$ spin coherent states in the limit of a large number of bosons \mathcal{N}_a . Below we will present numerical results simulating these classical dynamics; they can be interpreted as describing the evolution of either of these two states. For the sake of simplicity, we will explicitly refer to these states as coherent states.

Schrödinger cat states. To consider a state in which the full two point correlations of the bosons, $\Sigma_{n,m}^{(j)}$, must be considered, we add quantum correlations on site j . This ensures that the one body reduced density matrix is not pure and cannot be written in the mean field approximation, $\Sigma_{n,m}^{(j)} \neq b_{n,j}^* b_{m,j}$. As an example, we consider a state where each site is initialized in a ‘multimode Schrödinger cat state’ [365, 366], which are the multimode generalization of ‘entangled coherent states’ [367–369], given by the superposition of two bosonic coherent states $|\tilde{\gamma}^{(m)}\rangle$ with average occupation \mathcal{N}_a/L , defined in Eq. (8.8), with $m = \{1, 2\}$

$$|\psi_j\rangle = \frac{1}{\mathcal{D}} \left(|\tilde{\gamma}_j^{(1)}\rangle + |\tilde{\gamma}_j^{(2)}\rangle \right). \quad (8.10)$$

Here \mathcal{D} is a normalization constant. If $|\langle \tilde{\gamma}_j^{(1)} | \tilde{\gamma}_j^{(2)} \rangle| = 1$ the state in Eq. (8.10) reduces to the one in Eq. (8.8). Instead, if $|\langle \tilde{\gamma}_j^{(1)} | \tilde{\gamma}_j^{(2)} \rangle| < 1$, the one-body reduced density matrix is mixed, reflecting the presence of quantum correlations on site j ($\langle \hat{b}_{n,j}^\dagger \hat{b}_{m,j} \rangle_c \equiv \langle \hat{b}_{n,j}^\dagger \hat{b}_{m,j} \rangle - \langle \hat{b}_{n,j}^\dagger \rangle \langle \hat{b}_{m,j} \rangle \neq 0$). We anticipate that the collective dynamical response could be highly susceptible to quantum correlations in the multilevel atom case, while they do not play a role in the two-level case. As an instance, we discover the onset of chaos as $|\langle \hat{b}_{n,j}^\dagger \hat{b}_{m,j} \rangle_c|$ increases in the $N = 3$ levels case (cf. Sec. 8.5.2). We highlight that quantum features of the state can only enter in initial conditions since dynamics are incapable of building quantum correlations in the mean field limit (cf. Sec. 8.3).

8.4. CLASSIFICATION OF DYNAMICAL RESPONSES

Our main purpose is to investigate and classify the dynamical response of collective observables in multilevel cavity QED systems in the long-time limit. Specifically, we investigate the dynamics of the magnitude of the intra-level average coherences, defined as $|\sum_{j=1}^L \Sigma_{n,m}^{(j)}|/\mathcal{N}_a$ (for $n \neq m$). To this end, we formulate the dynamical reduction hypothesis, which generalizes a similar procedure used for the integrable $SU(2)$ limits of Eq. (8.1) and Eq. (8.2). The hypothesis conjectures that the dynamics of collective observables can be captured by the Hamiltonian dynamics of a few effective collective degrees of freedom (DOFs). In the integrable case, the effective Hamiltonian has been used to quantitatively predict the dynamical responses observed, which include relaxation and persistent oscillations either periodic or aperiodic [326–336, 370]. Despite lack of integrability, we still obtain in our case not simply relaxation, but also the persistent oscillatory responses present in the integrable case, together with the possibility to develop chaos (see Fig. 8.3 for example) [370–372]. Due to the generic non-integrable nature of multilevel systems an exact procedure for extracting the effective model is not available (see Ref. [288], where the authors have attempted to extend the technique of the $SU(2)$ case to a $SU(N)$ -symmetric interacting spin system).

Here, we conjecture that, if an effective model exists, it is solely determined by the symmetries of the microscopic many-body problem and the relevant effective DOFs. Once the effective Hamiltonian is fixed, we show that the classification of dynamical responses follows from the combination of 1) the Liouville-Arnold theorem [373], which sets the criteria to distinguish a regular from an irregular (likely chaotic) regime, and 2) of the number of symmetries under which a given observable of interest is not invariant. Analogously to the integrable case mentioned above, we offer a classification of dynamical responses richer than the mere distinction between desynchronization and synchronization.

 8.4.1. *Dynamical Reduction Hypothesis*

In Sec. 8.3 we argued that, in the $L \rightarrow \infty$ limit and for an initial state of the form given in Eq. (8.5), the dynamics of the cavity field and multilevel atoms are described by the equations of motion generated from a classical Hamiltonian composed of an extensive number (in the size L) of classical $SU(N)$ spins. The dynamical reduction hypothesis conjectures that the dynamics of collective observables are effectively described by a classical Hamiltonian composed of a finite number, X , of effective $SU(N)$ systems (cf.

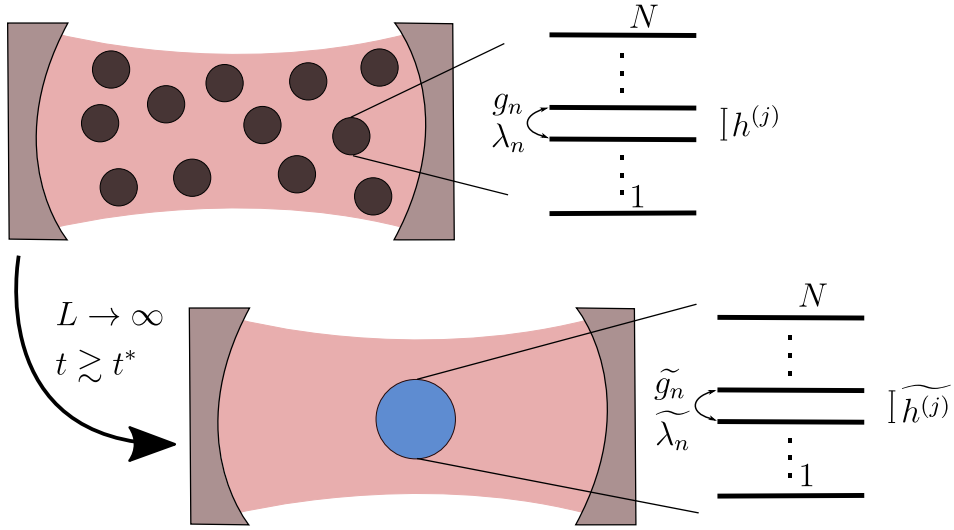


FIGURE 8.2. Sketch of \mathcal{N}_a atoms, each one hosting N levels (panels on the side), distributed over L sites (black dots), interacting via a common cavity field (red area). In the cartoon below we show the effective X -body system towards which the original many-body system is attracted in the long time $t \gtrsim t^*$. We show a single-body effective model ($X = 1$), since it is the one explicitly considered throughout this Chapter. We also show the internal structure of the single site both in the original many-body system and in the effective few-body description. Image taken from Ref. [4].

Fig. 8.2); or in other words, the emergent collective dynamics can be effectively captured by a few-body macroscopic system.

Specifically, we conjecture that a fully-connected many-body system with L -sites, each with local degrees of freedom $\mathbf{s}_j = \{s_{j,1}, s_{j,2}, \dots\}$, and classical Hamiltonian $H(\{\mathbf{s}_j\}_{j=1}^L)$ will, after a sufficiently long time $t \gtrsim t^*$ and in the thermodynamic limit $L \rightarrow \infty$, possess an effective X -site effective model describing the collective dynamics. The hypothesis supposes that the effective model will have X finite, even when L is in thermodynamics limit, and that the effective local degrees of freedom $\{\tilde{\mathbf{s}}_j\}_{j=1}^X$ will be governed by a classical effective Hamiltonian $\tilde{H}(\{\tilde{\mathbf{s}}_j\}_{j=1}^X)$. Hence, in order to predict dynamics of a collective observable $S(t) = f(\{\mathbf{s}_j(t)\}_{j=1}^L)$, we will assume the existence of a function \tilde{f} of the effective degrees of freedom, which will effectively reproduce the dynamics of $S(t)$. Note that in general, \tilde{f} is not necessarily of the same functional form of f . We can then compactly formulate the dynamical reduction hypothesis as

$$\begin{aligned} \lim_{L \rightarrow \infty} H(\{\mathbf{s}_j\}_{j=1}^L) &\xrightarrow{t \gtrsim t^*} \tilde{H}(\{\tilde{\mathbf{s}}_j\}_{j=1}^X), \\ \lim_{L \rightarrow \infty} S = f(\{\mathbf{s}_j\}_{j=1}^L) &\xrightarrow{t \gtrsim t^*} \tilde{f}(\{\tilde{\mathbf{s}}_j\}_{j=1}^X). \end{aligned} \tag{8.11}$$

The effective Hamiltonian \tilde{H} is of the same functional form in the integrable case [326, 333, 370], while it is not generally expected to be so for non-integrable systems [370]. Importantly, we assume that the effective Hamiltonian obeys the same global symmetries as the many-body Hamiltonian.

In the following we apply the dynamical reduction hypothesis (8.11) to craft various dynamical responses associated to the problem of synchronization in bosonic multilevel cavity QED summarized in Fig. 8.1. We believe that our conjecture has universal flavor and it is applicable to several other settings as we elaborate further in the concluding section.

8.4.2. *Classification of Dynamical Responses*

We construct a classification of dynamical phases by considering the different dynamics collective observables can display in the many-body system. In the case of cavity QED, we consider the magnitude of the intra-level average coherence $|\Sigma_{n,m}(t)| = |\sum_{j=1}^L \Sigma_{n,m}^{(j)}(t)|/L$ with $n \neq m$. These observables can distinguish between cases when the atoms are synchronized ($|\Sigma_{n,m}(t)| \neq 0$) or desynchronized ($|\Sigma_{n,m}(t)| = 0$), and in the case of synchronization we distinguish four dynamical responses.

Desynchronized phase:

- Phase-I: in the long time limit $|\Sigma_{n,m}(t)| \rightarrow 0$, as a result of classical dephasing processes in the microscopic model due to inhomogeneities in the local fields;

Synchronized phases:

- Phase-II: $|\Sigma_{n,m}(t)|$ relaxes to a stationary non-zero value;
- Phase-III: $|\Sigma_{n,m}(t)|$ displays self-generated Floquet dynamics (i.e. periodic oscillations) characterized by a spectrum with well-resolved commensurate frequencies;
- Phase-IV: $|\Sigma_{n,m}(t)|$ displays aperiodic oscillations characterized by a spectrum with well-resolved incommensurate frequencies;
- Phase-IV^{*}: $|\Sigma_{n,m}(t)|$ displays chaotic oscillations exponentially sensitive to small changes in the initial conditions and characterized by a spectrum with multiple broad peaks.

While Phase-I and Phase-II are quite generic in the presence of inhomogeneous dephasing, Phase-III, Phase-IV and Phase-IV^{*} are examples of self-generated non-relaxing responses in absence of an external drive. As previously mentioned, the dynamical

responses from Phase-I to Phase-IV were already observed in the integrable two-level case [326, 329, 330, 347], while the chaotic Phase-IV* is accessible only in non-integrable systems [372].

To predict and control when such phases occur we use the dynamical reduction hypothesis, and arguments based on symmetry and the Liouville-Arnold theorem. The Liouville-Arnold theorem [373] states that given a system with M degrees of freedom and Q conserved quantities, there exists a canonical transformation through ‘action-angle’ variables, such that Q ‘actions’ are constant, and Q ‘angles’ evolves periodically at a frequency imposed by the value of the corresponding conserved quantity [373–375]. Thus, if $2Q \geq M$, the dynamics is solely along tori and the system is said to be classically integrable. If instead $2Q < M$, there will be $(M - 2Q)$ degrees of freedom which evolve without any constraint and can in principle display chaotic behavior. Notice that $Q \geq 1$ since the effective Hamiltonian always obeys time translation symmetry such that the effective energy is always a conserved quantity.

To apply this theorem to describe the different phases with different effective models, we assume that an X site effective model has in total M DOFs. Phase-I can be described by an effective model with $X = 0$ sites, thus $M = 0$ DOFs, since no effective degree of freedom is necessary to capture a vanishing observable. In the microscopic models, the synchronized phases generally occurs when the all-to-all coupling is large enough with respect to the inhomogeneities in the local fields, and it can be captured by an effective model with $X \geq 1$ sites, thus, $M \geq 1$ DOFs, since we need at least one DOF for describing nontrivial behavior. Combining the number of DOFs M , the number of symmetries Q , and the number of symmetries under which the specific observable is invariant, it is possible to predict the specific synchronized dynamical response. We show that, in $SU(N)$ systems, an effective single-site Hamiltonian ($X = 1$) is already sufficient for observing all the dynamical responses from Phase-I up to Phase-IV*. This is in contrast to the $SU(2)$ integrable case in which an X -body effective Hamiltonian is necessary to capture Phase- $(X + 1)$ [326, 329, 330, 336, 347].

To apply this classification to multilevel cavity QED, we must identify the global symmetries present in such systems and the number of DOFs that could occur in the effective models. We identify the global symmetries and number of DOFs in Sec. 8.4.3, present a few examples of effective models in Sec. 8.4.4 and give the predictions for the allowed dynamical responses for different N -level systems in Sec. 8.4.5.

8.4.3. *Counting DOFs and symmetries*

Given a generic product state, as in Eq. (8.5), we conjecture an effective classical model composed of effective DOFs describing the matter and the cavity field separately. We assume that the effective cavity field is given by a bosonic amplitude \tilde{a} specified by two real numbers. As the detuning from the atomic transitions increases, the contribution from such DOFs becomes suppressed, and consequently can be neglected in the far detuned limit [336]. The effective matter's DOFs are either $SU(N)$ spins or bosonic amplitudes, depending on whether the collective observables $\Sigma_{n,m}(t)$ can be factorized or not.

If $\Sigma_{n,m}(t)$ cannot be factorized, the emergent effective classical model is composed of X $SU(N)$ -spins with elements $\tilde{\Sigma}_{n,m}^{(k)}$ where $n, m \in [1, N]$ and $k \in [1, X]$. Such an effective model has $M = X \times N^2$ matter DOFs, corresponding to the N^2 matrix elements for each effective spin $\tilde{\Sigma}^{(k)}$. Since the effective degrees of freedom are $SU(N)$ spins, the number of independent parameters is reduced due to the Casimir charges $\sum_{n=1}^N \tilde{\Sigma}_{n,n}^{(k)}$ and $\sum_{n,m=1}^N \tilde{\Sigma}_{n,m}^{(k)} \tilde{\Sigma}_{m,n}^{(k)}$, which are the conservation of the number of bosons and length of the $SU(N)$ spin on each site k . As a consequence, the number of independent matter DOFs is $M = X \times (N^2 - 2)$.

Instead, if $\Sigma_{n,m}(t)$ can be factorized, then the effective model in the $SU(N)$ spins further simplifies and involves only $X \times N$ effective bosonic amplitudes $\tilde{b}_{n,k}$ with $k \in [1, X]$ and $n \in [1, N]$. In this case, the number of matter DOFs is $M = X \times 2N$, being each bosonic amplitude specified by two real parameters. Assuming that the effective $SU(N)$ spins and effective bosons are related analogously to the microscopic ones via $\tilde{\Sigma}_{n,m}^k = \tilde{b}_{n,k}^* \tilde{b}_{m,k}$, the two Casimir charges defined above are still conserved. In this case they are dependent one from the other and can be linked to the local $U(1)$ symmetry $\tilde{b}_{n,k} \rightarrow e^{i\phi_k} \tilde{b}_{n,k}$ of the bilinears $\tilde{b}_{n,k}^* \tilde{b}_{m,k}$. Since the number of bosons is conserved, the corresponding conjugate variable, the sum of the phases of the bosonic amplitudes, is irrelevant and the number of nontrivial matter DOFs is $M = X \times (2N - 2)$.

Once the effective DOFs are identified, we can construct the effective Hamiltonian which governs their dynamics imposing the same symmetries of the many-body Hamiltonian in Eq. (8.1) and Eq. (8.2) in the classical limit. The first symmetry is time translation invariance, which implies the conservation of the energy, while the second is a global $U(1)$ symmetry present solely in absence of co-rotating processes. Specifically, for $\lambda_n = 0$ the Hamiltonian in Eq. (8.1) is invariant under $(\Sigma_{n,n+1}, a) \rightarrow (e^{i\theta} \Sigma_{n,n+1}, e^{i\theta} a)$ and thus conserves the number of total excitations, which in the two-level case is $[(\Sigma_{2,2} - \Sigma_{1,1})/2 + |a|^2]$ while in the generic multilevel case is a linear combination of $\{\Sigma_{n,m}\}$ and $|a|^2$ [358,

	Q	$N = 2$	$N = 3$	$N \geq 4$
$\tilde{g}, \tilde{\lambda} \neq 0$ and $\tilde{\omega}_0$ finite	1	IV*	IV*	IV*
$\tilde{g}, \tilde{\lambda} \neq 0$ and $\tilde{\omega}_0 \rightarrow \infty$	1	III	IV*	IV*
$\tilde{\lambda} = 0$ and $\tilde{\omega}_0$ finite	2	III	IV*	IV*
$\tilde{\lambda} = 0$ and $\tilde{\omega}_0 \rightarrow \infty$	2	II	III or IV*	IV*

TABLE 8.1. Summary of the dynamical responses of the magnitude of the intra-level average phase coherence captured by the effective Hamiltonians in Eq. (8.12) and Eq. (8.13). The number of matter DOFs is either $(2N - 2)$ or $(N^2 - 2)$ depending on whether $\tilde{\Sigma}$ can be factorized or not, respectively (cf. Sec. 8.4.3). If the cavity field detuning $\tilde{\omega}_0$ is finite, we need two additional DOFs to describe the modulus and phase of the actively participating cavity field. The presence of a $U(1)$ symmetry increases the number of conserved quantities Q by 1. For the $N = 3$ spin exchange model (last row) the system can display from Phase-I to either Phase-III or Phase-IV* depending on whether $\tilde{\Sigma}$ can be factorized or not, respectively. In all cases, all the responses with ‘less order’ than the one reported, could be in principle accessed tailoring the initial state and the parameters of the Hamiltonian. The same table holds in the case the Hamiltonian is spatially homogeneous, since the effective models are trivially equal to the microscopic ones (cf. Sec. 8.5). Table taken from Ref. [4].

376]. Analogously, for $\nu_{m,n}, \zeta_{n,m} = 0$ the atoms-only model in Eq. (8.2) is invariant under $\Sigma_{n,n+1} \rightarrow e^{i\theta} \Sigma_{n,n+1}$, which leads to the conservation of the number of atomic excitations (e.g. $(\Sigma_{2,2} - \Sigma_{1,1})$ in the two-level case).

Combining the effective DOFs and symmetries, we can now propose a possible set of effective models and predict the dynamical responses of collective observables via arguments based on symmetry and the Liouville-Arnold theorem.

8.4.4. Effective Models

In order to make concrete the above picture, here we present a set of possible effective models for multilevel cavity QED systems described by Eq. (8.1). As mentioned above, an exact derivation is not available in the generic multilevel case (see Refs. [326, 333, 370] where the effective few-body Hamiltonian can be derived from the Richardson-Gaudin integrability of the $SU(2)$ case). Nonetheless, considering the initial state to be a generic product state (cf. Eq. (8.5)), the effective DOFs are $SU(N)$ spins, and the simplest effective theory is given by the microscopic Hamiltonian in Eq. (8.1) with $L = 1$ (thus

$X = 1$ effective sites)

$$\begin{aligned}\tilde{H}(\tilde{\Sigma}_{n,m}, \tilde{a}) = & \tilde{\omega}_0 \tilde{a}^* \tilde{a} + \sum_{n=1}^N \tilde{h}_n \tilde{\Sigma}_{n,n} + \\ & + \sum_{n=1}^{N-1} \left[\tilde{g}_n \left(\tilde{\Sigma}_{n+1,n} \tilde{a} + h.c. \right) + \tilde{\lambda}_n \left(\tilde{\Sigma}_{n+1,n} \tilde{a}^* + h.c. \right) \right].\end{aligned}\quad (8.12)$$

Analogously, in the far-detuned cavity mode limit described by the Hamiltonian in Eq. (8.2), we propose the effective Hamiltonian

$$\begin{aligned}\tilde{H}_e(\tilde{\Sigma}_{n,m}) = & \sum_{n=1}^N \tilde{h}_n \tilde{\Sigma}_{n,n} + \\ & - \sum_{m,n=1}^{N-1} \left[\tilde{\chi}_{n,m} \tilde{\Sigma}_{n+1,n} \tilde{\Sigma}_{m,m+1} + \tilde{\zeta}_{n,m} \tilde{\Sigma}_{n,n+1} \tilde{\Sigma}_{m+1,m} + \right. \\ & \left. + \tilde{\nu}_{n,m} \tilde{\Sigma}_{n+1,n} \tilde{\Sigma}_{m+1,m} + \tilde{\nu}_{m,n} \tilde{\Sigma}_{n,n+1} \tilde{\Sigma}_{m,m+1} \right].\end{aligned}\quad (8.13)$$

Additionally, if the collective observables $\tilde{\Sigma}_{n,m}$ can be factorized, we conjecture effective models for the boson DOFs of the form

$$\tilde{H}(\tilde{b}_n, \tilde{a}) = \tilde{H}(\tilde{\Sigma}_{n,m} = \tilde{b}_n^* \tilde{b}_m, \tilde{a}) \quad (8.14)$$

$$\tilde{H}_e(\tilde{b}_n) = \tilde{H}_e(\tilde{\Sigma}_{n,m} = \tilde{b}_n^* \tilde{b}_m) \quad (8.15)$$

where we conjecture that the effective one-body reduced density matrix factorizes as $\tilde{\Sigma}_{n,m} = \tilde{b}_n^* \tilde{b}_m$. These effective models are trivially exact when the Hamiltonians in Eq. (8.1) and Eq. (8.2) are spatially homogeneous for $h_n^{(j)} = h_n$ at $W = 0$. Indeed, at $W = 0$ the many-body Hamiltonians trivially reduces to a few-body one due to the permutation symmetry under swapping of any pair of sites. Despite their apparent simplicity, the effective models here introduced allow us to obtain quantitatively the whole set of dynamical responses described in Sec. 8.4.2. Furthermore, we show in Sec. 8.6 that these models describe correctly the dynamics of collective observables also at moderate inhomogeneity, with a quantitative matching in the case of $N = 3$ spin-exchange interactions.

8.4.5. Classification for multilevel cavity QED

We are now in the position to discuss the possible dynamical phases for the $X = 1$ effective models introduced in Sec. 8.4.4 for different number of levels N . As already anticipated, we consider as collective variable the magnitude of the intra-level average coherences, which in the effective models are given by $|\tilde{\Sigma}_{n,m}(t)|$ with $n \neq m$. The results of this section are summarized in Table 8.1.

For a generic multilevel atom with $N \geq 4$ levels, the number of DOFs M is always larger than the $2Q \leq 4$ symmetries identified. Thus, generically, the effective model can show aperiodic oscillations (Phase-IV) and may even display chaotic behavior (Phase-IV*).

N = 2 level atoms. The case of $N = 2$ levels has been well studied [69, 377, 378] and in this section we discuss how our approach reproduces known results. The number of matter DOFs is $M = 2$, either considering an effective bosonic model, or with $SU(2)$ spins. Thus, it is not possible to access different dynamical responses upon introducing quantum correlations in the mean-field limits considered. If the cavity field actively participates to dynamics, we need to keep track of two additional DOFs given by the real and imaginary part of its amplitude.

Let us consider the two level system with a photon actively participating in dynamics. We can identify the two regimes corresponding to either the generalized Dicke model ($\tilde{\lambda}, \tilde{g} \neq 0$) or the Tavis-Cummings model ($\tilde{\lambda} = 0$). Both models have $M = 4$ DOFs, but a different number of conserved quantities. The generalized Dicke model conserves only the energy beyond the total spin (which we already taken into account), opening the option of chaos (Phase-IV*), as it has been seen for instance in Refs. [379–387]. Instead, the Tavis-Cummings model has one additional conserved charge (total number of excitations), is therefore integrable and in fact it shows regular dynamics [377, 388–390]. Under change to action-angle variables, the dynamics are seen as the evolution on a 3-tori, with 3 independent frequencies. Thus a general observable might show Phase-IV oscillations. Nevertheless, the magnitude of the mean coherence $|\tilde{\Sigma}_{1,2}(t)|$ only shows periodic oscillations (Phase-III) since it is invariant under two of the symmetries, specifically the $U(1)$ symmetries $(\tilde{\Sigma}_{1,2}, \tilde{a}) \rightarrow (e^{i\theta}\tilde{\Sigma}_{1,2}, e^{i\theta}\tilde{a})$ and $\tilde{b}_n \rightarrow e^{i\theta}\tilde{b}_n$, with $n = \{1, 2\}$, linked to the conservation of the total number of excitations and spin, respectively.

In the limit where the cavity mode is far detuned from the atomic transitions, the Tavis-Cummings model becomes a simple spin-exchange model with $M = 2Q = 2$ (the conservation of energy and of the total number of excitations are dependent). Since this model can only have two independent frequencies corresponding to the precession of the $U(1)$ angle variables, the observable $|\tilde{\Sigma}_{1,2}(t)|$ is constant yielding Phase-II. If the additional $U(1)$ symmetry is broken, one recovers the Lipkin-Meshkov-Glick (LMG) model, and the observable $|\tilde{\Sigma}_{1,2}(t)|$ can again oscillate with a single frequency and display Phase-III, as it is generically observed [364, 391–395].

N = 3 level atoms. In the three-level case, M depends on whether the model reduces to a bosonic model or to a $SU(3)$ spin system. In the bosonic case, the atomic sector is described by $M = 2N - 2 = 4$ real DOFs. In the generic $SU(3)$ case, the matter is described by $M = N^2 - 2 = 7$ DOFs. If the photon is an active DOFs, its

additional DOFs leads to $M \geq 6$ in either the bosonic or spin model, and since $Q \leq 2$ for any set of parameters, the dynamics can enter the chaotic Phase-IV*.

The case of the spin-exchange model, corresponding to $\tilde{\zeta}_{n,m} = \tilde{\nu}_{n,m} = 0$ in Eq. (8.13), is perhaps the most interesting, since depending on whether the model reduces to a bosonic model or a $SU(3)$ spin model, the dynamics can be either in Phase-III or Phase-IV (possibly IV*). Indeed, the three level bosonic model $\tilde{H}_e(\tilde{b})$ has $M = 4$ DOFs and $Q = 2$ conserved charges, corresponding to the total energy and ‘number of excitations’ $(\tilde{\Sigma}_{3,3} - \tilde{\Sigma}_{1,1})$, and it is therefore integrable. Again, two of the frequencies are absorbed in the invariance of $|\tilde{\Sigma}_{n,m}|$ under the two $U(1)$ symmetries, and thus all oscillations must be periodic, yielding Phase-III. If instead the initial state has $\tilde{\Sigma}_{nm} \neq \tilde{b}_n^* \tilde{b}_m$, we must consider the $SU(3)$ spin model $\tilde{H}_e(\tilde{\Sigma}_{n,m})$, and the extra number of degrees of freedom leads $M > 2Q = 4$ allowing the dynamics to be either Phase-IV or Phase-IV*. If $\tilde{\zeta}_{n,m}, \tilde{\nu}_{n,m} \neq 0$ the system loses a $U(1)$ symmetry, associated to the conservation of $(\tilde{\Sigma}_{3,3} - \tilde{\Sigma}_{1,1})$, and consequently can display chaotic behavior for both bosons or $SU(3)$ spins.

8.5. HOMOGENEOUS SYSTEMS

In this section, we consider the homogeneous case ($W = 0$) of Eq. (8.2), where the dynamical reduction hypothesis is true due to the permutation symmetry, and we test the predictions of Table 8.1. In Sec. 8.5.1 we consider permutation invariant coherent states, discussing the role of the interactions. In Sec. 8.5.2 we discuss the consequences of classical and quantum correlations in the initial state focusing on the $N = 3$ levels spin-exchange Hamiltonian, where we observe the onset of a chaotic phase.

For $W = 0$ both the Hamiltonians in Eqs. (8.1), (8.2) are permutationally invariant under swapping of any pair of sites, and they can be written as a function of the collective operators in Eq. (8.4). Thus, we can immediately achieve the thermodynamic limit $L \rightarrow \infty$ considering a single large $SU(N)$ spin. As a consequence, in the mean field limit we exactly obtain the classical Hamiltonians $\tilde{H}(\tilde{\Sigma}_{n,m}, \tilde{a})$ or $\tilde{H}_e(\tilde{\Sigma}_{n,m})$, depending on whether the cavity field is an active DOF or not, respectively. Here, unlike in the general case, the effective DOFs trivially relate to the original collective DOFs being $\Sigma_{n,m} = \tilde{f}(\tilde{\Sigma}_{n,m}) = \tilde{\Sigma}_{n,m}$, and the parameters of the effective Hamiltonians are equal to the original ones (e.g. $\tilde{\omega}_0 = \omega_0$). As discussed in Sec. 8.3, the choice of reducing the model to spin degrees of freedom, i.e. $\tilde{H}_e(\tilde{\Sigma}_{n,m})$, or to bosons, $\tilde{H}_e(\tilde{b}_n)$, depends only on the purity of the effective one-body reduced density matrix $\tilde{\Sigma}$, i.e. whether its elements

$\tilde{\Sigma}_{n,m}$ can be factorized as the product of bosonic operators. In the next sections we investigate both scenarios and confirm the prediction summarized in Table 8.1.

8.5.1. *Homogeneous coherent states*

We set as initial state a permutationally invariant (in space) coherent state with equal average occupation on each level ($\gamma_{n,j} = \gamma$ in Eq. (8.8)). Since the state is homogeneous in space, the average one-body reduced density matrix is pure, and can be factorized in the bosonic amplitudes as $\Sigma_{m,n} = b_m^* b_n$. Therefore, the effective model describing collective observables is either $\tilde{H}(b_n, a)$ or $\tilde{H}_e(b_n)$ (notice that we interchanged the effective bosonic amplitudes with the microscopic ones being equal in this case). We show results only in the case where the photon is not an active DOF. Generally, we expect that an active photon leads to a change of dynamical response from Phase- Y , displayed in its absence, to Phase- $(Y + 1)$, due to the additional DOFs [336]. Nonetheless, this effect is suppressed as the detuning of the cavity field frequency with respect to the atomic transitions increases, making our results approximately valid also for large but finite detunings.

In Fig. 8.3 we show the dynamics of the magnitude of the phase coherence $|\Sigma_{1,2}|$ in the spin-exchange model (Eq. (8.2) with $\nu_{n,m} = \zeta_{n,m} = 0$) in the homogeneous limit ($W = 0$) for different number of atomic levels $N \in \{2, 3, 4\}$. As predicted in Table 8.1, upon changing the number of levels, the system can display markedly different dynamical responses: for $N = 2$, $|\Sigma_{1,2}|$ displays Phase-II; for $N = 3$, $|\Sigma_{1,2}|$ displays Phase-III; for $N = 4$, $|\Sigma_{1,2}|$ displays chaotic behavior (Phase-IV*). We also observe the onset of aperiodic oscillations (Phase-IV) in the $N = 4$ case for different sets of parameters and initial states. This is a simple signature of the importance of considering multilevel atoms, although the model has all-to-all interactions.

8.5.2. *Chaos induced by quantum correlations*

In this section we discuss the impact of quantum correlations in the initial state in the spin-exchange model (Eq. (8.2) with $\nu_{n,m} = \zeta_{n,m} = 0$). We show that the subsequent dynamics is susceptible to quantum correlations, with particularly striking effects in the $SU(3)$ case, where we can craft a specific dynamical response by manipulating the initial state, from Phase-III up to Phase-IV* (chaos).

We set on each site the same multimode Schrödinger cat state (cf. Eq. (8.10)). As

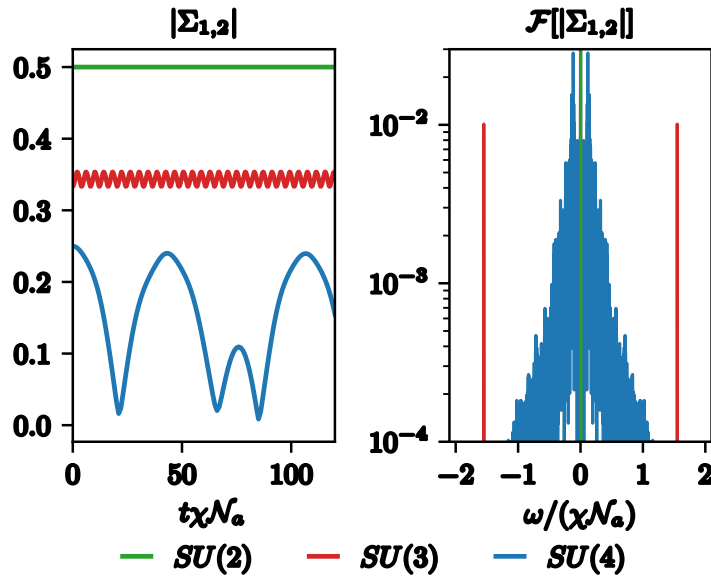


FIGURE 8.3. Left plot: Dynamics of the magnitude of the average phase coherence $|\Sigma_{1,2}(t)|$ in the homogeneous limit ($W = 0$) for the N -levels spin-exchange model (Eq. (8.2) with $\nu_{n,m} = \zeta_{n,m} = 0$) with $N = \{2, 3, 4\}$. The initial state is a permutation invariant (in space) coherent state with same average occupation on each level $n \in [1, N]$. The couplings $\chi_{n,m}$ are chosen such that we have genuine $SU(N)$ spins. For $N = 2$, $|\Sigma_{1,2}(t)|$ is constant (Phase-II); for $N = 3$, $|\Sigma_{1,2}(t)|$ displays periodic oscillations (Phase-III); for $N = 4$, there are not enough conserved quantities to constrain the space of accessible states and therefore $|\Sigma_{1,2}(t)|$ displays oscillations exponentially sensitive to small changes in initial conditions (Phase-IV*). Right plot: magnitude of the Fourier spectrum of $|\Sigma_{1,2}(t)|$. For $N = 2$ the only nonzero component is at $\omega = 0$, being $|\Sigma_{1,2}(t)|$ a constant; for $N = 3$ the spectrum has two well-resolved peaks; for $N = 4$ there are multiple broad peaks. Due to the permutation invariance under swapping of any pair of sites, the thermodynamic limit can be achieved by simulating a single site ($L = 1$) in the microscopic model in Eq. (8.2), or equivalently the effective model of Eq. (8.15). Image taken from Ref. [4].

discussed in Sec. 8.3.1, when $|\langle \tilde{\gamma}^{(1)} | \tilde{\gamma}^{(2)} \rangle| < 1$, the one-body reduced density matrix is mixed, the phase-coherences do not factorize ($\Sigma_{n,m} \neq b_n^* b_m$), and we have to keep track of all the bilinears $\Sigma_{n,m}$. Thus, the effective model passes from the one in the bosonic DOFs defined in Eq. (8.15) to the one in the $SU(N)$ spins defined in Eq. (8.13). Due to quantum correlations, the number of effective DOFs passes from $2N$ to N^2 and the constraint imposed by the conserved quantities no longer ensures classical integrability for $N > 2$. This is particularly striking in the $SU(3)$ case, where quantum correlations in the initial state can lead to a transition from a regular regime to a chaotic one. For this reason, we focus on the $SU(3)$ case in the following. Specifically, we consider as initial state a family of multimode Schrödinger cat state (cf. Eq. (8.10)) parameterized

via a parameter $p \in [0, 1/3]$ as

$$\begin{aligned}\gamma^{(1)} &= \sqrt{\frac{\mathcal{N}_a}{L}} \cdot (\sqrt{1/3+p}, \sqrt{1/3}, \sqrt{1/3-p}), \\ \gamma^{(2)} &= \sqrt{\frac{\mathcal{N}_a}{L}} \cdot (\sqrt{1/3}, \sqrt{1/3-p}, \sqrt{1/3+p}).\end{aligned}\tag{8.16}$$

The overlap $|\langle \tilde{\gamma}^{(1)} | \tilde{\gamma}^{(2)} \rangle|$ is exponentially suppressed both in p and \mathcal{N}_a/L , so that $\langle \tilde{\gamma}^{(1)} | \tilde{\gamma}^{(2)} \rangle = 0$ for any $p > 0$ in the limit $\mathcal{N}_a/L \rightarrow \infty$. We quantify quantum correlations by the connected two-point functions $(\Sigma_{n,m} - b_n^* b_m)$. Given the state in Eq. (8.16), the connected two-point functions are null at $p = 0$ and increase polynomially with p . As a consequence, the number of effective DOFs M needed is expected to increase with p . Based on our classification, we thus expect a change of the collective dynamical response displayed. This is manifest looking at the Fourier spectrum of $|\Sigma_{1,2}|$ (cf. Fig. 8.4(a)), where as p increases we observe a crossover from a regime with few commensurate peaks (Phase-III) to a regime with multiple incommensurate ones (Phase-IV), analogous to period doubling phenomena, and eventually the onset of chaos (Phase-IV*) for $p \gtrsim p^*$. The value p^* generally depends on the parameters of the Hamiltonian. We locate p^* computing the maximum Lyapunov exponent σ , which is the largest exponential rate at which nearby trajectories diverge and it is finite and positive in chaotic system and zero for regular Hamiltonian dynamics [396, 397]. We find $p^* \approx 0.3$ for $g_1/g_2 \approx 2$ (cf Fig. 8.4(b)). We refer to Appendix D.1 for the details about the calculation of the Lyapunov exponent and p^* .

We highlight that the interactions between $SU(3)$ spins are an essential ingredient for observing chaos. Indeed, for $g_1 = g_2$ (and thus $\chi_{1,1} = \chi_{2,2} = \chi_{1,2}$) dynamics take place in a $SU(2)$ subgroup of $SU(3)$, thus the number of DOFs reduces and there cannot be chaos as a consequence of the Arnold-Liouville theorem. While deep in the $SU(3)$ regime we have chaos for any $p \gtrsim p^*$, instead near the $SU(2)$ limits we observe regions in p of chaotic behavior embedded in regular ones (specifically Phase-IV). In Appendix D.2 we provide details on the Lyapunov exponent as a function of p and the ratio g_1/g_2 , passing from the $SU(2)$ ($g_1 = g_2$) to the $SU(3)$ spin case ($g_1 \neq g_2 \neq 0$).

In absence of interference effects ($\langle \tilde{\gamma}^{(1)} | \tilde{\gamma}^{(2)} \rangle = 0$), as it is for any $p > 0$ in the limit $\mathcal{N}_a/L \rightarrow \infty$ considered, the equations of motion of the collective observables $\Sigma_{n,m}$ are the same starting either from the Schrödinger cat state in Eq. (8.10), or from a state with half sites in the state $|\tilde{\gamma}^{(1)}\rangle$ and the other half in the state $|\tilde{\gamma}^{(2)}\rangle$. In this context, p effectively controls the ‘sharpness’ of a ‘kink’ in the initial spatial configuration of the $SU(3)$ spins, in analogy with domain walls in the $SU(2)$ case [347]. The primary difference is that in Ref. [347] it is only possible to generate Phase-III by considering

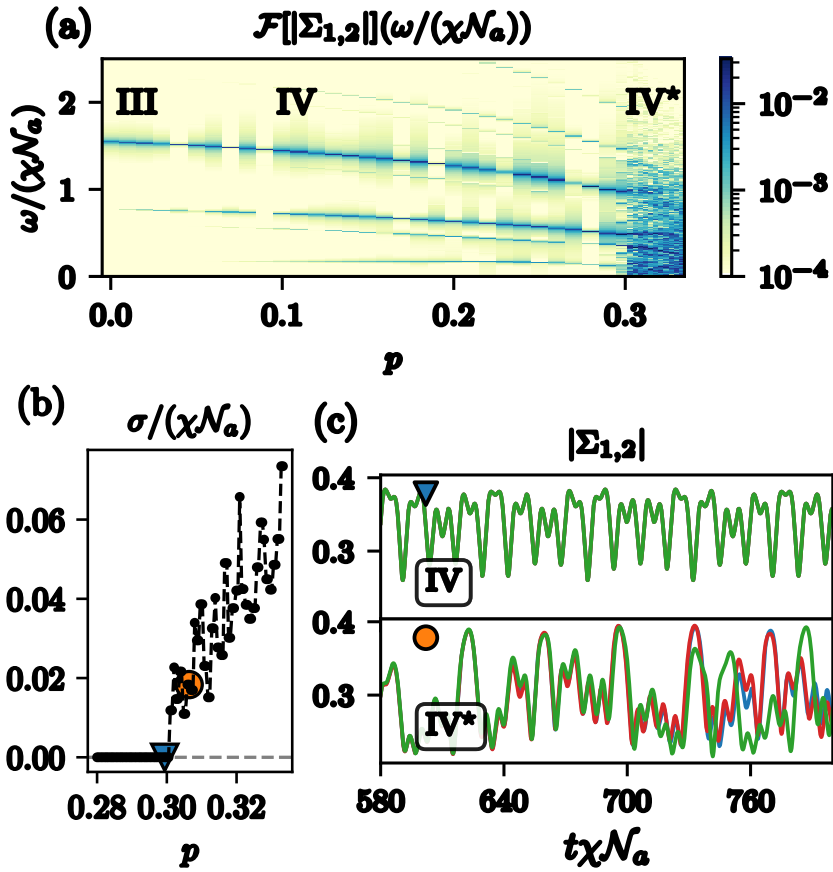


FIGURE 8.4. Dynamical response in the $N = 3$ levels spin-exchange model starting from a multimode Schrödinger cat state (cf. Eq. (8.16)) as a function of initial quantum correlations parameterized via p . We set $\mathcal{N}_a \rightarrow \infty$, $g_1/g_2 \approx 2$ and $W = 0$. (a) magnitude of the Fourier spectrum of the magnitude of the average coherence $|\Sigma_{1,2}|$ (the other $|\Sigma_{n,m}|$ behaves similarly) as a function of p , which displays a crossover from few commensurate peaks (Phase-III) to a regime with multiple incommensurate ones (Phase-IV), and eventually signals the onset of a chaotic phase (Phase-IV*). (b) Maximum Lyapunov exponent $\sigma/(\chi\mathcal{N}_a)$ as a function of p , which enables to locate the transition from a regular regime to a chaotic one at $p^* \approx 0.3$. (c) Dynamics of $|\Sigma_{1,2}(t)|$ starting from three nearly sampled initial states at two different values of $p \approx \{0.299, 0.306\}$ (marked in (b)), showing exponential sensitivity to changes in initial conditions in Phase-IV*. Image taken from Ref. [4].

an inhomogenous configuration of the local fields. Specifically, they consider a configuration such that the local fields are positive in half the sites and negative in the other half, and initializing the z -component of the spins along their corresponding local field, which is equivalent to a spatial ‘kink’. In analogy, we can notice that embedding a Schrödinger cat state is similar to the insertion of an internal ‘quantum kink’: the word ‘quantum’ highlights the presence of multi-particles entangled states, while ‘kink’ refers

to the phase-space representation of the state, which would be given by two coherent states pointing in opposite directions, but now in the internal Hilbert space of the atom.

The sharp feature in the Lyapunov exponent as a function of p in Fig. 8.4(b) looks similar to a first-order phase transition. A field theory investigation of this phenomenon is ongoing and it represents a natural and fruitful direction of outreach of our results.

8.5.3. Chaotic seeds in initial states

We now explore the option to induce a chaotic phase by initializing a fraction of the sites in a Schrödinger cat state, while keeping the other sites in a coherent state. We consider $|\psi_{\text{cat}}\rangle \sim (|\tilde{\gamma}^{(1)}\rangle + |\tilde{\gamma}^{(2)}\rangle)$ as defined in Eq. (8.16) with $p \in [0, 1/3]$. We initialize a fraction $F \in [0, 1]$ of sites in $|\psi_{\text{cat}}\rangle$ such that the initial state is

$$|\Psi\rangle = \otimes_{j=1}^{\lfloor FL \rfloor} |\psi_{\text{cat}}\rangle \otimes_{j=\lfloor FL \rfloor + 1}^L |\tilde{\gamma}^{(1)}\rangle, \quad (8.17)$$

where $\lfloor x \rfloor$ returns the least integer greater than or equal to x . The region initialized in $|\psi_{\text{cat}}\rangle$ could favor Phase-IV*, while the region initialized in a coherent state would favor a regular dynamical response (Phase-III). We observe that the chaotic region proliferates and drives the whole system into the chaotic Phase-IV* for $F \gtrsim F^*$, where F^* depends on the details of the initial state and parameters of the Hamiltonian. For the state in Eq. (8.17), $F^* \approx 0.5$ at $p \approx 1/3$. In Appendix D.3 we offer a more detailed analysis.

8.6. EFFECTS OF INHOMOGENEOUS FIELDS

Upon introducing inhomogeneous local fields ($W > 0$) the permutation symmetry is broken and the Hamiltonians in Eq. (8.1) and Eq. (8.2) cannot be straightforwardly written as a function of collective DOFs. Regardless, the dynamical responses observed in the homogeneous case ($W = 0$) are generally robust against finite inhomogeneity ($W > 0$), and we provide numerical evidence that the simple effective Hamiltonians defined in Sec. 8.4.4 describe quantitatively the many-body collective dynamics of the full model in a regime of moderate inhomogeneity W . In particular, we focus on the spin-exchange Hamiltonian in Eq. (8.2) for $\nu_{n,m} = \zeta_{n,m} = 0$,

$$H = \sum_{j=1}^L \sum_{n=1}^N h_n^{(j)} \Sigma_{n,n}^{(j)} - \sum_{m,n=1}^{N-1} \chi_{n,m} \Sigma_{n+1,n} \Sigma_{m,m+1}. \quad (8.18)$$

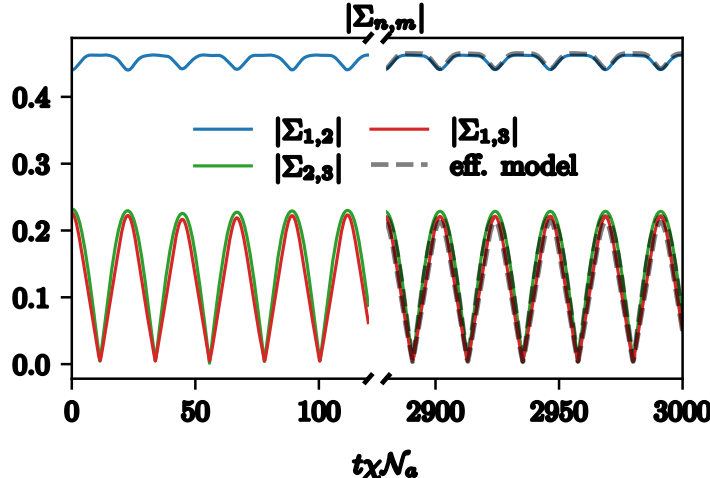


FIGURE 8.5. Dynamics of the magnitude of the average phase coherence $|\Sigma_{m,n}(t)|$ in the $N = 3$ levels spin-exchange model at fixed $g_2/g_1 \approx 10^{-2}$ and $W/(\chi\mathcal{N}_a) = 0.1$. The initial state is a permutationally invariant (in space) coherent state. The continuous lines are obtained simulating the full many-body dynamics with $L = 10^4$ sites. The dashed black lines are obtained simulating the effective model in Eq. (8.13) with parameters numerically obtained by the optimization of the cost function in Eq. (8.19). Image taken from Ref. [4].

To demonstrate the validity of the effective Hamiltonian, we numerically identify the parameters of the simple *ansatz* in Eq. (8.13) that reproduce the dynamics of collective observables. Our procedure can be summarized as follows:

- (1) we compute the time evolution of the collective observables $\Sigma_{n,m}(t)$ from the full many-body dynamics obtained via the Hamiltonian in Eq. (8.18);
- (2) we set the initial conditions $\{\tilde{\Sigma}_{n,m}(t = 0)\}$ and give a numerical ‘seed’ to the parameters $\{\tilde{h}_n, \tilde{\chi}_{n,m}, \tilde{\zeta}_{n,m}, \tilde{\nu}_{n,m}\}$ in the effective model in (8.13);
- (3) we compute the time evolution of the collective observables using the effective model in Eq. (8.13);
- (4) we vary the initial conditions and effective Hamiltonian parameters to minimize the average norm-1 distance between $\Sigma(t)$ computed in (i) and $\tilde{\Sigma}(t)$ computed using the effective model in (iii), i.e. we set as cost function

$$\epsilon_1 = \frac{1}{T} \int_0^T \sum_{n,m=1}^N |\tilde{\Sigma}_{n,m}(t) - \Sigma_{n,m}(t)| dt. \quad (8.19)$$

In Appendix D.4 we discuss the details of steps (ii) and (iv).

Since the dynamical reduction hypothesis has been extensively demonstrated to hold exactly for two-level atoms through integrability [326, 333, 370], we focus on the $N = 3$ levels case. In Fig. 8.5 we show the results obtained in the spin-exchange model at

$W/(\chi N_a) = 0.1$ by simulating the full many-body dynamics given by Eq. (8.18) (continuous line). We initialize the system in a permutation invariant coherent state (cf. Eq. (8.8)) which displays Phase-III at $W = 0$, and we consider photon-matter couplings $g_1 \neq g_2$, so that $\chi_{1,1} \neq \chi_{2,2} \neq \chi_{1,2}$ in Eq. (8.18). The black dashed lines are obtained from the numerically optimized single-body effective Hamiltonian. The dynamics of collective observables obtained via the effective Hamiltonian match well the dynamics obtained via the full many-body mean field Hamiltonian; this suggests not only that the dynamical response observed in the homogeneous case is robust, but also that the dynamical reduction hypothesis holds at finite W .

Due to exponential sensitivity to initial conditions the procedure described above does not converge with high enough accuracy in the $SU(3)$ system in the chaotic phase of Sec. 8.5.2, which however persists also for weak inhomogeneities.

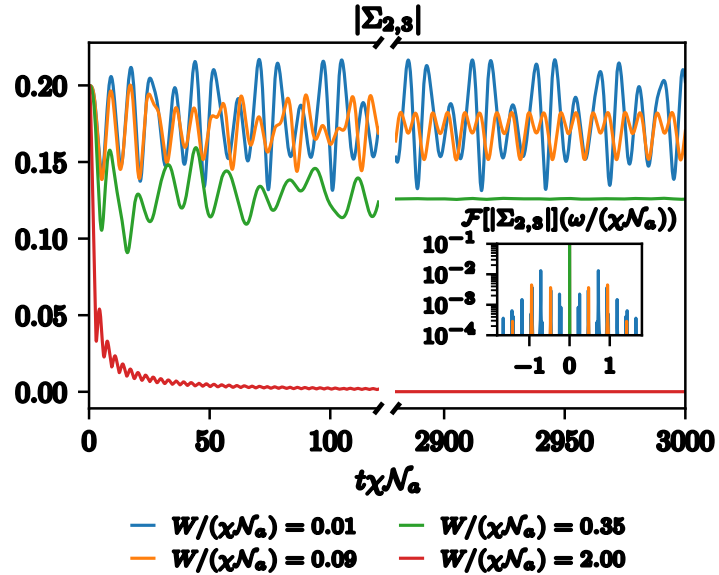


FIGURE 8.6. Dynamics of the magnitude of the average phase coherence $|\Sigma_{2,3}(t)|$ in the $N = 4$ levels spin-exchange model for $\chi_{1,2} \neq \chi_{2,3} \neq \chi_{3,4}$. The initial state is a permutation invariant (in space) coherent state. As $W/(\chi N_a)$ increases, the system displays different dynamical responses, passing from Phase-IV to Phase-III, then to Phase-II and eventually to Phase-I. The different phases are separated by crossover regions where the dynamical responses cannot be sharply identified (not shown here). In the inset we show the magnitude of the Fourier spectrum in the late time dynamics. The results shown are obtained with $L = 10^4$ sites and are not appreciably affected upon increasing L . Image taken from Ref. [4].

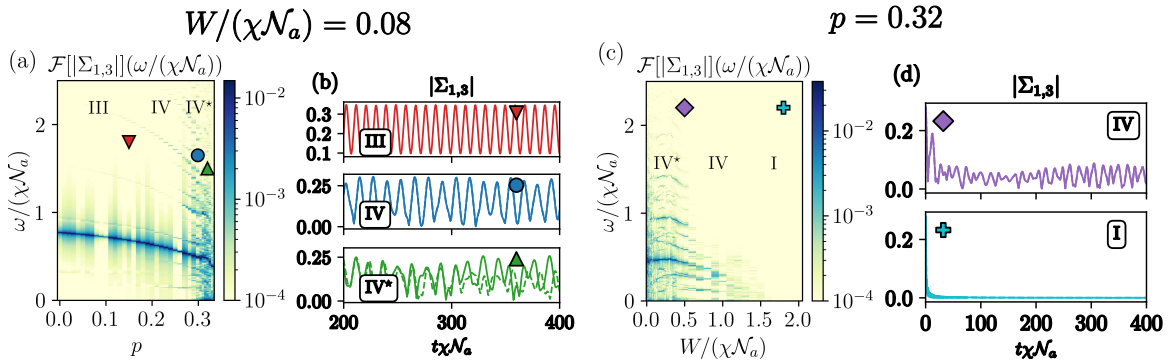


FIGURE 8.7. Dynamical response in the $N = 3$ levels spin-exchange model (Eq. (8.18)) with inhomogeneity $W/(\chi N_a)$ and $g_1/g_2 \approx 2$ ($\chi_{1,1} \neq \chi_{1,2} \neq \chi_{2,2}$), initializing a multimode Schrödinger cat state parameterized by p (cf. Eq. (8.16)) on each site. We focus on $|\Sigma_{1,3}|$; the other phase-coherences behave similarly. In the top panels we show the magnitude of the Fourier spectrum and dynamics of $|\Sigma_{1,3}|$, starting from two close-by initial states, changing p at fixed $W/(\chi N_a) = 0.08$. Instead, in the bottom panels we change $W/(\chi N_a)$ keeping $p = 0.32$ fixed. As p increases, and $W/(\chi N_a)$ is fixed, we can infer from the Fourier spectrum a crossover from a regime with well-resolved peaks with commensurate frequencies (Phase-III), to multiple peaks with incommensurate frequencies (Phase-IV) and eventually to spectrum with multiple broad peaks typical of chaotic dynamics (Phase-IV*). In (b) we show three examples of the different dynamical responses at $p = \{0.15, 0.299, 0.32\}$ (marked in the plot of the Fourier spectrum). As $W/(\chi N_a)$ increases the system passes from Phase-IV* to Phase-IV and eventually Phase-I. In the (d) panel we show the dynamics at $W/(\chi N_a) = \{0.5, 1.8\}$, corresponding to Phase-IV and I (marked in the plot of the Fourier spectrum), respectively. The results shown are obtained with $L = 10^4$ sites and are not appreciably affected upon increasing L . Image taken from Ref. [4].

8.6.1. Robustness of dynamical responses to inhomogeneities

Inhomogeneities in the local fields are generally expected to have an impact on the dynamics of collective observables. One could argue that for $W/(\chi N_a) \gg 1$ the local fields $\{h_n^{(j)}\}$ will dominate dynamics, and phase-coherences would be washed out (Phase-I). Here, we explore the dynamical responses at moderate inhomogeneity in spin-exchange Hamiltonian of Eq. (8.18) for $N = 3$ and $N = 4$ levels atoms. In the $N = 3$ levels case we initialize a multimode Schrödinger cat state on each site for which the dynamical response is chaotic (Phase-IV*) at $W = 0$. On the contrary, in the $N = 4$ levels case we consider a coherent state for which the dynamical response is aperiodic (Phase-IV) at $W = 0$. In both cases, $|\Sigma_{n,m}|$ displays dynamical responses different from Phase-I and Phase-II (relaxation) for $W/(\chi N_a) \lesssim 1$.

First, let us consider the $N = 4$ spin-exchange model in Eq. (8.18). In Fig. 8.6 we show the dynamics of $|\Sigma_{2,3}|$ for different values of inhomogeneity $W/(\chi\mathcal{N}_a)$. We fix as initial condition a permutation invariant (in space) coherent state with different amplitudes on each level. The intra-level phase coherences $|\Sigma_{n,m}|$ displays Phase-IV up to a finite value of inhomogeneity $W/(\chi\mathcal{N}_a)$. Upon increasing $W/(\chi\mathcal{N}_a)$, $|\Sigma_{n,m}|$ displays Phase-III, Phase-II and eventually Phase-I. The different dynamical responses are divided by regions (not shown in Fig. 8.6) where the distinction between the different dynamical responses becomes more blurry.

Similarly, in the $SU(3)$ case, the dynamical response generally passes from Phase- Y to Phase- $(Y - 1)$ as $W/(\chi\mathcal{N}_a)$ is increased (at fixed initial state), and with the dynamics eventually entering Phase-I due to the dominant inhomogeneous local fields (bottom panels in Fig. 8.7). Instead, as initial quantum correlations in the initial state increases with p , the dynamical response generally passes from Phase- Y to Phase- $(Y + 1)$ (top panels in Fig. 8.7). Additionally, we highlight that the dynamical responses are generally robust against small breaking of the permutation symmetry in the initial state.

The robustness of the various dynamical responses against inhomogeneous local fields for $W > 0$ can be ascribed to the many-body gap $\propto \chi\mathcal{N}_a$ that suppresses local spin flips and favors spin alignment. This mechanism has been shown to protect phase coherence in the spin-exchange model between $SU(2)$ spins [287, 303, 398], and it is likely present also in our N levels case. As W increases, this ‘many-body gap protection’ is less effective and dephasing processes between the $SU(N)$ takes over. As a result, within the framework of the dynamical reduction hypothesis, the number of effective sites required to describe dynamics is reduced and accordingly the dynamical responses change.

For instance, in the $SU(4)$ case (cf. Fig. 8.6), at moderate inhomogeneity the system has $M > 2Q$ effective DOFs, which lead to Phase-IV observed in the $W = 0$ case. As W becomes sizeable, dephasing starts to affect dynamics and, since $M \leq 2Q$, the system displays Phase-III, II and eventually I, upon increasing the degree of inhomogeneity. The effects of dephasing are apparent in the Fourier spectrum of $|\Sigma_{n,m}(t)|$ (cf. inset of Fig. 8.6), where the various Fourier components are ‘depleted’ as W increases until the whole spectrum becomes flat in Phase-I. Similarly in the $SU(3)$ case, inhomogeneity leads to a loss of effective phase-space, a reduction of the effective DOFs and correspondingly leads to a loss of chaos (the Lyapunov exponent vanishes). Along the same argument, the number of effective DOFs M increases as initial correlations in the initial state increase, thus the system could enter in a regime with different dynamical responses and eventually display chaotic behavior, as observed in the homogeneous case of Fig. 8.4. We highlight that the dynamical response displayed does not necessarily

have to pass smoothly from Phase- Y to Phase- $(Y \pm 1)$, but there can be a ‘jump’, as in the $SU(3)$ case where Phase-IV turns into Phase-I (see Fig. 8.7), without displaying Phase-III and Phase-II. This has been also reported in the integrable $SU(2)$ case [347].

8.7. EXPERIMENTAL IMPLEMENTATION

A possible experimental scheme to implement the couplings of Hamiltonian Eq. (8.2) is sketched in Fig. 8.8. Ensembles of N_a/L atoms are trapped at L fixed positions and collectively coupled to a single mode of a high finesse optical cavity with resonance frequency ω_c . At the same time, the atoms are subject to a multi-frequency laser field. The atoms are assumed to have a manifold of ground state sublevels which can be coupled using Raman transitions. If one leg of such a Raman transition is driven by a classical field while the second leg is coupled to the resonator mode, cavity-assisted Raman transitions can be implemented [286, 305, 321]. In a microscopic description, a photon from the laser field is scattered into the cavity, while the internal state of an atom in one of the ensembles is changed. The photon is delocalized over the cavity mode and can subsequently drive a second Raman transition in another atomic ensemble. In this process, the photon is absorbed by an atom and then emitted into the driving laser field via bosonic stimulation.

As example we consider ^{87}Rb atoms, where the $F = 1$ ground-state hyperfine manifold has $N = 3$ magnetic sublevels $m_F = (0, \pm 1)$. A sufficiently strong applied magnetic field leads to a non-degenerate level splitting due to linear and quadratic Zeeman shifts, as sketched in the figure. In combination with a two-frequency transverse laser field, this allows to drive state-selective, cavity assisted two-photon Raman transitions between these states, as indicated in Fig. 8.8b. The laser field is far detuned from atomic resonance to avoid any spontaneous decay of the excited atomic state. The frequencies ω_+ and ω_- of the transverse laser field are chosen to match the different atomic level splittings when a photon is absorbed from or emitted into the cavity mode. For example, an atom at a specific site can be transferred from $m_F = 0$ to $m_F = -1$ by absorbing a photon from the laser field at frequency ω_- and emitting a photon into the cavity. The very same cavity photon can then drive a transition at a different site where an atom in $m_F = 0$ absorbs that photon and undergoes a transition to $m_F = +1$ while emitting into the laser field at frequency ω_+ . These two-photon Raman transitions correspond to the processes proportional to g_n in Hamiltonian Eq. (8.2), where the coupling strengths g_n can be engineered via the single-photon Rabi frequencies Ω_+ and Ω_- .

The co-rotating terms proportional to λ_n in Hamiltonian Eq. (8.2) can be implemented

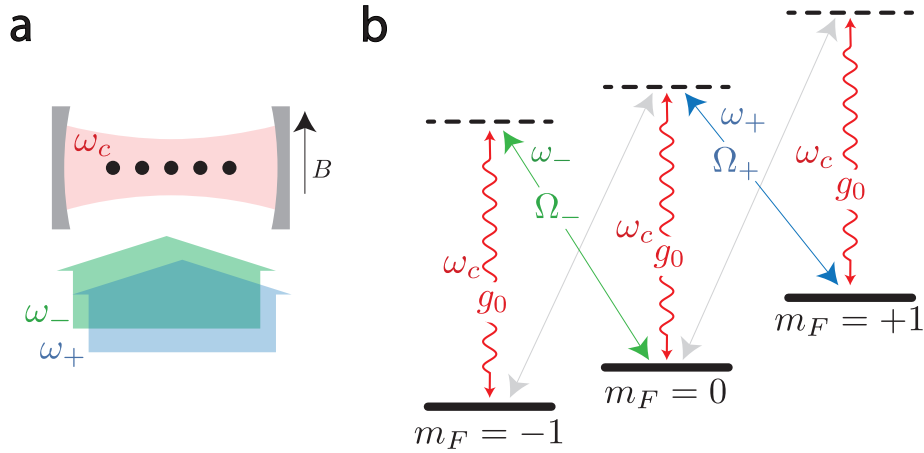


FIGURE 8.8. Suggested experimental implementation. (a) Ensembles of 3-level atoms in L traps (black dots) are coupled to a single mode of an optical cavity (red) and transversely illuminated by a two-frequency laser field (blue, green). (b) The applied magnetic field B leads to a non-degenerate atomic level splitting allowing to selectively drive cavity-assisted Raman transitions. Coupling via the transverse laser fields (the cavity) are shown as solid (wiggly) arrows. If additional frequency components (grey arrows) are introduced, co- and counter-rotating terms can be engineered. Image taken from Ref. [4].

if additional laser frequencies are added to the transverse laser field. Such couplings are indicated by the grey arrows in Fig. 8.8b. The relative strengths of the co- and counterrotating terms can be independently tuned via the respective Rabi rates of the driving laser fields [321].

This scheme can further be extended to $N > 3$ by choosing atomic states with larger magnetic sublevel manifolds as they can be found for example in lanthanide atoms. Finally, site dependent energies $h_n^{(j)}$ of the atomic modes can be introduced by applying a magnetic field gradient along the cavity axis in addition to the homogeneous magnetic field [323, 399]. In a realistic scenario also cavity decay due to losses at the mirrors has to be taken into account. Its influence can however be reduced by introducing a detuning between the cavity resonance and the frequency of the field scattered into the cavity mode.

8.8. DISCUSSION

 8.8.1. *Role of dissipation*

In our analysis we have considered the system completely isolated from the environment. In cavity-QED systems there are two main sources of dissipation, free-space emission of single-atom excitations and loss of the cavity field. Let us denote the rates of the two processes with η and κ , respectively, and their jump operators with $\hat{L}_n^{(j)} = \sqrt{\eta} \hat{\Sigma}_{n,n+1}^{(j)}$ and $\hat{L} = \sqrt{\kappa} \hat{a}$, where $j \in [1, L]$ and $n \in [1, N - 1]$. The relevant time scales for the coherent dynamics are set by the collective photon-matter couplings $\lambda_n \sqrt{\mathcal{N}_a}$ and $g_n \sqrt{\mathcal{N}_a}$. The different dynamical responses can be dominantly ascribed to Hamiltonian dynamics if $\lambda_n \sqrt{\mathcal{N}_a}, g_n \sqrt{\mathcal{N}_a} \gg \kappa, \eta$.

We provide a more accurate estimate in the far detuned cavity mode regime, where all our results have been derived. Focusing on the $SU(N)$ spin-exchange case for simplicity, the photon effectively induces elastic all-to-all interactions of strength $\chi_{n,m} = g_n g_m \omega_0 / ((\omega_0^2 + (\kappa/2)^2)$; in addition, the collective atomic transitions are radiatively broadened by the coupling to the cavity, leading to collective decays with rate per-particle $\Gamma_n = g_n^2 \kappa / (\omega_0^2 + (\kappa/2)^2)$ [273–277]. The coherent dynamics are fast with respect to the time scales of the dissipation if $\mathcal{N}_a \chi_{n,m} \gg \{\mathcal{N}_a \sqrt{\Gamma_n \Gamma_m}, \eta\}$, which translate to $\omega_0 \gg \kappa$ and $\mathcal{N}_a \chi_{n,m} \gg \eta$ (see Appendix D.5 for the complete derivation). In this parameters' regime, dynamics are basically ruled only by coherent evolution, at least up to times parametrically large in ω_0/κ and $\mathcal{N}_a \chi_{n,m}/\eta$.

 8.8.2. *Connection with $SU(N)$ fermionic systems*

As already anticipated in Sec. 8.3.1, the number of atoms per site \mathcal{N}_a/L is a conserved quantity in our system and our results can be extended to a large class of systems which can be mapped to the Hamiltonians in Eqs. (8.1) and (8.2). As an example, let us consider a N -level fermionic system with annihilation (creation) operators $\hat{c}_{n,j}^{(\dagger)}$ with $n \in [1, N]$ and site index j . We can define the pseudospins $\hat{\Sigma}_{n,m}^{(j)} \equiv \hat{c}_{n,j}^\dagger \hat{c}_{m,j}$ [265], which in turn can be expressed in terms of Schwinger bosons as $\hat{\Sigma}_{n,m}^{(j)} = \hat{b}_{n,j}^\dagger \hat{b}_{m,j}$. If via this procedure the fermionic Hamiltonian as a function of the Schwinger bosons is identical to one of the Hamiltonians here investigated, our results obtained via coherent states could be applied straightforwardly. Indeed, the mean field at the level of the Schwinger bosons is mathematically equivalent to simulating pure single-particle states $|\psi_j\rangle = \sum_{n=1}^N \langle \hat{b}_{n,j} \rangle |n_j\rangle$, with the caveat of interpreting the bosonic amplitudes as probability amplitudes [288].

8.8.3. *Roadway towards a universal dynamical reduction hypothesis*

Here, we have formulated and tested a reduction hypothesis for the dynamics of $SU(N)$ cavity QED systems with atoms in a multilevel ladder configuration. We found that the reduction hypothesis was a useful description for a variety of systems with different initial states, levels, inhomogeneous fields, and light matter interactions. This plethora of applications calls naturally for a broader framework. Our classification of dynamical responses based on the dynamical reduction hypothesis and the Arnold-Liouville theorem might possess the flavor of universality. It would be in fact extremely interesting to encompass all the specific examples mentioned above, under the lenses of the symmetries both of the local DOFs and of the light-matter interactions. Similarly to renormalization group approaches, one could explore the basins of attraction of the effective few-body models presented here. Upon changing the symmetries and the conservation laws of a given macroscopic model, one could expect to distinguish a set of irrelevant perturbations in which the reduction hypothesis remains valid, and set of relevant perturbations in which the reduction hypothesis fails and no effective few-body model describes the dynamics of collective observables.

From our numerical experiments it seems natural that perturbations that do not dramatically change the long-range nature of the interactions would be irrelevant. We would therefore expect similar dynamical responses in the presence of different photon-assisted transitions (e.g. from the n -th level to any m -th level via a single-photon process), or of squeezed terms (e.g. $\propto (b^\dagger b^\dagger a + h.c.)$), where the information about the state cannot be retrieved solely by the $SU(N)$ coherences, but would also require terms such as $\langle b^\dagger b^\dagger \rangle$ [322]. Investigations into the latter perturbations might disclose connections between multi-mode squeezing and the generation of universal dynamical responses. It is also completely natural to investigate the impact of different level configurations, for instance, studying the case of two degenerate subspaces of excited and ground states [278, 279, 354]. A preliminary analysis suggests that they are also irrelevant perturbations and that a reduction hypothesis still holds here. Finally we note that $SU(N)$ generalizations of BCS models [349–352] would, under a generalized Anderson pseudo-spin mapping, have a similar form as to the models we study here and also be describable by a reduction hypothesis.

In contrast, any perturbation that introduces short range interactions could be expected to be relevant to the effective few-body Hamiltonian basin of attraction. This appears to be the case in the context of time crystals [324, 325, 400–403], where short range interactions generally melt the time crystal at late times and lead to generically

asynchronous relaxation. Separability of the interactions will also likely play a role: systems with separable interactions seem describable by an effective few-body model [336, 404]; while models with inseparable interactions can lead to glassy relaxation [405–407] and cannot be described by effective few-body models [404, 408]. Furthermore, systems with a number of atomic levels comparable to the number of sites, $N \sim L$, may also pose obstacles in defining an effective few-body theory, but could be relevant for experiments in synthetic dimensions [353, 354]. Naturally the effects of dissipation would also not be captured by a few-body Hamiltonian picture, but instead potentially be described by a few-body dissipative model such as a Lindblad master equation.

The strong numerical-oriented approach we have taken here has provided serious evidence of a description using an effective few-body model, even demonstrating a near perfect ability to capture the dynamics of collective observables. Still, an analytic approach could yield important insights and provide a more solid ground for classifying different perturbations as relevant or irrelevant to the few-body attractive basin. Considering the variety of AMO systems modeled by collective interactions, finding such description would constitute a significant step forward in understanding universality out of equilibrium [409, 410].

APPENDIX A

Supplemental information for Chapter 3

A.1. ROLE OF ON-SITE DENSITY-DENSITY INTERACTION

In Chapter 3, we focus on a simplified version of the model without on-site density-density interactions, to keep to a minimum the amount of technical details in the course of the presentation. In the following, we address the role of on-site density-density interactions, focusing on the localization properties of the ground state and comparing them with the statements in Chapter 3 resulting from numerics performed at $U > 0$ and $\epsilon = 0$.

Starting from the Hamiltonian in Eq. (3.5), we consider $U = 0$ and $\epsilon \geq 0$. For $\epsilon = 0$, the model does not display localization at finite s in the bosonic limit, as extensively discussed in Sec. 3.2. On the other hand, for $\epsilon > 0$, the ground state is localized for $s > s_c$ in the bosonic limit, with s_c being parametrically small in ϵ . We perform the same scaling analysis as a function of the cutoff Λ discussed in Sec. 3.2. In Fig. A.1, we show the inverse of the localization length ξ swiping s for different values of Λ at fixed ϵ . The scaling analysis suggests that the transition point $s_c(\Lambda, \epsilon)$ converges to a finite value independent of Λ for $\Lambda \rightarrow \infty$. The overall qualitative picture is therefore unaffected if one considers on-site or nearest-neighbor nonlinearities.

A nonzero value of ϵ introduces, however, anharmonic spacings between ground states with different values of n_0 . Indeed, we have, for the energy of the ground state, $E(n_0) \approx n_0/2 + \epsilon n_0^2/2$. This additional anharmonicity has an impact on the adiabatic protocol discussed in Sec. 3.3, since each adiabatically evolved state $\mathcal{U}|n_0\rangle_0 \otimes \bigotimes_{j>0} |0\rangle_j$ in Eq. (3.17) would acquire a phase with a nonlinear dependence in n_0 , which technically complicates state preparation without altering the main physical message. Nonetheless, it is still possible to tame the effect of this nonlinearity by considering a small enough ϵ , at the cost of having a smaller e^{-s} (larger s) and therefore working effectively deeper in the localized phase. These types of unnecessary technical complications are at the root of our choice of working throughout the main text with $\epsilon = 0$ and $U > 0$.

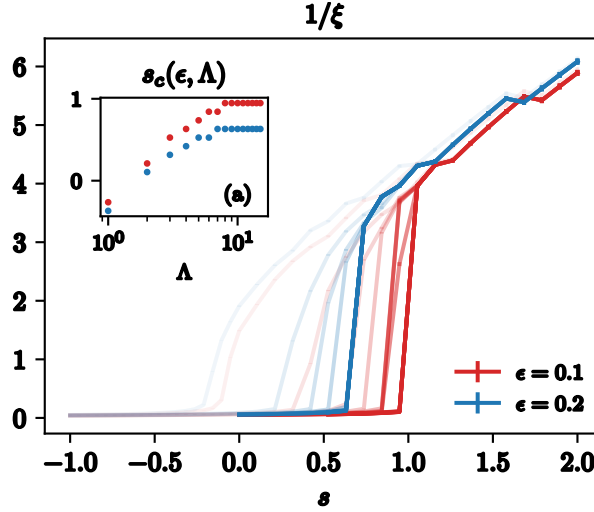


FIGURE A.1. The inverse of the localization length ξ in a system of $L = 15$ “active” sites in the symmetry sector $n_0 = 1$, $\beta_r=0$. The main plot shows the inverse of the localization length ξ^{-1} as a function of s for different values of $\Lambda \in [1, 15]$ and ϵ at $U = 0$. The darker lines correspond to larger values of Λ . The inset (a) shows the behavior of $s_c(\epsilon, \Lambda)$ as a function of Λ for $\epsilon = 0.1$ (red) and $\epsilon = 0.2$ (blue) at $U = 0$. Image taken from Ref. [1].

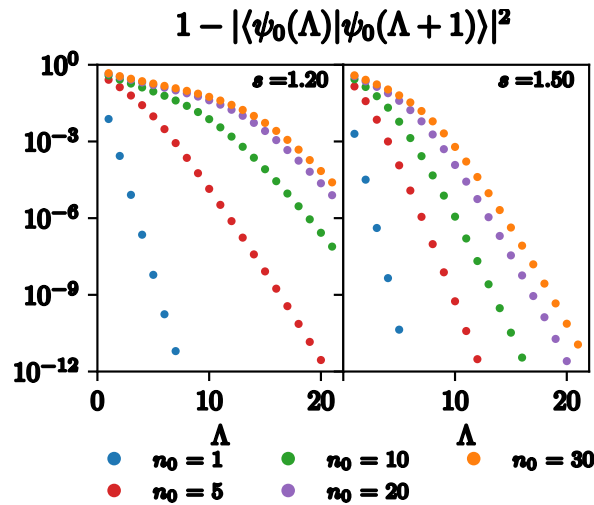


FIGURE A.2. The scaling analysis of $1 - |\langle \psi_0(\Lambda) | \psi_0(\Lambda + 1) \rangle|^2$ as a function of Λ at fixed $U = 0.1$ and $s = \{1.2, 1.5\}$ for different values of $n_0 \in [1, 30]$. The dots and squares refer to the numerical results obtained at $s = 1.2$ and $s = 1.5$, respectively. The overlap tends exponentially fast to 1 in Λ . The decay is slower as n_0 increases at fixed s and U . Image taken from Ref. [1].

A.2. SCALING ANALYSIS IN Λ

In the main text, we show that the bosonic system displays a delocalized-localized transition at finite s if $U > 0$. Here, we show that the ground state is not only localized but it is weakly dependent on the physical cutoff Λ . This provides quantitative proof that we can investigate the bosonic system with a finite Λ in the localized phase.

We fix the symmetry sector n_0 and $(s > s_c(U), U > 0)$ in the localized phase. We compute $|\psi_0(\Lambda)\rangle$ for different values of Λ . We calculate $1 - |\langle\psi_0(\Lambda)|\psi_0(\Lambda+1)\rangle|^2$ as a function of Λ (see Fig. A.2). The fidelity $|\langle\psi_0(\Lambda)|\psi_0(\Lambda+1)\rangle|^2$ approaches 1 exponentially fast in Λ . The more the system is in the localized phase and n_0 is small, the faster is the convergence. This gives the first evidence that the ground state of the actual bosonic system is well described with small effective cutoffs.

We compute the variance of the Hamiltonian given in Eq. (3.1) over the ground state $|n_0\rangle_0 \otimes |\psi_0(\Lambda)\rangle$, taking into account the bosonic nature of the original Hamiltonian in Eq. (3.1). This quantity is exactly zero if the state $|n_0\rangle_0 \otimes |\psi_0(\Lambda)\rangle$ is an eigenstate of H . We aim to see how this quantity goes to zero as a function of Λ . In order to do so, we write the Hamiltonian given in Eq. (3.1) as the sum of two terms $H = H_- + H_+$. H_- acts on the Hilbert space spanned by states with an occupation number up to Λ , while H_+ acts on the Hilbert space spanned by states with an occupation number greater than Λ . We label the sectors on which H_\pm acts nontrivially as the \mathcal{H}_\pm sectors, respectively. We apply the same procedure to the number operator and the annihilation(creation) operator:

$$\begin{aligned}\hat{n} &= \sum_{k=0}^{\Lambda} k |k\rangle\langle k| + \sum_{k=\Lambda+1}^{\infty} k |k\rangle\langle k| \\ &= \hat{n}_- + \hat{n}_+, \\ \hat{a} &= \sum_{k=0}^{\Lambda} \sqrt{k} |k-1\rangle\langle k| + \sum_{k=\Lambda+1}^{\infty} \sqrt{k} |k-1\rangle\langle k| \\ &= \hat{a}_- + \hat{a}_+.\end{aligned}\tag{A.1}$$

The commutator $[\hat{n}_-, \hat{n}_+] = 0$, while $[\hat{a}_-, \hat{a}_+] = \sqrt{\Lambda(\Lambda+1)} |\Lambda-1\rangle\langle\Lambda+1| \neq 0$. This is because the operators $\hat{a}_\pm^{(\dagger)}$ connect the two sectors \mathcal{H}_\pm . From Eq. (A.1), we straightforwardly obtain the expressions for H_\pm :

$$\begin{aligned}H_\pm &= -\frac{1}{2} \sum_i \hat{n}_{i,\pm} \left[e^{-s} \left(\hat{a}_{i+1,\pm}^\dagger + \hat{a}_{i+1,\pm} \right) + \right. \\ &\quad \left. - U \hat{n}_{i+1,\pm} - 1 \right].\end{aligned}\tag{A.2}$$

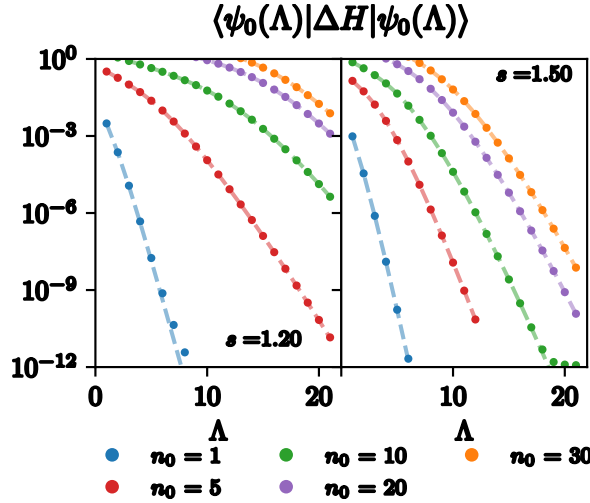


FIGURE A.3. The scaling analysis of $\langle \psi_0(\Lambda) | \Delta H | \psi_0(\Lambda) \rangle$ as a function of Λ at fixed $U = 0.1$ and $s = \{1.2, 1.5\}$ for different values of $n_0 \in [1, 30]$. The dots refer to the numerical results. The dashed lines are the analytical estimation given by Eq. (A.4). The variance ΔH decays exponentially fast in Λ . The decay is slower as n_0 increases at fixed s and U . Image taken from Ref. [1].

In our numerical scheme, we fix a finite cutoff Λ . Therefore we are computing the ground state $|\psi_0(\Lambda)\rangle$ of H_- . Since \hat{a}_\pm are noncommuting operators, the two Hamiltonians H_- and H_+ do not commute as well. Therefore, it is not ensured that $|\psi_0(\Lambda)\rangle$ is an eigenstate of the full Hamiltonian H . We compute the variance ΔH over $|\psi_0(\Lambda)\rangle$ of the Hamiltonian $H = H_- + H_+$,

$$\Delta H = \langle H_+ H_+ \rangle + \langle \{H_+, H_-\} \rangle + \langle H_- H_- \rangle - \langle H \rangle^2, \quad (\text{A.3})$$

to check whether $|\psi_0(\Lambda)\rangle$ is an eigenstate of H . The terms in H_\pm that preserve the sectors \mathcal{H}_\pm give a zero contribution in Eq. (A.3). Indeed, the ones that keep the system in the \mathcal{H}_- sector give a zero contribution since $|\psi_0(\Lambda)\rangle$ is an eigenstate within this sector by definition. Instead, the ones that keep the system in the \mathcal{H}_+ sector trivially give zero since we do not have any occupation larger than Λ . The only contribution comes from the operators $\hat{a}_\pm^{(\dagger)}$ or, more precisely, the term $(\sqrt{\Lambda + 1}|\Lambda + 1\rangle\langle\Lambda| + h.c.)$ which connects the two sectors. Using Eq. (A.2), we straightforwardly obtain

$$\Delta H = \Lambda \frac{e^{-2s}}{4} \sum_{j=0}^{L-1} \langle n_j^2 \rangle \langle \mathcal{P}_{j+1, \Lambda} \rangle, \quad (\text{A.4})$$

where $\mathcal{P}_{j,k} = |k\rangle_{jj}\langle k|$ is the projector on the Fock state with occupation k on site j . The first term of the sum ($j = 0$) encodes the information about the fixed symmetry sector, since $\langle \hat{n}_0^2 \rangle = n_0^2$. The variance given in Eq. (A.4) depends on the mean occupation number and on the projector over the Fock space on Λ . In the main text, we show that the system displays a localized phase in the bosonic limit, $\Lambda \rightarrow \infty$, if $U > 0$. This

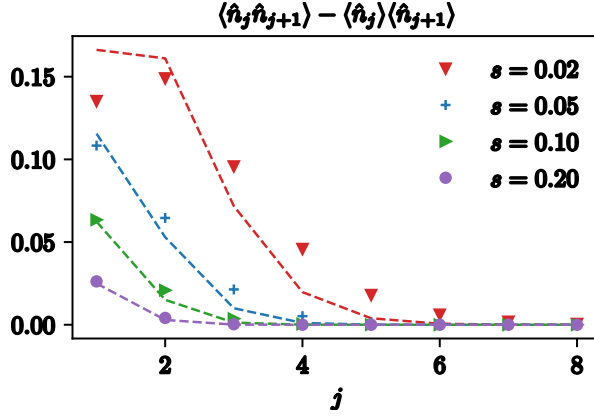


FIGURE A.4. The points correspond to the quantity computed on the ground state obtained via the DMRG; the continuous lines are the results obtained assuming that the state is Gaussian. We fix $U = 1$, $n_0 = 1$, and $\Lambda = 15$. Image taken from Ref. [1].

enables us to estimate Eq. (A.4) in the localized phase. In the localized phase, the average occupation number of the ground state is $\langle \hat{n}_j \rangle \sim e^{-j/\xi}$ (cf. Eq. (3.6)). The exponential decay of the occupation number along the chain reflects on the behavior of the expectation value of $\mathcal{P}_{k,j}$, which decays exponentially fast in k (cf. Eq. (3.7)). Therefore, the series in Eq. (A.4) is finite for $\Lambda \rightarrow \infty$ and $L \rightarrow \infty$, since each term is exponentially suppressed. In Fig. A.3, we numerically compute the variance ΔH over $|\psi_0(n_0, \Lambda)\rangle$ for different values of Λ and n_0 . Rigorously, the cutoff Λ limits the accessible n_0 , since $\langle \hat{n}_i \rangle \leq \Lambda$. Nevertheless, because n_0 appears as a constant in the Hamiltonian, we can also compute the ground state $|\psi_0(n_0, \Lambda)\rangle$ for $n_0 > \Lambda$. The numerical results match Eq. (A.4) perfectly. The variance goes exponentially fast to zero. Therefore, an eigenstate of H_- is an eigenstate of the fully bosonic system as well, with a reasonably small cutoff Λ when $U > 0$.

A.3. GAUSSIANITY AND NON-GAUSSIANITY IN THE GROUND STATE

In Fig. A.4, we show the correlator $\Delta_j = \langle \hat{n}_j \hat{n}_{j+1} \rangle - \langle \hat{n}_j \rangle \langle \hat{n}_{j+1} \rangle$ as a function of j for different values of s at fixed $U = 1$. We compare Δ_j computed on the ground state obtained via the DMRG and the one computed assuming that the same state is Gaussian in the operators $\{\hat{a}_j^{(\dagger)}\}_{j=1}^L$, which we call Δ_j^G .

A.4. NUMERICAL METHODS

In this appendix, we provide the details of the parameters adopted for simulating a single stochastic trajectory at the core of the quantum trajectories method, while we refer to Ref. [168, 169] for details of the algorithm. As stated in the main text, we resort to tensor networks in order to numerically integrate a single trajectory. The deterministic part of the dynamics given by the action of the effective Hamiltonian defined in Eq. (3.29) is performed via the time-evolving block-decimation (TEBD) algorithm with second-order Suzuki-Trotter decomposition. When a jump occurs, the corresponding jump operator is easily applied being a single-site gate. We fix a time step $\delta t = 5 \times 10^{-3}$, a maximal bond dimension $\chi_{\max} = 75$ and we keep the singular values greater than 10^{-10} . We verify that the results are not affected by the time step δt and χ_{\max} . All the simulations are performed using the ITensor library [411].

APPENDIX B

Supplemental information for Chapter 4

B.1. DYNAMICS OF ENTANGLEMENT ENTROPY IN THE QUANTUM EAST MODEL

In Fig. 4.3(a) we have located a state-dependent mobility edge for initial product states using the time-complexity as an indicator. Specifically, we used the way the max bond-dimension χ_{\max} grows in time as an indicator to identify states whose dynamics are ‘hard’ or ‘easy’ to simulate. Based on this, we located a ‘hard’ and ‘easy’ regime as a function of the Hamiltonian parameters and energy density of the initial state. Here we present the data for the growth of max entanglement entropy (S_{\max}) which is the largest value of von Neumann entropy across all bipartitions of the state. Due to the

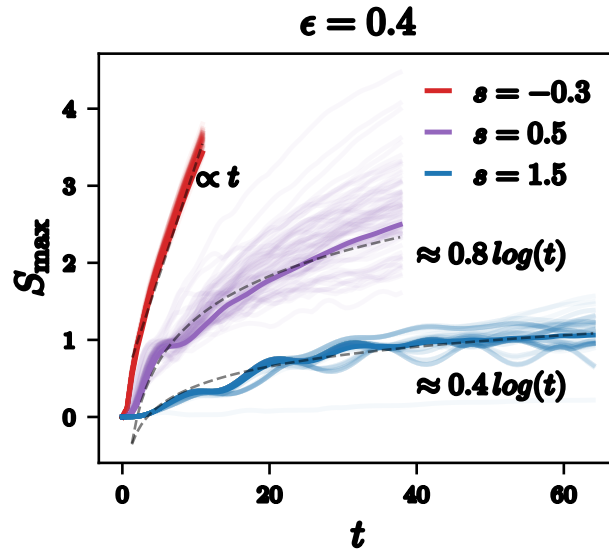


FIGURE B.1. Dynamics of the maximum entanglement entropy of ~ 100 product states (cf. Eq. (4.3)) at fixed normalized energy $\epsilon = (\langle H \rangle - E_{\min})/(E_{\max} - E_{\min}) = 0.4$ and different values of s . Deep in the delocalized phase ($s = -0.3$), we observe a linear growth of S_{\max} as expected for typical thermalizing systems. Instead, in the localized phase ($s > 0$), we observe a logarithmic growth of S_{\max} with a coefficient parametrically small in s . This indicates the presence of localization and the suppression of the spread of entanglement rate in the system with increasing and positive s . Image taken from Ref. [2].

connection between the MPS representation of the state and the entanglement entropy ($S \sim \log \chi$), we expect that an exponential growth of χ ($\chi \propto e^{rt}$) translates to a linear growth of S ($S \propto t$), while instead a polynomial growth of χ ($\chi \propto t^\alpha$) translates to a logarithmic growth of S ($S \propto \log(t)$).

In Fig. B.1, we show the dynamics of S_{\max} for a sample of initial product states at a fixed $\epsilon = 0.4$ and different s . We perform linear ($\propto t$) and logarithmic ($\propto \log(t)$) fits. For states deep in the delocalized regime ($s = -0.3$), we have a linear growth of S_{\max} , which is expected in the thermal regime. It also supports the data presented in Fig 4.3(b), where we observe exponential growth of χ_{\max} for $s = -0.3$. In the localized phase $s > 0$, we observe logarithmic growth of S_{\max} . This behavior indicates the presence of localization and non-thermal properties and suppression of the rate at which entanglement spreads in the state upon increasing s . The logarithmic growth in the $s > 0$ regime agrees with data in Fig 4.3(b) where we get polynomial growth of χ_{\max} for the displayed values of s and ϵ .

B.2. FINITE SIZE SCALING

In Sec. 4.4.1, we have provided evidence of a so-called ‘state-dependent mobility edge’ in the spin version of the quantum East model. We studied the model on a system size of $L = 30$, and the way the max bond-dimension χ_{\max} grows in time was used as an indicator to classify ‘hard’ or ‘easy’ regimes. Here, we perform a finite-size scaling analysis to ensure that our results are unaffected by the system size considered.

As we have established that the spatial structure plays a vital role in the dynamics, particularly in the crossover regime, we investigate the dynamics of product states for different system sizes L , being careful in keeping the spatial structures. Also, we consider states having the same energy density $\epsilon = (\langle \psi | \hat{H} | \psi \rangle - E_{\text{GS}}) / (E_{\max} - E_{\text{GS}})$ as we tune the system size L .

In Fig. B.2(a) we show the dynamics of the max bond-dimension χ_{\max} for different values of L and energy density ϵ . Each curve with a specific color consists of five overlapping curves for system size $L \in [30, 60, 90, 120, 150]$, which cannot be distinguished due to the absence of finite-size effects at the timescales reached. The overlap gives a clear indication that our results are unaffected by the system size considered. Figs. B.2(b-c) show the data for the extracted growth rates r and α from these product states for different ϵ and L . Fig. B.2(b) shows the exponential growth rate r as a function of system size L , whereas Fig. B.2(c) shows the power-law exponent α as a

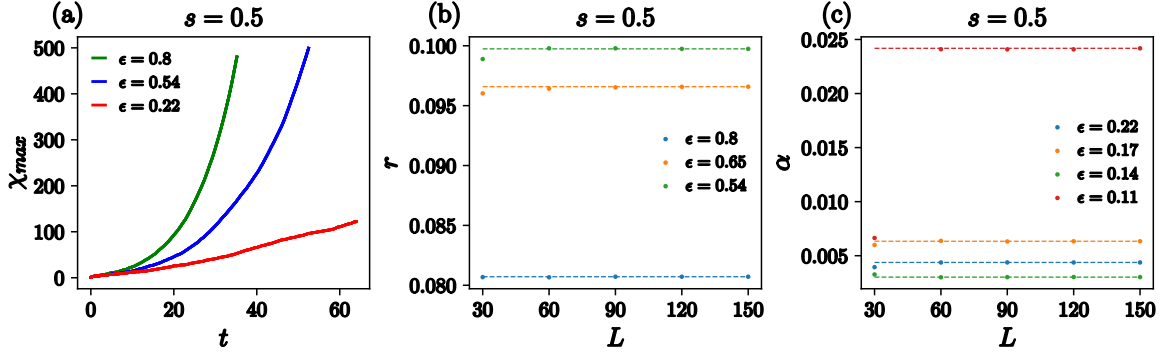


FIGURE B.2. Dynamics of product states (cf. Eq. (4.3)) with similar spatial structure and same ϵ are initialized across different system sizes $L \in [30, 60, 90, 120, 150]$. (a) Evolution of χ vs t for different ϵ , and each color consists of five overlapping plots for $L \in [30, 60, 90, 120, 150]$, which cannot be distinguished due to the absence of finite-size effects. (b) Extracted exponential growth rate r as a function of L for different ϵ . (c) Extracted power-law α as a function of L for different ϵ . Both r and α are independent of the system size L , indicating the insensitivity of our results to finite-size effects. Image taken from Ref. [2].

function of system size L . It's clear that the growth rates are constant and unaffected by finite-size effects.

B.3. ROLE OF EQUILIBRIUM LOCALIZATION LENGTH ξ

In Sec. 4.4.4 we have used the localization length of the ground state ξ as a typical length scale also out-of-equilibrium. By doing so, we were able to address the key role of the spatial structure of the states in the localized phase ($s > 0$). To further prove the predictive power of ξ , in Fig. B.3 we show the same data as in Fig. 4.4 but without ξ . We see that the ‘hard’ and the ‘easy’ states completely overlap and we are not able to differentiate between different complexity regimes. Such observation highlights the key role of the localization length ξ of the ground state in governing the dynamics of product states, even at finite energies.

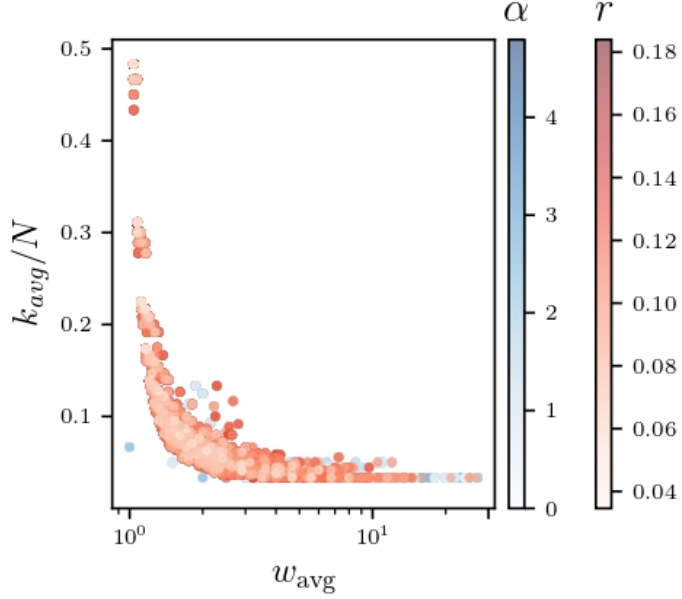


FIGURE B.3. Same data presented in Fig. 4.4 but without rescaling the distance between cluster excitations w , i.e. the number of consecutive $|0\rangle$, and the average size of the clusters k_{avg} , i.e. the number of excitations $|1\rangle$, with the localization length ξ of the ground state at the corresponding s . The red dots correspond to ‘hard’ (exponential growth) states with r the corresponding rate. The blue dots correspond to ‘easy’ (polynomial growth) states with α as the power-law exponent. Both ‘hard’ and ‘easy’ states overlap because the effect of ξ on growth dynamics is not considered, highlighting the key role of ξ also out-of-equilibrium. Image taken from Ref. [2].

APPENDIX C

Supplemental information for Chapter 7

C.1. PERTURBATIVE CONSTRUCTION OF THE GENERATOR S OF THE SCHRIEFFER-WOLFF TRANSFORMATION

We write the Hamiltonian H_0 and the perturbation V as a function of the operators $\hat{c}_{\ell,j}^{(\dagger)}$ defined in Eq. (7.4)

$$H_0 = \sum_{j=1}^L \sum_{\ell=0}^{\infty} \omega_{\ell,j} |\ell, j\rangle \langle \ell, j| \equiv \sum_{j=1}^L \sum_{\ell=0}^{\infty} \omega_{\ell,j} p_{\ell,j}, \quad V = g \sum_{j=1}^{L-1} \sum_{\ell,s=0}^{\infty} (c_{\ell,j}^{\dagger} c_{s,j+1} + h.c.), \quad (\text{C.1})$$

where $\omega_{\ell,j} = (\omega_j - E_C/2) j + E_C j^2/2$ and we introduce $p_{\ell,j} \equiv |\ell, j\rangle \langle \ell, j|$ for convenience. We compute the generator $\eta = [H_0, V]$

$$\eta = \sum_{j=1}^L \sum_{\ell,s=0}^{\infty} g (\tilde{\Delta}_{\ell,j+1} - \tilde{\Delta}_{s,j}) (c_{s,j}^{\dagger} c_{\ell,j+1} - c_{s,j} c_{\ell,j+1}^{\dagger}), \quad (\text{C.2})$$

where $\tilde{\Delta}_{\ell,j} = \omega_{\ell+1,j} - \omega_{\ell,j} = (\omega_j + E_C \ell)$. Following Ref. [270], the *ansatz* for the generator S of the SW transformation is $S = \sum_{j=1}^L \sum_{\ell,s} A_{j,\ell,s} (c_{s,j} c_{\ell,j+1}^{\dagger} - c_{s,j}^{\dagger} c_{\ell,j+1})$. We compute $[S, H_0]$ and we impose $[S, H_0] = -V$. This condition is satisfied if $A_{j,\ell,s} = g / (\tilde{\Delta}_{\ell,j+1} - \tilde{\Delta}_{s,j})$. Therefore

$$S = \sum_{j=1}^{L-1} S_{j,j+1}, \quad S_{j,j+1} \equiv \sum_{\ell,s=0}^{\infty} \frac{g}{\tilde{\Delta}_{\ell,j+1} - \tilde{\Delta}_{s,j}} (c_{s,j} c_{\ell,j+1}^{\dagger} - c_{s,j}^{\dagger} c_{\ell,j+1}). \quad (\text{C.3})$$

C.2. COMMUTATOR OF THE HAMILTONIAN WITH THE GENERATOR S OF THE SCHRIEFFER-WOLFF TRANSFORMATION

We write the perturbation $V = \sum_{j=1}^{L-1} V_{j,j+1}$, where $V_{j,j+1} = g \sum_{\ell,s=0}^{\infty} (c_{\ell,j}^\dagger c_{s,j+1} + h.c.)$. We compute the commutators $[S_{j-1,j}, V_{j,j+1}]$, $[S_{j,j+1}, V_{j,j+1}]$ and $[S_{j-1,j}, V_{j,j+1}]$

$$\begin{aligned}
[S_{j,j+1}, V_{j,j+1}] &= \sum_{\ell,s} \frac{2g^2 E_C}{(\tilde{\Delta}_{\ell+1,j+1} - \tilde{\Delta}_{s,j})(\tilde{\Delta}_{\ell,j+1} - \tilde{\Delta}_{s+1,j})} c_{s,j} c_{s+1,j} c_{\ell+1,j+1}^\dagger c_{\ell,j+1}^\dagger + \\
&+ \sum_{\ell,s} \frac{g^2}{\tilde{\Delta}_{\ell-1,j+1} - \tilde{\Delta}_{s,j}} \ell p_{s,j} p_{\ell,j+1} + \\
&+ \sum_{\ell,s} \frac{2g^2 E_C}{(\tilde{\Delta}_{\ell-1,j+1} - \tilde{\Delta}_{s,j})(\tilde{\Delta}_{\ell,j+1} - \tilde{\Delta}_{s-1,j})} s \ell p_{s,j} p_{\ell,j+1} + \\
&- \sum_{\ell,s} \frac{g^2}{\tilde{\Delta}_{\ell,j+1} - \tilde{\Delta}_{s-1,j}} s p_{s,j} p_{\ell,j+1} + h.c. , \\
[S_{j,j+1}, V_{j-1,j}] &= \sum_{\ell,s,q} \frac{g^2 E_C}{(\tilde{\Delta}_{\ell,j+1} - \tilde{\Delta}_{s,j})(\tilde{\Delta}_{\ell,j+1} - \tilde{\Delta}_{s-1,j})} s c_{q,j-1} p_{s,j} c_{\ell,j+1}^\dagger + \\
&+ \sum_{\ell,s,q} \frac{g^2}{\tilde{\Delta}_{\ell,j+1} - \tilde{\Delta}_{s,j}} c_{q,j-1} p_{s,j} c_{\ell,j+1}^\dagger + \\
&- \sum_{\ell,s,q} \frac{g^2 E_C}{(\tilde{\Delta}_{\ell,j+1} - \tilde{\Delta}_{s,j})(\tilde{\Delta}_{\ell,j+1} - \tilde{\Delta}_{s+1,j})} c_{q,j-1}^\dagger c_{s,j} c_{s+1,j} c_{\ell,j+1}^\dagger + h.c. , \\
[S_{j-1,j}, V_{j,j+1}] &= \sum_{\ell,s,k} \frac{g^2 E_C}{(\tilde{\Delta}_{\ell,j} - \tilde{\Delta}_{s,j})(\tilde{\Delta}_{\ell-1,j} - \tilde{\Delta}_{s,j-1})} \ell c_{s,j-1} p_{\ell,j} c_{k,j+1}^\dagger + \\
&- \sum_{\ell,s,k} \frac{g^2}{\tilde{\Delta}_{\ell,j} - \tilde{\Delta}_{s,j-1}} c_{s,j-1} p_{\ell,j} c_{k,j+1}^\dagger + \\
&- \sum_{\ell,s,k} \frac{g^2 E_C}{(\tilde{\Delta}_{\ell,j} - \tilde{\Delta}_{s,j-1})(\tilde{\Delta}_{\ell+1,j} - \tilde{\Delta}_{s,j-1})} c_{s,j-1} c_{\ell+1,j}^\dagger c_{\ell,j}^\dagger c_{k,j+1} + h.c. ,
\end{aligned} \tag{C.4}$$

which constitute the building blocks for computing $[S, V]$. We consider a drive field acting on site j , $H_{\text{drive},j} = \Omega_j (e^{i\alpha_j t} a_j + h.c.)$. We compute the commutator $[S, H_{\text{drive},j}] =$

$[S_{j-1,j}, H_{\text{drive},j}] + [S_{j,j+1}, H_{\text{drive},j}]$:

$$\begin{aligned}
 [S_{j-1,j}, H_{\text{drive},j}] &= \sum_{\ell,s} \frac{g\Omega_j E_C}{(\tilde{\Delta}_{\ell-1,j} - \tilde{\Delta}_{s,j-1})(\tilde{\Delta}_{\ell,j} - \tilde{\Delta}_{s,j-1})} e^{i\alpha_j t} \ell c_{s,j-1} p_{\ell,j} + \\
 &\quad - \sum_{\ell,s} \frac{g\Omega_j}{\tilde{\Delta}_{\ell,j} - \tilde{\Delta}_{s,j-1}} e^{i\alpha_j t} c_{s,j-1} p_{\ell,j} + \\
 &\quad - \sum_{\ell,s} \frac{g\Omega_j E_C}{(\tilde{\Delta}_{\ell+1,j} - \tilde{\Delta}_{s,j-1})(\tilde{\Delta}_{\ell,j} - \tilde{\Delta}_{s,j-1})} e^{-i\alpha_j t} c_{s,j-1} c_{\ell+1,j}^\dagger c_{\ell,j}^\dagger + h.c. , \\
 [S_{j,j+1}, H_{\text{drive},j}] &= \sum_{\ell,s} \frac{g\Omega_j E_C}{(\tilde{\Delta}_{\ell,j+1} - \tilde{\Delta}_{s,j})(\tilde{\Delta}_{\ell,j+1} - \tilde{\Delta}_{s+1,j})} e^{-i\alpha_j t} s p_{s,j} c_{\ell,j+1}^\dagger + \\
 &\quad + \sum_{\ell,s} \frac{g\Omega_j}{\tilde{\Delta}_{\ell,j+1} - \tilde{\Delta}_{s,j}} e^{-i\alpha_j t} p_{s,j} c_{\ell,j+1}^\dagger + h.c. \\
 &\quad - \sum_{\ell,s} \frac{\Omega_j g E_C}{(\tilde{\Delta}_{\ell,j+1} - \tilde{\Delta}_{s,j})(\tilde{\Delta}_{\ell,j+1} - \tilde{\Delta}_{s+1,j})} e^{i\alpha_j t} c_{s,j} c_{s+1,j} c_{\ell,j+1}^\dagger + h.c.
 \end{aligned} \tag{C.5}$$

C.3. LOW-ANHARMONICITY LIMIT

In the following, we explicitly consider the results with $L = 4$ superconducting qubits for clarity. The generalization to a larger number of superconducting qubits is straightforward. We work in the limit $E_C \ll \Delta_{ij}$, such that $\tilde{\Delta}_{\ell,j+1} - \tilde{\Delta}_{s,j} \approx \Delta_{j+1,j} = \omega_{j+1} - \omega_j$. We neglect the contributions coming from the the commutators of the drive fields controlled by $\{\epsilon_j\}$, since, as we show, they give subleading corrections. From Eqs. (C.4) and (C.5) and using the identities $\sum_{\ell=0}^{\infty} c_{\ell,j} = a_j$, $\sum_{\ell=0}^{\infty} \ell p_{\ell,j} = n_j$ and $\sum_{\ell=0}^{\infty} p_{\ell,j} = 1$, we obtain

$$\begin{aligned}
[S, V] &\approx +\frac{2g^2E_C}{\Delta_{12}^2}a_1a_1a_2^\dagger a_2^\dagger + \frac{2g^2E_C}{\Delta_{12}^2}n_1n_2 + \frac{g^2}{\Delta_{12}}n_1 - \frac{g^2}{\Delta_{12}}n_2 + \frac{g^2E_C}{\Delta_{23}^2}a_1n_2a_3^\dagger - \frac{g^2}{\Delta_{23}}a_1a_3^\dagger - \frac{g^2E_C}{\Delta_{23}^2}a_1^\dagger a_2a_2a_3^\dagger + \\
&+ \frac{g^2E_C}{\Delta_{12}^2}a_1n_2a_3^\dagger + \frac{g^2}{\Delta_{12}}a_1a_3^\dagger - \frac{g^2E_C}{\Delta_{12}^2}a_1^\dagger a_2a_2a_3^\dagger + \frac{2g^2E_C}{\Delta_{23}^2}a_2a_2a_3^\dagger a_3^\dagger + \frac{2g^2E_C}{\Delta_{23}^2}n_2n_3 + \frac{g^2}{\Delta_{23}}n_2 - \frac{g^2}{\Delta_{23}}n_3 + \\
&+ \frac{g^2E_C}{\Delta_{34}^2}a_2n_3a_4^\dagger - \frac{g^2}{\Delta_{34}}a_2a_4^\dagger - \frac{g^2E_C}{\Delta_{34}^2}a_2^\dagger a_3a_3a_4^\dagger + \\
&+ \frac{g^2E_C}{\Delta_{23}^2}a_2n_3a_4^\dagger + \frac{g^2}{\Delta_{23}}a_2a_4^\dagger - \frac{g^2E_C}{\Delta_{23}^2}a_2^\dagger a_3a_3a_4^\dagger + \frac{2g^2E_C}{\Delta_{34}^2}a_3a_3a_4^\dagger a_4^\dagger + \frac{2g^2E_C}{\Delta_{34}^2}n_3n_4 + \frac{g^2}{\Delta_{34}}n_3 - \frac{g^2}{\Delta_{34}}n_4 + h.c. , \\
[S, H_{\text{drive}}] &\approx +\frac{gE_C\Omega_1}{\Delta_{12}^2} \left\{ n_1 \left(e^{-i\alpha_1 t} a_2^\dagger + h.c. \right) - \left(e^{i\alpha_1 t} a_1 a_1 a_2^\dagger + h.c. \right) \right\} - \frac{g\Omega_1}{\Delta_{12}} \left(e^{-i\alpha_1 t} a_2^\dagger + h.c. \right) + \\
&+ \frac{gE_C\Omega_2}{\Delta_{12}^2} \left\{ n_2 \left(e^{-i\alpha_2 t} a_1^\dagger + h.c. \right) - \left(e^{i\alpha_2 t} a_2 a_2 a_1^\dagger + h.c. \right) \right\} + \frac{g\Omega_2}{\Delta_{12}} \left(e^{-i\alpha_2 t} a_1^\dagger + h.c. \right) + \\
&+ \frac{gE_C\Omega_2}{\Delta_{23}^2} \left\{ n_2 \left(e^{-i\alpha_2 t} a_3^\dagger + h.c. \right) - \left(e^{i\alpha_2 t} a_2 a_2 a_3^\dagger + h.c. \right) \right\} - \frac{g\Omega_2}{\Delta_{23}} \left(e^{-i\alpha_2 t} a_3^\dagger + h.c. \right) + \\
&+ \frac{gE_C\Omega_3}{\Delta_{23}^2} \left\{ n_3 \left(e^{-i\alpha_3 t} a_2^\dagger + h.c. \right) - \left(e^{i\alpha_3 t} a_3 a_3 a_2^\dagger + h.c. \right) \right\} + \frac{g\Omega_3}{\Delta_{23}} \left(e^{-i\alpha_3 t} a_2^\dagger + h.c. \right) + \\
&+ \frac{gE_C\Omega_3}{\Delta_{34}^2} \left\{ n_3 \left(e^{-i\alpha_3 t} a_4^\dagger + h.c. \right) - \left(e^{i\alpha_3 t} a_3 a_3 a_4^\dagger + h.c. \right) \right\} - \frac{g\Omega_3}{\Delta_{34}} \left(e^{-i\alpha_3 t} a_4^\dagger + h.c. \right).
\end{aligned} \tag{C.6}$$

C.4. ROTATING FRAME OF REFERENCE

We focus again on the four superconducting qubits system (cf. Appendix C.3). We change the frame of reference via the unitary transformation $U = \exp(it(\alpha_1 n_2 + \alpha_2 n_3 + \alpha_3 n_4))$, from which

$$\begin{aligned}
UH_{\text{drive}}U^\dagger &= \Omega_1(e^{i\alpha_1 t}a_1 + h.c.) + \Omega_2(e^{i(\alpha_2-\alpha_1)t}a_2 + h.c.) + \Omega_3(e^{i(\alpha_3-\alpha_2)t}a_3 + h.c.) + \\
&\quad + \epsilon_2(a_2 + h.c.) + \epsilon_3(a_3 + h.c.) + \epsilon_4(a_4 + h.c.) \\
U[S, V]U^\dagger &\approx +\frac{2g^2E_C}{\Delta_{12}^2}e^{2i\alpha_1 t}a_1a_1a_2^\dagger a_2^\dagger + \frac{2g^2E_C}{\Delta_{12}^2}n_1n_2 + \frac{g^2}{\Delta_{12}}n_1 - \frac{g^2}{\Delta_{12}}n_2 + \\
&\quad + \frac{g^2E_C}{\Delta_{23}^2}e^{i\alpha_2 t}a_1n_2a_3^\dagger - \frac{g^2}{\Delta_{23}}e^{i\alpha_2 t}a_1a_3^\dagger - \frac{g^2E_C}{\Delta_{23}^2}e^{-i(2\alpha_1-\alpha_2)t}a_1^\dagger a_2a_2a_3^\dagger + \\
&\quad + \frac{g^2E_C}{\Delta_{12}^2}e^{i\alpha_2 t}a_1n_2a_3^\dagger + \frac{g^2}{\Delta_{12}}e^{i\alpha_2 t}a_1a_3^\dagger - \frac{g^2E_C}{\Delta_{12}^2}e^{-i(2\alpha_1-\alpha_2)t}a_1^\dagger a_2a_2a_3^\dagger + \\
&\quad + \frac{2g^2E_C}{\Delta_{23}^2}e^{-2i(\alpha_1-\alpha_2)t}a_2a_2a_3^\dagger a_3^\dagger + \frac{2g^2E_C}{\Delta_{23}^2}n_2n_3 + \frac{g^2}{\Delta_{23}}n_2 - \frac{g^2}{\Delta_{23}}n_3 + \\
&\quad + \frac{g^2E_C}{\Delta_{34}^2}e^{i(\alpha_3-\alpha_1)t}a_2n_3a_4^\dagger - \frac{g^2}{\Delta_{34}}e^{i(\alpha_3-\alpha_1)t}a_2a_4^\dagger - \frac{g^2E_C}{\Delta_{34}^2}e^{i(\alpha_1-2\alpha_2+\alpha_3)t}a_2^\dagger a_3a_3a_4^\dagger + \\
&\quad + \frac{g^2E_C}{\Delta_{23}^2}e^{-i(\alpha_1-\alpha_3)t}a_2n_3a_4^\dagger - \frac{g^2}{\Delta_{23}}e^{-i(\alpha_1-\alpha_3)t}a_2a_4^\dagger + \frac{g^2E_C}{\Delta_{23}^2}e^{i(\alpha_1-2\alpha_2+\alpha_3)t}a_2^\dagger a_3a_3a_4^\dagger + \\
&\quad + \frac{2g^2E_C}{\Delta_{34}^2}e^{-2i(\alpha_2-\alpha_3)t}a_3a_3a_4^\dagger a_4^\dagger + \frac{2g^2E_C}{\Delta_{34}^2}n_3n_4 - \frac{g^2}{\Delta_{34}}n_3 + \frac{g^2}{\Delta_{34}}n_4 + h.c.
\end{aligned} \tag{C.7}$$

$$\begin{aligned}
U[S, H_{\text{drive}}]U^\dagger &\approx +\frac{g\Omega_1 E_C}{\Delta_{12}^2} \left\{ n_1 \left(a_2^\dagger + h.c. \right) - \left(e^{2i\alpha_1 t}a_1a_1a_2^\dagger + h.c. \right) \right\} - \frac{g\Omega_1}{\Delta_{12}} \left(a_2^\dagger + h.c. \right) + \\
&\quad + \frac{g\Omega_2 E_C}{\Delta_{12}^2} \left\{ n_2 \left(e^{-i\alpha_2 t}a_1^\dagger + h.c. \right) - \left(e^{i(\alpha_2-2\alpha_1)t}a_2a_2a_1^\dagger + h.c. \right) \right\} + \frac{g\Omega_2}{\Delta_{12}} \left(e^{-i\alpha_2 t}a_1^\dagger + h.c. \right) + \\
&\quad + \frac{g\Omega_2 E_C}{\Delta_{23}^2} \left\{ n_2 \left(a_3^\dagger + h.c. \right) - \left(e^{2i(\alpha_2-\alpha_1)t}a_2a_2a_3^\dagger + h.c. \right) \right\} - \frac{g\Omega_2}{\Delta_{23}} \left(a_3^\dagger + h.c. \right) + \\
&\quad + \frac{gE_C\Omega_3}{\Delta_{23}^2} \left\{ n_3 \left(e^{-i(\alpha_3-\alpha_1)t}a_2^\dagger + h.c. \right) - \left(e^{i(\alpha_3-2\alpha_2+\alpha_1)t}a_3a_3a_2^\dagger + h.c. \right) \right\} + \frac{g\Omega_3}{\Delta_{23}} \left(e^{-i(\alpha_3-\alpha_1)t}a_2^\dagger + h.c. \right) + \\
&\quad + \frac{gE_C\Omega_3}{\Delta_{34}^2} \left\{ n_3 \left(a_4^\dagger + h.c. \right) - \left(e^{2i(\alpha_3-\alpha_2)t}a_3a_3a_4^\dagger + h.c. \right) \right\} - \frac{g\Omega_3}{\Delta_{34}} \left(a_4^\dagger + h.c. \right).
\end{aligned} \tag{C.8}$$

We discard all the oscillating terms employing the RWA in the limits,

$$\alpha_1 \gg \max \left(\Omega_1, \frac{g^2 E_C}{\Delta_{12}^2}, \frac{g\Omega_1 E_C}{\Delta_{12}^2} \right), \quad (\text{C.9})$$

$$\alpha_2 \gg \max \left(\frac{g^2}{\Delta_{12}}, \frac{g^2}{\Delta_{23}}, \frac{g^2 E_C}{\Delta_{12}^2}, \frac{g^2 E_C}{\Delta_{23}^2}, \frac{g\Omega_2}{\Delta_{12}} \right), \quad (\text{C.10})$$

$$|\alpha_1 - \alpha_2| \gg \max \left(\Omega_2, \frac{g\Omega_2 E_C}{\Delta_{23}^2}, \frac{g^2 E_C}{\Delta_{23}^2} \right), \quad (\text{C.11})$$

$$|\alpha_2 - \alpha_3| \gg \max \left(\Omega_3, \frac{g\Omega_3 E_C}{\Delta_{34}^2}, \frac{g^2 E_C}{\Delta_{34}^2} \right), \quad (\text{C.12})$$

$$|2\alpha_1 - \alpha_2| \gg \max \left(\frac{g^2 E_C}{\Delta_{23}^2}, \frac{g^2 E_C}{\Delta_{12}^2}, \frac{g\Omega_2 E_C}{\Delta_{12}^2} \right), \quad (\text{C.13})$$

$$|\alpha_3 - \alpha_1| \gg \max \left(\frac{g^2 E_C}{\Delta_{34}^2}, \frac{g^2}{\Delta_{34}}, \frac{g^2 E_C}{\Delta_{23}^2}, \frac{g^2}{\Delta_{23}}, \frac{g E_C \Omega_3}{\Delta_{23}^2}, \frac{g\Omega_3}{\Delta_{23}} \right), \quad (\text{C.14})$$

$$|\alpha_1 - 2\alpha_2 + \alpha_3| \gg \max \left(\frac{g^2 E_C}{\Delta_{34}^2}, \frac{g^2 E_C}{\Delta_{23}^2}, \frac{g E_C \Omega_3}{\Delta_{34}^2} \right). \quad (\text{C.15})$$

which are satisfied in the dispersive regime and at low-anharmonicity E_C limit via a staggered configuration of the drive field frequencies with a little dishomogeneity, as discussed in Chapter 7. Discarding the oscillating terms in Eq. (C.7) and Eq. (C.8) we obtain

$$\begin{aligned} \tilde{H} = & \sum_{j=1}^4 \left(\tilde{\omega}_j \hat{n}_j + \frac{E_C}{2} \hat{a}_j^\dagger \hat{a}_j^\dagger \hat{a}_j \hat{a}_j \right) + \sum_{j=1}^3 \left(\frac{2g^2 E_C}{\Delta_{j,j+1}^2} \hat{n}_j \hat{n}_{j+1} + \frac{g\Omega_j E_C}{\Delta_{j,j+1}^2} \hat{n}_j \left(\hat{a}_{j+1} + \hat{a}_{j+1}^\dagger \right) \right) + \\ & + \sum_{j=2}^4 \left(\epsilon_j - \frac{g\Omega_{j-1}}{\Delta_{j-1,j}} \right) \left(a_j + a_j^\dagger \right). \end{aligned} \quad (\text{C.16})$$

Since we do not want local fields $\propto (a_j + a_j^\dagger)$ we fix the condition $\epsilon_j = g\Omega_{j-1}/\Delta_{j-1,j}$ with $j = 2, 3, 4$. We obtain

$$\tilde{H} = \sum_{j=1}^4 \left(\tilde{\omega}_j \hat{n}_j + \frac{E_C}{2} \hat{a}_j^\dagger \hat{a}_j^\dagger \hat{a}_j \hat{a}_j \right) + \sum_{j=1}^3 \left(\frac{2g^2 E_C}{\Delta_{j,j+1}^2} \hat{n}_j \hat{n}_{j+1} + \frac{g\Omega_j E_C}{\Delta_{j,j+1}^2} \hat{n}_j \left(\hat{a}_{j+1} + \hat{a}_{j+1}^\dagger \right) \right). \quad (\text{C.17})$$

In the dispersive regime, the drive fields amplitudes $\{\epsilon_j\}$ are very small compared to the drive fields controlled by $\{\Omega_j\}$. Therefore, it is appropriate to neglect the contributions coming from their commutators with S . The above calculations can be straightforwardly generalized to the multisite case, since the superconducting circuits in the bulk will behave analogously to the second one in the case treated explicitly above.

APPENDIX D

Supplemental information for Chapter 8

D.1. COMPUTATION OF THE LYAPUNOV EXPONENT

Here we give further details about the calculation of the Lyapunov exponent referring specifically to the results in Sec. 8.5.2. We extract the Lyapunov exponent investigating the divergence of R nearly sampled initial conditions. We use as measure of the distance of two trajectories the Frobenius norm of the difference of the average one-body reduced density matrices, namely

$$\Delta\Sigma(i, j, t) = \sqrt{\sum_{n,m=1}^N |\Sigma_{n,m}(i, t) - \Sigma_{n,m}(j, t)|^2} \quad (\text{D.1})$$

where $i, j \in [1, R]$ label the trajectory and t is the time. The R initial states are sampled such that $\Delta\Sigma(i, j \neq i, t = 0) \approx 10^{-8}$. Then, we compute the average distance over all

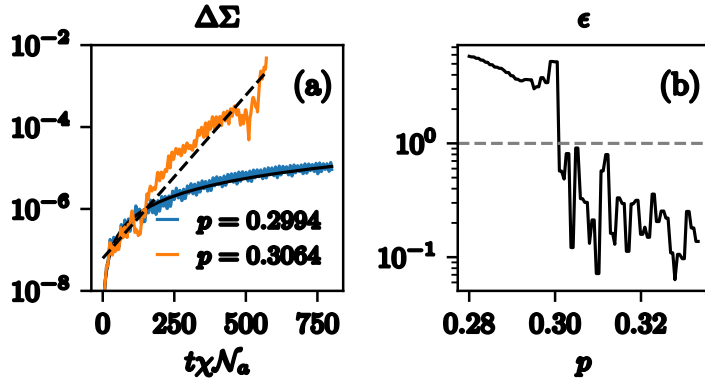


FIGURE D.1. (a): Dynamics of the average distance between $R = 12$ nearly sampled trajectories starting from two multimode Schrödinger cat states parameterized by p (cf. Eq. (8.16)) in the $N = 3$ levels spin-exchange model. We fix two different values of $p = \{0.2994, 0.3064\}$. The continuous line is the polynomial fit. The dashed line is the exponential fit. (b): Relative error between the exponential fit and the polynomial fit. When $\epsilon > 1$ ($\epsilon < 1$) the polynomial (exponential) fit better approximates the data. The horizontal dashed gray line is at $\epsilon = 1$. Notice the sharp change of ϵ around $p \approx 0.3$. The parameters of the simulations are the same as the one in Fig. 8.4 in the main text. Image taken from Ref. [4].

the trajectories

$$\Delta\Sigma(t) = \frac{2}{R(R-1)} \sum_{i=1}^R \sum_{j=i+1}^R \Delta\Sigma(i, j, t). \quad (\text{D.2})$$

The dynamics is regular when $\Delta\Sigma(t)$ grows polynomially in time, while it is chaotic if $\Delta\Sigma(t)$ grows exponentially in time, with the largest Lyapunov exponent equal to the rate of the exponential. In Fig. D.1(a) we show two paradigmatic examples in the regular phase and chaotic phase. Specifically, referring to the results in Fig. 8.4, we fix $p \lesssim p^*$ and $p \gtrsim p^*$ with $p^* \approx 0.3$, in order to highlight the abrupt change of the behavior of $\Delta\Sigma(t)$. In Fig. D.1(b) we show the relative error ϵ between the exponential fit and the polynomial fit. When $\epsilon > 1$ ($\epsilon < 1$) the polynomial (exponential) fit better approximates the data. We checked that our results are not affected by decreasing the time step.

D.2. CHAOS INDUCED UPON TRADING $SU(2)$ WITH $SU(3)$ INTERACTIONS IN THREE-LEVEL SYSTEM

Here, we investigate the onset of a chaotic phase in the three-level spin-exchange model starting from a separable state in Eq. (8.5) with $|\psi_j\rangle$ in a Schrödinger cat state parameterized by p via Eq. (8.16). In Fig. D.2 we show the maximum Lyapunov exponent as a function of the ratio $g_1/g_2 = \tan(\theta)$ and p in the homogeneous case ($W = 0$). For $\theta/\pi = \{0, 0.25, 0.5\}$ the Hamiltonian can be written in terms of a $SU(2)$ subgroup of $SU(3)$, and since dynamics are therefore restricted to that subgroup there is no chaos for any value of p . Furthermore, for $\theta/\pi = \{0, 0.5\}$ we have $g_1 = 0$ and $g_2 = 0$, respectively, thus we recover the $SU(2)$ two-level system limit. As θ/π deviates from the $SU(2)$ limits, the system displays chaotic behavior for sufficiently large p . Deep in the $SU(3)$ limit, we observe chaos for any $p \gtrsim p^*$, while near the $SU(2)$ limit there are islands of chaotic behavior embedded in regular ones. We compute the Lyapunov exponent following the procedure described in Appendix D.1. Additionally, we manually set $\sigma/(\chi\mathcal{N}) = 0$ when it is less than 0.01, since our procedure was signaling chaos in regions where, by direct inspection, there were no signatures of it.

D.3. CHAOS INDUCED BY A FINITE FRACTION OF SCHRÖDINGER CAT STATES IN $SU(3)$ SPIN-EXCHANGE HAMILTONIAN

Here, we provide additional details about the results discussed in Sec. 8.5.3. We consider the Schrödinger cat state $|\psi_{\text{cat}}\rangle \sim (|\tilde{\gamma}^{(1)}\rangle + |\tilde{\gamma}^{(2)}\rangle)$ defined in Eq. (8.16) and parameterized

via p , while we consider $|\tilde{\gamma}^{(1)}\rangle$ as coherent state. We initialize a fraction F of Schrödinger cat states $|\psi_{\text{cat}}\rangle$, such that the initial state is

$$|\Psi\rangle = \otimes_{j=1}^{\lfloor FL \rfloor} |\psi_{\text{cat}}\rangle \otimes_{j=\lfloor FL \rfloor+1}^L |\tilde{\gamma}^{(1)}\rangle, \quad (\text{D.3})$$

where $\lfloor x \rfloor$ returns the least integer greater than or equal to x . The evolution is governed by the $SU(3)$ spin-exchange Hamiltonian at $W = 0$ and $g_1/g_2 \approx 2$ (in units adopted in Fig. D.2 it corresponds to $\theta/\pi = 0.36$). In Fig. D.3 we show the Lyapunov exponent as a function of p and F . For $F < F^*$ the system displays regular dynamics, while for $F > F^*$ the system enters in a chaotic regime. The Lyapunov exponent is computed following the same procedure discussed in Appendix D.1.

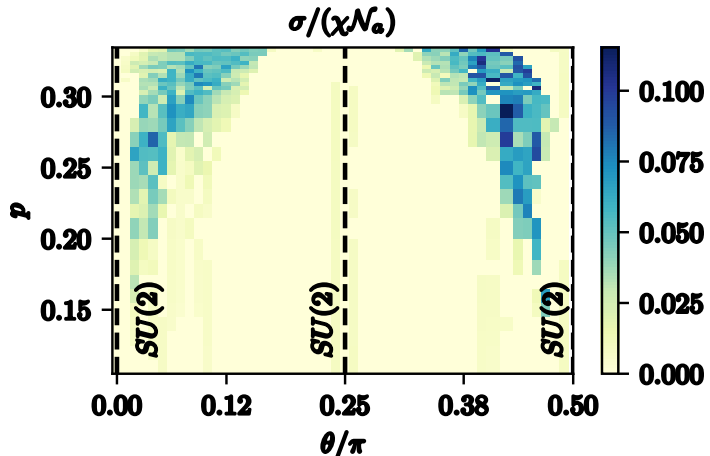


FIGURE D.2. Lyapunov exponent as a function of p and θ in the $N = 3$ spin-exchange model. The initial state is a multimode Schrödinger cat state parameterized by p via Eq. (8.16). We set $\mathcal{N}_a \rightarrow \infty$ and $W = 0$. The vertical dashed lines are along the $SU(2)$ limit, where the dynamics is effectively taking place in a $SU(2)$ subgroup of $SU(3)$. The all-to-all couplings are parameterized such that $\chi_{1,1} < \chi_{2,2}$ for $\theta/\pi \in [0, 0.25]$, $\chi_{1,1} > \chi_{2,2}$ for $\theta/\pi \in (0.25, 0.5]$ and $\chi_{1,1} = \chi_{2,2}$ at $\theta/\pi = 0.25$. In the $SU(2)$ limits ($\theta/\pi = \{0, 0.25, 0.5\}$) the dynamical response is regular for any value of p , since the couplings constrict the dynamics to take place in a $SU(2)$ subspace of $SU(3)$. Deep in the $SU(3)$ limit ($\theta/\pi \approx 0.1$ and $\theta/\pi \approx 0.4$), $|\Sigma_{n,m}|$ displays exponential sensitivity for any value of $p \gtrsim p^*$, with p^* dependent on θ . Near the $SU(2)$ two-level limits ($\theta/\pi = \{0, 0.5\}$) we observe chaotic regions embedded in regular ones. Image taken from Ref. [4].

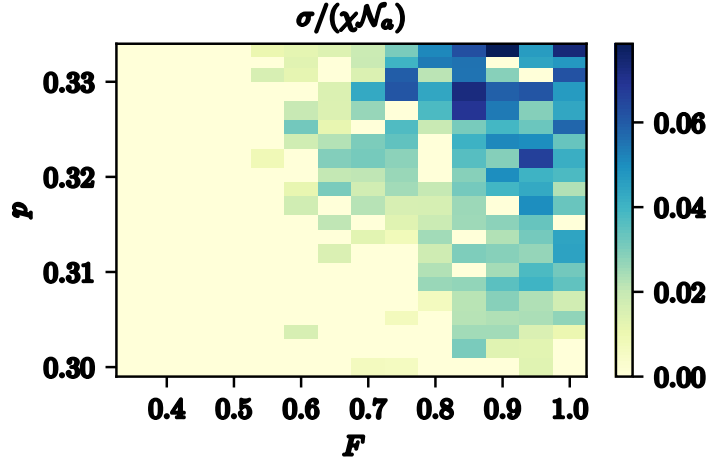


FIGURE D.3. Lyapunov exponent for the $N = 3$ levels spin-exchange Hamiltonian in the homogeneous case ($W = 0$) as a function of the initialized fraction F of multimode Schrödinger cat states in the state in Eq. (D.3). The results were obtained simulating $L = 100$ sites at fixed $g_1/g_2 \approx 2$ (in the units adopted in Fig. D.2 it corresponds to $\theta/\pi = 0.36$). The results are not affected upon increasing L . Image taken from Ref. [4].

D.4. OPTIMIZATION PROCEDURE

Here we give further details about the practical implementation of steps (ii) and (iv) in the optimization procedure discussed in Sec. 8.6. We set as initial guess for the initial state $\tilde{\Sigma}_{n,m}(t = 0) = \Sigma_{n,m}(t = \tau)$, with the time τ large enough, such that the initial transient dynamics is neglected. We set $\tilde{h}_n = \sum_{j=1}^L h_j^{(n)}/L = 0$ and $\tilde{\chi}_{n,m} = \chi_{n,m}$, as initial guesses for the parameters. Throughout the procedure, we keep $\tilde{\zeta}_{n,m} = \tilde{\nu}_{n,m} = 0$ since they control processes absent in the bare model. Then, we numerically optimize both the initial state $\{\tilde{\Sigma}_{n,m}(t = 0)\}$ and the parameters $\{\tilde{h}_n, \tilde{\chi}_{n,m}\}$ in order to minimize the cost function in Eq. (8.19) in the main text. The optimization procedure stops when the relative change between two consecutive iterations of the guessed solutions is less than $\approx 10^{-2}$.

We also test the convergence of the optimization procedure modifying the cost function. Specifically, we consider as cost function the average norm-2 distance

$$\epsilon_2 = \frac{1}{T} \int_0^T \sqrt{\sum_{n,m=1}^N \left| \tilde{\Sigma}_{n,m}(t) - \Sigma_{n,m}(t) \right|^2} dt, \quad (\text{D.4})$$

and compare with the one based on the norm-1 cost function in Eq. (8.19). We test the two procedures using the same parameters and initial state of Fig. 8.5 in the main text, namely $W/(\chi N_a) = 0.1$, $g_2/g_1 \approx 10^{-2}$ and a permutationally invariant (in space) bosonic coherent state. Once the two procedures converged, we compare them computing the norm-1 distance between the optimized $\tilde{\Sigma}(t)$ and $\Sigma(t)$ obtained from the

full many-body dynamics. We obtain $\epsilon_1/\epsilon_2 \approx 0.6$ (where ϵ_2 is the norm-1 computed at the end of the optimization procedure based on the minimization of the norm-2 in Eq. (D.4)) showing a slight advantage of norm-1 over the norm-2 in the optimization procedure.

D.5. DYNAMICS WITH CAVITY LOSSES

The dynamics of the matter-light system can be described by the master equation for the density matrix

$$\frac{d\hat{\rho}}{dt} = -i[\hat{H}, \hat{\rho}] + \mathcal{L}_c[\hat{\rho}] + \mathcal{L}_a[\hat{\rho}]. \quad (\text{D.5})$$

Here, \hat{H} is the Hamiltonian in Eq. (8.1), where now the photon is an active DOF, and

$$\begin{aligned} \mathcal{L}_c[\hat{\rho}] &= \frac{\kappa}{2} (2\hat{a}\hat{\rho}\hat{a}^\dagger - \hat{a}^\dagger\hat{a}\hat{\rho} - \hat{\rho}\hat{a}^\dagger\hat{a}), \\ \mathcal{L}_a[\hat{\rho}] &= \frac{\eta}{2} \sum_{j=1}^L \sum_{n=1}^{N-1} \left(2\hat{\Sigma}_{n,n+1}^{(j)}\hat{\rho}\hat{\Sigma}_{n+1,n}^{(j)} - \hat{\Sigma}_{n+1,n}^{(j)}\hat{\Sigma}_{n,n+1}^{(j)}\hat{\rho} - \hat{\rho}\hat{\Sigma}_{n+1,n}^{(j)}\hat{\Sigma}_{n,n+1}^{(j)} \right) \end{aligned} \quad (\text{D.6})$$

are the Lindblad terms that describe the cavity-photon loss with decay rate κ and emission of single-atom excitation with rate η . From now on we set $\lambda_n = 0$ in the Hamiltonian \hat{H} and we consider the far detuned regime of the cavity mode as we are mainly interested in the spin-exchange interaction case. We perform adiabatic elimination such that [273–277]

$$\hat{a}(t) \approx - \sum_{n=1}^{N-1} \frac{ig_n\hat{\Sigma}_{n,n+1}(t)}{(i\omega_0 + \kappa/2)}. \quad (\text{D.7})$$

In this regime the dynamics of the density matrix of the matter DOFs $\hat{\rho}_m$ is given by the matter-only master equation

$$\frac{d\hat{\rho}_m}{dt} = -i[\hat{H}_{\text{ad}}, \hat{\rho}_m] + \mathcal{L}_\Gamma[\hat{\rho}_m] + \mathcal{L}_a[\hat{\rho}_m]. \quad (\text{D.8})$$

Here, \hat{H}_{ad} is the Hamiltonian given in Eq. (8.2), with $\nu_{n,m} = \zeta_{n,m} = 0$ and all-to-all couplings per-particle

$$\chi_{n,m} = \frac{g_n g_m \omega_0}{\omega_0^2 + (\kappa/2)^2}. \quad (\text{D.9})$$

The dissipative part $\mathcal{L}_\Gamma[\hat{\rho}_m]$ is given by

$$\mathcal{L}_\Gamma[\hat{\rho}_m] = \sum_{n,m=1}^{N-1} \frac{\sqrt{\Gamma_n \Gamma_m}}{2} \left(2\hat{\Sigma}_{n,n+1}\hat{\rho}_m\hat{\Sigma}_{m+1,m} - \{\hat{\Sigma}_{n+1,n}\hat{\Sigma}_{m,m+1}, \hat{\rho}_m\} \right), \quad (\text{D.10})$$

where

$$\Gamma_n = \frac{g_n^2 \kappa}{\omega_0^2 + (\kappa/2)^2}, \quad (\text{D.11})$$

is the decay rate per-particle of the collective DOFs. Imposing $\mathcal{N}_a \chi_{n,m} \gg \mathcal{N}_a \sqrt{\Gamma_n \Gamma_m}$ and $\mathcal{N}_a \chi_{n,m} \gg \eta$ we obtain the conditions discussed in the main text.

Bibliography

- [1] R. J. Valencia-Tortora, N. Pancotti, and J. Marino. “Kinetically Constrained Quantum Dynamics in Superconducting Circuits”. In: *PRX Quantum* 3 (2 2022), p. 020346.
- [2] M. Badbaria et al. *State-dependent mobility edge in kinetically constrained models*. 2024. arXiv: [2407.12909 \[cond-mat.stat-mech\]](https://arxiv.org/abs/2407.12909).
- [3] R. J. Valencia-Tortora et al. “Rydberg Platform for Nonergodic Chiral Quantum Dynamics”. In: *Phys. Rev. Lett.* 132 (22 2024), p. 223201.
- [4] R. J. Valencia-Tortora et al. “Crafting the dynamical structure of synchronization by harnessing bosonic multilevel cavity QED”. In: *Phys. Rev. Res.* 5 (2 2023), p. 023112.
- [5] R. Javier Valencia Tortora, P. Calabrese, and M. Collura. “Relaxation of the order-parameter statistics and dynamical confinement”. In: *Europhysics Letters* 132.5 (Dec. 2020), p. 50001.
- [6] A. P. Chaudhari et al. “Zeno crossovers in the entanglement speed of spin chains with noisy impurities”. In: *Journal of Statistical Mechanics: Theory and Experiment* 2022.10 (Oct. 2022), p. 103101.
- [7] U. Javed et al. *Zeno physics of the Ising chain with symmetry-breaking boundary dephasing*. 2024. arXiv: [2404.04255 \[cond-mat.str-el\]](https://arxiv.org/abs/2404.04255).
- [8] S. Lloyd. “Universal Quantum Simulators”. In: *Science* 273.5278 (Aug. 1996), 1073–1078.
- [9] J. Preskill. “Quantum Computing in the NISQ era and beyond”. In: *Quantum* 2 (Aug. 2018), p. 79.
- [10] A. J. Daley et al. “Practical quantum advantage in quantum simulation”. In: *Nature* 607.7920 (July 2022), 667–676.
- [11] A. Miessen et al. “Quantum algorithms for quantum dynamics”. In: *Nature Computational Science* 3.1 (Dec. 2022), 25–37.
- [12] S. de Léséleuc et al. “Observation of a symmetry-protected topological phase of interacting bosons with Rydberg atoms”. In: *Science* 365.6455 (Aug. 2019), 775–780.
- [13] G. Semeghini et al. “Probing topological spin liquids on a programmable quantum simulator”. In: *Science* 374.6572 (Dec. 2021), pp. 1242–1247.

- [14] M. Iqbal et al. “Non-Abelian topological order and anyons on a trapped-ion processor”. In: *Nature* 626.7999 (Feb. 2024), 505–511.
- [15] H. Bernien et al. “Probing many-body dynamics on a 51-atom quantum simulator”. In: *Nature* 551.7682 (Nov. 2017), pp. 579–584.
- [16] J. Zhang et al. “Observation of a many-body dynamical phase transition with a 53-qubit quantum simulator”. In: *Nature* 551.7682 (Nov. 2017), pp. 601–604.
- [17] V. Lienhard et al. “Observing the Space- and Time-Dependent Growth of Correlations in Dynamically Tuned Synthetic Ising Models with Antiferromagnetic Interactions”. In: *Phys. Rev. X* 8 (2 2018), p. 021070.
- [18] E. Guardado-Sánchez et al. “Probing the Quench Dynamics of Antiferromagnetic Correlations in a 2D Quantum Ising Spin System”. In: *Phys. Rev. X* 8 (2 2018), p. 021069.
- [19] H. Kim et al. “Detailed Balance of Thermalization Dynamics in Rydberg-Atom Quantum Simulators”. In: *Phys. Rev. Lett.* 120 (18 2018), p. 180502.
- [20] J. Bermejo-Vega et al. “Architectures for Quantum Simulation Showing a Quantum Speedup”. In: *Phys. Rev. X* 8 (2 2018), p. 021010.
- [21] B. Fauseweh. “Quantum many-body simulations on digital quantum computers: State-of-the-art and future challenges”. In: *Nature Communications* 15.1 (Mar. 2024).
- [22] C. Monroe et al. “Programmable quantum simulations of spin systems with trapped ions”. In: *Rev. Mod. Phys.* 93 (2 2021), p. 025001.
- [23] J. Eisert, M. Friesdorf, and C. Gogolin. “Quantum many-body systems out of equilibrium”. In: *Nature Physics* 11.2 (Feb. 2015), 124–130.
- [24] R. P. Feynman. “Simulating physics with computers”. In: *International Journal of Theoretical Physics* 21.6-7 (June 1982), pp. 467–488.
- [25] P. W. Shor. “Fault-tolerant quantum computation”. In: *Proceedings of 37th conference on foundations of computer science*. IEEE. 1996, pp. 56–65.
- [26] J. Roffe. “Quantum error correction: an introductory guide”. In: *Contemporary Physics* 60.3 (2019), pp. 226–245.
- [27] D. Bluvstein et al. “Logical quantum processor based on reconfigurable atom arrays”. In: *Nature* 626.7997 (Dec. 2023), 58–65.
- [28] D. Bluvstein et al. “A quantum processor based on coherent transport of entangled atom arrays”. In: *Nature* 604.7906 (Apr. 2022), 451–456.
- [29] J. Ramette et al. “Any-To-Any Connected Cavity-Mediated Architecture for Quantum Computing with Trapped Ions or Rydberg Arrays”. In: *PRX Quantum* 3 (1 2022), p. 010344.
- [30] A. Kitaev. “Fault-tolerant quantum computation by anyons”. In: *Annals of Physics* 303.1 (Jan. 2003), 2–30.

- [31] C. W. von Keyserlingk et al. “Operator Hydrodynamics, OTOCs, and Entanglement Growth in Systems without Conservation Laws”. In: *Phys. Rev. X* 8 (2 2018), p. 021013.
- [32] A. Nahum, S. Vijay, and J. Haah. “Operator Spreading in Random Unitary Circuits”. In: *Phys. Rev. X* 8 (2 2018), p. 021014.
- [33] A. Chan, A. De Luca, and J. T. Chalker. “Solution of a Minimal Model for Many-Body Quantum Chaos”. In: *Phys. Rev. X* 8 (4 2018), p. 041019.
- [34] T. Rakovszky, F. Pollmann, and C. W. von Keyserlingk. “Diffusive Hydrodynamics of Out-of-Time-Ordered Correlators with Charge Conservation”. In: *Phys. Rev. X* 8 (3 2018), p. 031058.
- [35] V. Khemani, A. Vishwanath, and D. A. Huse. “Operator Spreading and the Emergence of Dissipative Hydrodynamics under Unitary Evolution with Conservation Laws”. In: *Phys. Rev. X* 8 (3 2018), p. 031057.
- [36] D. E. Parker et al. “A Universal Operator Growth Hypothesis”. In: *Phys. Rev. X* 9 (4 2019), p. 041017.
- [37] R. Nandkishore and D. A. Huse. “Many-body localization and thermalization in quantum statistical mechanics”. In: *Annu. Rev. Condens. Matter Phys.* 6.1 (2015), pp. 15–38.
- [38] D. A. Abanin et al. “Colloquium: Many-body localization, thermalization, and entanglement”. In: *Reviews of Modern Physics* 91.2 (2019), p. 021001.
- [39] A. Prem, J. Haah, and R. Nandkishore. “Glassy quantum dynamics in translation invariant fracton models”. In: *Phys. Rev. B* 95 (15 2017), p. 155133.
- [40] R. M. Nandkishore and M. Hermele. “Fractons”. In: *Annual Review of Condensed Matter Physics* 10.1 (Mar. 2019), pp. 295–313.
- [41] V. Khemani, M. Hermele, and R. Nandkishore. “Localization from Hilbert space shattering: From theory to physical realizations”. In: *Phys. Rev. B* 101 (17 2020), p. 174204.
- [42] P. Sala et al. “Ergodicity Breaking Arising from Hilbert Space Fragmentation in Dipole-Conserving Hamiltonians”. In: *Phys. Rev. X* 10 (1 2020), p. 011047.
- [43] T. Rakovszky et al. “Statistical localization: From strong fragmentation to strong edge modes”. In: *Phys. Rev. B* 101 (12 2020), p. 125126.
- [44] M. Pretko, X. Chen, and Y. You. *Fracton Phases of Matter*. 2020. arXiv: [2001.01722 \[cond-mat.str-el\]](https://arxiv.org/abs/2001.01722).
- [45] M. Pretko and L. Radzihovsky. “Fracton-elasticity duality”. In: *Physical review letters* 120.19 (2018), p. 195301.
- [46] S. Scherg et al. “Observing non-ergodicity due to kinetic constraints in tilted Fermi-Hubbard chains”. In: *Nature Communications* 12.1 (July 2021).
- [47] C. J. Turner et al. “Weak ergodicity breaking from quantum many-body scars”. In: *Nature Physics* 14.7 (2018), pp. 745–749.

- [48] C. J. Turner et al. "Quantum scarred eigenstates in a Rydberg atom chain: Entanglement, breakdown of thermalization, and stability to perturbations". In: *Phys. Rev. B* 98 (15 2018), p. 155134.
- [49] W. W. Ho et al. "Periodic Orbits, Entanglement, and Quantum Many-Body Scars in Constrained Models: Matrix Product State Approach". In: *Phys. Rev. Lett.* 122 (4 2019), p. 040603.
- [50] S. Ok et al. "Topological many-body scar states in dimensions one, two, and three". In: *Phys. Rev. Research* 1 (3 2019), p. 033144.
- [51] M. Schecter and T. Iadecola. "Weak Ergodicity Breaking and Quantum Many-Body Scars in Spin-1 XY Magnets". In: *Phys. Rev. Lett.* 123 (14 2019), p. 147201.
- [52] V. Khemani, C. R. Laumann, and A. Chandran. "Signatures of integrability in the dynamics of Rydberg-blockaded chains". In: *Phys. Rev. B* 99 (16 2019), 161101(R).
- [53] A. Hudomal et al. "Quantum scars of bosons with correlated hopping". In: *Communications Physics* 3.1 (June 2020), pp. 1–12.
- [54] S. Moudgalya, N. Regnault, and B. A. Bernevig. "Entanglement of exact excited states of Affleck-Kennedy-Lieb-Tasaki models: Exact results, many-body scars, and violation of the strong eigenstate thermalization hypothesis". In: *Phys. Rev. B* 98 (23 2018), p. 235156.
- [55] J. Feldmeier et al. "Anomalous diffusion in dipole-and higher-moment-conserving systems". In: *Physical Review Letters* 125.24 (2020), p. 245303.
- [56] M. Serbyn, D. A. Abanin, and Z. Papić. "Quantum many-body scars and weak breaking of ergodicity". In: *Nature Physics* 17.6 (May 2021), pp. 675–685.
- [57] J.-Y. Desaules et al. "Proposal for Realizing Quantum Scars in the Tilted 1D Fermi-Hubbard Model". In: *Phys. Rev. Lett.* 126 (21 2021), p. 210601.
- [58] C. J. Turner et al. "Correspondence Principle for Many-Body Scars in Ultracold Rydberg Atoms". In: *Phys. Rev. X* 11 (2 2021), p. 021021.
- [59] M. Magoni, P. P. Mazza, and I. Lesanovsky. "Emergent Bloch Oscillations in a Kinetically Constrained Rydberg Spin Lattice". In: *Phys. Rev. Lett.* 126 (10 2021), p. 103002.
- [60] H. Zhao et al. "Orthogonal quantum many-body scars". In: *arXiv preprint arXiv:2102.07672* (2021).
- [61] K. Baumann et al. "Dicke quantum phase transition with a superfluid gas in an optical cavity". In: *Nature* 464.7293 (2010), pp. 1301–1306.
- [62] H. Ritsch et al. "Cold atoms in cavity-generated dynamical optical potentials". In: *Reviews of Modern Physics* 85.2 (2013), p. 553.
- [63] F. Mivehvar et al. "Cavity QED with quantum gases: new paradigms in many-body physics". In: *Advances in Physics* 70.1 (2021), pp. 1–153.

- [64] A. T. Black, H. W. Chan. "Observation of Collective Friction Forces due to Spatial Self-Organization of Atoms: From Rayleigh to Bragg Scattering". In: *Phys. Rev. Lett.* 91 (20 2003), p. 203001.
- [65] H. Tanji-Suzuki et al. "Vacuum-Induced Transparency". In: *Science* 333.6047 (20 Sept. 2011), pp. 1266–1269.
- [66] J. G. Bohnet et al. "A steady-state superradiant laser with less than one intracavity photon". In: *Nature* 484.7392 (20 2012), pp. 78–81.
- [67] P. Kirton and J. Keeling. "Suppressing and Restoring the Dicke Superradiance Transition by Dephasing and Decay". In: *Phys. Rev. Lett.* 118 (12 2017), p. 123602.
- [68] P. Kirton and J. Keeling. "Superradiant and lasing states in driven-dissipative Dicke models". In: *New Journal of Physics* 20.1 (20 2018), p. 015009.
- [69] P. Kirton et al. "Introduction to the Dicke model: From equilibrium to nonequilibrium, and vice versa". In: *Advanced Quantum Technologies* 2.1-2 (20 2019), p. 1800043.
- [70] F. Carollo and I. Lesanovsky. "Exactness of Mean-Field Equations for Open Dicke Models with an Application to Pattern Retrieval Dynamics". In: *Phys. Rev. Lett.* 126 (23 2021), p. 230601.
- [71] E. Fiorelli et al. *Mean-field dynamics of open quantum systems with collective operator-valued rates: validity and application*. 2023. arXiv: [2302.04155 \[cond-mat.stat-mech\]](https://arxiv.org/abs/2302.04155).
- [72] K. Huang. *Statistical mechanics*. Vol. 91. John Wiley & Sons, 2008, p. 203001.
- [73] A. M. Kaufman et al. "Quantum thermalization through entanglement in an isolated many-body system". In: *Science* 353.6301 (20 2016), pp. 794–800.
- [74] M. Ueda. "Quantum equilibration, thermalization and prethermalization in ultracold atoms". In: *Nature Reviews Physics* 2.12 (20 Oct. 2020), 669–681.
- [75] M. Rigol, V. Dunjko, and M. Olshanii. "Thermalization and its mechanism for generic isolated quantum systems". In: *Nature* 452.7189 (20 Apr. 2008), 854–858.
- [76] E. B. Rozenbaum, S. Ganeshan, and V. Galitski. "Lyapunov Exponent and Out-of-Time-Ordered Correlator's Growth Rate in a Chaotic System". In: *Phys. Rev. Lett.* 118 (8 2017), p. 086801.
- [77] J. Marino and A. M. Rey. "Cavity-QED simulator of slow and fast scrambling". In: *Phys. Rev. A* 99 (5 2019), p. 051803.
- [78] G. Bentsen et al. "Treelike Interactions and Fast Scrambling with Cold Atoms". In: *Phys. Rev. Lett.* 123 (13 2019), p. 130601.
- [79] Y. Alavirad and A. Lavasani. "Scrambling in the Dicke model". In: *Physical Review A* 99.4 (20 2019), p. 043602.
- [80] L. Amico et al. "Entanglement in many-body systems". In: *Rev. Mod. Phys.* 80 (2 2008), pp. 517–576.

- [81] J. M. Deutsch, H. Li, and A. Sharma. “Microscopic origin of thermodynamic entropy in isolated systems”. In: *Phys. Rev. E* 87 (4 2013), p. 042135.
- [82] A. Dymarsky, N. Lashkari, and H. Liu. “Subsystem eigenstate thermalization hypothesis”. In: *Phys. Rev. E* 97 (1 2018), p. 012140.
- [83] J. Berges, S. Floerchinger, and R. Venugopalan. “Entanglement and thermalization”. In: *Nuclear Physics A* 982 (20 Feb. 2019), 819–822.
- [84] J. M. Deutsch. “Quantum statistical mechanics in a closed system”. In: *Phys. Rev. A* 43 (4 1991), pp. 2046–2049.
- [85] M. Srednicki. “Chaos and quantum thermalization”. In: *Phys. Rev. E* 50 (2 1994), pp. 888–901.
- [86] A. Polkovnikov et al. “Colloquium: Nonequilibrium dynamics of closed interacting quantum systems”. In: *Reviews of Modern Physics* 83.3 (20 2011), p. 863.
- [87] L. D’Alessio et al. “From quantum chaos and eigenstate thermalization to statistical mechanics and thermodynamics”. In: *Advances in Physics* 65.3 (20 May 2016), 239–362.
- [88] G. De Palma et al. “Necessity of Eigenstate Thermalization”. In: *Phys. Rev. Lett.* 115 (22 2015), p. 220401.
- [89] J. M. Deutsch. “Eigenstate thermalization hypothesis”. In: *Reports on Progress in Physics* 81.8 (20 July 2018), p. 082001.
- [90] D. A. Huse et al. “Localization-protected quantum order”. In: *Phys. Rev. B* 88 (1 2013), p. 014206.
- [91] M. T. Batchelor. “Beautiful Models: 70 Years of Exactly Solved Quantum Many-Body Problems”. In: *Journal of Physics A: Mathematical and General* 38.14 (20 Mar. 2005), 3245–3246.
- [92] L. Vidmar and M. Rigol. “Generalized Gibbs ensemble in integrable lattice models”. In: *Journal of Statistical Mechanics: Theory and Experiment* 2016.6 (20 June 2016), p. 064007.
- [93] P. W. Anderson. “Absence of Diffusion in Certain Random Lattices”. In: *Phys. Rev.* 109 (5 1958), pp. 1492–1505.
- [94] D. Basko, I. Aleiner, and B. Altshuler. “Metal–insulator transition in a weakly interacting many-electron system with localized single-particle states”. In: *Annals of Physics* 321.5 (20 May 2006), 1126–1205.
- [95] F. Alet and N. Laflorencie. “Many-body localization: An introduction and selected topics”. In: *Comptes Rendus Physique* 19.6 (20 2018), pp. 498–525.
- [96] M. Serbyn, Z. Papić, and D. A. Abanin. “Universal Slow Growth of Entanglement in Interacting Strongly Disordered Systems”. In: *Physical Review Letters* 110.26 (20 June 2013), p. 203001.

- [97] J. H. Bardarson, F. Pollmann, and J. E. Moore. "Unbounded Growth of Entanglement in Models of Many-Body Localization". In: *Phys. Rev. Lett.* 109 (1 2012), p. 017202.
- [98] A. Chandran et al. "Constructing local integrals of motion in the many-body localized phase". In: *Phys. Rev. B* 91 (8 2015), p. 085425.
- [99] V. Ros, M. Müller, and A. Scardicchio. "Integrals of motion in the many-body localized phase". In: *Nuclear Physics B* 891 (20 2015), pp. 420–465.
- [100] J. Z. Imbrie, V. Ros, and A. Scardicchio. "Local integrals of motion in many-body localized systems". In: *Annalen der Physik* 529.7 (20 2017), p. 1600278.
- [101] D. A. Huse, R. Nandkishore, and V. Oganesyan. "Phenomenology of fully many-body-localized systems". In: *Physical Review B* 90.17 (20 2014), p. 174202.
- [102] W. De Roeck and F. m. c. Huveneers. "Stability and instability towards delocalization in many-body localization systems". In: *Phys. Rev. B* 95 (15 2017), p. 155129.
- [103] T. Thiery et al. "Many-body delocalization as a quantum avalanche". In: *Physical review letters* 121.14 (20 2018), p. 140601.
- [104] M Schulz et al. "Phenomenology of anomalous transport in disordered one-dimensional systems". In: *Journal of Statistical Mechanics: Theory and Experiment* 2020.2 (20 Feb. 2020), p. 023107.
- [105] J. Šuntajs et al. "Quantum chaos challenges many-body localization". In: *Physical Review E* 102.6 (20 2020), p. 062144.
- [106] A. Morningstar et al. "Avalanches and many-body resonances in many-body localized systems". In: *Phys. Rev. B* 105 (17 2022), p. 174205.
- [107] D. Abanin et al. "Distinguishing localization from chaos: Challenges in finite-size systems". In: *Annals of Physics* 427 (20 2021), p. 168415.
- [108] S. R. Taylor and A. Scardicchio. "Subdiffusion in a one-dimensional Anderson insulator with random dephasing: Finite-size scaling, Griffiths effects, and possible implications for many-body localization". In: *Phys. Rev. B* 103 (18 2021), p. 184202.
- [109] D. Sels and A. Polkovnikov. "Dynamical obstruction to localization in a disordered spin chain". In: *Phys. Rev. E* 104 (5 2021), p. 054105.
- [110] D. Sels. "Bath-induced delocalization in interacting disordered spin chains". In: *Phys. Rev. B* 106 (2 2022), p. L020202.
- [111] P. Sierant and J. Zakrzewski. "Challenges to observation of many-body localization". In: *Phys. Rev. B* 105 (22 2022), p. 224203.
- [112] D. Sels and A. Polkovnikov. "Thermalization of Dilute Impurities in One-Dimensional Spin Chains". In: *Phys. Rev. X* 13 (1 2023), p. 011041.
- [113] H. P. Lüschen et al. "Signatures of Many-Body Localization in a Controlled Open Quantum System". In: *Phys. Rev. X* 7 (1 2017), p. 011034.

- [114] . “Critical Behavior near the Many-Body Localization Transition in Driven Open Systems”. In: *Phys. Rev. Lett.* 125 (11 2020), p. 116601.
- [115] M. V. Medvedyeva, T. c. ž. Prosen. “Influence of dephasing on many-body localization”. In: *Phys. Rev. B* 93 (9 2016), p. 094205.
- [116] R. Nandkishore, S. Gopalakrishnan, and D. A. Huse. “Spectral features of a many-body-localized system weakly coupled to a bath”. In: *Phys. Rev. B* 90 (6 2014), p. 064203.
- [117] R. Nandkishore and S. Gopalakrishnan. “Many body localized systems weakly coupled to baths”. In: *Annalen der Physik* 529.7 (9 2017), p. 1600181.
- [118] M. H. Fischer, M. Maksymenko, and E. Altman. “Dynamics of a Many-Body-Localized System Coupled to a Bath”. In: *Phys. Rev. Lett.* 116 (16 2016), p. 160401.
- [119] G. Carleo et al. “Localization and Glassy Dynamics Of Many-Body Quantum Systems”. In: *Scientific Reports* 2 (9 2012), p. 243.
- [120] E. V. H. Doggen, I. V. Gornyi, and D. G. Polyakov. “Stark many-body localization: Evidence for Hilbert-space shattering”. In: *Phys. Rev. B* 103 (10 2021), p. L100202.
- [121] W. De Roeck and F. Huveneers. “Scenario for delocalization in translation-invariant systems”. In: *Phys. Rev. B* 90 (16 2014), p. 165137.
- [122] M. Schiulaz, A. Silva, and M. Müller. “Dynamics in many-body localized quantum systems without disorder”. In: *Phys. Rev. B* 91 (18 2015), p. 184202.
- [123] Z. Papić, E. M. Stoudenmire, and D. A. Abanin. “Many-body localization in disorder-free systems: The importance of finite-size constraints”. In: *Ann. of Phys.* 362 (9 2015), pp. 714 –725.
- [124] L. Barbiero et al. “Out-of-equilibrium states and quasi-many-body localization in polar lattice gases”. In: *Phys. Rev. B* 92 (18 2015), 180406(R).
- [125] N. Y. Yao et al. “Quasi-Many-Body Localization in Translation-Invariant Systems”. In: *Phys. Rev. Lett.* 117 (24 2016), p. 240601.
- [126] A. Smith et al. “Disorder-Free Localization”. In: *Phys. Rev. Lett.* 118 (26 2017), p. 266601.
- [127] R. Mondaini et al. “Comment on “Systematic Construction of Counterexamples to the Eigenstate Thermalization Hypothesis””. In: *Phys. Rev. Lett.* 121 (3 2018), p. 038901.
- [128] M. Schulz et al. “Stark Many-Body Localization”. In: *Phys. Rev. Lett.* 122 (4 2019), p. 040606.
- [129] E. van Nieuwenburg, Y. Baum, and G. Refael. “From Bloch oscillations to many-body localization in clean interacting systems”. In: *Proc. Natl. Acad. Sci. USA* 116.19 (9 2019), pp. 9269–9274.
- [130] N. Shiraishi and T. Mori. “Shiraishi and Mori Reply”. In: *Phys. Rev. Lett.* 121 (3 2018), p. 038902.

- [131] M. Kormos et al. “Real-time confinement following a quantum quench to a non-integrable model”. In: *Nature Physics* 13.3 (9 2017), pp. 246–249.
- [132] A. J. A. James, R. M. Konik, and N. J. Robinson. “Nonthermal States Arising from Confinement in One and Two Dimensions”. In: *Phys. Rev. Lett.* 122 (13 2019), p. 130603.
- [133] W. Morong et al. “Observation of Stark many-body localization without disorder”. In: *arXiv preprint arXiv:2102.07250* 93 (9 2021), p. 094205.
- [134] T. Gunawardana and B. Buća. “Dynamical 1-bits in Stark many-body localization”. In: *arXiv preprint arXiv:2110.13135* 93 (9 2021), p. 094205.
- [135] B. Buća et al. “Quantum many-body attractors”. In: *arXiv preprint arXiv:2008.11166* 93 (9 2020), p. 094205.
- [136] F. Ritort and P. Sollich. “Glassy dynamics of kinetically constrained models”. In: *Advances in physics* 52.4 (9 2003), pp. 219–342.
- [137] C. Chamon. “Quantum Glassiness in Strongly Correlated Clean Systems: An Example of Topological Overprotection”. In: *Phys. Rev. Lett.* 94 (4 2005), p. 040402.
- [138] J. P. Garrahan. “Aspects of non-equilibrium in classical and quantum systems: Slow relaxation and glasses, dynamical large deviations, quantum non-ergodicity, and open quantum dynamics”. In: *Physica A: Statistical Mechanics and its Applications* 504 (9 Aug. 2018), pp. 130–154.
- [139] J. M. Hickey, S. Genway, and J. P. Garrahan. “Signatures of many-body localisation in a system without disorder and the relation to a glass transition”. In: *J. Stat. Mech.* 2016.5 (9 2016), p. 054047.
- [140] M. van Horssen, E. Levi, and J. P. Garrahan. “Dynamics of many-body localization in a translation-invariant quantum glass model”. In: *Phys. Rev. B* 92 (10 2015), 100305(R).
- [141] Z. Lan et al. “Quantum Slow Relaxation and Metastability due to Dynamical Constraints”. In: *Phys. Rev. Lett.* 121 (4 2018), p. 040603.
- [142] J. Feldmeier, F. Pollmann, and M. Knap. “Emergent Glassy Dynamics in a Quantum Dimer Model”. In: *Phys. Rev. Lett.* 123 (4 2019), p. 040601.
- [143] C. Castelnovo et al. “From quantum mechanics to classical statistical physics: Generalized Rokhsar–Kivelson Hamiltonians and the “Stochastic Matrix Form” decomposition”. In: *Ann. of Phys.* 318.2 (9 2005), pp. 316 –344.
- [144] J. P. Garrahan et al. “First-order dynamical phase transition in models of glasses: an approach based on ensembles of histories”. In: *Journal of Physics A: Mathematical and Theoretical* 42.7 (9 2009), p. 075007.
- [145] P Chleboun, A Faggionato, and F Martinelli. “Time scale separation in the low temperature East model: rigorous results”. In: *J. Stat. Mech.* 2013.04 (9 2013), p. L04001.

- [146] H. Kim et al. "Slowest local operators in quantum spin chains". In: *Phys. Rev. E* 92 (1 2015), p. 012128.
- [147] S. Gopalakrishnan et al. "Hydrodynamics of operator spreading and quasiparticle diffusion in interacting integrable systems". In: *Physical Review B* 98.22 (9 2018), 220303(R).
- [148] S. Gopalakrishnan. "Operator growth and eigenstate entanglement in an interacting integrable Floquet system". In: *Physical Review B* 98.6 (9 2018), 060302(R).
- [149] M. C. Bañuls and J. P. Garrahan. "Using Matrix Product States to Study the Dynamical Large Deviations of Kinetically Constrained Models". In: *Phys. Rev. Lett.* 123 (20 2019), p. 200601.
- [150] L. Causer et al. "Dynamics and large deviation transitions of the XOR-Fredrickson-Andersen kinetically constrained model". In: *Phys. Rev. E* 102 (5 2020), p. 052132.
- [151] N. Pancotti et al. "Quantum East Model: Localization, Nonthermal Eigenstates, and Slow Dynamics". In: *Phys. Rev. X* 10 (2 2020), p. 021051.
- [152] P. Brighi, M. Ljubotina, and M. Serbyn. "Hilbert space fragmentation and slow dynamics in particle-conserving quantum East models". In: *SciPost Physics* 15.3 (9 2023), p. 093.
- [153] T. Bhore, J.-Y. Desaules, and Z. Papić. "Deep thermalization in constrained quantum systems". In: *Physical Review B* 108.10 (9 2023), p. 104317.
- [154] K. Klobas, C. De Fazio, and J. P. Garrahan. "Exact" hydrophobicity" in deterministic circuits: dynamical fluctuations in the Floquet-East model". In: *arXiv preprint arXiv:2305.07423* 93 (9 2023), p. 094205.
- [155] B. Bertini, P. Kos, and T. c. v. Prosen. "Localized Dynamics in the Floquet Quantum East Model". In: *Phys. Rev. Lett.* 132 (8 2024), p. 080401.
- [156] M. Aspelmeyer, T. J. Kippenberg, and F. Marquardt. "Cavity optomechanics". In: *Rev. Mod. Phys.* 86 (4 2014), pp. 1391–1452.
- [157] A. Chandran et al. "Quantum many-body scars: A quasiparticle perspective". In: *Annual Review of Condensed Matter Physics* 14 (9 2023), pp. 443–469.
- [158] S. Moudgalya, B. A. Bernevig, and N. Regnault. "Quantum many-body scars and Hilbert space fragmentation: a review of exact results". In: *Reports on Progress in Physics* 85.8 (9 2022), p. 086501.
- [159] X WANG et al. "Quantum information with Gaussian states". In: *Physics Reports* 448.1–4 (9 Aug. 2007), 1–111.
- [160] D. F. Walls and G. J. Milburn. *Quantum optics*. Vol. 93. Berlin, Germany: Springer Science & Business Media, 2007, p. 094205.
- [161] U. Schollwöck. "The density-matrix renormalization group in the age of matrix product states". In: *Annals of Physics* 326.1 (9 2011). January 2011 Special Issue, pp. 96–192.

- [162] J. Sakurai and J. Napolitano. *Modern Quantum Mechanics*. Vol. 93. Cambridge, England: Cambridge University Press, 2017, p. 094205.
- [163] A. Messiah. *Quantum Mechanics*. Vol. 93. Dover Books on Physics. Mineola, NY: Dover Publications, 2014, p. 094205.
- [164] A. Blais et al. “Circuit quantum electrodynamics”. In: *Rev. Mod. Phys.* 93 (2 2021), p. 025005.
- [165] T. Barthel and U. Schollwöck. “Dephasing and the Steady State in Quantum Many-Particle Systems”. In: *Phys. Rev. Lett.* 100 (10 2008), p. 100601.
- [166] B. Yurke and D. Stoler. “The dynamic generation of Schrödinger cats and their detection”. In: *Physica B + C* 151.1-2 (9 1988), pp. 298–301.
- [167] G. Kirchmair et al. “Observation of quantum state collapse and revival due to the single-photon Kerr effect”. In: *Nature* 495.7440 (9 2013), 205–209.
- [168] D. Jaschke, S. Montangero, and L. D. Carr. “One-dimensional many-body entangled open quantum systems with tensor network methods”. In: *Quantum Science and Technology* 4.1 (9 Nov. 2018), p. 013001.
- [169] A. J. Daley. “Quantum trajectories and open many-body quantum systems”. In: *Advances in Physics* 63.2 (9 Mar. 2014), pp. 77–149.
- [170] P. E. Dolgirev et al. “Non-Gaussian correlations imprinted by local dephasing in fermionic wires”. In: *Physical Review B* 102.10 (9 2020), 100301(R).
- [171] M. Žnidarič, A. Scardicchio, and V. K. Varma. “Diffusive and subdiffusive spin transport in the ergodic phase of a many-body localizable system”. In: *Physical review letters* 117.4 (9 2016), p. 040601.
- [172] C. Sünderhauf et al. “Localization with random time-periodic quantum circuits”. In: *Phys. Rev. B* 98 (13 2018), p. 134204.
- [173] S. Pai, M. Pretko, and R. M. Nandkishore. “Localization in Fractonic Random Circuits”. In: *Phys. Rev. X* 9 (2 2019), p. 021003.
- [174] S. Moudgalya and O. I. Motrunich. “Hilbert Space Fragmentation and Commutant Algebras”. In: *Phys. Rev. X* 12 (1 2022), p. 011050.
- [175] I. Mondragon-Shem et al. “Many-body mobility edge due to symmetry-constrained dynamics and strong interactions”. In: *Phys. Rev. B* 92 (6 2015), p. 064203.
- [176] D. J. Luitz, N. Laflorencie, and F. Alet. “Many-body localization edge in the random-field Heisenberg chain”. In: *Phys. Rev. B* 91 (8 2015), p. 081103.
- [177] P. Naldesi, E. Ercolessi, and T. Roscilde. “Detecting a many-body mobility edge with quantum quenches”. In: *SciPost Physics* 1.1 (9 Oct. 2016), p. 094205.
- [178] T. Kohlert et al. “Observation of many-body localization in a one-dimensional system with a single-particle mobility edge”. In: *Physical review letters* 122.17 (9 2019), p. 170403.

- [179] I. Lesanovsky and J. P. Garrahan. “Kinetic Constraints, Hierarchical Relaxation, and Onset of Glassiness in Strongly Interacting and Dissipative Rydberg Gases”. In: *Phys. Rev. Lett.* 111 (21 2013), p. 215305.
- [180] C. Pérez-Espigares et al. “Glassy dynamics due to a trajectory phase transition in dissipative Rydberg gases”. In: *Phys. Rev. A* 98 (2 2018), 021804(R).
- [181] M. M. Valado et al. “Experimental observation of controllable kinetic constraints in a cold atomic gas”. In: *Phys. Rev. A* 93 (4 2016), 040701(R).
- [182] I. Lesanovsky and J. P. Garrahan. “Out-of-equilibrium structures in strongly interacting Rydberg gases with dissipation”. In: *Phys. Rev. A* 90 (1 2014), 011603(R).
- [183] D. Gribben, I. Lesanovsky, and R. Gutiérrez. “Quench dynamics of a dissipative Rydberg gas in the classical and quantum regimes”. In: *Phys. Rev. A* 97 (1 2018), 011603(R).
- [184] M. Ostmann et al. “Localization in spin chains with facilitation constraints and disordered interactions”. In: *Phys. Rev. A* 99 (6 2019), 060101(R).
- [185] M. Marcuzzi et al. “Facilitation Dynamics and Localization Phenomena in Rydberg Lattice Gases with Position Disorder”. In: *Phys. Rev. Lett.* 118 (6 2017), p. 063606.
- [186] H. Kim and D. A. Huse. “Ballistic Spreading of Entanglement in a Diffusive Nonintegrable System”. In: *Phys. Rev. Lett.* 111 (12 2013), p. 127205.
- [187] A. Ehrenberg et al. “Simulation Complexity of Many-Body Localized Systems”. In: *arXiv preprint arXiv:2205.12967* 93 (9 2022), p. 094205.
- [188] E. H. Lieb and D. W. Robinson. “The finite group velocity of quantum spin systems”. In: *Communications in mathematical physics* 28.3 (9 1972), pp. 251–257.
- [189] M. C. Bañuls et al. “Dynamics of quantum information in many-body localized systems”. In: *Phys. Rev. B* 96 (17 2017), p. 174201.
- [190] G. Vidal. “Efficient Classical Simulation of Slightly Entangled Quantum Computations”. In: *Phys. Rev. Lett.* 91 (14 2003), p. 147902.
- [191] J. Gray. “quimb: A python package for quantum information and many-body calculations”. In: *Journal of Open Source Software* 3.29 (9 Sept. 2018), p. 819.
- [192] Z. Lan et al. “Quantum slow relaxation and metastability due to dynamical constraints”. In: *Physical review letters* 121.4 (9 2018), p. 040603.
- [193] L. Zadnik and J. P. Garrahan. “Slow heterogeneous relaxation due to constraints in dual XXZ models”. In: *Physical Review B* 108.10 (9 2023), p. L100304.
- [194] J. Haah et al. “Quantum Algorithm for Simulating Real Time Evolution of Lattice Hamiltonians”. In: *SIAM Journal on Computing* 52.6 (9 Jan. 2021), FOCS18–250–FOCS18–284.

- [195] V. Khemani, F. Pollmann, and S. L. Sondhi. “Obtaining Highly Excited Eigenstates of Many-Body Localized Hamiltonians by the Density Matrix Renormalization Group Approach”. In: *Phys. Rev. Lett.* 116 (24 2016), p. 247204.
- [196] S. Aaronson and A. Arkhipov. *The Computational Complexity of Linear Optics*. 2010. arXiv: [1011.3245 \[quant-ph\]](https://arxiv.org/abs/1011.3245).
- [197] A. P. Lund, M. J. Bremner, and T. C. Ralph. “Quantum sampling problems, BosonSampling and quantum supremacy”. In: *npj Quantum Information* 3.1 (9 Apr. 2017), p. 094205.
- [198] A. Deshpande et al. “Dynamical Phase Transitions in Sampling Complexity”. In: *Phys. Rev. Lett.* 121 (3 2018), p. 030501.
- [199] Y. Han, X. Chen, and E. Lake. “Exponentially slow thermalization and the robustness of Hilbert space fragmentation”. In: *arXiv preprint arXiv:2401.11294* 93 (9 2024), p. 094205.
- [200] S. Choi et al. “Emergent SU(2) Dynamics and Perfect Quantum Many-Body Scars”. In: *Phys. Rev. Lett.* 122 (22 2019), p. 220603.
- [201] F. M. Surace et al. “Lattice Gauge Theories and String Dynamics in Rydberg Atom Quantum Simulators”. In: *Phys. Rev. X* 10 (2 2020), p. 021041.
- [202] A. Lerose et al. “Quasilocalized dynamics from confinement of quantum excitations”. In: *Phys. Rev. B* 102 (4 2020), 041118(R).
- [203] Y. Li, P. Sala, and F. Pollmann. “Hilbert space fragmentation in open quantum systems”. In: *Phys. Rev. Res.* 5 (4 2023), p. 043239.
- [204] G. De Tomasi et al. “Dynamics of strongly interacting systems: From Fock-space fragmentation to many-body localization”. In: *Phys. Rev. B* 100 (21 2019), p. 214313.
- [205] L. Herviou, J. H. Bardarson, and N. Regnault. “Many-body localization in a fragmented Hilbert space”. In: *Phys. Rev. B* 103 (13 2021), p. 134207.
- [206] S. Moudgalya et al. “Thermalization and Its Absence within Krylov Subspaces of a Constrained Hamiltonian”. In: *Memorial Volume for Shoucheng Zhang*. Vol. 93. WORLD SCIENTIFIC, Sept. 2021, 147–209.
- [207] L. Zhao et al. “Observation of quantum thermalization restricted to Hilbert space fragments”. In: *arXiv preprint arXiv:2403.09517* 93 (9 2024), p. 094205.
- [208] F. Balducci et al. “Interface dynamics in the two-dimensional quantum Ising model”. In: *Phys. Rev. B* 107 (2 2023), p. 024306.
- [209] G. H. Wannier. “Wave Functions and Effective Hamiltonian for Bloch Electrons in an Electric Field”. In: *Phys. Rev.* 117 (2 1960), pp. 432–439.
- [210] G. H. Wannier. “Dynamics of Band Electrons in Electric and Magnetic Fields”. In: *Rev. Mod. Phys.* 34 (4 1962), pp. 645–655.

- [211] S. Maity and R. Hamazaki. “Kinetically constrained models constructed from dissipative quantum dynamics”. In: *arXiv preprint arXiv:2403.12548* 93 (9 2024), p. 094205.
- [212] F. Liu et al. “Confined Quasiparticle Dynamics in Long-Range Interacting Quantum Spin Chains”. In: *Phys. Rev. Lett.* 122 (15 2019), p. 150601.
- [213] A. Clerk. “Introduction to quantum non-reciprocal interactions: from non-Hermitian Hamiltonians to quantum master equations and quantum feedforward schemes”. In: *SciPost Physics Lecture Notes* 93 (9 Mar. 2022), p. 094205.
- [214] K. Fang et al. “Generalized non-reciprocity in an optomechanical circuit via synthetic magnetism and reservoir engineering”. In: *Nature Physics* 13.5 (9 Jan. 2017), 465–471.
- [215] Y.-X. Wang, C. Wang, and A. A. Clerk. “Quantum Nonreciprocal Interactions via Dissipative Gauge Symmetry”. In: *PRX Quantum* 4 (1 2023), p. 010306.
- [216] P. Zhang et al. “Many-body Hilbert space scarring on a superconducting processor”. In: *Nature Physics* 19.1 (9 2023), pp. 120–125.
- [217] T. Kohlert et al. “Exploring the Regime of Fragmentation in Strongly Tilted Fermi-Hubbard Chains”. In: *Phys. Rev. Lett.* 130 (1 2023), p. 010201.
- [218] W. L. Tan et al. “Domain-wall confinement and dynamics in a quantum simulator”. In: *Nature Physics* 17.6 (9 Mar. 2021), 742–747.
- [219] P. Scholl et al. “Quantum simulation of 2D antiferromagnets with hundreds of Rydberg atoms”. In: *Nature* 595.7866 (9 July 2021), pp. 233–238.
- [220] D. Bluvstein et al. “Controlling quantum many-body dynamics in driven Rydberg atom arrays”. In: *Science* 371.6536 (9 Mar. 2021), pp. 1355–1359.
- [221] A. Browaeys and T. Lahaye. “Many-body physics with individually controlled Rydberg atoms”. In: *Nature Physics* 16.2 (9 Jan. 2020), pp. 132–142.
- [222] H. Labuhn et al. “Tunable two-dimensional arrays of single Rydberg atoms for realizing quantum Ising models”. In: *Nature* 534.7609 (9 June 2016), 667–670.
- [223] S. Ebadi et al. “Quantum phases of matter on a 256-atom programmable quantum simulator”. In: *Nature* 595.7866 (9 July 2021), pp. 227–232.
- [224] A. Keesling et al. “Quantum Kibble–Zurek mechanism and critical dynamics on a programmable Rydberg simulator”. In: *Nature* 568.7751 (9 Apr. 2019), pp. 207–211.
- [225] A. Kamal, J. Clarke, and M. H. Devoret. “Noiseless non-reciprocity in a parametric active device”. In: *Nature Physics* 7.4 (9 Jan. 2011), pp. 311–315.
- [226] A. McDonald, T. Pereg-Barnea, and A. A. Clerk. “Phase-Dependent Chiral Transport and Effective Non-Hermitian Dynamics in a Bosonic Kitaev-Majorana Chain”. In: *Phys. Rev. X* 8 (4 2018), p. 041031.
- [227] P. Lodahl et al. “Chiral quantum optics”. In: *Nature* 541.7638 (9 Jan. 2017), 473–480.

- [228] H. Pichler et al. “Quantum optics of chiral spin networks”. In: *Phys. Rev. A* 91 (4 2015), p. 042116.
- [229] X. Wang et al. “Tunable Chiral Bound States with Giant Atoms”. In: *Phys. Rev. Lett.* 126 (4 2021), p. 043602.
- [230] M. Fruchart et al. “Non-reciprocal phase transitions”. In: *Nature* 592.7854 (9 Apr. 2021), pp. 363–369.
- [231] S.-H. Wei et al. “Towards real-world quantum networks: a review”. In: *Laser & Photonics Reviews* 16.3 (9 2022), p. 2100219.
- [232] P. Kitson et al. *Rydberg atomtronic devices*. 2023. arXiv: [2310.18242 \[quant-ph\]](https://arxiv.org/abs/2310.18242).
- [233] D. Jaksch et al. “Fast Quantum Gates for Neutral Atoms”. In: *Phys. Rev. Lett.* 85 (10 2000), pp. 2208–2211.
- [234] C. Ates et al. “Many-body theory of excitation dynamics in an ultracold Rydberg gas”. In: *Phys. Rev. A* 76 (1 2007), p. 013413.
- [235] C. Chen et al. “Continuous symmetry breaking in a two-dimensional Rydberg array”. In: *Nature* 616.7958 (9 Feb. 2023), 691–695.
- [236] A. Omran et al. “Generation and manipulation of Schrödinger cat states in Rydberg atom arrays”. In: *Science* 365.6453 (9 Aug. 2019), 570–574.
- [237] M. Ostmann et al. “Synthetic lattices, flat bands and localization in Rydberg quantum simulators”. In: *Quantum Science and Technology* 4.2 (9 2019), 02LT01.
- [238] V. Lienhard et al. “Realization of a Density-Dependent Peierls Phase in a Synthetic, Spin-Orbit Coupled Rydberg System”. In: *Phys. Rev. X* 10 (2 2020), p. 021031.
- [239] F. Perciavalle et al. “Controlled flow of excitations in a ring-shaped network of Rydberg atoms”. In: *Phys. Rev. A* 108 (2 2023), p. 023305.
- [240] G. H. Fredrickson and H. C. Andersen. “Kinetic Ising Model of the Glass Transition”. In: *Phys. Rev. Lett.* 53 (13 1984), pp. 1244–1247.
- [241] A. Blais, S. M. Girvin, and W. D. Oliver. “Quantum information processing and quantum optics with circuit quantum electrodynamics”. In: *Nature Physics* 16.3 (9 Mar. 2020), pp. 247–256.
- [242] A. Joshi, K. Noh, and Y. Y. Gao. “Quantum information processing with bosonic qubits in circuit QED”. In: *Quantum Science and Technology* 6.3 (9 2021), p. 033001.
- [243] A. Eickbusch et al. *Fast Universal Control of an Oscillator with Weak Dispersive Coupling to a Qubit*. 2021. arXiv: [2111.06414 \[quant-ph\]](https://arxiv.org/abs/2111.06414).
- [244] W.-L. Ma et al. “Quantum control of bosonic modes with superconducting circuits”. In: *Science Bulletin* 66.17 (9 Sept. 2021), pp. 1789–1805.
- [245] C.-H. Wang et al. “Photon-Number-Dependent Hamiltonian Engineering for Cavities”. In: *Physical Review Applied* 15.4 (9 Apr. 2021), p. 044026.

- [246] C. S. Wang et al. “Efficient Multiphoton Sampling of Molecular Vibronic Spectra on a Superconducting Bosonic Processor”. In: *Phys. Rev. X* 10 (2 2020), p. 021060.
- [247] A. Wallraff et al. “Strong coupling of a single photon to a superconducting qubit using circuit quantum electrodynamics”. In: *Nature* 431.7005 (9 Sept. 2004), pp. 162–167.
- [248] A. A. Houck, H. E. Türeci, and J. Koch. “On-chip quantum simulation with superconducting circuits”. In: *Nature Physics* 8.4 (9 Apr. 2012), pp. 292–299.
- [249] J. Koch et al. “Charge-insensitive qubit design derived from the Cooper pair box”. In: *Phys. Rev. A* 76 (4 2007), p. 042319.
- [250] N. E. Frattini et al. “3-wave mixing Josephson dipole element”. In: *Applied Physics Letters* 110.22 (9 May 2017), p. 222603.
- [251] I. Carusotto et al. “Photonic materials in circuit quantum electrodynamics”. In: *Nature Physics* 16.3 (9 Mar. 2020), pp. 268–279.
- [252] Y. Yanay et al. “Two-dimensional hard-core Bose–Hubbard model with superconducting qubits”. In: *npj Quantum Information* 6.1 (9 June 2020), pp. 1–12.
- [253] O. Mansikkamäki, S. Laine, and M. Silveri. “Phases of the disordered Bose–Hubbard model with attractive interactions”. In: *Phys. Rev. B* 103 (22 2021), p. L220202.
- [254] S. Schmidt and J. Koch. “Circuit QED lattices: Towards quantum simulation with superconducting circuits”. In: *Annalen der Physik* 525.6 (9 Apr. 2013), pp. 395–412.
- [255] M. H. Devoret and R. J. Schoelkopf. “Superconducting Circuits for Quantum Information: An Outlook”. In: *Science* 339.6124 (9 Mar. 2013), pp. 1169–1174.
- [256] P. Roushan et al. “Spectroscopic signatures of localization with interacting photons in superconducting qubits”. In: *Science* 358.6367 (9 Dec. 2017), pp. 1175–1179.
- [257] Y. Ye et al. “Propagation and Localization of Collective Excitations on a 24-Qubit Superconducting Processor”. In: *Phys. Rev. Lett.* 123 (5 2019), p. 050502.
- [258] B. Chiaro et al. *Direct measurement of non-local interactions in the many-body localized phase*. 2020. arXiv: [1910.06024 \[cond-mat.dis-nn\]](https://arxiv.org/abs/1910.06024).
- [259] B. Josephson. “Possible new effects in superconductive tunnelling”. In: *Physics Letters* 1.7 (9 1962), pp. 251–253.
- [260] M. Tinkham. *Introduction to superconductivity*. Vol. 93. Mineola, NY: Courier Corporation, 2004, p. 094205.
- [261] A. Noguchi et al. “Fast parametric two-qubit gates with suppressed residual interaction using the second-order nonlinearity of a cubic transmon”. In: *Phys. Rev. A* 102 (6 2020), p. 062408.
- [262] F. Yan et al. “The flux qubit revisited to enhance coherence and reproducibility”. In: *Nature Communications* 7.1 (9 Nov. 2016), pp. 1–9.

- [263] L. DiCarlo et al. “Demonstration of two-qubit algorithms with a superconducting quantum processor”. In: *Nature* 460.7252 (9 June 2009), pp. 240–244.
- [264] R. Barends et al. “Superconducting quantum circuits at the surface code threshold for fault tolerance”. In: *Nature* 508.7497 (9 Apr. 2014), pp. 500–503.
- [265] A. Auerbach. *Interacting Electrons and Quantum Magnetism*. Vol. 93. Graduate Texts in Contemporary Physics. New York, NY: Springer New York, 2012, p. 094205.
- [266] E. Magesan and J. M. Gambetta. “Effective Hamiltonian models of the cross-resonance gate”. In: *Phys. Rev. A* 101 (5 2020), p. 052308.
- [267] S. Sheldon et al. “Procedure for systematically tuning up cross-talk in the cross-resonance gate”. In: *Phys. Rev. A* 93 (6 2016), 060302(R).
- [268] A. D. Córcoles et al. “Process verification of two-qubit quantum gates by randomized benchmarking”. In: *Phys. Rev. A* 87 (3 2013), 030301(R).
- [269] A. Blais et al. “Quantum-information processing with circuit quantum electrodynamics”. In: *Phys. Rev. A* 75 (3 2007), p. 032329.
- [270] R. U. Haq, S. S. Bharadwaj, and T. A. Wani. *An Explicit Method for Schrieffer-Wolff Transformation*. 2019. arXiv: [1901.08617 \[cond-mat.str-el\]](https://arxiv.org/abs/1901.08617).
- [271] E. Jaynes and F. Cummings. “Comparison of quantum and semiclassical radiation theories with application to the beam maser”. In: *Proceedings of the IEEE* 51.1 (9 1963), 89–109.
- [272] A. Asenjo-Garcia et al. “Exponential Improvement in Photon Storage Fidelities Using Subradiance and “Selective Radiance” in Atomic Arrays”. In: *Phys. Rev. X* 7 (3 2017), p. 031024.
- [273] M. V. Medvedyeva, T. c. ř. Prosen. *Quantum Optics*. Vol. 93. Springer Berlin Heidelberg, 2008, p. 094205.
- [274] S. B. Jäger et al. “Lindblad Master Equations for Quantum Systems Coupled to Dissipative Bosonic Modes”. In: *Phys. Rev. Lett.* 129 (6 2022), p. 063601.
- [275] F. m. c. Damanet, A. J. Daley, and J. Keeling. “Atom-only descriptions of the driven-dissipative Dicke model”. In: *Phys. Rev. A* 99 (3 2019), p. 033845.
- [276] M. Xu et al. “Supercooling of Atoms in an Optical Resonator”. In: *Phys. Rev. Lett.* 116 (15 2016), p. 153002.
- [277] S. B. Jäger et al. “Semiclassical theory of synchronization-assisted cooling”. In: *Phys. Rev. A* 95 (6 2017), p. 063852.
- [278] A. Piñeiro Orioli, J. K. Thompson, and A. M. Rey. “Emergent Dark States from Superradiant Dynamics in Multilevel Atoms in a Cavity”. In: *Phys. Rev. X* 12 (1 2022), p. 011054.
- [279] R. Lin et al. “Dissipation-Engineered Family of Nearly Dark States in Many-Body Cavity-Atom Systems”. In: *Phys. Rev. Lett.* 128 (15 2022), p. 153601.

- [280] M. Hayn, C. Emery, and T. Brandes. “Phase transitions and dark-state physics in two-color superradiance”. In: *Phys. Rev. A* 84 (5 2011), p. 053856.
- [281] Y. Xu, D. Fallas Padilla, and H. Pu. “Multicriticality and quantum fluctuation in a generalized Dicke model”. In: *Phys. Rev. A* 104 (4 2021), p. 043708.
- [282] J. Fan, G. Chen, and S. Jia. “Atomic self-organization emerging from tunable quadrature coupling”. In: *Phys. Rev. A* 101 (6 2020), p. 063627.
- [283] P. Kongkhambut et al. “Realization of a Periodically Driven Open Three-Level Dicke Model”. In: *Phys. Rev. Lett.* 127 (25 2021), p. 253601.
- [284] J. Skulte et al. “Parametrically driven dissipative three-level Dicke model”. In: *Phys. Rev. A* 104 (6 2021), p. 063705.
- [285] J. G. Cosme, J. Skulte, and L. Mathey. “Time crystals in a shaken atom-cavity system”. In: *Phys. Rev. A* 100 (5 2019), p. 053615.
- [286] E. J. Davis et al. “Photon-Mediated Spin-Exchange Dynamics of Spin-1 Atoms”. In: *Phys. Rev. Lett.* 122 (1 2019), p. 010405.
- [287] E. J. Davis et al. “Protecting Spin Coherence in a Tunable Heisenberg Model”. In: *Phys. Rev. Lett.* 125 (6 2020), p. 060402.
- [288] M. A. Perlin et al. “Engineering infinite-range SU (n) interactions with spin-orbit-coupled fermions in an optical lattice”. In: *Physical Review A* 105.2 (9 2022), p. 023326.
- [289] D. Hemmer et al. “Squeezing the angular momentum of an ensemble of complex multilevel atoms”. In: *Phys. Rev. A* 104 (2 2021), p. 023710.
- [290] L. M. Norris et al. “Enhanced Squeezing of a Collective Spin via Control of Its Qudit Subsystems”. In: *Phys. Rev. Lett.* 109 (17 2012), p. 173603.
- [291] M. A. Norcia et al. “Frequency Measurements of Superradiance from the Strontium Clock Transition”. In: *Phys. Rev. X* 8 (2 2018), p. 021036.
- [292] F. Brennecke et al. “Real-time observation of fluctuations at the driven-dissipative Dicke phase transition”. In: *Proceedings of the National Academy of Sciences* 110.29 (9 2013), pp. 11763–11767.
- [293] J. Léonard et al. “Monitoring and manipulating Higgs and Goldstone modes in a supersolid quantum gas”. In: *Science* 358.6369 (9 2017), pp. 1415–1418.
- [294] R. M. Kroeze et al. “Spinor Self-Ordering of a Quantum Gas in a Cavity”. In: *Phys. Rev. Lett.* 121 (16 2018), p. 163601.
- [295] M. Landini et al. “Formation of a Spin Texture in a Quantum Gas Coupled to a Cavity”. In: *Phys. Rev. Lett.* 120 (22 2018), p. 223602.
- [296] K. Baumann et al. “Exploring Symmetry Breaking at the Dicke Quantum Phase Transition”. In: *Phys. Rev. Lett.* 107 (14 2011), p. 140402.
- [297] J. Klinder et al. “Observation of a Superradiant Mott Insulator in the Dicke-Hubbard Model”. In: *Phys. Rev. Lett.* 115 (23 2015), p. 230403.

- [298] V. D. Vaidya et al. “Tunable-Range, Photon-Mediated Atomic Interactions in Multimode Cavity QED”. In: *Phys. Rev. X* 8 (1 2018), p. 011002.
- [299] D Nagy et al. “Self-organization of a laser-driven cold gas in a ring cavity”. In: *Europhysics Letters (EPL)* 74.2 (9 Apr. 2006), pp. 254–260.
- [300] D. Nagy, G. Szirmai, and P. Domokos. “Self-organization of a Bose-Einstein condensate in an optical cavity”. In: *The European Physical Journal D* 48.1 (9 Apr. 2008), pp. 127–137.
- [301] J. Klinder et al. “Dynamical phase transition in the open Dicke model”. In: *Proceedings of the National Academy of Sciences* 112.11 (9 2015), pp. 3290–3295.
- [302] M. R. Bakhtiari et al. “Nonequilibrium phase transition of interacting bosons in an intra-cavity optical lattice”. In: *Phys. Rev. Lett.* 114.12 (9 2015), p. 123601.
- [303] M. A. Norcia et al. “Cavity-mediated collective spin-exchange interactions in a strontium superradiant laser”. In: *Science* 361.6399 (9 July 2018), pp. 259–262.
- [304] J. A. Muniz et al. “Exploring dynamical phase transitions with cold atoms in an optical cavity”. In: *Nature* 580.7805 (9 2020), pp. 602–607.
- [305] Z. Zhiqiang et al. “Nonequilibrium phase transition in a spin-1 Dicke model”. In: *Optica* 4.4 (9 2017), pp. 424–429.
- [306] K. C. Cox et al. “Deterministic squeezed states with collective measurements and feedback”. In: *Phys. Rev. Lett.* 116.9 (9 2016), p. 093602.
- [307] R. J. Lewis-Swan et al. “Robust Spin Squeezing via Photon-Mediated Interactions on an Optical Clock Transition”. In: *Phys. Rev. Lett.* 121 (7 2018), p. 070403.
- [308] E. Pedrozo-Peña et al. “Entanglement on an optical atomic-clock transition”. In: *Nature* 588.7838 (9 2020), pp. 414–418.
- [309] S. Colombo et al. “Time-reversal-based quantum metrology with many-body entangled states”. In: *Nature Physics* 18.8 (9 2022), pp. 925–930.
- [310] G. Barontini et al. “Deterministic generation of multiparticle entanglement by quantum Zeno dynamics”. In: *Science* 349.6254 (9 Sept. 2015), pp. 1317–1321.
- [311] O. Hosten et al. “Quantum phase magnification”. In: *Science* 352.6293 (9 June 2016), pp. 1552–1555.
- [312] I. D. Leroux, M. H. Schleier-Smith. “Implementation of Cavity Squeezing of a Collective Atomic Spin”. In: *Phys. Rev. Lett.* 104 (7 2010), p. 073602.
- [313] H. Keßler et al. “Observation of a dissipative time crystal”. In: *Phys. Rev. Lett.* 127.4 (7 2021), p. 043602.
- [314] P. Kongkhambut et al. “Observation of a continuous time crystal”. In: *Science* 377.6606 (7 Aug. 2022), pp. 670–673.
- [315] N. Dogra et al. “Dissipation-induced structural instability and chiral dynamics in a quantum gas”. In: *Science* 366.6472 (7 Dec. 2019), pp. 1496–1499.

- [316] D. Dreon et al. “Self-oscillating pump in a topological dissipative atom–cavity system”. In: *Nature* 608.7923 (7 Aug. 2022), pp. 494–498.
- [317] Y. Guo et al. “Sign-changing photon-mediated atom interactions in multimode cavity quantum electrodynamics”. In: *Phys. Rev. Lett.* 122.19 (7 2019), p. 193601.
- [318] B. P. Marsh et al. “Enhancing associative memory recall and storage capacity using confocal cavity QED”. In: *Physical Review X* 11.2 (7 2021), p. 021048.
- [319] P. Wolf et al. “Observation of Subradiant Atomic Momentum States with Bose-Einstein Condensates in a Recoil Resolving Optical Ring Resonator”. In: *Phys. Rev. Lett.* 121 (17 2018), p. 173602.
- [320] Z. Zhang et al. “Dicke-model simulation via cavity-assisted Raman transitions”. In: *Phys. Rev. A* 97 (4 2018), p. 043858.
- [321] F. Ferri et al. “Emerging Dissipative Phases in a Superradiant Quantum Gas with Tunable Decay”. In: *Phys. Rev. X* 11 (4 2021), p. 041046.
- [322] J. Marino et al. “Spectrum, Landau–Zener theory and driven-dissipative dynamics of a staircase of photons”. In: *New Journal of Physics* 21.1 (7 2019), p. 013009.
- [323] A. Periwal et al. “Programmable interactions and emergent geometry in an array of atom clouds”. In: *Nature* 600.7890 (7 2021), pp. 630–635.
- [324] K. Seetharam et al. “Dynamical scaling of correlations generated by short- and long-range dissipation”. In: *Phys. Rev. B* 105 (18 2022), p. 184305.
- [325] J. Marino. “Universality Class of Ising Critical States with Long-Range Losses”. In: *Phys. Rev. Lett.* 129 (5 2022), p. 050603.
- [326] E. A. Yuzbashyan et al. “Quantum quench phase diagrams of an *s*-wave BC-S-BEC condensate”. In: *Phys. Rev. A* 91 (3 2015), p. 033628.
- [327] J. Dukelsky, S. Pittel, and G. Sierra. “Colloquium: Exactly solvable Richardson–Gaudin models for many-body quantum systems”. In: *Rev. Mod. Phys.* 76 (3 2004), pp. 643–662.
- [328] R. Richardson. “New Class of Solvable and Integrable Many-Body Models”. In: *arXiv preprint cond-mat/0203512* 104 (7 2002), p. 073602.
- [329] R. A. Barankov and L. S. Levitov. “Synchronization in the BCS Pairing Dynamics as a Critical Phenomenon”. In: *Phys. Rev. Lett.* 96 (23 2006), p. 230403.
- [330] R. A. Barankov, L. S. Levitov, and B. Z. Spivak. “Collective Rabi Oscillations and Solitons in a Time-Dependent BCS Pairing Problem”. In: *Phys. Rev. Lett.* 93 (16 2004), p. 160401.
- [331] M. Gaudin. “Diagonalisation d'une classe d'hamiltoniens de spin”. In: *Journal de Physique* 37.10 (7 1976), pp. 1087–1098.
- [332] R. Richardson and N. Sherman. “Exact eigenstates of the pairing-force Hamiltonian”. In: *Nuclear Physics* 52 (7 1964), pp. 221–238.

- [333] E. A. Yuzbashyan, O. Tsyplyatyev, and B. L. Altshuler. "Relaxation and Persistent Oscillations of the Order Parameter in Fermionic Condensates". In: *Phys. Rev. Lett.* 96 (9 2006), p. 097005.
- [334] E. A. Yuzbashyan et al. "Solution for the dynamics of the BCS and central spin problems". In: *Journal of Physics A: Mathematical and General* 38.36 (7 2005), pp. 7831–7849.
- [335] E. A. Yuzbashyan et al. "Nonequilibrium cooper pairing in the nonadiabatic regime". In: *Phys. Rev. B* 72 (22 2005), 220503(R).
- [336] S. P. Kelly et al. "Resonant light enhances phase coherence in a cavity QED simulator of fermionic superfluidity". In: *arXiv preprint arXiv:2202.05851* 104 (7 2022), p. 073602.
- [337] S. Smale et al. "Observation of a transition between dynamical phases in a quantum degenerate Fermi gas". In: *Science advances* 5.8 (7 2019), eaax1568.
- [338] F. Piazza and H. Ritsch. "Self-Ordered Limit Cycles, Chaos, and Phase Slippage with a Superfluid inside an Optical Resonator". In: *Phys. Rev. Lett.* 115 (16 2015), p. 163601.
- [339] B. Zhu et al. "Dicke time crystals in driven-dissipative quantum many-body systems". In: *New Journal of Physics* 21.7 (7 July 2019), p. 073028.
- [340] K. Tucker et al. "Shattered time: can a dissipative time crystal survive many-body correlations?" In: *New Journal of Physics* 20.12 (7 Dec. 2018), p. 123003.
- [341] O. Chelpanova et al. "Intertwining of lasing and superradiance under spintronic pumping". In: *Phys. Rev. B* 108 (10 2023), p. 104302.
- [342] A. Lerose et al. "Chaotic Dynamical Ferromagnetic Phase Induced by Nonequilibrium Quantum Fluctuations". In: *Phys. Rev. Lett.* 120 (13 2018), p. 130603.
- [343] S. B. Jäger et al. "Dynamical Phase Transitions to Optomechanical Superradiance". In: *Phys. Rev. Lett.* 123 (5 2019), p. 053601.
- [344] S. B. Jäger, M. J. Holland, and G. Morigi. "Superradiant optomechanical phases of cold atomic gases in optical resonators". In: *Phys. Rev. A* 101 (2 2020), p. 023616.
- [345] E. I. R. Chiacchio and A. Nunnenkamp. "Dissipation-Induced Instabilities of a Spinor Bose-Einstein Condensate Inside an Optical Cavity". In: *Phys. Rev. Lett.* 122 (19 2019), p. 193605.
- [346] V. Ceban, P. Longo, and M. A. Macovei. "Fast phonon dynamics of a nanomechanical oscillator due to cooperative effects". In: *Phys. Rev. A* 95 (2 2017), p. 023806.
- [347] R. J. Lewis-Swan et al. "Cavity-QED Quantum Simulator of Dynamical Phases of a Bardeen-Cooper-Schrieffer Superconductor". In: *Phys. Rev. Lett.* 126 (17 2021), p. 173601.

- [348] A. Shankar et al. “Simulating Dynamical Phases of Chiral $p+ip$ Superconductors with a Trapped ion Magnet”. In: *PRX Quantum* 3 (4 2022), p. 040324.
- [349] E. Ibarra-García-Padilla et al. “Universal thermodynamics of an $SU(N)$ Fermi-Hubbard model”. In: *Phys. Rev. A* 104 (4 2021), p. 043316.
- [350] K. R. A. Hazzard et al. “High-temperature properties of fermionic alkaline-earth-metal atoms in optical lattices”. In: *Phys. Rev. A* 85 (4 2012), 041604(R).
- [351] L. Bonnes et al. “Adiabatic Loading of One-Dimensional $SU(N)$ Alkaline-Earth-Atom Fermions in Optical Lattices”. In: *Phys. Rev. Lett.* 109 (20 2012), p. 205305.
- [352] S.-K. Yip, B.-L. Huang, and J.-S. Kao. “Theory of $SU(N)$ Fermi liquids”. In: *Phys. Rev. A* 89 (4 2014), p. 043610.
- [353] M. Mamaev et al. *Resonant dynamics of strongly interacting $SU(n)$ fermionic atoms in a synthetic flux ladder*. 2022.
- [354] A. Chu et al. *Photon-mediated correlated hopping in a synthetic ladder*. 2022.
- [355] L. Pezzè et al. “Quantum metrology with nonclassical states of atomic ensembles”. In: *Rev. Mod. Phys.* 90 (3 2018), p. 035005.
- [356] J. F. Rodriguez-Nieva, A. P. Orioli, and J. Marino. “Universal prethermal dynamics and self-similar relaxation in the two-dimensional Heisenberg model”. In: *arXiv preprint arXiv:2106.00023* 104 (7 2021), p. 073602.
- [357] M. Reitz, C. Sommer, and C. Genes. “Langevin Approach to Quantum Optics with Molecules”. In: *Phys. Rev. Lett.* 122 (20 2019), p. 203602.
- [358] J. A. Campos-Gonzalez-Angulo, R. F. Ribeiro, and J. Yuen-Zhou. “Generalization of the Tavis–Cummings model for multi-level anharmonic systems”. In: *New Journal of Physics* 23.6 (7 2021), p. 063081.
- [359] C. Cohen-Tannoudji, J. Dupont-Roc, and G. Grynberg. *Atom—Photon Interactions*. Vol. 104. Wiley, Apr. 1998, p. 073602.
- [360] F. Brennecke et al. “Cavity QED with a Bose–Einstein condensate”. In: *Nature* 450.7167 (7 Nov. 2007), pp. 268–271.
- [361] H. Zhang and C. D. Batista. “Classical spin dynamics based on $SU(N)$ coherent states”. In: *Physical Review B* 104.10 (7 2021), p. 104409.
- [362] K. Huang. *Introduction to statistical physics*. Vol. 104. Chapman and Hall/CRC, 2009, p. 073602.
- [363] M. C. Gutzwiller. “Effect of Correlation on the Ferromagnetism of Transition Metals”. In: *Phys. Rev. Lett.* 10 (5 1963), pp. 159–162.
- [364] B. Sciolla and G. Biroli. “Dynamical transitions and quantum quenches in mean-field models”. In: *Journal of Statistical Mechanics: Theory and Experiment* 2011.11 (7 Nov. 2011), P11003.
- [365] P. Zapletal, A. Nunnenkamp, and M. Brunelli. “Stabilization of Multimode Schrödinger Cat States Via Normal-Mode Dissipation Engineering”. In: *PRX Quantum* 3 (1 2022), p. 010301.

- [366] L. Pezzè et al. "Heralded Generation of Macroscopic Superposition States in a Spinor Bose-Einstein Condensate". In: *Phys. Rev. Lett.* 123 (26 2019), p. 260403.
- [367] B. C. Sanders. "Entangled coherent states". In: *Phys. Rev. A* 45 (9 1992), pp. 6811–6815.
- [368] B. C. Sanders. "Review of entangled coherent states". In: *Journal of Physics A: Mathematical and Theoretical* 45.24 (7 May 2012), p. 244002.
- [369] V. Dodonov. "Nonclassical states in quantum optics: asqueezed'review of the first 75 years". In: *Journal of Optics B: Quantum and Semiclassical Optics* 4.1 (7 2002), R1.
- [370] J. A. Scaramazza, P. Smacchia, and E. A. Yuzbashyan. "Consequences of integrability breaking in quench dynamics of pairing Hamiltonians". In: *Phys. Rev. B* 99 (5 2019), p. 054520.
- [371] Y. Dong et al. "Dynamical phases in quenched spin-orbit-coupled degenerate Fermi gas". In: *Nature communications* 6.1 (7 2015), pp. 1–9.
- [372] A. Zabalo and E. A. Yuzbashyan. "Time reversal symmetry protected chaotic fixed point in the quench dynamics of a topological p -wave superfluid". In: *Phys. Rev. B* 104 (10 2021), p. 104505.
- [373] H. Goldstein, C. Poole, and J. Safko. *Classical Mechanics*. Vol. 104. Addison Wesley, 2002, p. 073602.
- [374] V. I. Arnold. *Mathematical Methods of Classical Mechanics*. Vol. 104. Springer New York, 1978, p. 073602.
- [375] O. Babelon, D. Bernard, and M. Talon. *Introduction to Classical Integrable Systems*. Vol. 104. Cambridge University Press, Apr. 2003, p. 073602.
- [376] J. A. Campos-Gonzalez-Angulo and J. Yuen-Zhou. "Generalization of the Tavis–Cummings model for multi-level anharmonic systems: Insights on the second excitation manifold". In: *The Journal of Chemical Physics* 156.19 (7 2022), p. 194308.
- [377] N. M. Bogoliubov, R. K. Bullough, and J Timonen. "Exact solution of generalized Tavis - Cummings models in quantum optics". In: *Journal of Physics A: Mathematical and General* 29.19 (7 Oct. 1996), pp. 6305–6312.
- [378] A. Glick, H. Lipkin, and N. Meshkov. "Validity of many-body approximation methods for a solvable model: (III). Diagram summations". In: *Nuclear Physics* 62.2 (7 1965), pp. 211–224.
- [379] C. Emary and T. Brandes. "Chaos and the quantum phase transition in the Dicke model". In: *Physical Review E* 67.6 (7 2003), p. 066203.
- [380] M. A. Bastarrachea-Magnani et al. "Chaos in the Dicke model: quantum and semiclassical analysis". In: *Physica Scripta* 90.6 (7 May 2015), p. 068015.
- [381] J. Chávez-Carlos et al. "Quantum and Classical Lyapunov Exponents in Atom-Field Interaction Systems". In: *Phys. Rev. Lett.* 122 (2 2019), p. 024101.

- [382] S. Pilatowsky-Cameo et al. “Positive quantum Lyapunov exponents in experimental systems with a regular classical limit”. In: *Physical Review E* 101.1 (7 2020), 010202(R).
- [383] J. Chávez-Carlos et al. “Classical chaos in atom-field systems”. In: *Phys. Rev. E* 94 (2 2016), p. 022209.
- [384] Y. Alavirad and A. Lavasani. “Scrambling in the Dicke model”. In: *Physical Review A* 99.4 (7 2019), p. 043602.
- [385] M. A. Bastarrachea-Magnani et al. “Delocalization and quantum chaos in atom-field systems”. In: *Phys. Rev. E* 93 (2 2016), p. 022215.
- [386] S. Lerma-Hernández et al. “Dynamical signatures of quantum chaos and relaxation time scales in a spin-boson system”. In: *Physical Review E* 100.1 (7 2019), p. 012218.
- [387] M. A. Bastarrachea-Magnani et al. “Regularity and chaos in cavity QED”. In: *Physica Scripta* 92.5 (7 Apr. 2017), p. 054003.
- [388] P. Barmettler, D. Fioretto, and V. Gritsev. “Non-equilibrium dynamics of Gaudin models”. In: *EPL (Europhysics Letters)* 104.1 (7 Oct. 2013), p. 10004.
- [389] R. Bonifacio and G. Preparata. “Coherent Spontaneous Emission”. In: *Phys. Rev. A* 2 (2 1970), pp. 336–347.
- [390] J. Keeling. “Quantum corrections to the semiclassical collective dynamics in the Tavis-Cummings model”. In: *Phys. Rev. A* 79 (5 2009), p. 053825.
- [391] M. O. Scully and M. S. Zubairy. *Quantum optics*. 1999.
- [392] A. Das et al. “Infinite-range Ising ferromagnet in a time-dependent transverse magnetic field: Quench and ac dynamics near the quantum critical point”. In: *Phys. Rev. B* 74 (14 2006), p. 144423.
- [393] S. P. Kelly, E. Timmermans, and S.-W. Tsai. “Detecting macroscopic indefiniteness of cat states in bosonic interferometers”. In: *Phys. Rev. A* 100 (3 2019), p. 032117.
- [394] S. P. Kelly, E. Timmermans, and S.-W. Tsai. “Thermalization and its breakdown for a large nonlinear spin”. In: *Phys. Rev. A* 102 (5 2020), p. 052210.
- [395] N. Defenu et al. “Dynamical Critical Scaling of Long-Range Interacting Quantum Magnets”. In: *Phys. Rev. Lett.* 121 (24 2018), p. 240403.
- [396] A. E. Tarkhov, S. Wimberger, and B. V. Fine. “Extracting Lyapunov exponents from the echo dynamics of Bose-Einstein condensates on a lattice”. In: *Phys. Rev. A* 96 (2 2017), p. 023624.
- [397] P. Gaspard. “Chaos, scattering and statistical mechanics”. In: *Chaos* 104 (7 2005), p. 073602.
- [398] A. M. Rey et al. “Many-body protected entanglement generation in interacting spin systems”. In: *Phys. Rev. A* 77 (5 2008), p. 052305.

- [399] G. Bentsen et al. “Treelike Interactions and Fast Scrambling with Cold Atoms”. In: *Phys. Rev. Lett.* 123 (13 2019), p. 130601.
- [400] K. Seetharam et al. “Correlation engineering via nonlocal dissipation”. In: *Physical Review Research* 4.1 (7 2022), p. 013089.
- [401] S. P. Kelly et al. “Stroboscopic aliasing in long-range interacting quantum systems”. In: *SciPost Phys. Core* 4 (7 2021), p. 021.
- [402] R. Khasseh, A. Russomanno, and R. Fazio. “Fragility of classical Hamiltonian period doubling to quantum fluctuations”. In: *Phys. Rev. B* 104 (13 2021), p. 134309.
- [403] G. Passarelli et al. *Dissipative time crystals with long-range Lindbladians*. 2022.
- [404] G. Bentsen et al. “Integrable and Chaotic Dynamics of Spins Coupled to an Optical Cavity”. In: *Phys. Rev. X* 9 (4 2019), p. 041011.
- [405] P. Strack and S. Sachdev. “Dicke Quantum Spin Glass of Atoms and Photons”. In: *Phys. Rev. Lett.* 107 (27 2011), p. 277202.
- [406] S. Gopalakrishnan, B. L. Lev, and P. M. Goldbart. “Frustration and Glassiness in Spin Models with Cavity-Mediated Interactions”. In: *Phys. Rev. Lett.* 107 (27 2011), p. 277201.
- [407] S. P. Kelly, R. Nandkishore, and J. Marino. “Exploring many-body localization in quantum systems coupled to an environment via Wegner-Wilson flows”. In: *Nuclear Physics B* 951 (7 Feb. 2020), p. 114886.
- [408] M. Buchhold et al. “Dicke-model quantum spin and photon glass in optical cavities: Nonequilibrium theory and experimental signatures”. In: *Phys. Rev. A* 87 (6 2013), p. 063622.
- [409] J. Marino et al. “Dynamical phase transitions in the collisionless pre-thermal states of isolated quantum systems: theory and experiments”. In: *Reports on Progress in Physics* 85.11 (7 Oct. 2022), p. 116001.
- [410] W. Berdanier, J. Marino, and E. Altman. “Universal Dynamics of Stochastically Driven Quantum Impurities”. In: *Phys. Rev. Lett.* 123 (23 2019), p. 230604.
- [411] M. Fishman, S. R. White, and E. M. Stoudenmire. “The ITensor Software Library for Tensor Network Calculations”. In: *SciPost Phys. Codebases* 104 (7 2022), p. 4.